*NASA Conference Publication 2423*
*Revised*

# 20th Aerospace Mechanisms Symposium

*Proceedings of a symposium hosted by*
*Lewis Research Center*
*Cleveland, Ohio*
*May 7-9, 1986*

Lockheed

NASA

*NASA Conference Publication 2423*
*Revised*

# 20th Aerospace Mechanisms Symposium

*Proceedings of a symposium cosponsored by National Aeronautics and Space Administration, the California Institute of Technology, and Lockheed Missiles and Space Company, Inc., and hosted by Lewis Research Center May 7-9, 1986*

NASA
National Aeronautics and Space Administration
**Scientific and Technical Information Branch**
1986

"For some inexplicable reason, when dealing with a multimillion-dollar piece of equipment the part that fails is always a seven-dollar seal, a seventy-cent bolt, or even more likely, a seven-cent solder joint."
-Norman Augustine, Augustine's Laws, 1983.

## PREFACE

Twenty years ago this month, symposium founders, Dr. George Herzl of Lockheed Missiles & Space Company and Dr. William J. Schimandle of the Jet Propulsion Laboratory, held the first Aerospace Mechanisms Symposium at the University of Santa Clara. Their original goal of bringing leading developers and users of aerospace mechanisms together in order to collectively share their design, development, and operational experiences is still the primary focus of this symposium.

In many ways, it is remarkable that a small, self-supported colloquium such as ours, devoted to a specialized and sometimes under appreciated subject, has enjoyed sustained support and interest from the aerospace community at large. This must be due in part to the dedication of the Lockheed people who continue to provide the impetus and continuity for this symposium from year to year and from location to location. Unquestionably, the efforts and support of the Symposium Organizing Committee, representing government, industry, and academia on both sides of the Atlantic Ocean, is yet another factor. One more important ingredient is the people who give freely of their time to speak and to attend.

However, perhaps the most cogent reason for us to continue to reconvene this symposium lies in the recognition, some 20 years later, that there is still a pressing need to make our spacecraft even more capable and reliable. We are all painfully reminded of this point in the wake of STS 51-L mission tragedy. This is not to imply that progress has been lacking in the design and application of aerospace mechanisms. On the contrary, one merely has to examine the ongoing wave of technical advances in the underlying disciplines to appreciate the growth in this area. Notable technical strides have been made in electromagnetics, tribology, computer simulation, structural analysis, material sciences, digital controls, and robotics, to mention a few.

The real art of our craft lies first in the ability to recognize the utility of such accomplishments and second in the ability to know how to best apply them to meet the operational requirements at hand. In light of these critical traits, our aim has been to showcase recent accomplishments in the supporting technical disciplines and to illustrate, by prior example, the application of new design approaches. This will likely continue to be the hallmark of this continuous series of symposia.

To this end, on May 7-9, 1986, the 20th Aerospace Mechanisms Symposium, cosponsored by the National Aeronautics and Space Administration, the California Institute of Technology, and the Lockheed Missiles & Space Company, was hosted by the NASA Lewis Research Center in Cleveland, Ohio. NASA Lewis now takes its rightful place with the other NASA centers who have hosted this Symposium at least once. Participants from West Germany, The Netherlands, Great Britain, Switzerland, Japan, and elsewhere joined their United States industry, government, and academia counterparts to hear 22 formal technical presentations, contribute to a special panel discussion, exchange technical points of view, and become acquainted both professionally and socially.

As documented in this Proceedings, a diversity of topics was addressed. These included deployable structures, electromagnetic devices, tribology, thermal/mechanical/hydraulic actuators, latching devices, positioning mechanisms, robotic manipulators, and computerized mechanisms synthesis. In addition, a discussion led by an international team of distinguished experts was conducted to help illuminate future trends and directions in mechanism technology. This panel, ably led by Mr. H. Mervyn Briscoe, retired from the European Space Research & Technology Center, featured Dr. Werner Auer from Teldix GmbH, West Germany; Mr. Daniel P. Kuban, Oakridge National Laboratory; and Mr. Phillip Studder, NASA Goddard Space Flight Center.

The strength and real foundation of every conference is centered on the people who help plan, promote, conduct, and participate in it. The most visible are the program participants. The authors, who are obviously the essential ingredient, deserve special recognition for their long, hard hours of effort, often transparent to many of us. Acknowledgement is also due for the contributions made on the part of the session chairmen. They are Dr. Werner Auer of Teldix GmbH, West Germany; Mr. Howard M. Jones, Spar Aerospace Ltd., Canada; Mr. Ervin V. Zaretsky, NASA Lewis Research Center; Mr. William H. Teimer, Allied-Bendix Aerospace Guidance Division; Mr. John C. Stammreich, Rexnord-TAM; and Mr. Barry S. Leonard, Lockheed Missiles & Space Company.

Special thanks to Dr. J. Stuart Fordyce, Director of Aerospace Technology, and Mr. Robert G. Hoffman, Chief of Test Installations Division, for telling us about the people, programs, and facilities at NASA Lewis. Bouquets to Ms. Marcia Smith, Executive Director of the National Commission on Space, who gave freely of her time and energy to present us with the story of the Soviet space programs. Her talk was a memorable contribution to our banquet evening at the Crawford Auto-Aviation Museum.

In addition to the Symposium Organizing Committee, there are numerous people at NASA Lewis, Lockheed, and Cal. Tech. who contributed to the success of this Symposium. Among those at Lewis are members of the Technical Information Services Division, particularly Ms. Marilyn V. Weaver who had editorial responsibility for this Proceedings and Ms. Joan M. Weddle who assisted her. A special debt of gratitude is due Karen Wester, Symposium Coordinator, who who had the often enormous burden of making the necessary arrangements for

conference functions and processing registrants. The assistance of Toni Gerda is also gratefully acknowledged in these matters. Compliments to Ed Wegner of Lockheed, an unsung hero, who continues to surprise us with fresh, eye-catching program layouts year after year. Professors David Welch and Erik Antonsson at Cal. Tech. deserve special recognition for their help with program planning.

Finally, one would be remiss not to recognize the selfless endeavors of Dr. Charles Coale and Mr. Joe Wilson of Lockheed, each of whom has devoted vast quantities of personal time and energy to preserve the high professional quality associated with this symposium. Their collective efforts are the true underpinning of this annual gathering.

Mr. Doug Rohn, a most capable Symposium Vice-Chairman, and the writer express our sincere gratitude to all of those who graciously contributed to the overall success of this symposium.

Stuart H. Loewenthal
Host Chairman

CONTENTS

*SESSION VII*

*Chairman: Mr. Barry S. Leonard, Lockheed Missiles & Space Co.*

## ORGANIZING COMMITTEE

The papers presented at the Symposium were selected and reviewed by the Organizing Committee. Authors are responsible for the content and the technical accuracy of their respective papers. The committee was composed of the following personnel:

| | |
|---|---|
| General Chairman | Charles W. Coale<br>Lockheed Missiles & Space Company |
| Administrative Chairman | David F. Welch<br>California Institute of Technology |
| Operations Chairman | Joseph F. Wilson<br>Lockheed Missiles & Space Company |

Host Center - NASA Lewis Research Center, Cleveland, Ohio

| | |
|---|---|
| Chairman | Stuart H. Loewenthal |
| Vice Chairman | Douglas A. Rohn |
| Symposium Coordinator | Karen J. Wester |

Committee Members

| | |
|---|---|
| Erik K. Antonsson | California Institute of Technology |
| Richard H. Bentall | European Space Research & Technology Centre |
| Thomas F. Bonner, Jr. | NASA Johnson Space Center |
| Kenneth C. Curry | Jet Propulsion Laboratory |
| Charles R. Darwin | NASA Marshall Space Flight Center |
| David F. Englebert | NASA Ames Research Center |
| Harvey H. Horiuchi | Jet Propulsion Laboratory |
| Carl D. Lamb | NASA Marshall Space Flight Center |
| Allen J. Louviere | NASA Johnson Space Center |
| Ronald E. Mancini | NASA Ames Research Center |
| Peter A. Minderman | NASA Kennedy Space Center |

| | |
|---|---|
| Bowden W. Ward, Jr. | NASA Goddard Space Flight Center |
| Nathan D. Watson | NASA Langley Research Center |

Advisory Committee

| | |
|---|---|
| Paul W. Bomke | Jet Propulsion Laboratory |
| Aleck C. Bond (Ret.) | NASA Johnson Space Center |
| H. Mervyn Briscoe (Ret.) | European Space Research & Technology Centre |
| Otto H. Fedor | Lockheed Space Operations Company |
| Angelo Giovannetti (Ret.) | NASA Ames Research Center |
| Frank T. Martin (Ret.) | NASA Goddard Space Flight Center |
| James H. Parks (Ret.) | NASA Langley Research Center |
| Alfred L. Rinaldo | Lockheed Missiles & Space Company |

PROGRAM

WEDNESDAY, 7 MAY 1986

10:00 REGISTRATION AND COFFEE
Grand Ballroom, Harley Hotel -- Cleveland West

12:00 LUNCH (Also Wednesday Authors Luncheon)

1:00 SYMPOSIUM OPENING

INTRODUCTORY REMARKS
Mr. Stuart Loewenthal, Host Chairman
NASA Lewis Research Center
Dr. Charles W. Coale, General Chairman
Lockheed Missiles & Space Co., Sunnyvale, CA

WELCOME
Dr. J. Stuart Fordyce, Director of Aerospace Technology
NASA Lewis Research Center

1:30 SESSION I
Dr. Werner Auer, Session Chairman
TELDIX, GmbH, Heidelberg, West Germany

•Design and Development of a Telescopic Axial Boom
Roland Felkai, MBB/ERNO, Space System Group,
Bremen, West Germany

•Extendable Retractable Telescope Mast for Deployable Structures
Manfred Schmid, Dornier System GmbH,
Friedrichshafen, West Germany
M. Aguirre, European Space Agency/ESTeC,
Noordwijk, The Netherlands

•Design and Test of an Electromagnetic Coupling
William J. Anderson, NASTEC, Inc., Cleveland, OH

3:00 COFFEE BREAK

3:15 SESSION II
Mr. Howard M. Jones, Session Chairman
Spar Aerospace Ltd., Weston, Ontario, Canada

•Slip Ring Experience in Long Duration Space Applications
Damon D. Phinney, Ball Aerospace Systems Division,
Boulder, CO

•The Design and Analysis of a Keel Latch for Use on the Hubble Space Telescope
John A. Calvert and Melanie B. Stinson, NASA Marshall Space Flight Center, Huntsville, AL

•A Mirror Transport Mechanism for Use at Cryogenic Temperatures
Kenneth W. Stark and Meredith Wilson, NASA Goddard Space Flight Center, Greenbelt, MD

•Shutter Mechanism for Calibration of the Cryogenic Diffused Infrared Background Experiment (DIRBE) Instrument
Allen Tyler, NASA Goddard Space Flight Center, Greenbelt MD

7:00 WELCOMING RECEPTION
October Room, Harley Hotel -- Cleveland West

THURSDAY, 8 MAY 1986

7:00 (Thursday Authors Breakfast)

8:00 SESSION III
Mr. Erwin V. Zaretsky, Session Chairman
NASA Lewis Research Center

•Towards an Optimised Sputtered $MoS_2$ Lubricant Film
E.W. Roberts, European Space Tribology Laboratory, Risley, Warrington, England

•Rolling Element Bearings in Space
J.W. Kannel and K.F. Dufrane, Battelle Columbus Division, Columbus, OH

•Duty Cycle Testing and Performance Evaluation of the SM-229 Teleoperator
Robert S. Stoughton, University of California-Santa Barbara, Goleta, CA
Daniel P. Kuban, Oak Ridge National Laboratory, Oak Ridge, TN

•Pseudo-Prototyping of Aerospace Mechanical Dynamic Systems with a Generalized Computer Program
Vikram N. Sohoni and Milton A. Chace, Mechanical Dynamics, Inc., Ann Arbor, MI

10:30 COFFEE BREAK

10:45 SESSION IV

Mr. William H. Teimer, Session Chairman
Allied-Bendix Aerospace, Guidance Div., Teterboro, NJ

•A Dual-Wound DC Brush Motor Gearhead
Barrie W. Henson, European Space Agency/ESTeC,
Noordwijk, The Netherlands

•Redundancy for Electric Motors in Spacecraft Applications
Robert J. Smith and Alastair R. Flew, Moore Reed and Co.,
Ltd., Andover, Hampshire, England

•RF Switch Positioner for Communications Satellite Network
A.G. Storaasli, H.P. Griesser, and R.W. Grant,
Hughes Aircraft Co., El Sequndo, CA

•Evaluation of a High Torque Backlash-Free Roller Actuator
Bruce M. Steinetz and Douglas A. Rohn,
NASA Lewis Research Center
William J. Anderson, NASTEC, Inc., Cleveland, OH

12:45 LUNCHEON

Buffet Luncheon, "Beside the Pool," Harley Hotel

2:00 SESSION V - PANEL DISCUSSION "FUTURE DIRECTIONS IN MECHANISMS"

Moderator:
Mr. H. Mervyn Briscoe, European Space Agency, ESTeC (Ret.)
Panelists:
Dr. Werner Auer, Teldix GmbH, Heidelberg, West Germany
Mr. Daniel P. Kuban, Oakridge National Laboratory
Mr. Phillip Studer, NASA Goddard Space Flight Center

4:00 PREVIEW - Evening Activities

EVENING SOCIAL ACTIVITIES

Crawford Auto-Aviation Museum
10825 East Blvd. (Case Western Reserve Area)

5:00 Bus to the Crawford Museum
6:00 Tour of the Museums: Crawford Auto-Aviation Museum and
Historical Museum
6:30 Social Hour - Lower level, Crawford Museum
7:30 Banquet - Upper level rotunda, Crawford Museum

8:30 Banquet Program
Master of Ceremonies, Mr. Stuart Loewenthal, NASA Lewis Research Center
Introduction of Guest Speaker
Mr. Barry S. Leonard, Director of Spacecraft Engineering, Lockheed Missiles & Space Co., Sunnyvale, CA
Banquet Address - "Soviet Space Programs: Are They Ahead?"
Ms. Marcia Smith, Executive Director of The National Commission on Space, Washington D.C.

FRIDAY, 9 MAY 1986

7:00 (Friday Authors Breakfast)

8:00 SESSION VI
Mr. John C. Stammreich, Session Chairman
Rexnord-TAM, Torrance, CA

•A Precision, Thermally-Activated Driver for Space Application
Robert C. Murray and Robert F. Walsh, PRC Kentron, Aerospace Technologies Div., Hampton, VA
William H. Kinard, NASA Langley Research Center, Hampton, VA

•Space Station Rotary Joint Mechanisms
Glen W. Driskill, Sperry Corp., Aerospace & Marine Group, Phoenix, AZ

•A Hydraulic Mechanism to Limit Torosional Loads Between the IUS and Space Transportation System Orbiter
James R. Farmer, Boeing Aerospace Co., Seattle, WA

•Design and Development of a Large-Diameter, High-Pressure, Fast-Acting Propulsion Valve and Valve Actuator
K.V. Srinivasan, S & Q Corp., Morgan Hill, CA

10:00 COFFEE BREAK

10:15 SESSION VII
Mr. Barry S. Leonard, Session Chairman
Lockheed Missiles & Space Co., Sunnyvale, CA

•Discrete Mechanism Damping Effects in the Solar Array Flight Experiment
Earl D. Pinson, Lockheed Missiles & Space Co., Sunnyvale CA

•A Mechanism for Precise Linear and Angular Adjustment Utilizing Flexures
J.R. Ellis, NASA Lewis Research Center, Cleveland, OH

•Weight and Power Savings Shaft Encoder Interfacing Techniques for Aerospace Applications
Donald H. Breslow, Itek Measurement Systems, Newton, MA

11:45 NASA LEWIS - A CENTER OVERVIEW
Mr. Robert G. Hoffman, Chief of Test Installations Division, NASA Lewis Research Center

HERZL AWARD
Mr. Frank T. Martin, NASA Goddard Space Flight Center (Ret), Greenbelt, MD

CLOSING REMARKS
Mr. Stuart Loewenthal, Host Chairman
NASA Lewis Research Center
Mr. Charles Coale, General Chairman
Lockheed Missiles & Space Co., Sunnyvale, CA

12:30 LUNCH

1:30 TOUR OF NASA LEWIS FACILITIES
Mr. Douglas A. Rohn, Tour Chairman
NASA Lewis Research Center

# DESIGN AND DEVELOPMENT OF A TELESCOPIC AXIAL BOOM

Roland Felkai*

A special telescopic boom has been design-optimized, developed and qualified to carry an S-band Antenna for the DFS-Deutscher Fernmelde Satellit (German Telecommunication Satellite) - KOPERNIKUS. This paper describes the "design driver" requirements, the alternatives investigated and the final technical solution, the tests performed, and identifies the special problem areas encountered during its development.

## INTRODUCTION

The design of the DFS-Boom was driven by the following system/subsystem requirements:

- undeployed length of the boom without antenna of 0.908 meter and deployed length of 1.675 meters. The large undeployed length (limited by the launcher fairing) is designed to provide a limited transmission capability in the event of a failure in the driving/deployment mechanisms. Refer to Figures 1, 2, and 3.

- vertical mounting on the antenna platform as depicted in Figures 1 and 4.

- deployment of the boom just after the separation of the last stage of the launcher (ARIANE 3/4); i.e., during the transfer orbit.

- relatively high stiffness of the boom in order to avoid excessive dynamic cross coupling and the resulting higher or harmful amplifications.

The following basic properties have been determined by test and/or analysis:

- undeployed lateral modes = 55 Hz Requirement ($\geq$ 50 Hz)

- undeployed axial mode = 480 Hz Requirement ($\geq$ 60 Hz)

*MBB-ERNO Space Systems Group, Bremen, West Germany.

- mass $\leq$ 2.6 kg
- minimum thermal deformations $\leq$ 0.5 mm (measured at the top)
- Though retractability of the boom in orbit is not required, it has been incorporated in the design to aid ground testing.
- deployment time: 60 sec. (approximately)
- alignment requirements for the boom; - deflection (measured at the top): $\leq 1°$
  - rotation (measured at the top): $\leq 5°$
- One of the most demanding requirements derives from the integration and guidance of the highly sensitive coaxial cable which is incorporated into the boom. It is required that the minimum bend radius be above 1 in. (25.4 mm) at any stage of stowage or deployment.

## DESCRIPTION OF THE DESIGN

A considerable development effort was spent in finding the best solution for the guidance of the coaxial cable, particularly to satisfy the minimum bend radius requirement.

The final solution, to be described later, crystallized after analysis of a number of alternatives. Thus, for example, in one solution disc-like parts were envisaged to protect individual semicircular cable loops from being forced into a bending radius below the minimum value. Extension and retraction was ensured by means of spiral springs and guide rails (see Fig. 5). Guiding concepts which were based on the "Nuernberger Schere" (lazy tongs) principle were also considered. All these concepts, however, were either too complicated, too heavy, too expensive, or involved too high a risk.

Another solution, which had been favoured for a long time is shown in Figure 6.

The cable penetrates from the antenna platform (see Fig. 4) through the lower plate of the boom into the inner boom space and directly into the cable box, which is positioned along the boom, parallel to the drive. Between the plate and the cable box, the cable attachment is such as to avoid tensile stresses in the cable. In the cable box the cable is stored in a snake-shaped manner; this storage needs a minimum of cable length, since the cable can nearly be drawn straight. Also no torsional loading occurs.

In order to prevent the bending radius of the cable falling below its minimum value ($R_{min} \geq 25.4$ mm) "shaping beads" are attached to the cable. These beads sit loosely over the cable and guide the cable into the snake

form during deployment (and retraction) of the boom. Being a close (sliding) fit with the walls of the cable box they also serve to prevent, during launch, any lateral movements of the cable generated by vibrations. Adjacent beads are linked with wire springs to define the bend radius of the cable and, additionally, to prevent mutual torsion between the beads. Since these beads are attached to the cable with clearance they do not obstruct cable deformation during extension (see Fig. 6).

At the upper end the cable box lead-in section is in the form of a funnel in order to provide guidance to the shaping beads during retraction, and avoid twisting of the cable.

As an additional precaution, the upper end of the cable is fixed with a clamp, to prevent tensile forces loading the connectors.

As it was not certain from theoretical analysis whether this solution would work flawlessly, a simple model was manufactured (see Fig. 7). Tests with this model have shown that the shaping bead guidance system works well.

Although this method of cable guidance fulfilled the functional requirements, a number of additional concepts were investigated in order to find a lighter weight solution. After evaluation of the advantages and disadvantages of all the alternatives, the "centre cable guide" solution crystallized as the final weight-optimum cable guide system.

The centre cable guide concept is a simple and reliable design, meeting all the requirements with the lowest weight and is comprised of the following components:

- two telescopic tubes with guide rings and end connection plates
- cable supports and guide plates
- telescopic drive mechanism
- electrical equipment

The main design features are depicted in Figure 8; a description of the main components is as follows:

### Telescopic Tubes

The main body of the boom consists of two Carbon Fiber Reinforced Plastic (CFRP) tubes. The inner tube is fixed at the bottom end to the Antenna Platform (see Fig. 4) by means of a ribbed Aluminum flange plate, which also provides a mounting facility for the worm gear. In addition, three support plates have been incorporated inside the inner tube. The first carries a motor and a cable guide elbow, the second carries a cable guide having a slot for cable support in the undeployed condition, and the third carries a bracket supporting the cable guide half ring. Further, two guide rings have been incorporated near the top to provide smooth sliding of

the outer tube over the inner tube. A guide rail along the outer surface of the inner tube slides on a machined part of CFRP bonded on the inside surface of the outer tube, which prevents rotation of the outer tube during deployment.

The outer tube is made from CFRP in order to ensure sufficient stiffness, minimum mass, and low thermal deformation. It carries an Aluminum connection plate at its top end as a mounting facility for the S-band Antenna. The cable support guide rail, an Aluminum framework, is hung on the lower side of this connection plate.

It is a peculiarity of this design to have the bigger diameter tube as deployable and the smaller diameter tube as fixed, this being contrary to other more common telescopic booms. This type of arrangement was selected to prevent bending of the coaxial cable beyond its permitted 1 in. radius, to fix the cable supports, and to introduce pre-compression in the outer tube against the inner tube during the launch phase, thus preventing fretting between the tubes. Further, this design approach allows the accommodation of motor plus worm gear drive and cable, etc. inside the inner tube to achieve a compact design solution and a maximum deployment length in comparison with the stowed length.

### Cable Supports and Guides

The support of the coaxial cable needed for the transference of signals to and from the S-band antenna necessitated a guidance and support scheme. This consists of two elbows, one half circular guide and two holding slots in the support plates, fixed in the inner tube at appropriately separated locations. In addition, a support framework is hung from the top S-band connection bracket.

This elaborate arrangement has been dictated by the need to guarantee proper fixation/support of the coaxial cable during launch, to ensure smooth and reliable flexure during deployment and to avoid bending the cable below its allowable minimum radius of 1 in.

### Telescopic Drive Mechanism

This device performs two main functions, namely, deployment of the boom and secondly, precompression of the outer tube against the inner tube, to avoid mutual fretting during launch. The mechanism comprises:

-- DC motor with brake (TRW-Globe, Type 5A3396, Micro Switch Honeywell, Type MS 23547-1 and -2)

-- steel telescopic car antenna (Bosch-modified to suit space application) driven by a wire wrapped in a stiff plastic cover. The top end of this wire is attached to the S-band antenna's mounting plate, the other end being fixed to the drum.

- a plastic drum onto which the wire is wound. This drum is connected to the worm gear transmission.

-- The worm gear shaft is driven by the DC motor, but with one end extending outside the box. Although the design concept is for the motor to provide the necessary pre-compression between the inner and outer tubes, the shaft extension allows this pre-launch adjustment to be done by hand, if necessary.

  By means of special tools, therefore, the worm gear shaft can be torqued so that a predefined tension in the drive core wire can be achieved. This tension in the wire is controlled through strain gauges. The self-blocking behaviour of the worm gear and brakes on the motor shaft avoid unwanted release of the tension in the wire.

-- an aluminum box, which houses the drum, the worm gear and at the same time supports the motor through an adapter bracket. This box is mounted on the fixing flange of the inner tube. The motor and the telescopic antenna are additionally supported within the inner tube by means of a CFRP-bracket.

-- The complete drive mechanism along with the cable and its guides, etc. is fully accommodated inside the inner tube, having fixation brackets at the base and a mounting facility for the payload (here an S-band antenna) on the top of the deployable tube. The design adopted thus provides a very compact telescopic boom assembly.

## Electrical Equipment

In addition to the DC motor mentioned above, there are three switches, two power/signal lines and a cable (Raychem, Type 44, AWG 22 and 26). The lines and the cable are led out of the boom through sockets. These lines provide the motor with electric power and at the same time serve as signal carriers for the switches. In this manner, the boom electrical design is simple, consisting of only a few space-qualified parts.

## FUNCTIONAL DESCRIPTION

For deployment of the boom, an initiating signal is transmitted. This signal releases the motor brakes and starts the motor. The resulting rotation of the drum unwinds the wires of the telescopic drive, thereby deploying the outer tube, which in turn switches a signal line, transmitting confirmation of the deployment process.

A second switch is activated as soon as the outer tube is fully deployed, signifying the end position of the boom. A third switch disconnects the flow of the current to the motor. This last switch was located at such a place that a small overdrive of the motor and/or thermal expansion is possible and admissible.

For the purpose of ground testing, a device in the EGSE circuit (see Fig. 3) was incorporated to limit the current flow to the motor during retraction of the boom. This was necessary to avoid overloading the motor. In this case the end switch was not used, so that precompression could be achieved.

## DEVELOPMENT AND QUALIFICATION TESTS

In order to establish the sensitivity limits of the coaxial cable system and verify the functional capabilities of the envisaged cable storage and guidance devices, several component tests were performed at an early stage. These included the determination of the load capability of the drive, and the frictional resistance of all moving elements.

With the full-scale, qualification model, manufactured to flight-product assurance standards, the following development and qualification tests were performed:

### 1. Electromechanical Functional Test

The parameters of the deployment were measured in ambient and in thermal vacuum environments. The margins in the load-carrying capability of the drive, the deployment time, the alignment at the top of the boom, and the input electrical current and voltage were determined.

The following main results were obtained:

| | |
|---|---|
| Minimum compressive force margin: | 100 N |
| Deployment time: | 45 sec. |
| Deployment qualification | |
| Temperature range: | $-5°C \leq T \leq +60°C$ |
| Vacuum: | $10^{-5}$ mbar = $10^{-3}$ Pascal |

### 2. Vibration Test (see Fig. 10)

The general behaviour of the boom during simulated lift-off was investigated during sine and random vibration testing with the following results:

Inputs

| | |
|---|---|
| Sine frequency range: | 5 - 100 Hz |
| Maximum input excitation: | 6 g lateral |
| | 12 g axial |
| Sweep rate: | 2 oct/min |
| Random frequency range: | 5 - 2000 Hz |
| Input: 0.2 $g^2$/Hz; composite: | 20 $g_{rms}$ |
| Duration: | 2 min/axis |

Results

| | |
|---|---|
| lateral eigenfrequency in stowed position: | 55 Hz |
| axial eigenfrequency in stowed position: | 480 Hz |
| maximum response acceleration: | 57 g at the top of the boom |
| | 100 g (about) at the motor. |

3. Thermal-Vacuum Test in Deployed Position (see Fig. 11)

This test simulated thermal conditions to be experienced during the mission. The aim of this test was to show that the high thermal deflection difference between aluminum and CFRP would not lead to a delamination or other destruction of parts of the boom. The worst-case temperature range tested was: $-100°C \leq t \leq +100°C$

4. Electromagnetic Cleanliness Test

The aim was to verify the emission and the inrush current values caused by the electromotor.

Before and after tests numbers 2 to 4, the function of the boom was tested with a simple go - no go test.

The boom passed all tests and is now space qualified.

ACKNOWLEDGMENT

The author wished to thank MBB-ERNO for the permission to publish this paper and would also like to acknowledge the assistance of the many engineers and technicians at MBB-ERNO and other companies who contributed to the project.

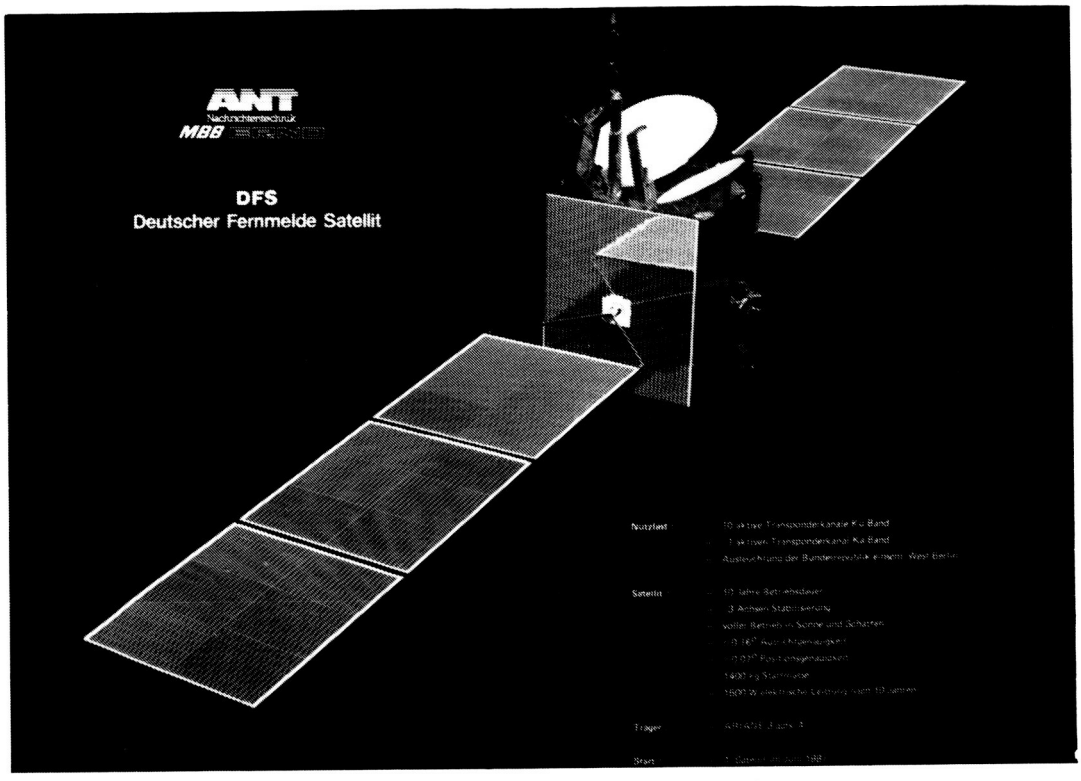


Figure 1. - KOPERNIKUS satellite.

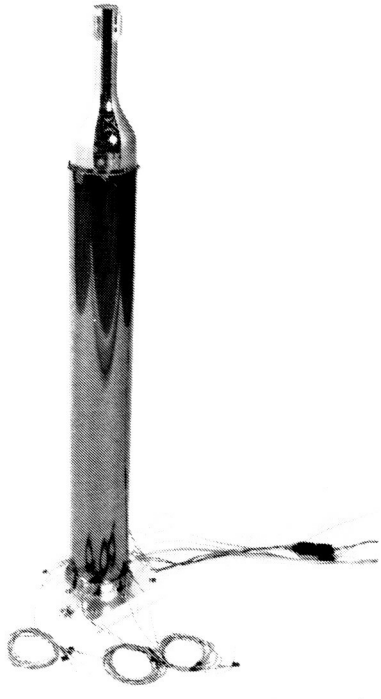

Figure 2. - S-Band antenna boom in stowed position.


Figure 3. - S-Band antenna boom in deployed condition.

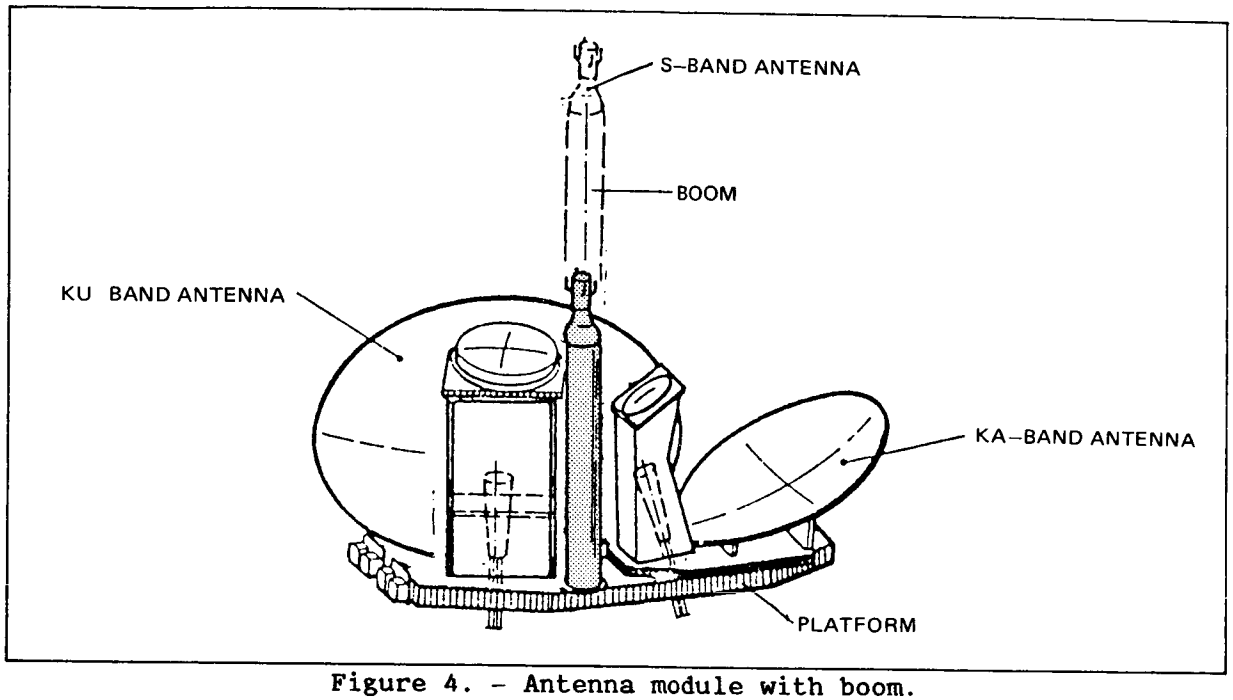


Figure 4. - Antenna module with boom.

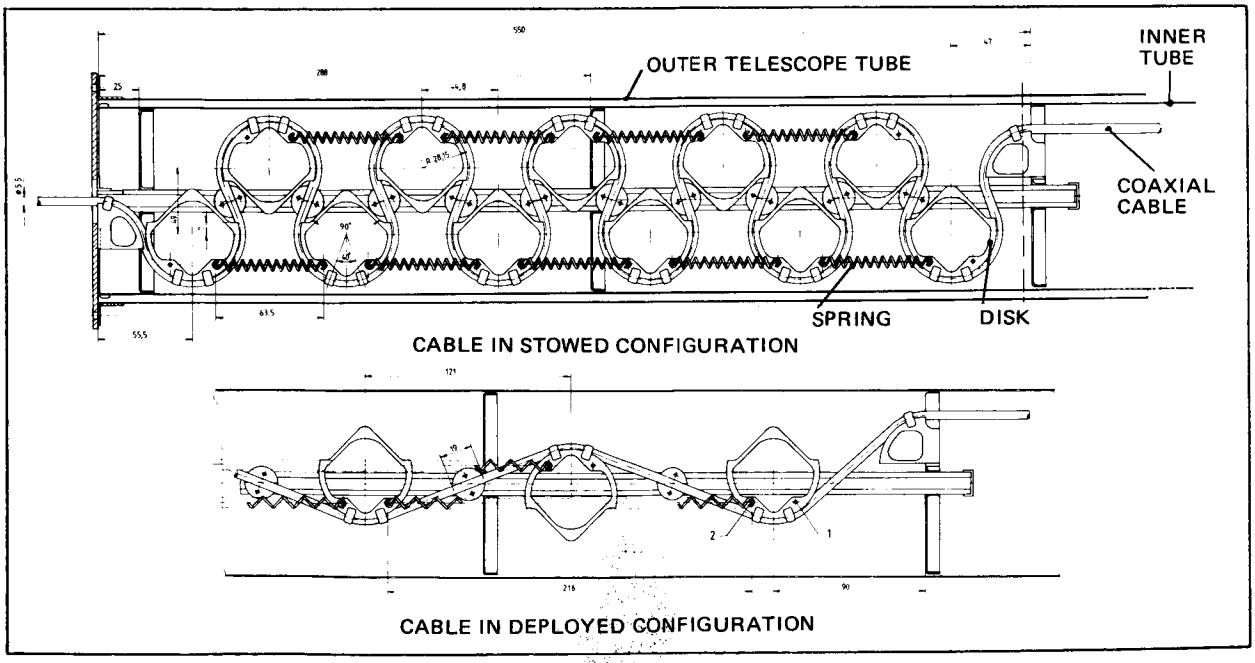


Figure 5. - Cable guidance with discs.

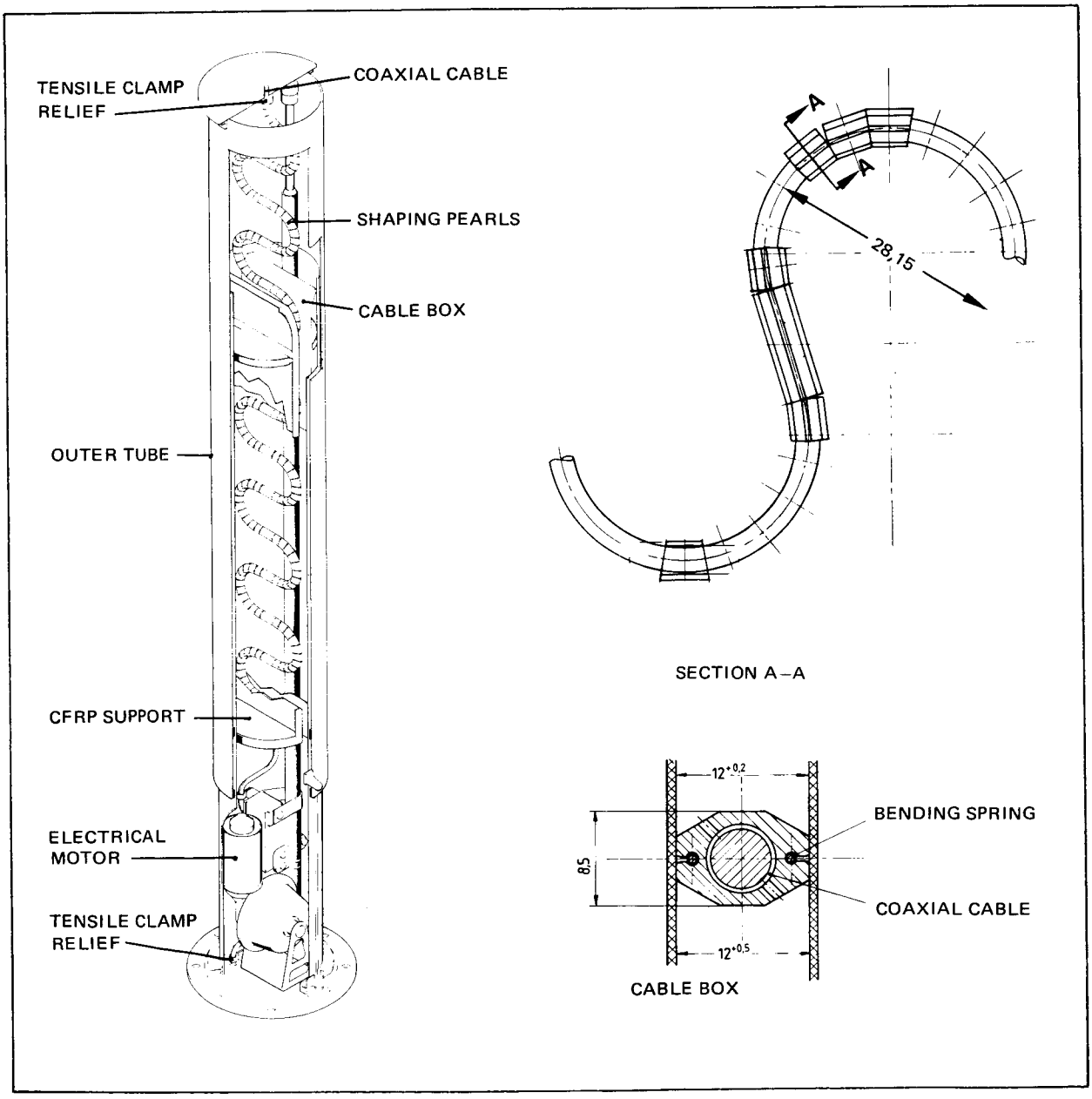


Figure 6. - Boom with cable guidance provided by "shaping beads."

ORIGINAL PAGE IS
OF POOR QUALITY

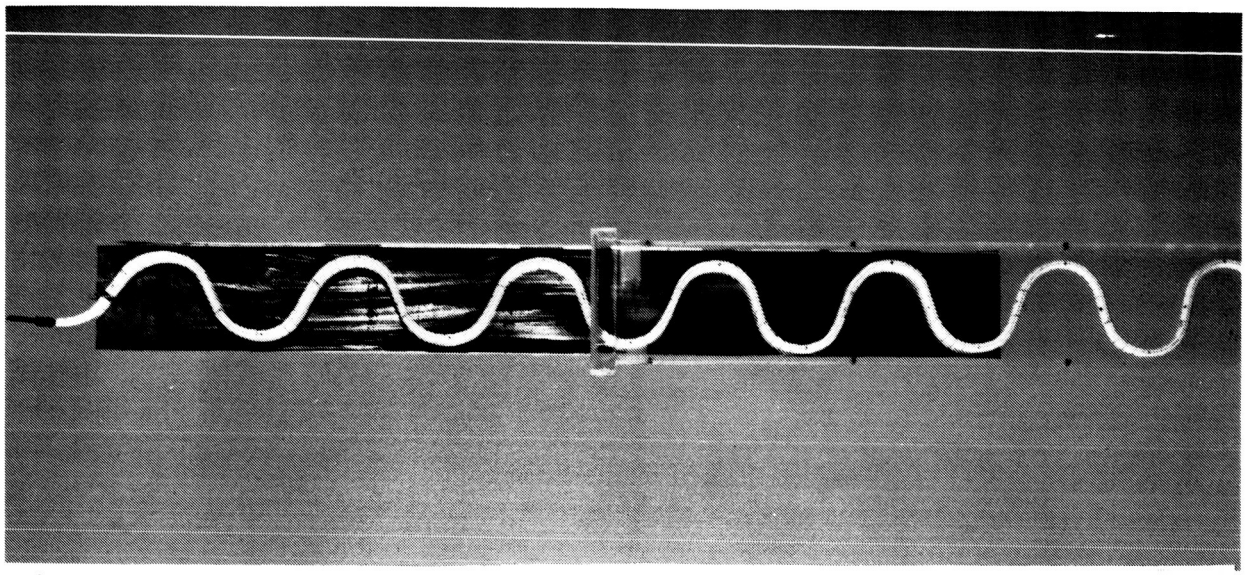

Figure 7. - Simple functional model for shaping bead cable guidance system.

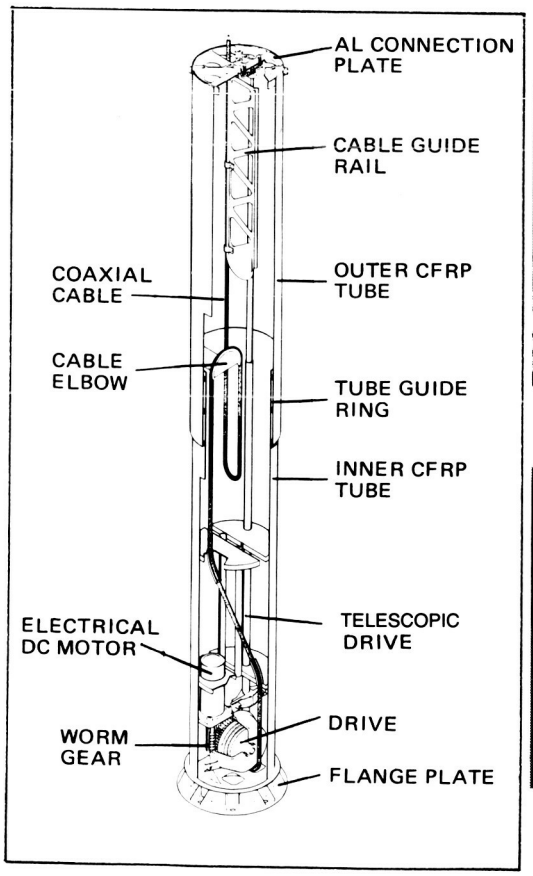


Figure 8. - Final design boom with cable guide rail.

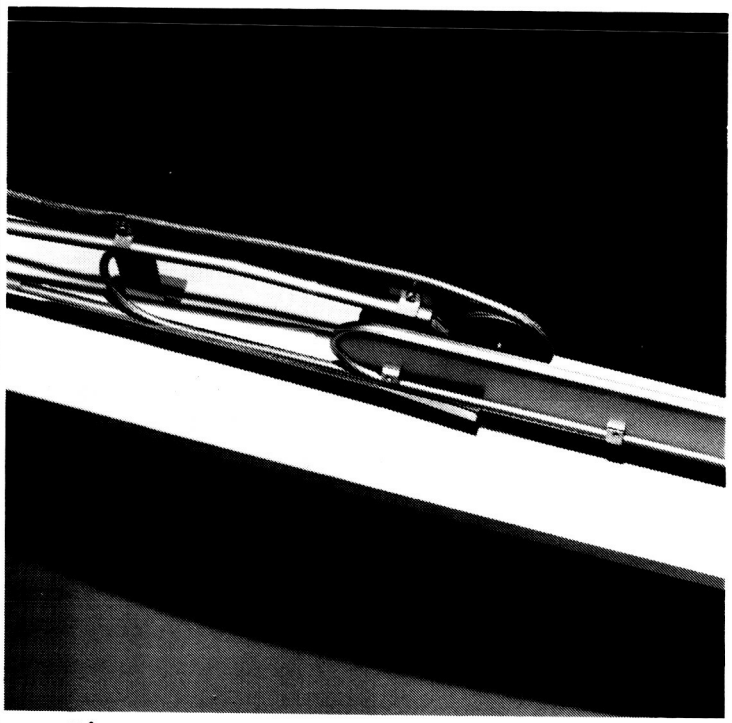

Figure 9. - Simple functional model for solution with cable guide rail.

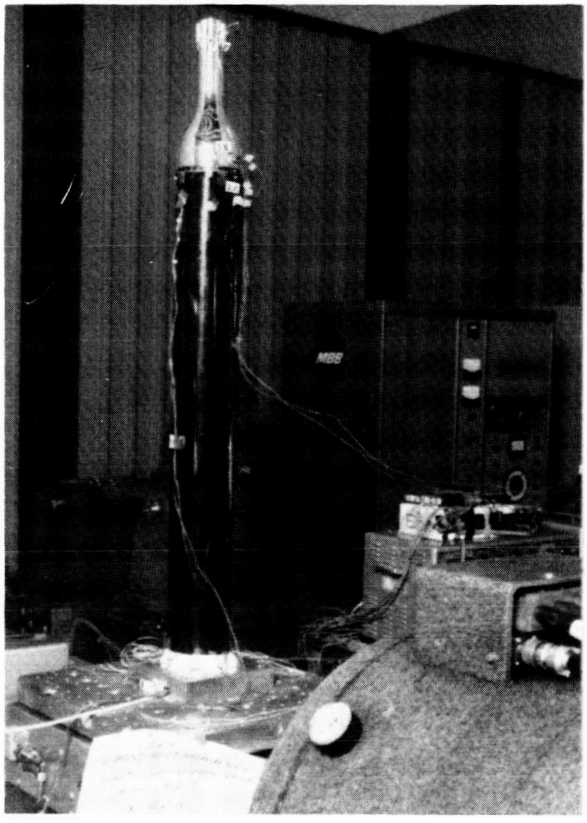

Figure 10. - Vibration test.

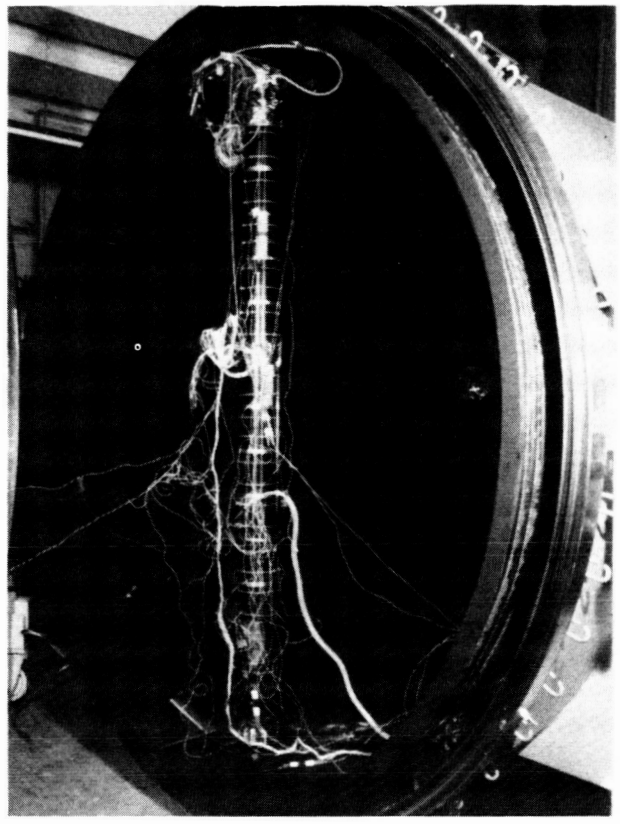

Figure 11. - Thermal vacuum test.

# EXTENDABLE RETRACTABLE TELESCOPIC MAST FOR DEPLOYABLE STRUCTURES

M. Schmid* and M. Aguirre**

The Extendable and Retractable Mast (ERM) which is presently developed by DORNIER in the frame of an ESA-contract, will be used to deploy and retract large foldable structures. The design is based on a telescopic carbon-fibre structure with high stiffness, strength and pointing accuracy. To verify the chosen design, a breadboard model of an ERM was built and tested under thermal vacuum (TV)-conditions. It is planned as a follow-on development to manufacture and test an Engineering Model Mast. The Engineering Model will be used to establish the basis for an ERM-family covering a wide range of requirements.

## INTRODUCTION

The continuous trend to larger, heavier and retrievable spacecraft demands a new generation of strong and stiff masts in order to support large deployable structures. Such Extendable and Retractable Masts are already manufactured at DORNIER for use as radio link masts for ground application (Fig. 1). By developing and refining the deployment principle of these masts to take into account specific space requirements, a design satisfying a wide range of applications can be realized.

This design, which was carried out under cover of an ESA-contract, establishes the basis for a family of masts of use mainly in the carrying of large payloads.

At the present time two main space applications for an Extendable and Retractable Mast are proposed. They are the deployment of a Solar Array and the positioning of an Unfurlable Antenna.

The most important design-drivers were as follows:
- improvement of the state of the art in terms of strength and stiffness per unit deployed mass
- small total mass and stowed volume
- high interface adaptability
- need for tubes built from advanced composite materials
- high deployment length
- high number of possible deployment/retraction cycles
- good pointing accuracy

*) DORNIER SYSTEM GmbH, Friedrichshafen, Germany.
**) ESTEC, Noordwijk, Netherlands.

## TECHNICAL CONCEPT

The ERM is defined as a hybrid structural/mechanical device that can be stored in a minimum volume whilst yielding maximum deployed length, strength and stiffness.

The baseline for design and analysis of such an ERM was given by a set of requirements covering the applications of a) a Solar Array Mast with a deployment length of up to 40 m and b) an Antenna Mast of 20 m extended length as baseline. Investigations have shown that, within the required stowed length of 3 m for the 40 m ERM, a deployable length of up to 60 m can be reached without changing the stowed envelope length. Most of the required performance data (e.g. high stiffness and strength, good pointing accuracy, low thermal distortions, and low mass) can only be fulfilled by application of carbon-fibre technology in combination with a structurally optimized mast concept. Consequently a design was evolved which is based on the use of thin-walled telescopic tube-sections with circular cross-sections manufactured from Carbon Fibre Reinforced Plastics (CFRP). Comparison with hexagonal and triangular cross-sections and frameworks have shown that the circular design gives a good relation between stiffness and mass and, in addition, good thermostability and pointing accuracy. The good pointing accuracy expected at the ERM-tip is achieved by the use of an accurate and thermostable CFRP structure and by designing for minimum backlash in the tube joints. The design of the tube joints incorporates special guiding elements and these allow adjustment to very small backlash between the different tube sections. Furthermore the given mass budget requires a lightweight design of the electronics and electromechanical components and of the chosen thermal hardware. The ERM design optimization process has shown that the only significant difference between an ERM designed for use with a Solar Array and one designed for use with an Antenna is choice of thermal hardward defined according to mission requirements.

The ERM telescopic mast is driven by a spindle, powered by a brushless DC-motor which is coupled via a gear stage directly to the spindle. Each of the nested tube sections is provided with a threaded nut at its lower end. In the storage mode the nuts are retained by the unthreaded storage-section of the spindle with only the topmost nut engaging the thread. Deployment starts by virtue of the spindle pushing the engaged nut forward, rotational movement of the adjacent tube section being prevented by longitudinal stringers attached to the next outer tube. Shortly before the moving nut leaves the spindle an end-stop draws out the next outer tube of the storage-section and engages the corresponding nut to the spindle thread, whilst the nut of the preceding tube section leaves the spindle. At the same time a special latching system located on the upper end of each tube-section locks the extended tube to the next outer tube. This procedure can be repeated until the mast has reached its fully deployed position. During retraction the process is reversed. During deployment and retraction the ERM can be stopped at any arbitrary position

without losing key performance characteristics. Figure 2 shows the ERM tube-stack principle.

The maximum deployment length which can be reached by the mast is given mainly by the required envelope (length and diameter) and by the choice of the overlapping length; this corresponds to the thickness of the threaded nuts moving on the spindle. To optimize the tube-stack with respect to maximum stiffness and deployment length for minimum mass, a tube stack was chosen which has variable overlapping lengths, thus providing an almost constant ratio between tube diameter and overlapping length (Fig. 3). A payload interface is provided on top of the inner tube section and, if required by the application, on top of each outer tube section.

The dependency between deployment length and number of tube sections of the chosen ERM design is such that with a 3 m stowed envelope length a deployed length of up to 70 m can be reached whilst with a stack length of 2.25 m a deployment length of approximately 30 m can be achieved. However to reach an optimal design it is not adequate to go to very long deployed lengths at a given stowed envelope. This limitation for the optimal design is given by the chosen overlapping length which becomes longer for increasing tube diameters; consequently the deploying part of each tube section becomes shorter with the chosen number of tube sections. To minimize mass for a required deployment length the stowed envelope length should be chosen in a way that the dependency between deployment length and necessary number of tube sections is quasi-linear (Fig. 4). The curves according to Figure 4 reach a maximum and decrease again for increasing number of tube sections because of the decreasing extended length of each tube at certain value of the maximum overlapping length.

Table I gives an overview of ERM performance characteristics as achieved by the chosen design. This data has been categorized into Launch Characteristics (for the stowed and deploying mast) and Mission Characteristics (for the deployed mast).

TABLE I. - ERM PERFORMANCE CHARACTERISTICS

| | 40 m Solar Array Mast | 20 m Antenna Mast |
|---|---|---|
| **Launch Characteristics** | | |
| stowed envelope length | 3 m | 2,25 m |
| stowed envelope diameter | 0.5 m | 0.4 m |
| overall ERM-mass 1) | 90 kg | 50 kg |
| number of tube sections | 18 | 13 |
| 1st natural frequency, stowed conf. | 115 Hz | 140 Hz |
| deployment speed, nominal | 20 mm/s | 10 mm/s |
| gear stage concept | spur gear 1 : 10 | planetary gear up to 1 : 25 |
| power consumption, nominal | 80 W | |
| peak power consumption | 200 W | |
| drive | brushless DC | |
| orbiter interface | basic flange and two hardpoints on top | |
| payload interface | hole pattern | |
| **Mission Characteristics** | | |
| deployed length | 40 m | 20 m |
| payload capability 2) | 40 kg on top<br>plus 10 kg/m line load<br>plus 100 N eccentric load | 120 kg on top |
| max. bending moment | 2800 Nm | 2300 Nm |
| average bending stiffness | $7 \cdot 10^5$ Nm$^2$ | $4 \cdot 10^5$ Nm$^2$ |
| 1st natural frequency, depl. conf. 3) | 0.06 Hz | 0.1 Hz |
| random translational deployment error | < 100 mm | < 30 mm |
| random angular deployment error | < 2 m rad | < 1.5 m rad |
| power lines to payload 4) | 4 + 1 grounding | |
| signal lines to payload 4) | 15 | |

1) without thermal hardware and cable follow-up mechanism

2) offset of eccentric force 0.5 m to CL / offset of Antenna Mast tip mass 6 m

3) 240 kg on tip and 70 kg distributed / 120 kg on Antenna Mast tip with 6 m offset and 40 kg distributed along Mast.

4) spring driven cable follow-up mechanism with slip rings is provided optionally for both Mast concepts

## DESIGN DETAILS

### Tube Structure

The tube structure is manufactured out of 6 layers of high-modulus carbon fibre epoxy resin in a symmetrical fibre lay-up. The resulting wall thickness of the CFRP tubes is only about 0.5 mm. The lay-up is optimized to reach high bending stiffness at a near zero thermal expansion coefficient.

A CFRP sandwich-plate carrying a Teflon-bronze thread is glued to the bottom of each tube section. At the upper end of the tubes a stiffening carbon fibre end-cone is mounted. On the inner surface of each tube segment three longitudinal stringers are mounted to prevent rotational movement of the next inner tube segment during extension and to provide torsional stiffness in the tube joints. To guide each tube relative to its neighbour it was necessary to develop special lightweight teflon-bronze guiding elements mounted to the upper and lower ends of the overlapping lengths. The space between two adjacent tubes was chosen as 10 mm, this being the minimum value required by the guiding elements and the inter-tube latching system. To avoid local loading of the thin-walled tube segments the guiding elements attached to the whole circumference of each moving tube are mated directly to the smooth inner surface of the next outer tube section. Because of the big influence of backlash on pointing accuracy it was necessary to shape the CFRP-tube sections and their guiding surfaces to very high accuracy (corresponding to a backlash of 0.1 mm). If, during integration or test, an ERM CFRP-tube should be damaged, it is possible to integrate a new tube-section without loss of performance by means of a procedure which involves simultaneous refurbishment of the teflon-bronze guiding elements. Figure 5 shows an ERM CFRP-tube with completely integrated guiding elements.

In order to minimize tip deflections, a mission dependant thermal design has been derived. Depending on the application, SSM-foil or white thermal point will be used while, to fulfill extreme pointing accuracy requirements, multilayer insulation can also be applied.

### Mechanisms

The mechanisms necessary to operate the ERM are mainly those in the following assemblies:

- Latching mechanisms (latching of the adjacent tube sections)
- Drive mechanisms (gear stage with drive, launch locking device and spindle)
- Cable follow-up mechanism

Special problems were posed by the functional requirements of the ERM latching system:

- mutual latching of the stowed tube segments in the stowed configuration and achievement of a defined tube by tube extension during deployment
- sequential latching of adjacent tube sections as each reach their required extension.
- delatching of the retracting tube segments
- latching of the tube sections after retraction.

To assure these tasks a self-acting latching system was developed where all functions are satisfied by a single mechanical system. Each tube section has three latches mounted equidistantly around the circumference of its upper end. The latches are accessible for ground maintenance routines in the deployed configuration. Figure 6 shows a latching unit before integration with its tube-section.

The hollow Aluminium spindle used to deploy the tube-sections is coated with Ematal and reinforced by a CFRP-tube (Fig. 7) to reduce the axial coefficient of thermal expansion and, at the same time, to increase bending stiffness. As separate hardware options, the spindle can be driven either by a normal spur gear stage or by a planetary gear, this providing flexibility with respect to application dependant deployment speed, torque and power requirements. The brushless DC-drive is controlled by a fully redundant ERM Deployment Electronics Unit (DEU). Inductive position indicators provide signals to the DEU so that each required ERM position can be reached. To avoid inadvertent deployment of unsupported payloads due to vibration loads during launch, a magnetic clutch is incorporated to fix the gear stage in the required position.

Depending on the ERM emission, it may be necessary to provide power and signals to the payload. This task is performed by a cable follow-up mechanism which can be attached to the upper end of the outermost tube. A flat cable is guided along the extending tube sections in a manner rather like a fishing line on the rod. The mechanism is driven by a constant torque spring motor so that the cable is wound onto a drum during the retraction process.

Use of an external guidance system for the ERM cable gives advantages of accessibility not only during assembly (and disassembly) but also in the event of failure in orbit. To cover the latter eventuality, an astronaut-override is included in the design.

## DEVELOPMENT STATUS

The detailed design phase started in 1984 and includes design, manufacturing and development testing activities. In addition, a complete set of manufacturing drawings will be produced for a qualification model ERM.

To verify functional performance of the ERM design a breadboard model, consisting of three tube sections, was built. This was tested in vacuum over the temperature range +85 to -100 deg C at ESTEC. The overall number of duty cycles (1 cycle = 1 extension + 1 retraction) was more than 600. The two extending CFRP-tube-sections had diameters of 405 and 425 mm respectively and each were of about 1.2 m length. The tubes were shaped according to the chosen ERM-design and equipped with design-representative guiding and latching systems. All friction interfaces, including the spindle-nut interface, were design representative. The outermost tube was manufactured in Aluminium. This acted as a dummy tube used to support the CFRP-tubes and to verify the latching function in the stowed configuration. The model was driven by a standard brushless AC-motor, modified for vacuum application. Figure 8 shows the ERM breadboard model during ambient functional testing.

During duty cycle testing in vacuum the spindle torque necessary to deploy and retract the system was measured as a function of deployed position, an eccentric resistive force of 100 N being applied at a distance of 0.5 m from the mast centerline. Figure 9 shows the dependency of peak torque on testing temperature.

The increase of torque at low temperatures is caused mainly by the difference in the coefficients of thermal expansion (CTE) between the Aluminium spindle and the Teflon-bronze nut. The slight increase of torque at high temperature is attributed to a reduction of backlash in the tube joints. During post test visual inspection, no serious degradation effects on the tube-structure or other structural parts could be found. Measurement of play between the teflon-bronze guiding elements and the adjacent CFRP-tube surface showed, however, that the medium backlash-value, as measured around the circumference of the tubes, had increased to around 0.29 mm from about 0.15 mm measured before testing. The degradation of the guiding elements was caused mainly by the axial eccentric force applied during TV-testing. The test set-up during thermal vacuum testing is shown in Figure 10.

## CONCLUSION

By its use of CFRP technology, the ERM achieves an advantageous combination of high strength and stiffness and low mass. Because of the lack of hinges and fittings, which are necessary for example for deployable truss structures, good pointing accuracy can be reached with the ERM-design if the number of tube-sections is minimized. This minimization process results in a relatively long stowed envelope with a small outer diameter. For example deployed lengths of 6 m to 40 m result in stowed lengths of between 1.5 and 3.3 m.

For the next stage in the development of the ERM it is planned to build and test an Engineering Model (EM) with a deployed length of about 15 m consisting of 6 tube-sections. The EM will have a tube stack length of about 3 m and an outer diameter of 0.4 m. In the center of the tube stack 8 additional tube-sections could be mounted, leading to a maximum deployed length of about 32 m.

The EM will be subjected to a qualification test programme, consisting of the following:

- Functional performance
- Sinus vibration and acoustic noise
- Thermal vacuum duty cycle testing
- Static load test
- Alignment and pointing accuracy

In addition consideration is being given to the possibility of in-orbit testing for verification of pointing accuracy and dynamic behavior.

For the reasons given above, the ERM telescopic mast is a most promising system for achieving long deployed lengths with a high stiffness and a high pointing accuracy. Such applications are apparent in the large deployable structures envisaged in the Space Station and Columbus Programmes. Figure 11 shows such ERM application on the Columbus Resource Module, for the positioning of communication antennas and solar array panels.

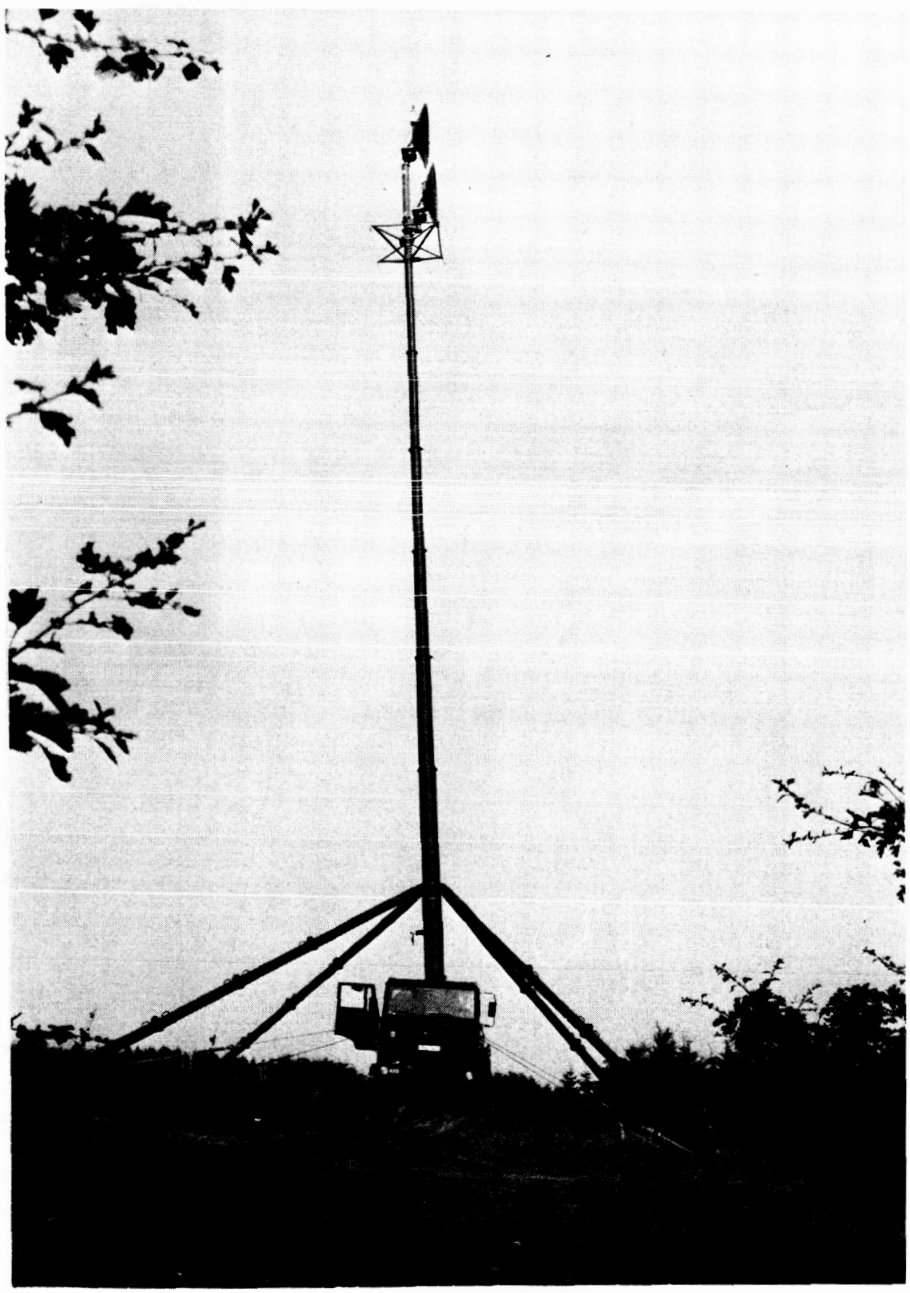

Figure 1. - DORNIER radio link mast for ground application.

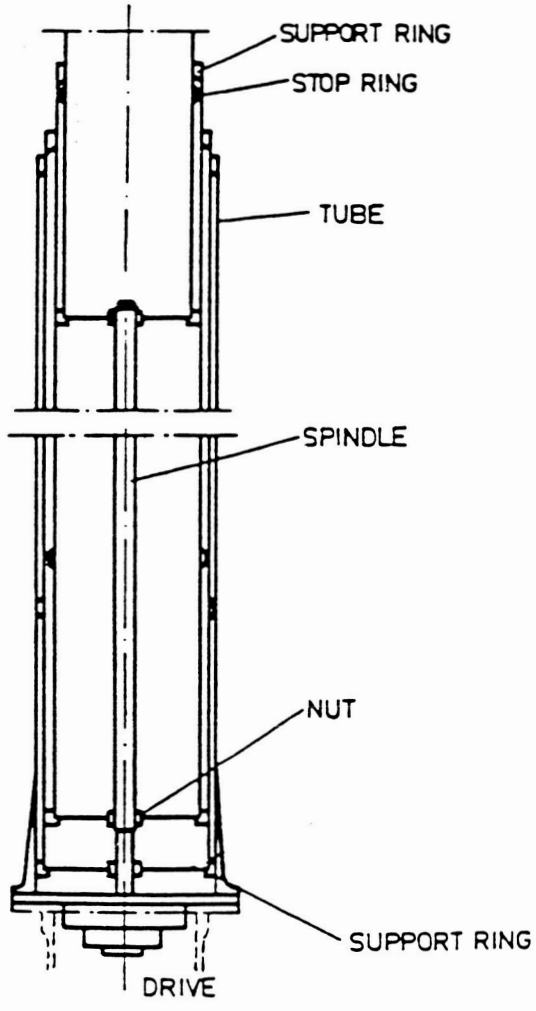


Figure 2. - ERM tube stack and working principle.

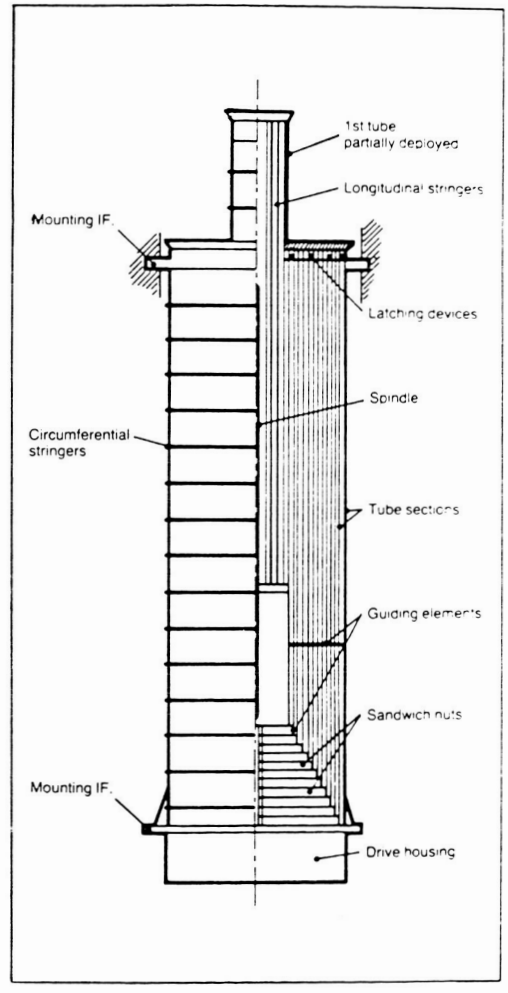


Figure 3. - Chosen ERM configuration with variable overlapping length.

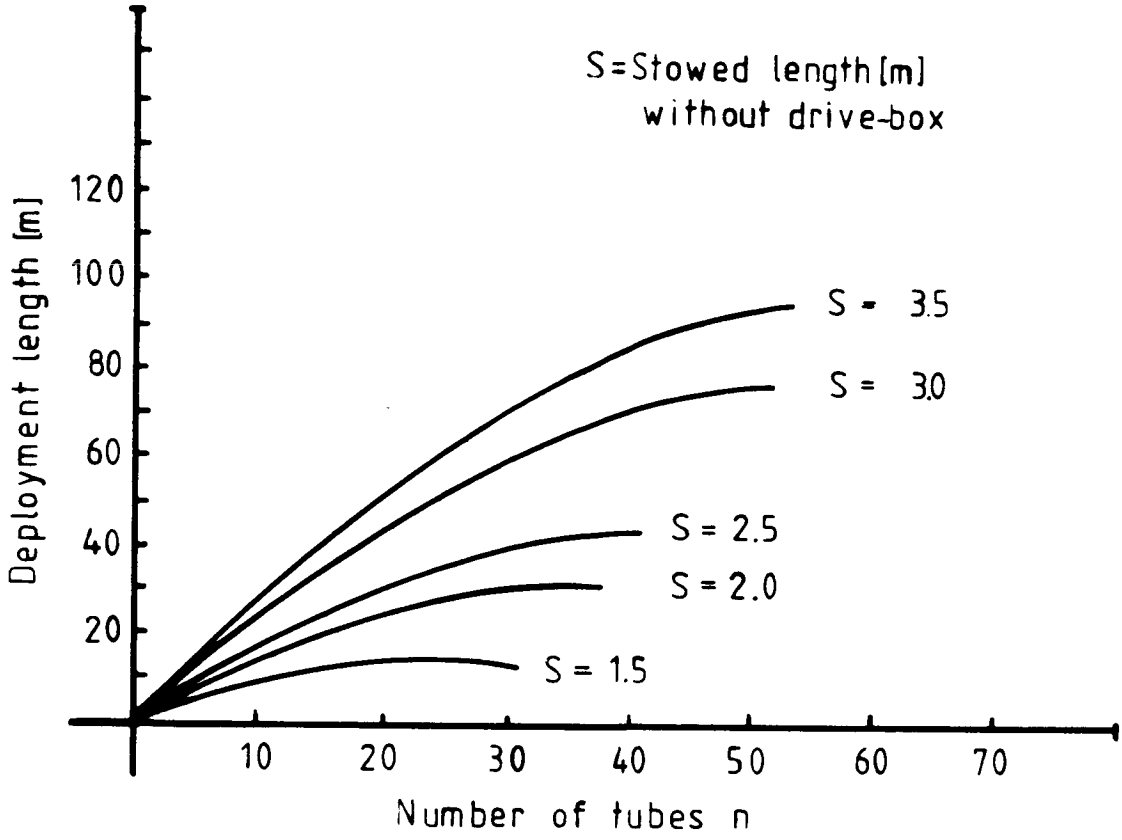


Figure 4. - Deployment length as function of number of tube-sections.

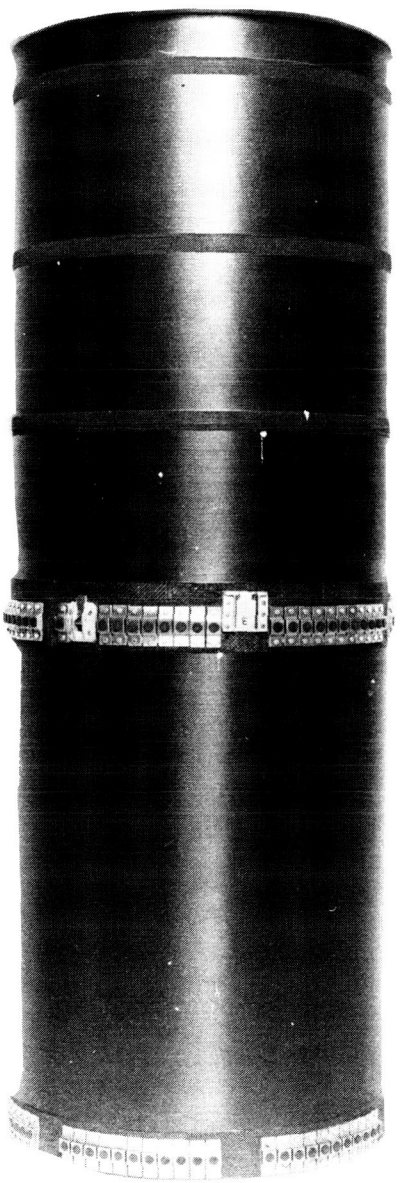

Figure 5. - ERM tube fully integrated with guiding elements.

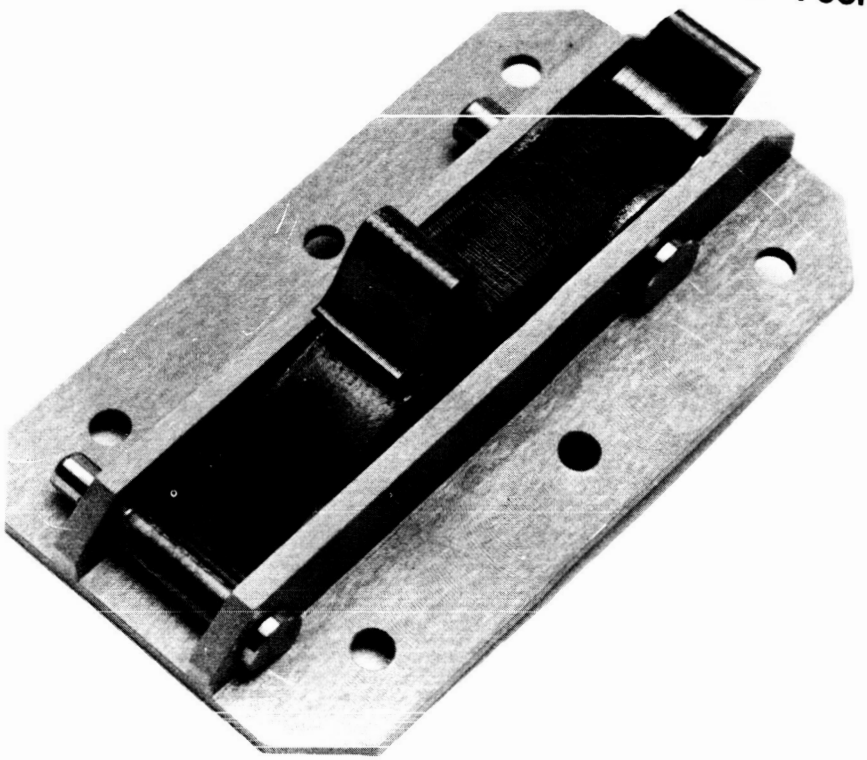

Figure 6. - Deployment latching unit.

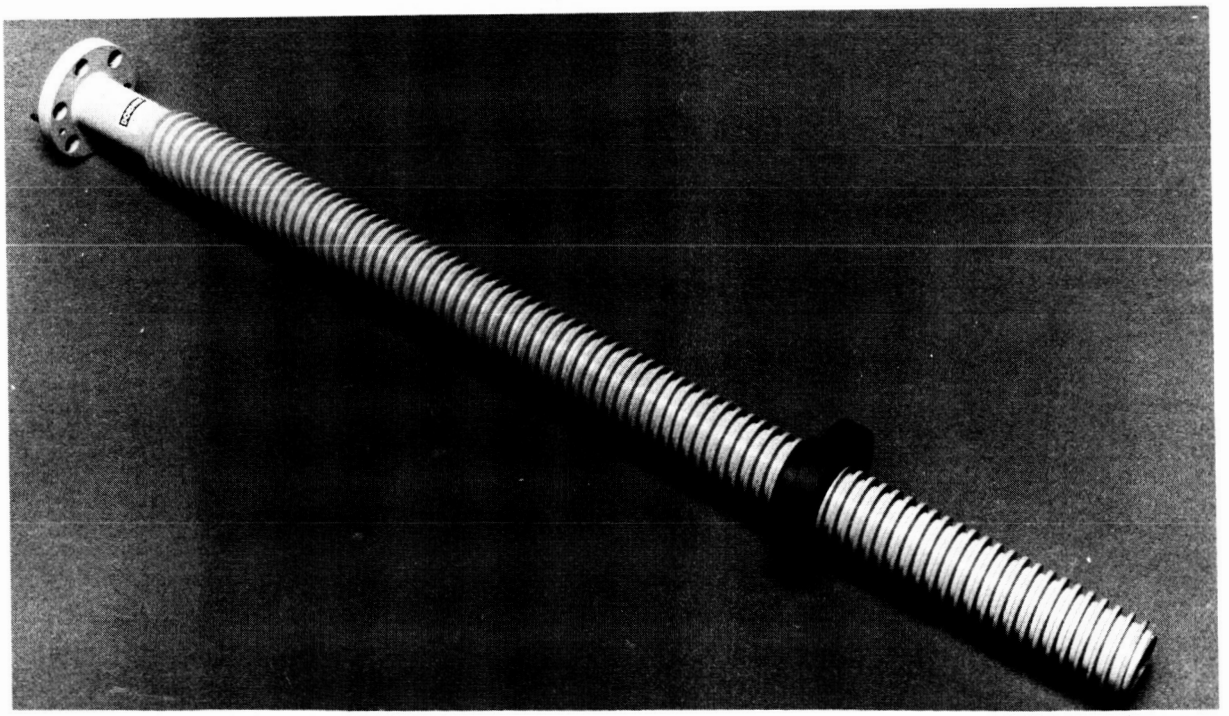

Figure 7. - Hollow aluminium spindle, ematal-coated.

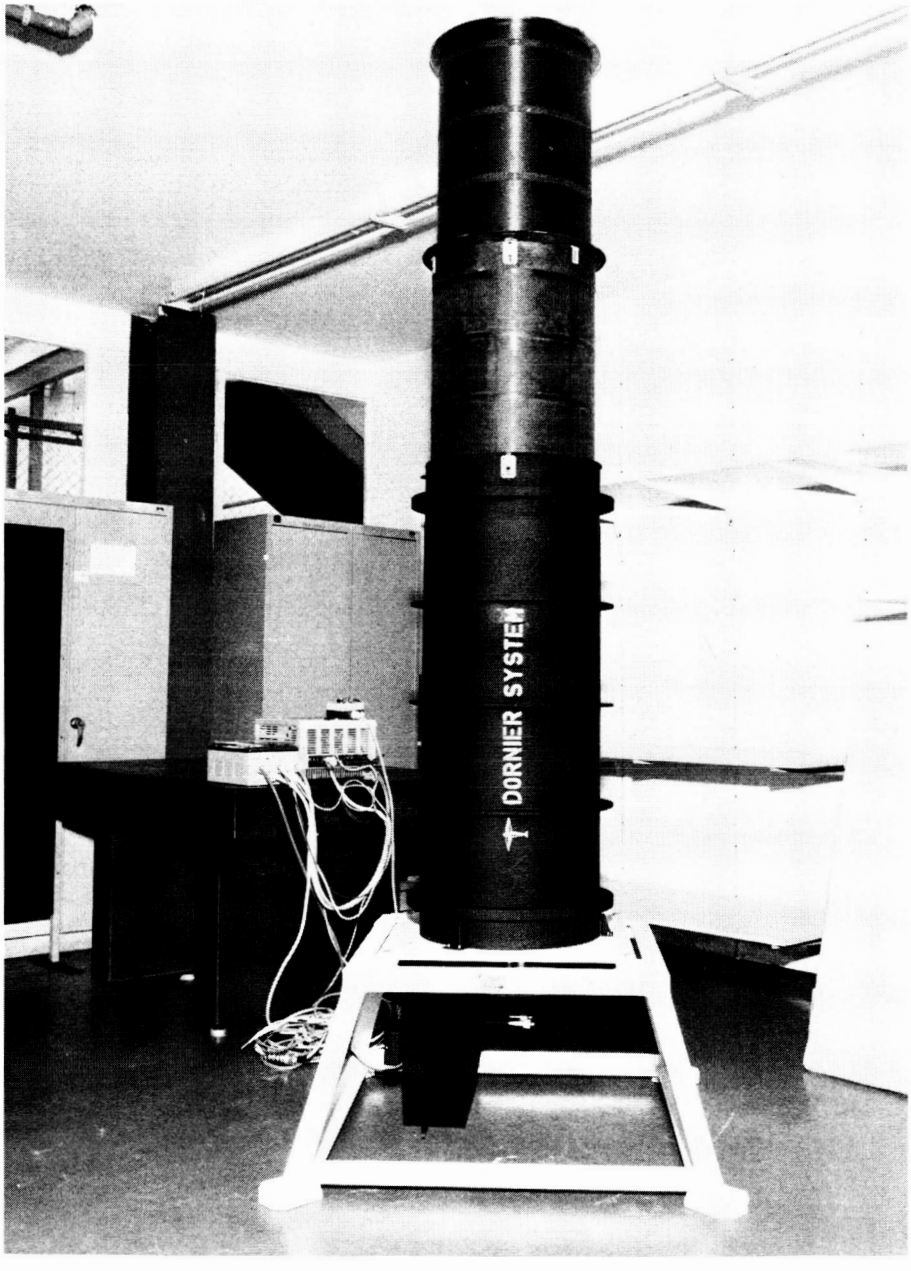


Figure 8. - Breadboard model during functional testing.

Dependency between Peak Torque and testing Temperature

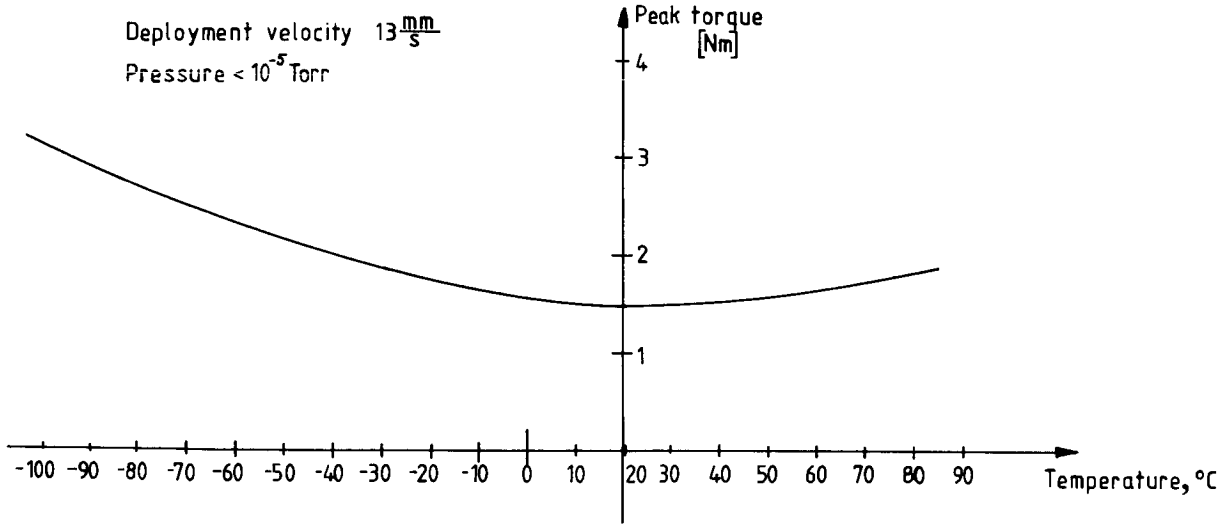


Figure 9. - Peak spindle torque required for different test temperatures.

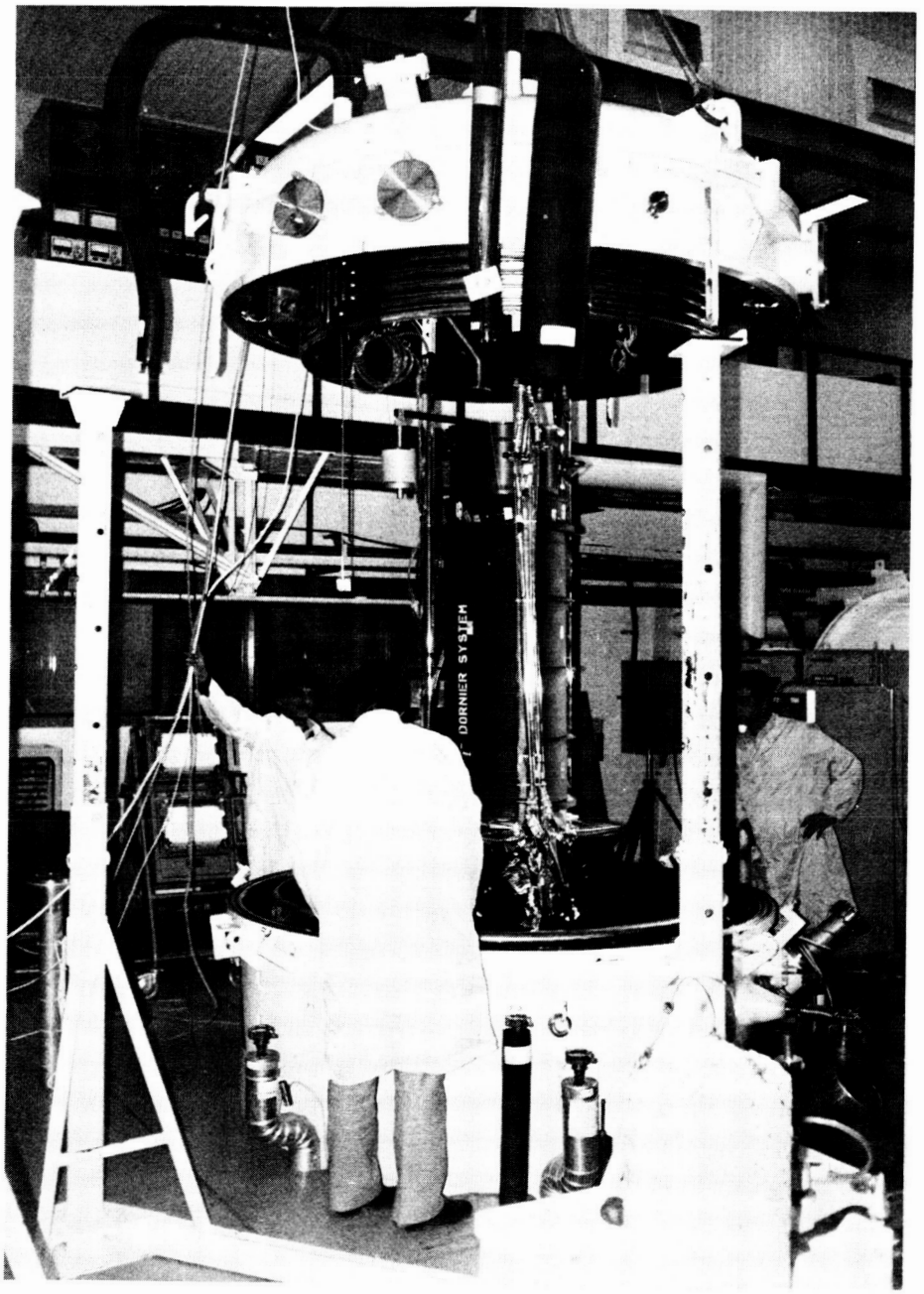


Figure 10. - Breadboard model during thermal vacuum (TV)-testing.

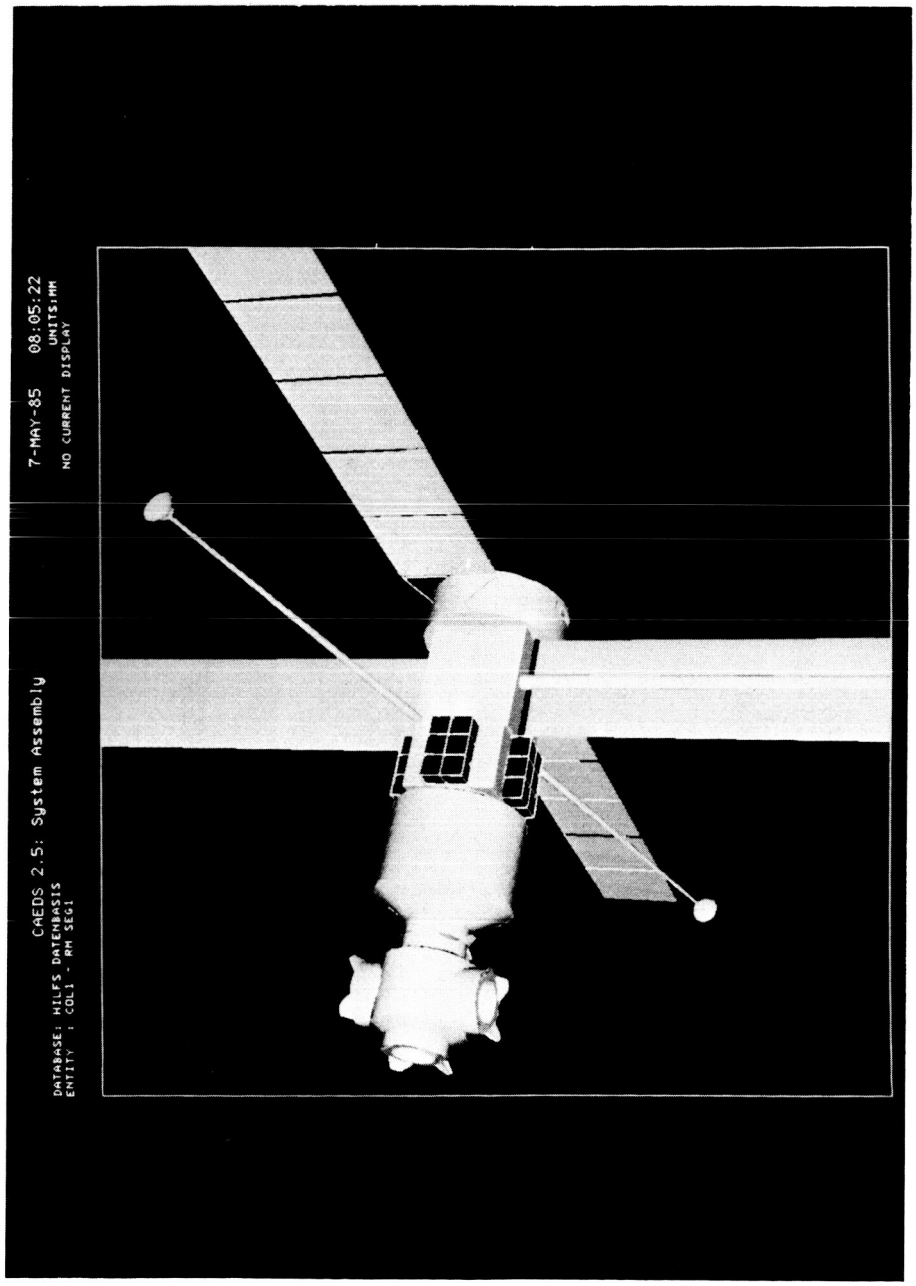


Figure 11. - Solar array and antenna masts on Columbus Resource Module.

N87-16324

# DESIGN AND TESTING OF AN ELECTROMAGNETIC COUPLING

William J. Anderson*

Hostile environments such as the hard vacuum of space, and exposure to water or caustic fluids have fostered the development of devices which allow mechanical rotary feed throughs with positive sealing without the use of conventional dynamic seals. One such device is an electromagnetic coupling which transfers motion across a hermetic seal by means of a rotating magnetic field.

Static pull-out torque and dynamic heat build-up and pull-out torque tests of a synchronous reluctance homopolar coupling are reported herein. Coupling efficiencies are estimated for a range of speeds and torques.

## INTRODUCTION

In Ref. 1 it was determined that the most promising electromagnetic coupling concept to explore would be a synchronous reluctance type coupling of the homopolar type. Both the driving and driven rotors have the same number of poles. With the poles aligned, DC current, flowing through a stationary field coil, sets up magnetic flux locking the two rotors together and transmitting torque. Synchronous operation assures a speed ratio of 1 and avoids heat producing losses at operating speeds.

A non-metallic stationary membrane extends through the air gap between the driving and driven rotors, hermetically sealing off the member connected to the flywheel. The flywheel operates inside the hermetically sealed chamber at a pressure of about 0.1 torr. The original design concept proposed was partially based on work reported in Ref. 2. Ref. 2 reports successful static test data, but no dynamic tests were conducted. Further work reported in Ref. 3 indicated serious vibration problems during operation at full load and the rated speed of 24,000 rpm. Vibration problems were thought to originate from poor balancing, non-concentric bearing seats or the presence of critical speeds. Vibration problems persisted, despite corrective measures. Because of the particular design of the coupling with a cantilevered rotor and high magnetic flux density, it was thought that the vibration problems could have resulted from unbalanced magnetic pull.

Another design, which greatly attenuates unbalanced magnetic pull effects, is reported in Ref. 4 (U.S. Patent 2488827). Because of its potential advantages, the design approach of Ref. 4 was chosen for this

*NASTEC, INC., Cleveland, Ohio.

investigation. The EM coupling investigated was designed to be used in conjunction with a 45.7 cm (18 inch) diameter, 63.6 Kg (140 pound) flywheel which stores 0.87 Kw hours (70 horsepower minutes) at 20,000 rpm.

## DESIGN OF THE ELECTROMAGNETIC COUPLING

A design which attenuates magnetic pull (shown in figure 1) was chosen for this investigation. By sandwiching the driving member (part 1) between the inner and outer sections of the driven member (part 2) no significant variations of magnetic flux density can occur under the poles. This is so because the magnetic permeance for any two air gaps per pole (in series, magnetically) varies very little with eccentricity. Hermetic seals (part 5) of two different materials were subjected to static pressure and deflection tests to determine practical air gaps. Three rotors with working air gaps (6 in figure 1) of 1.27, 1.78 and 2.16 mm (Rotor nos. 50, 70 and 85) were tested.

Details of the electrical design of the EM coupling were determined as part of the work done under Contract NAS 3-20803 to the NASA-Lewis Research Center. Design of the coupling included the choice of coupling diameters, the number of poles, depth of interpolar space, pole width, rim thickness and air gaps with the required maximum torque of 32.3 N-Meter (23.8 ft.lb.) at 20,000 rpm the following coupling dimensions were chosen (see figure 2):

### Inner Working Air-Gap

| | |
|---|---|
| Number of Poles | $p = 16$ |
| Axial rotor (pole) length | $l = 44.5$ mm |
| Driven member | $R_i = 60.$ mm |
| Air-gap length | $g_i = 1.78$ mm |
| Depth of interpolar space | $h_i = 7.62$ mm ($h_1 = h_2 = h_i$) |
| Rim thickness | $m_i = 6.99$ mm |
| Pole width | $w_p = 8.89$ mm or 0.162 radians ($\alpha_{0i}$) |

Outer Working Air-Gap

| | |
|---|---|
| Number of Poles | $p = 16$ |
| Axial rotor (pole) length | $l = 44.5$ mm |
| Driven member | $R_o = 78.$ mm |
| Air-gap length | $g_o = 1.78$ mm |
| Depth of interpolar space | $h_o = 7.62$ mm ($h_3 = h_4 = h_o$) |
| Rim thickness | $m_o = 8.26$ mm |
| Pole width | $w_p = 10.16$ mm or 0.129 radians ($\alpha_{oo}$) |

$\frac{\alpha\pi}{p}$ = 0.196 radians (either gap)

## ANALYSIS OF ELECTROMAGNETIC COUPLING TESTS

### Static Tests

The coupling was tested with each of the three different driving rotors to determine the maximum or pull-out torque ($T_{max}$ or POT) as a function of the coil current. Fig. 3 shows static pull-out torque vs. coil current. As expected, an increase in the magnetic air gap corresponds to a decrease in the pull-out torque. The "bending over" in the curve for Rotor 70 was not anticipated. Though first thought attributable to magnetic saturation, subsequent testing failed to uphold this assumption. Therefore, the data for Rotor 70 at 10 amperes is questionable.

### Dynamic Tests

There were two types of dynamic test performed on the coupling: load tests and heat runs. Mechanical power was provided by a two pole electric motor driving through an eddy current coupling, a Lebow torque meter and a 7:1 ratio speed increasing gearbox (figure 4). The shaft speed was controlled by the eddy current coupling. The Lebow torque sensor provided input torque data. A Kahn waterbrake dynamometer with torque meter provided the load.

### Heat Runs

Heat runs were performed on the coupling to determine the temperature rise of the excitation coil under stabilized conditions. The temperature of the coil was measured by thermocouple and resistance methods. The thermocouple was located adjacent to the coil. By measuring the coil voltage and current, the resistance of the coil is calculated. By comparing the calculated resistance to the measured resistance at ambient temperature,

the temperature of the coil during the test can be determined using known temperature-resistance relationships.

Heat runs were performed on Rotor 70 with a 10 amp coil current and a 55.7 N-Meter (41 ft.lb.) load at 10,000 and 17,000 rpm. Heat runs were also performed on the coupling with Rotor 85 installed with a 7 amp coil current and a 27.2 N-Meter (20 ft.lb.) load. Rotor 85 was tested with and without the hermetic seal at 15,000 rpm and with the seal at 10,000 rpm. The Rotor 70 heat runs are shown on Fig. 5. A comparison of the Rotor 85 heat runs with the hermetic seal at two different speeds is shown on Fig. 6. Fig. 7 shows the Rotor 85 heat runs with and without the hermetic seal at the same speed. In figures 5-7, the abscissa or time axis was shifted for one heat run against the other. Because a device of this size warms rapidly, and because the initial setting for current, speed and load take a finite time, the displacement of the running times best represents the relative heat run temperatures as if the tests performed were begun at the same time. For each heat run, the test was concluded prior to the stabilization of the coil temperature. In most cases, the test was stopped due to excessive temperatures in the coil or in the coupling drive system. Comparing one heat run to another, the coil temperatures acted as expected, in a relative sense. In absolute terms, however, the coil temperatures were too hot, exceeding the calculated temperatures considerably. It is believed that the high coil temperatures were partially the result of additional stray load losses in the coupling and partially due to the less than perfect heat dissipation ability of the embedded excitation coil.

## Load Tests

Load tests were performed with driving Rotors 70 and 85 to determine feasibility of design as well as to provide data for determining efficiency and pull-out capability.

Pull-out torque capability for the EM coupling determined from dynamic tests is compared to the previously shown static torque capability on Fig. 8. The dynamic pull-out torque, at a particular coil current is determined by averaging the test results at various speeds. While specific data points may be somewhat errant, the static and dynamic pull-out torques are similar for the same coil current and the inverse relationship between working air gap and pull-out torque is as expected.

The efficiency of the EM coupling was determined for Rotor 85. Input and output torque readings were taken at 5, 7 and 9 amp coil currents at the nominal speeds of 10,000, 15,000 and 20,000 rpm. At each of the current/speed combinations, the load was increased until pull-out occurred. From this data the efficiency is determined over a wide range of speed, load and coil current combinations.

The location of the Lebow torque sensor on the input side of the speed increaser or gearbox, made it necessary to determine gearbox losses so those could be subtracted out. Gearbox losses were unknown and had to be

estimated from a matrix of tests conducted over a wide range of speeds and loads. Gearbox losses at no load were obtained with the gearbox driving an unloaded rotor. Losses under load were estimated from the matrix of test data using the knowledge that there are no torque dependent losses in the EM coupling.

The input power and output power were calculated from the torque readings. The difference between the input power and the output power is the loss in the EM coupling and the gearbox. Subtracting gearbox losses, the EM coupling losses are found. Table 1 shows the calculation of the EM coupling losses for the 9 amp coil current tests at the speeds of interest.

The efficiency of the EM coupling, neglecting the coil $I^2R$ losses, was calculated based on the above losses. The relationship between efficiency and torque for Rotor 85 is shown on Fig. 9. It should be noted that the EM coupling losses are independent of the load or torque transmitted. The losses depend only on speed and coil current.

In order to determine the true efficiency of the coupling, it is necessary to include the coil $I^2R$ losses. Because the resistance of the copper in the coil depends on temperature, and because the heat runs were generally terminated prior to thermal stabilization, it is necessary to estimate the steady state coil temperatures. Table 2 indicates the estimated stabilized temperatures for the three speeds and three coil currents used for the Rotor 85 load test.

Based on the coil temperatures in Table 2, the coil $I^2R$ losses are calculated, and the efficiencies are recalculated. Fig. 10 shows the EM coupling efficiency vs. torque, including the coil losses. Since the stray load losses and coil temperatures were higher than anticipated, future modifications to the design should result in better efficiencies than those indicated in Fig. 10.

## SUMMARY OF RESULTS

An electromagnetic coupling to be used as a driving element for a 63.6 Kg (140 lb) flywheel which stores 0.87 Kw hours (70 horsepower minutes) at 20,000 rpm was designed and tested. The coupling design utilizes a driving member which is sandwiched between the inner and outer sections of the driven member. With this design the magnetic flux density under the poles does not vary significantly if the driving and driven members are eccentric, so that unbalanced magnetic pull effects are attenuated. The coupling tested had 16 poles and an outside diameter of approximately 17.8 cm.

Coupling efficiencies were calculated for speeds to 20,000 rpm and output torques to 45 Newton meters. Coupling efficiency at maximum torque was estimated to be about 94 percent, including the torque loss across the coupling and $I^2R$ losses in the coil. Because of the uncertainties in

calculating gearbox losses, calculated coupling efficiencies could be in error by an estimated $\pm 5$ percent.

Pull-out torque capability exceeded the maximum design requirement of 32 Newton meters, but coil heating was a persistent problem. Both static and dynamic pull-out torque tests were conducted. As expected, pull-out torque increased with decreasing working air gap (3 values of air gap were investigated).

Several tests were run to determine the temperature rise of the excitation coil. Coil temperature was measured by a thermocouple located adjacent to the coil, and calculated indirectly by the resistance method. As expected, coil temperatures calculated by the resistance method were higher than those measured by the thermocouple. In most cases these tests were stopped before the coil temperature stabilized because of excessive temperatures in the coil or in the coupling drive system. Coil temperatures varied as expected with load and speed but were much higher than predicted by design.

In an overall sense the test results are encouraging, but they also indicate a need for more work, especially in the following areas:
1) Reduction of losses, including finding out if any sizeable stray load losses, perhaps caused by small manufacturing or design asymmetries, stray magnetic fields, etc., exist and how to minimize them.
2) Improved heat dissipation ability to the coupling, e.g.: ribbed housing, forced air cooling, etc.
3) Improved torque generating ability, by reviewing if torque per AT (ampereturn) could be further maximized, especially as a function of number of poles chosen for the design.
4) Investigation of stronger hermetic seal materials, which would make it possible to reduce working air gap lengths.

## References


1. Feasibility Study and System Design of a Dynamic Energy Storage System-Flywheel Car, Contract NAS 3-18562, 1977.

2. Contract AF 33(657) - 8486, BPS Nr. 2(2-8128) - 61083, Item Nr. II Aeronautical Systems Division, Air Force Systems Command, United States Air Force, Wright-Patterson Air Force Base, Ohio. Contractor: Thompson Ramo Wooldridge Inc., Cleveland, Ohio.
"Applied Research on a Hermetically Sealed Drive Coupling for Space Power Transmission." Five Quarterly Progress Reports, starting August 1962: NR. 282 710, 289 017, 296 921, 404 751, 417 287

3. As 2) Above, Sixth Quarterly Progress Report NR. 423 887

4. a) U.S. Patent 2 488 827, Nov. 22, 1949, "Magnetic Coupling", to Nicolo Pensabene, Bridgewater, England.
b) U.S. Patent 3 943 391, March 9, 1976, "Electromagnetic Coupling Having a Electromagnetic Winding", to H. Fehr, Montmorency, France.
c) U.S. Patent 3 974 408, Aug. 10, 1976, "Asynchronous Synchronizable Magnetic Coupling", to H. Fehr (et al), Montmorency, France.

TABLE 1

DETERMINATION OF COUPLING LOSSES WITH 9 AMP COIL CURRENT

| INPUT TORQUE NM | INPUT TORQUE in.lb. | OUTPUT TORQUE NM | OUTPUT TORQUE ft.lb. | INPUT POWER, Kw | OUTPUT POWER, Kw | TOTAL LOSSES, Kw | GEARBOX LOSSES, Kw | COUPLING LOSSES, Kw |
|---|---|---|---|---|---|---|---|---|
| | | | | 10,000 RPM | | | | |
| 127.2 | 1125 | 14.2 | 10.5 | 19.02 | 14.91 | 4.11 | 2.4 | 1.71 |
| 164.3 | 1454 | 18.7 | 13.8 | 24.59 | 19.60 | 4.99 | 3.2 | 1.79 |
| 183.1 | 1620 | 21.0 | 15.5 | 27.39 | 22.02 | 5.37 | 3.8 | 1.57 |
| 254.2 | 2249 | 29.3 | 21.6 | 38.03 | 30.68 | 7.35 | 5.7 | 1.65 |
| 294.0 | 2601 | 34.6 | 25.5 | 43.98 | 36.22 | 7.76 | 7.1 | .66 |
| 358.3 | 3170 | 41.0 | 30.2 | 53.60 | 42.90 | 10.70 | 8.7 | 2.00 |
| | | | | 15,000 RPM | | | | |
| 104.9 | 928 | 10.9 | 8.0 | 23.54 | 17.04 | 6.50 | 3.1 | 3.40 |
| 129.8 | 1148 | 14.2 | 10.5 | 29.12 | 22.37 | 6.75 | 3.9 | 2.85 |
| 155.4 | 1375 | 17.0 | 12.5 | 34.88 | 26.63 | 8.25 | 4.6 | 3.65 |
| 171.7 | 1519 | 18.7 | 13.8 | 38.53 | 29.40 | 9.13 | 5.0 | 4.13 |
| 185.7 | 1643 | 20.6 | 15.2 | 41.67 | 32.39 | 9.28 | 5.6 | 3.68 |
| 230.5 | 2039 | 25.8 | 19.0 | 51.72 | 40.48 | 11.24 | 7.1 | 4.14 |
| 288.0 | 2548 | 32.6 | 24.0 | 64.63 | 51.13 | 13.50 | 9.1 | 4.40 |
| 317.4 | 2808 | 35.8 | 26.4 | 71.22 | 56.23 | 14.97 | 10.1 | 4.87 |
| 354.9 | 3140 | 40.0 | 29.5 | 79.64 | 62.85 | 16.79 | 11.5 | 5.29 |
| 377.5 | 3340 | 42.9 | 31.6 | 84.72 | 67.33 | 17.39 | 12.4 | 4.99 |
| | | | | 20,000 RPM | | | | |
| 127.2 | 1126 | 13.0 | 9.6 | 38.08 | 27.27 | 10.81 | 5.0 | 5.81 |
| 145.7 | 1289 | 14.2 | 10.5 | 40.89 | 29.83 | 11.06 | 5.3 | 5.76 |
| 163.3 | 1445 | 17.2 | 12.7 | 48.38 | 35.72 | 12.66 | 6.1 | 6.56 |

TABLE 2

ESTIMATED COIL TEMPERATURE (°C)

| Speed (rpm) | Coil Current (amps) | | |
|---|---|---|---|
| | 5 | 7 | 9 |
| 10,000 | 160 | 230 | 290 |
| 15,000 | 190 | 270 | 340 |
| 20,000 | 230 | 320 | 490 |

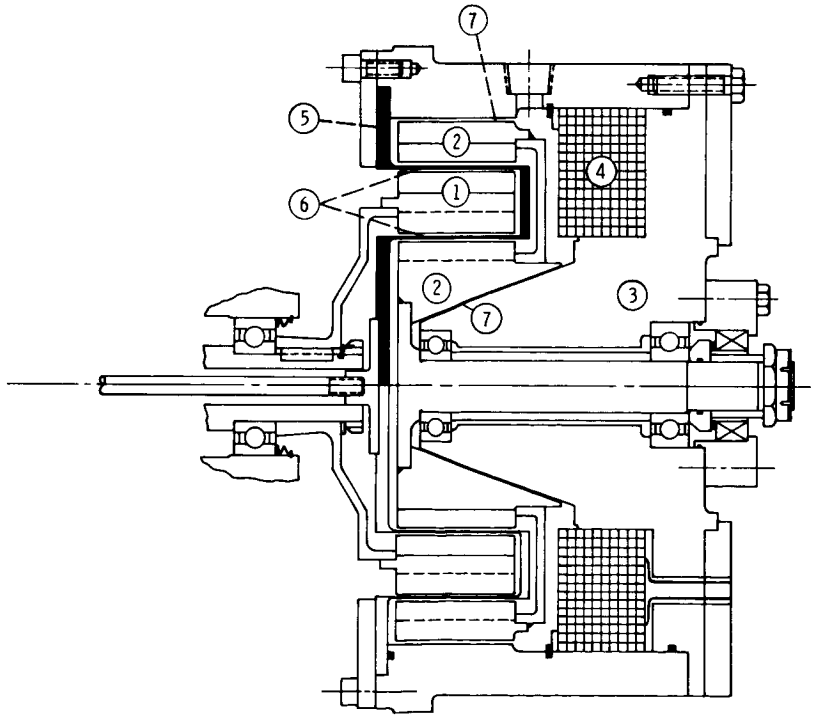


1 Driving rotor
2 Driven rotor
3 Stator
4 Electric coil
5 Hermetic seal
6 Working air-gap
7 Parasitic air-gap

Figure 1. - Electromagnetic coupling.

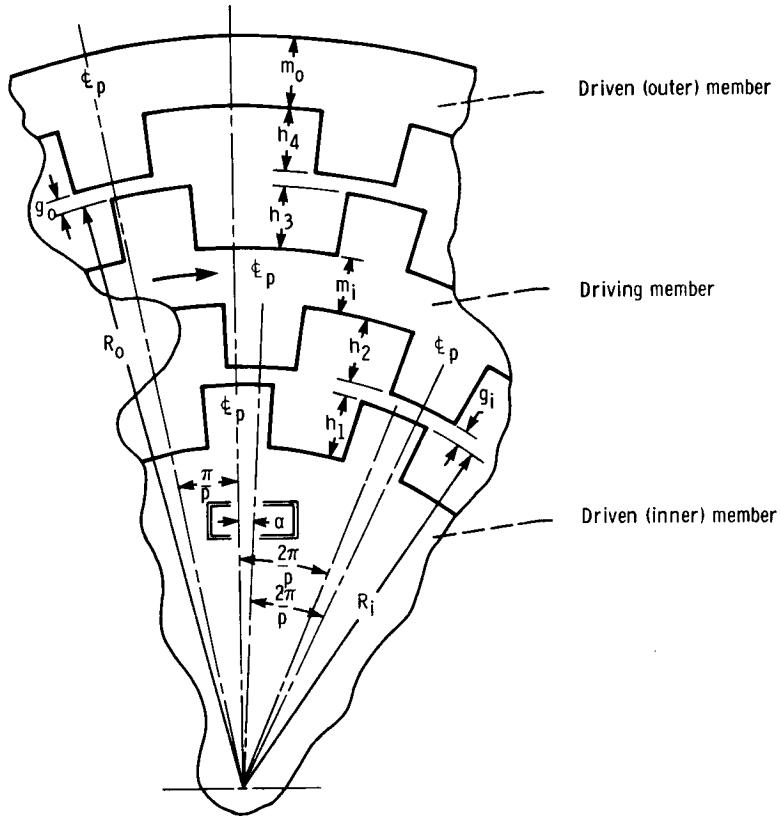


Figure 2. - Geometry of electromagnetic coupling with driven and driving members displaced by $\alpha$ (not ot scale).

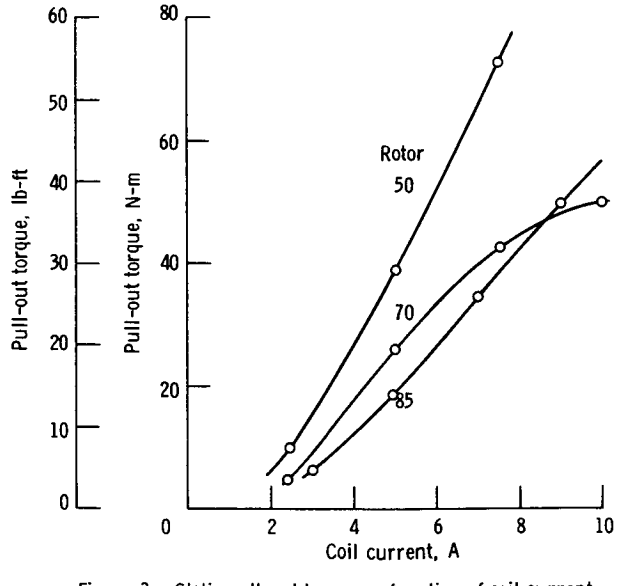


Figure 3. - Static pull-out torque as function of coil current for three test rotors.

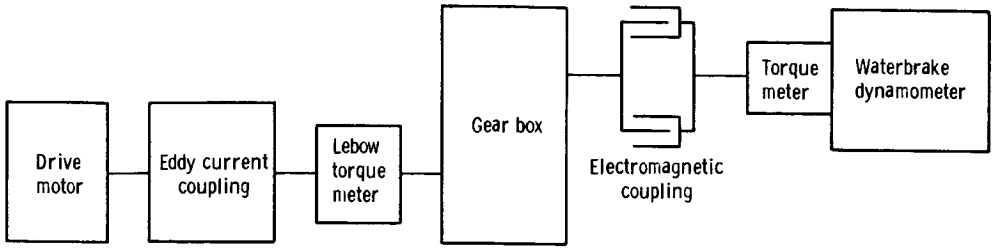


Figure 4. - Arrangement for dynamic testing.

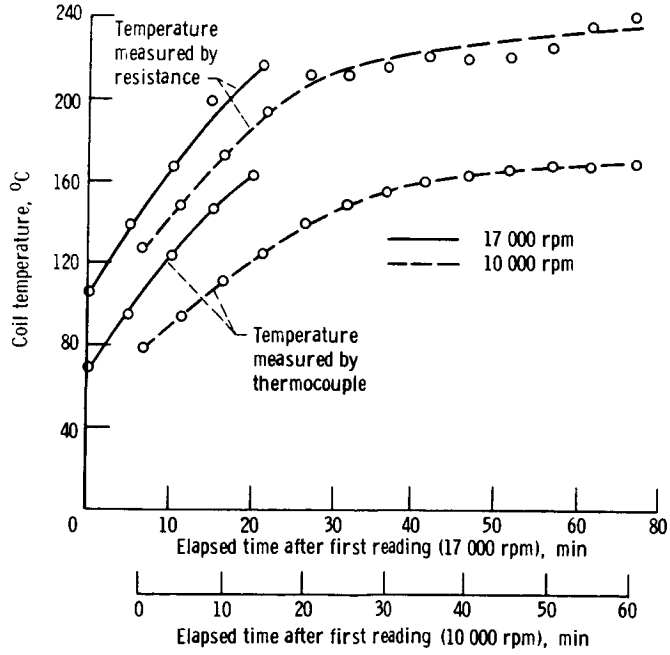


Figure 5. - Heat run; rotor 70 with hermetic seal; current, 10 A; load, 55.7 N-m (41 ft-lb).

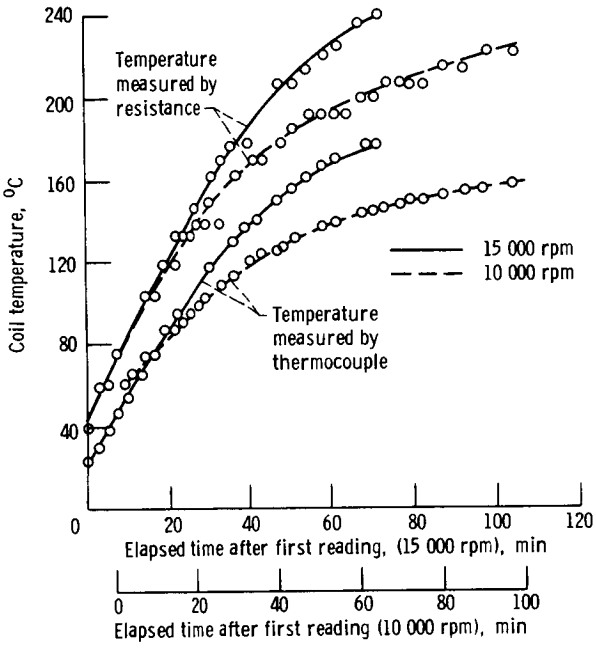


Figure 6. - Heat run; rotor 85 with hermetic seal; current, 7 A; load, 27.15 N-m (20 ft-lb).

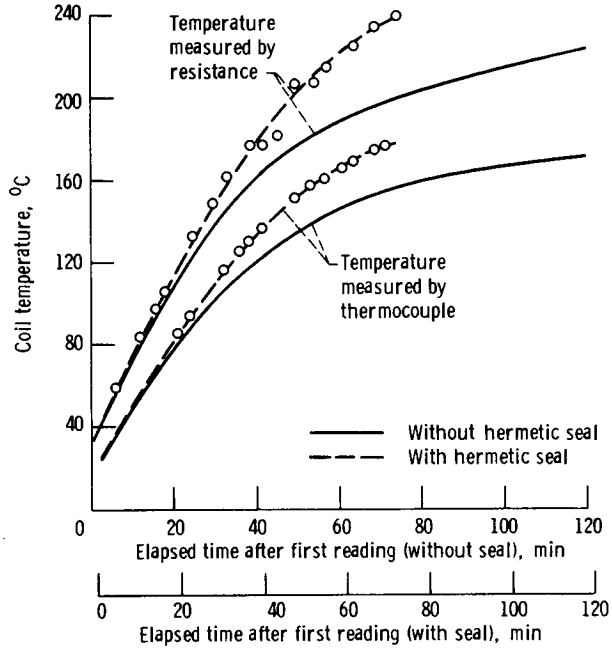


Figure 7. - Heat run; rotor 85; speed, 15 000 rpm; current, 7 A; load, 27.15 N-m (20 ft-lb).

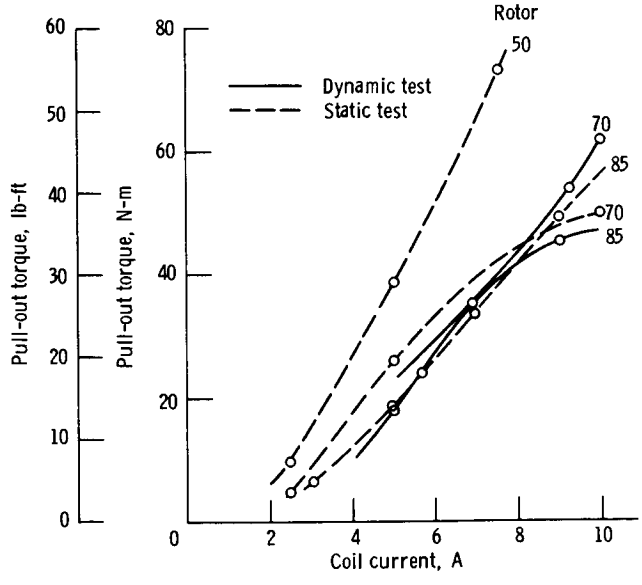


Figure 8. - Pull-out torque as function of coil current for rotors 50, 70, and 85.

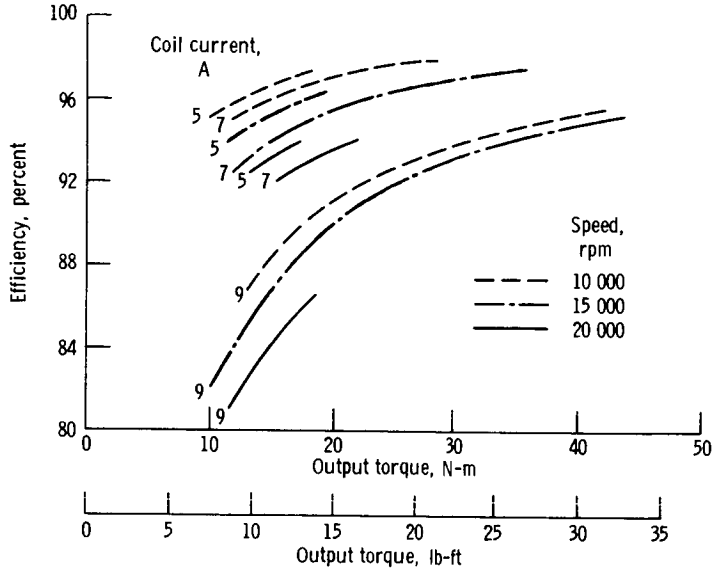


Figure 9. - Efficiency as function of output torque for rotor 85. $I^2R$ losses are not included.

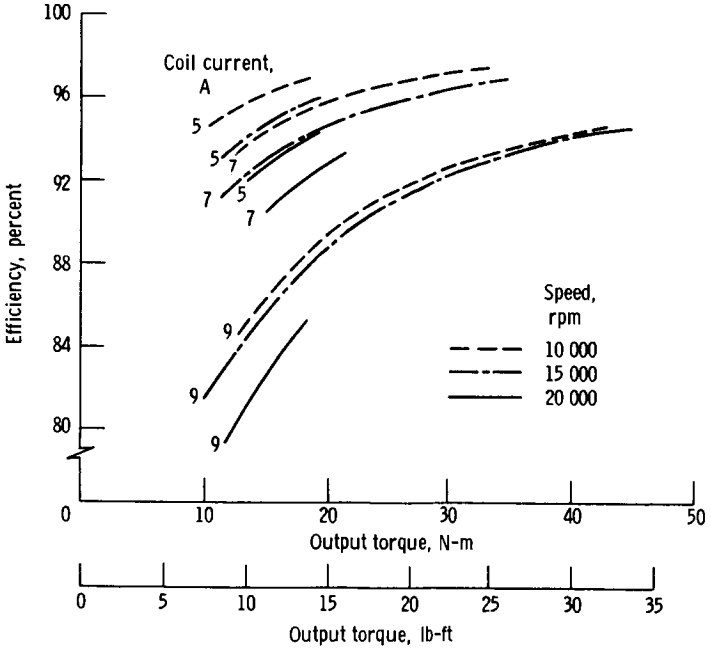


Figure 10. - Efficiency as function of output torque for rotor 85. $I^2R$ losses are included.

# SLIP RING EXPERIENCE IN LONG DURATION SPACE APPLICATIONS

Damon D. Phinney*

## INTRODUCTION

In 1978 SEASAT suffered a disastrous power system failure after three months of successful operation. The probable cause was a short somewhere inside a slip ring assembly. It was also concluded that mistakes had been made in the original slip ring specification (for a project other than SEASAT) and in the way the slip ring was used. The power transfer requirement could easily have been satisfied except for these mistakes. Unfortunately, few in the aerospace community have had an opportunity to read the SEASAT failure report. The widely disseminated news that a satellite was destroyed by a slip ring failure has led to a totally undeserved skepticism of these highly developed and very useful mechanisms.

This paper reviews Ball Aerospace System Division (BASD) experience with slip rings in space, presenting design and application experience for several different types. Ball flew the very first slip ring used in space in its first Orbiting Solar Observatory (OSO-1) satellite, launched in 1962. Since then, more than 40 BASD drives using slip ring assemblies for power and signal transfer have been orbited. Continuous operating lifetimes up to eight years at 60 rpm have been demonstrated. We have also specified, purchased, and/or lubricated as many or more slip rings for other space prime contractors. We have no knowledge of any orbit failure of a Ball-processed slip ring assembly. The cumulative orbit operating lifetime of these units comes to hundreds of years and billions of revolutions.

## SLIP RING SOURCES

BASD does not make slip rings, and sources for the slip rings described in this paper are:

- Electro-Miniatures Corp, Moonachie, NJ
- KDI Electro-Tec, Blacksburg, VA
- Poly-Scientific Division, Litton Industries Inc., Blacksburg, VA

If it seems unusual for this paper to be originated at a company that does not produce the mechanism being described, it is because component users in the space community often have more visibility of results than the suppliers.

## BALL AEROSPACE ROLE IN SLIP RING APPLICATIONS

When a slip ring is to be used in a BASD drive, our role includes the following:

- Preparation of a definitive procurement specification. Often this is preceded by preliminary design studies of the slip ring assembly itself to establish approaches compatible with the overall drive concept as well as realistic envelope and performance requirements. It is important to maintain some initial flexibility at this stage to be

*Ball Aerospace Systems Division, Boulder, Colorado.

able to take full advantage of the supplier's special knowledge and experience. For instance, despite his objections, the SEASAT slip ring supplier was forced to put more rings into the assembly than available space permitted for a sound design. The excessively crowded assembly may have contributed to the eventual problem.

- Detailed reviews of the supplier's design, materials selections, and processes
- Inspection of critical manufacturing and test operations at the supplier's facility
- Lubrication of bearings used in the assembly
- Lubrication of the rings and brushes when self-lubricating materials are not used
- Hard vacuum run-in tests at Ball followed by disassembly, run-in wear debris removal, reassembly, and checkout
- Brush force measurement (100%) and tweaking if necessary during final assembly
- Slip ring performance evaluation during drive acceptance tests, which always include thermal vacuum operation

Our suppliers' contributions should not be minimized. The early OSO slip rings, which will be described here, were built up from discrete standard components and were completely disassembled and rebuilt at Ball. Subsequent major slip rings used by Ball have come from Electro-Tec or Poly-Scientific and have been complete special assemblies for each application, designed in detail by their suppliers. BASD hard vacuum materials technology was very important, especially in the early days, but now both Poly-Scientific and Electro-Tec have more than 20 years experience with hundreds of slip rings for space use. On the other hand, before self-lubricating brush and ring combinations came into use for space drives, Ball Aerospace lubricants for hard vacuum played a very major part in our slip ring success, and continue to do so when lubricated assemblies are called for.

## FIRST OSO SLIP RINGS

Ball's OSO scientific satellites were spin stabilized at 30 rpm and received power and signals from a despun solar array on which sun-pointed instruments were mounted. OSO-1, launched in 1962, was the world's first dual-spin satellite, and contained the first slip ring used in an unsealed mechanism in space. Between 1962 and 1969, six OSOs of the initial configuration were flown, accumulating a total of more than 18 years of operating time before shut down. With the despin drive turned off during orbit night, about 200 million drive revolutions or three billion slip ring revolutions were accumulated with no known slip ring problem.

Figure 1 shows three views of the 22-ring Electro-Miniatures assembly used on OSO-6. Previous units were similar but used fewer rings. Slip rings are coin-silver discs clamped against opposite sides of a laminated phenolic washer by short tubular phenolic spacers. Brushes are silver graphite buttons

on the ends of beryllium copper leaf springs, two per ring. The buttons are 0.090 in. in diameter and 0.060 in. long, with hemispherical ends. The hard vacuum rating was 3 amperes per ring. Brush springs are stacked between rectangular phenolic spacers. The two large cylindrical objects are porous sintered nylon blocks impregnated with lubricating oil. No bearings were used in the slip ring itself; the rotor was mounted on the end of the despin drive shaft and the brush rigging was fastened to the drive housing inside a sheet metal cover.

It is difficult to believe that one of these units with its tiny brushes operated at 30 rpm for more than five years (60 minutes on, 30 minutes off) in OSO-5. One contributing factor was the effectiveness of the lubricating oil (used to replace the effect of water vapor in air for terrestrial applications) and the wear mechanism that this oil helped to promote. A small amount of brush wear, generated during early operation, remained under the brush pad, effectively eliminating further wear (see Reference 1).

This simple design from the earliest days of space mechanism experience is included because it illustrates one viable approach for which components are still available from Electro-Miniatures, although the phenolic insulators have been replaced by more modern plastics.

## WIRE BRUSHED SLIP RING, SINGLE GROOVE TYPE

Another type of slip ring widely used for low power and signal applications has hard gold wire brushes and soft gold rings with a hard gold flash. Rings are V-grooved so that brushes are laterally stabilized while the bottom of the groove provides a lodgement for wear debris away from the brush track. In the more common configuration, the brush wire is formed into a U-shape with both ends in the ring groove, as seen in Figure 2.

The advantage of this design is high ring density. Ball Aerospace has used them with 25 rings per inch in 40- and 66-ring assemblies. Many more rings can be provided, and even closer ring spacing is used, especially with very tiny slip rings. With 15 mil brush wires, a ring and brush set would be conservatively rated for 2 amperes in vacuum.

The rotor consists of rings embedded in epoxy cast over a metal shaft rather than being assembled by stacking individual components. Rings are plated into grooves machined in the plastic, machined to final shape, and then flashed with hard gold. For space applications, a ceramic filler is usually added to the epoxy to bring its expansion coefficient down into the range of the shaft and ring materials. Brushes are made from gold alloy wire rolled into rectangular cross-section or flattened at the ends in the ring contact zone. An epoxy casting creates a brush block which holds the brushes for every other ring as seen in Figure 2. The housing is slotted to let the brushes onto the rings and provide access to the brush ends for brush force checking and adjustment. Brush force must be set carefully. Our rings have used 3-5 gm and, with our lubricants, the friction coefficient may vary between 0.3 and 0.8.

A liquid lubricant is necessary if significant rotation is involved. Ball's most widely used lubricant consists of a highly refined mineral oil with EP additive. Recently, a synthetic oil with improved characteristics has come into use. With the mineral oil, reservoirs are placed along the brush access slots in the housing, as seen in Figure 2. Vapor pressure of the new oil is so low that surface films are sufficient for multi-year missions and reservoirs are not required.

It might seem that these slip rings could not possibly last very long with their tiny brush wires, but such is not the case. When suitably lubricated, the brushes, for practical purposes, do not wear. Rings only wear until the hard flash is penetrated, then wear effectively ceases. In hard vacuum tests on 40-ring assemblies running at 30 rpm, Ball demonstrated this in two tests lasting 6 and 18 months. In both units, ring wear scars stopped at the soft gold interface. Ring wear in the 18-month sample, based on measured wear scar cross-sections, was actually slightly less than that of the 6-month specimen, possibly because the hard gold was not quite as thick. Figure 3 includes microphotos of four representative ring wear scars from the 18-month life test specimen.

This wear-limiting phenomenon suggests a means of reducing the amount of wear debris occurring during flight. Units are run-in to establish the wear scar, then debris is removed. Debris occurs in the form of microscopic particles.

A high-resistance short between two rings occurred during the 18-month life test. A minute crack in one of the 0.010 thick epoxy barriers between rings was discovered, into which wear debris had infiltrated. Cracks in debris barriers cannot be tolerated and must be weeded out by microscopic inspection. Fortunately they rarely occur.

When we needed a new OSO slip ring with 40 rings in the same space as the 22-ring assembly on OSO-6, the wire brushed configuration, was adopted. The units were made by Poly-Scientific and two of these underwent the life tests referred to above. The assemblies were 2.15 in. in diameter by 2.5 in. long.

Two BASD spacecraft flew with these slip rings. OSO-7 operated continuously at 30 rpm for 2.8 years and then re-entered. P78-1 operated continuously for 6.4 years at 30 rpm until it was intentionally shut down. We are not aware of any slip ring problems on these two spacecraft.

## WIRE BRUSHED SLIP RING, DOUBLE GROOVED TYPE

A variation of the slip ring just described uses rings with two V-grooves. Brush wires are bent into a tight hairpin and the ends lie side-by-side in the two grooves, instead of straddling the ring. This design was used in the slip rings for DSCS-II despin drives developed in the early 1970s. At that time there was some indication from our suppliers that wear on a slip ring with trailing brushes (brushes put in tension by the friction force) might be less than on stubbing brushes. It also seemed likely that with a single brush in each groove, the brushes would seat more perfectly. Since DSCS-II drives required 5-year design lives and at that time we had only the 18-month life test on gold-gold rings to guide us, we adopted the double V-groove ring design, shown isometrically on Figure 4.

Two variations of the DSCS-II slip rings were built, one with 90 rings and another with 100. Each of these had 58 signal rings on a 0.5 in. diameter section of the rotor, with the balance being power rings rated at two amperes each on a 1 in. diameter. Signal brushes used 0.012 in. diameter wires flattened at the ends while power brushes were 0.015 in. diameter. Axial ring pitches were 0.066 and 0.078 in. for signal and power, respectively, including 0.015 in. wide debris barriers. The 100 ring unit was 9.38 in. long by 2.62 in. in diameter and weighed less than 3 lb.

The DCSC-II slip rings, made by Electro-Tec, were very successful. A 6-year thermal vacuum life test at 60 rpm was conducted on one unit by Aerospace Corporation, while TRW tested several others for up to three years. Ten units

have been flown in space, and six are still in operation. Launched in pairs, these six had been going 8.1, 7.1 and 6.1 years as of January 1986.

In light of the demonstrated life beyond five years at 30 rpm with single groove rings in the P78-1 spacecraft, which was not launched until 1979, it would now appear that the precaution of side-by-side brushes is unnecessary. Wire brush single-groove gold-gold slip rings, which are made by both Electro-Tec and Poly-Scientific, will be smaller and lighter. Furthermore, it is likely that the amount of new wear debris after cleanup of run-in wear will be less. Although wear debris has not been a demonstrated problem, less must be better.

## SLIP RING WITH SELF-LUBRICATING CONTACTS

Toward the end of the 1960s, Ball Aerospace participated in a slip ring materials test program with INTELSAT and Poly-Scientific. Several brush and ring combinations in self-lubricating and fluid-lubricated combinations were evaluated at the COMSAT Laboratories of INTELSAT in two multi-specimen test sets. Each set was run in a hard vacuum at 100 rpm for more than a year (52.5 E+6 revolutions/year). Of the self-lubricated materials, composite brushes of silver, molybdenum disulfide and graphite (85, 12 and 3 percent respectively) running on coin silver (90/10 silver/copper) were found to be most satisfactory. Although noise and wear occurred in air, little or no wear occurred during the vacuum test and noise was low (Reference 2). This material combination has subsequently been widely used by Ball and other United States space equipment designers. Details of some BASD experiences follow.

## GPS SOLAR ARRAY DRIVE

The Global Positioning System (GPS) spacecraft made by Rockwell International has two solar arrays, each driven by a separate single-ended drive made by BASD. Since axial space for solar array drives was very restricted in the initial block of GPS space vehicles, the slip ring assembly was installed inside the shaft with the brush assembly bolted into the shaft, and the slip ring rotor cantilevered from a nonrotating plate at the inboard end of the housing. No separate slip ring bearings were used. These assemblies contained 35 rings including 4 power rings (10 amperes each), 30 signal rings, and one electrical bonding ring. Figure 5 shows this assembly from the back of one brush block and from one side looking through a brush inspection slot. The assembly is 4.75 in. long by 1.75 in. in diameter. In the GPS slip ring, brush assemblies consisted of small rectangular blocks of the $Ag/MoS_2/C$ brush material on the ends of U-shaped beryllium copper finger springs. Power rings used four brushes, each operated at a nominal 147 amperes/in.$^2$. Braided copper shunts in parallel with the springs helped carry current from the brush pads to the leads. Signal rings used two brushes each that were individually fastened to a molded plastic brush support structure. Rings were solid coin silver molded in ceramic-filled epoxy over a stainless steel cruciform arbor.

Early in the development of this drive a vibration test on sample brushes in contact with a dummy slip ring rotor showed brush resonance at approximately 300 Hz. Brushes moved laterally and twisted from the weights of the overhung brush pads. The random input was 0.5 $g^2$/Hz in the brush resonance range.

Brush resonance caused chipped brush pads resulting from brushes beating against the raised plastic debris barriers between rings. Coating the brush springs with thin films of polyurethane completely eliminated this problem. Since it was suspected that thermal expansion coefficient mismatch between the

urethane and beryllium copper brush springs could cause brush force changes, measurements on several brushes were made at room ambient temperature and -30°F. Changes of approximately 1 gm from initial test fixture settings of 15 gm were observed; in all cases these were increases and considered entirely acceptable.

To minimize vibration problems on brush assemblies of this type, brush pads should be of minimum height (≤0.090 in.). There is a natural tendency to provide relatively long brushes in long-life applications, but with these brushes running on silver rings, wear is negligible even under continuous rotation at 60 or 100 rpm. The best brush design will only be long enough to allow conformity to the ring curvature plus a shallow layer above any infiltration of solder or brazing material from the brush-spring interface.

Power brushes are operated at current densities in the 100-150 ampere/in.$^2$ range for space applications, and contact pressures of 6 psi. Signal brushes commonly have pad face areas in the 7E-3 in.$^2$ range (0.06 x 0.12 in.) or less, and brush force is set at about 20 gm. Reference 3 describes an experience with brush spring force settings that is worth being aware of, although we at Ball have never encountered the problem described therein.

For calculating friction torque, a friction coefficient of 0.25 to 0.50 will cover the range.

While the Ag/$MoS_2$/C brush on silver is outstanding in vacuum, it is not so good in air. The $MoS_2$ helps provide lubrication in the absence of air but may lead to formation of intermittent high-resistance films in air, especially at higher humidity levels. Ball Aerospace has experienced high electrical noise levels during or immediately following operation of slip rings of this type in air. The noise can be eliminated by operation in dry nitrogen or vacuum but sometimes many revolutions are needed for ring cleanup. For this reason, slip rings with this brush material should only be operated in dry nitrogen or vacuum. If exposure to humidity occurs statically, subsequent vacuum or dry nitrogen exposure to remove any adsorbed water before operation is started will prevent any problems.

As of 1 January 1986, nine GPS satellites with 18 array drives have been launched. Array motion varies from a few degrees to 360 degrees per orbit (two orbits per Earth day) and occurs in steps of approximately 0.1 degree. Total drive operating time on 1 January 1986 was 89.5 years with 7.8 years on the oldest pair. No slip ring problem known to Ball Aerospace has ever occurred.

## HIGH POWER SLIP RINGS

Within the past year, two 50,000 revolution thermal vacuum life tests were successfully completed at Ball Aerospace on 61-ring slip ring assemblies from Electro-Tec. These units included four 48-ampere and two 24-ampere 125 Vdc rings (15 kW total power capacity). Features of this slip ring will be discussed for the insights they provide into the high power transfer units required for new large spacecraft such as Space Station.

The 48 ampere rings were 2.38 in. diameter fine silver with a hard silver flash, plated up in 0.25 in. wide grooves in a ceramic-filled epoxy. Raised barriers 0.188 in. high and 0.20 in. wide separated pairs of high side and return rings. The barriers were grooved 0.090 in. deep and stationary discs mounted on the brush blocks fit down into the grooves, providing virtually complete isolation between rings and preventing line-of-sight between exposed hot elements and ground. Surface creepage distance between rings of opposite polarity was 0.75 in. (enough for more than 500V). The remainder of the power

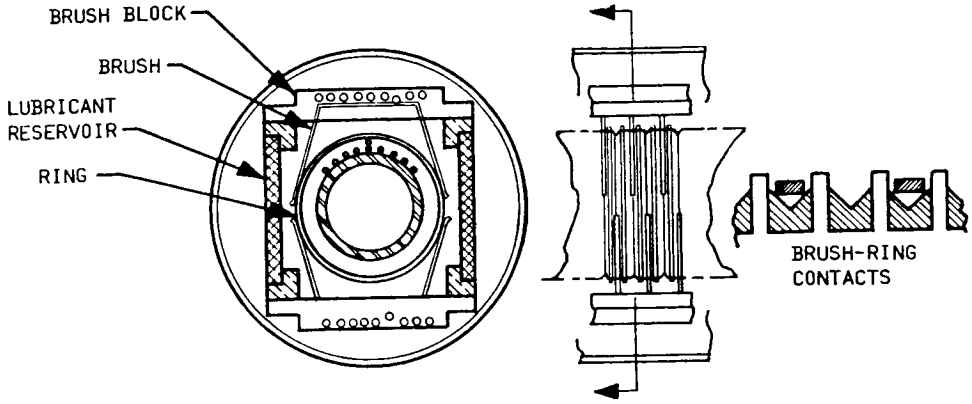


Figure 2. - Wire brushes slip ring details.

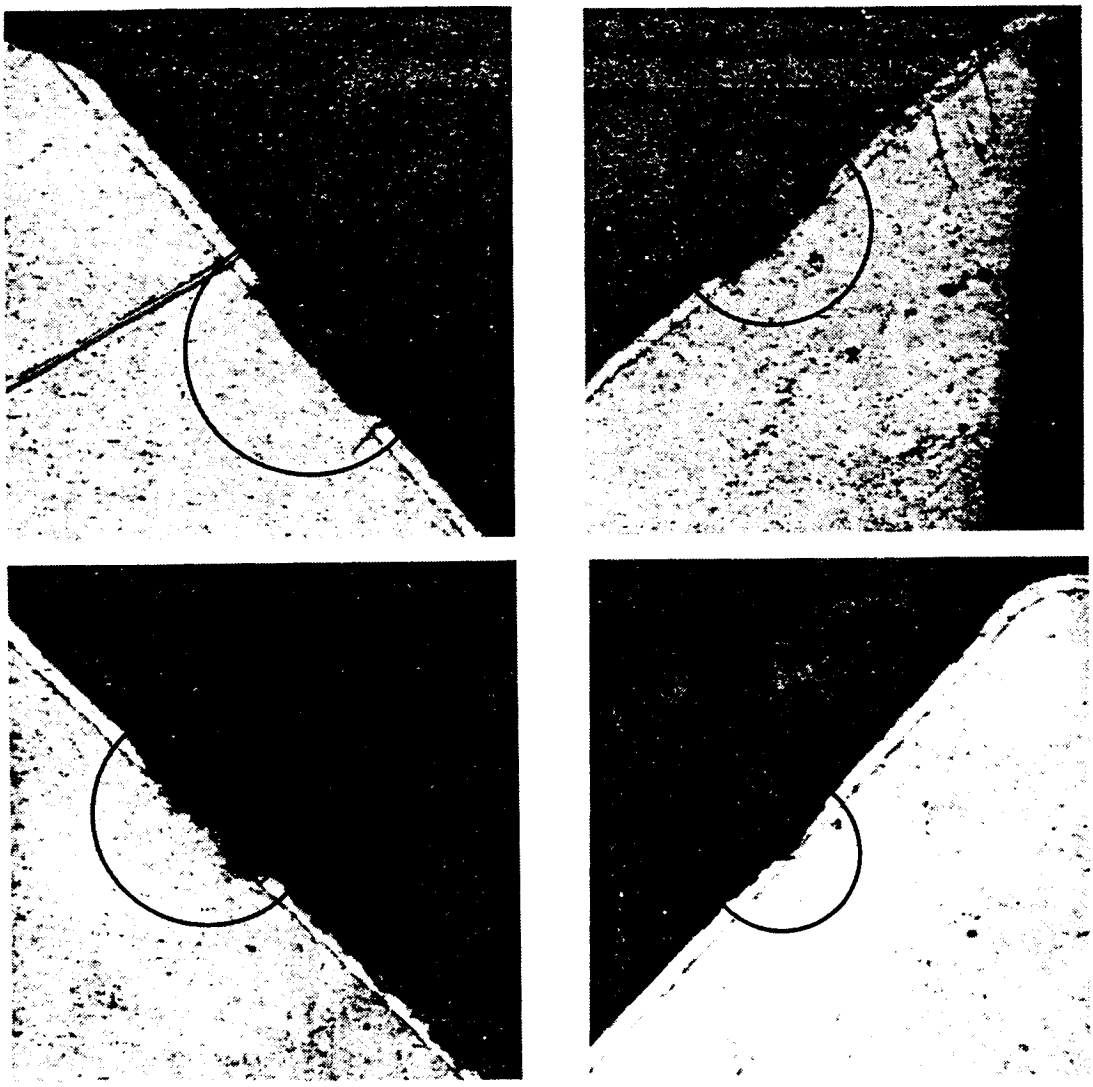

Figure 3. - Wear scars on gold slip rings after 18 months at 30 rpm.

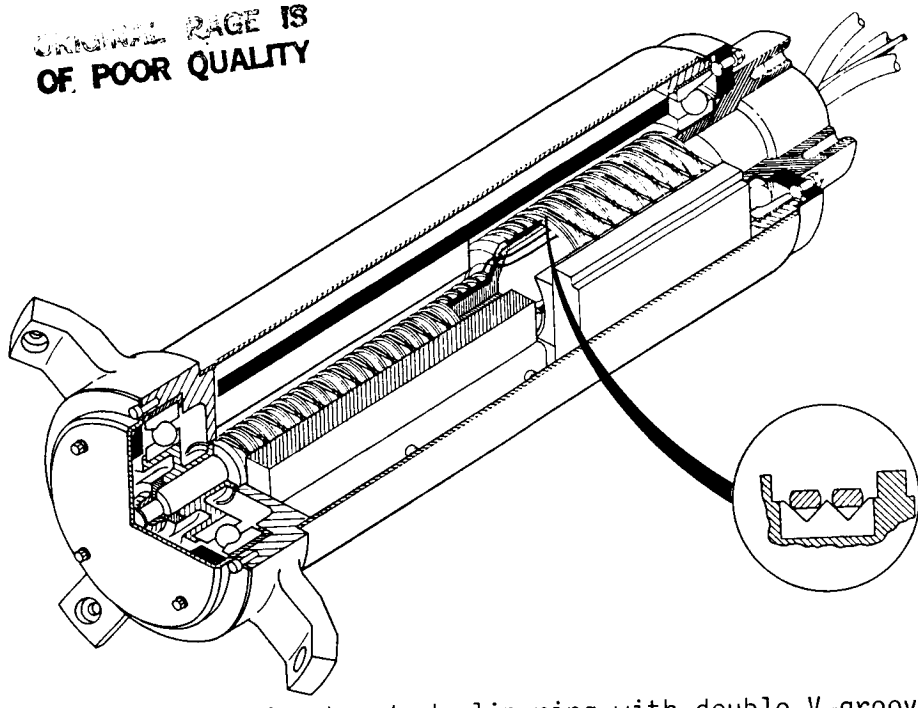

Figure 4. - Wire brushed slip ring with double V-groove rings and side-by-side brushes.

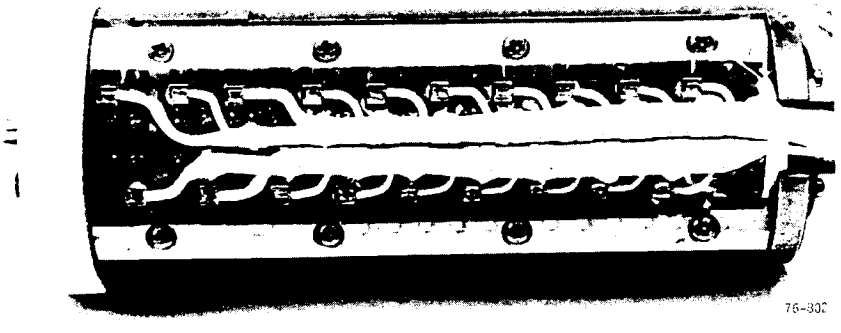

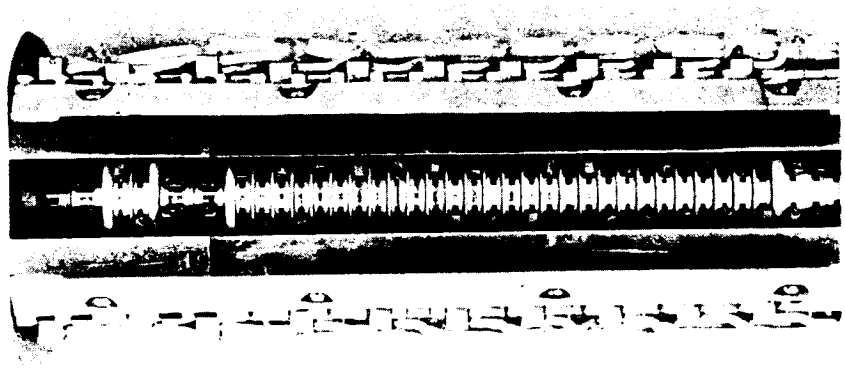

Figure 5. - GPS block 1 slip ring assembly.

# DESIGN AND ANALYSIS OF A KEEL LATCH FOR USE ON THE HUBBLE SPACE TELESCOPE

John Calvert and Melanie Stinson*

This paper will be divided into two parts. The first part will deal with the mechanical design of the keel latch. The second part will be the stress analysis of the keel latch.

The first part will present (1) background information; (2) mechanical design requirements; (3) some of the initial design considerations; (4) the design considerations that led to the selection of the final design; (5) the mechanics of the final design; (6) testing that has been and will be accomplished to verify that design requirements have been met; and (7) future tests.

## BACKGROUND INFORMATION

One of the initial requirements of the Hubble Space Telescope (HST), now scheduled for launch in the summer of 1986, was that it must have the capability of being maintained or refurbished on orbit. To meet this requirement, the Marshall Space Flight Center (MSFC) was directed to design, develop, fabricate, and test the necessary space support equipment (SSE) that will allow this requirement to be met. This HST SSE will be flown on a dedicated on-orbit maintenance mission.

The current planning for the HST maintenance mission is to have the orbiter approach the HST in order that the HST can be captured by the remote manipulator system (RMS). The RMS will then place the HST into a flight support system maintenance platform (FSSMP) with the HST longitudinal axis in a vertical position (see Figure 1). The FSSMP is the same hardware as used during the solar maximum repair mission. The FSSMP has the capability to rotate the HST about its longitudinal axis or to tilt it forward into a stowed position (Figure 2). All maintenance will be performed on the HST while it is in the vertical position (Figure 1). The HST will be tilted forward 57.5 degrees to its stowed position for the orbiter primary reaction control system firings or astronaut sleep cycles. When the HST is in the stowed position, it will be restrained by having its keel fitting secured by a structural keel latch.

*NASA Marshall Space Flight Center, Alabama.

## MECHANICAL DESIGN REQUIREMENTS

The following are the design requirements for the structural keel latch as defined in the HST On Orbit Maintenance Mission Space Support Equipment Design and Performance Requirements document.

## KEEL LATCH DEVICE

The ORU carrier shall include a structural keel latch for engagement to the HST STA 240 keel trunnion, when the HST is tilted to the stowed position by the MP. Design of the keel latch shall take into account the orbiter primary reaction control system (PRCS) thruster loads when the HST is latched to the carrier structure. The keel latch shall have a capture range to accommodate an HST keel misalignment of ±2.54 cm (±1 in.) in the Y transverse direction and ±3.81 cm (±1.5 in.) in the X (longitudinal) direction. MP positioning shall correct for Z (vertical) direction alignment requirements (see Figure 1 for axis orientation). Engagement of the keel latch to the HST keel trunnion shall be provided for by a remote operation. The design of the keel latch for disconnect from the HST shall provide for a redundant remote control operation from the orbiter crew compartment. Backup disengagements shall be by means of a manual operation. The keel latch shall be designed to dampen the impact load of the HST while being tilted to the stowed position at the maximum rate without damage to the latch device or the HST.

The impact load would occur if there were a malfunction of the flight support system maintenance platform during the tilting of the HST and the HST keel fitting were allowed to impact the keel latch at maximum tilting velocity.

The keel latch also had to meet the following requirements:

Resist the following loads:

Y ± 623 kg (±1,375 lb)

Z + 812.8 kg, - 735.3 kg (+1,792 - 1.621 lb)

X no load (the HST attachment shall have freedom to move to the X direction to accommodate HST thermal growth).

The keel latch shall not apply more than 38.3 kg (85 lb) to the HST keel fitting during latching operations.

The keel latch must be two-failure tolerant for all crew safety operations. Astronaut EVA may be required after second failure.

## INITIAL CONSIDERATIONS AND CONCEPTS

Figure 3 shows one of the initial concepts that was considered. It had two jaws that were driven by two individual motor drive units (MDU). As shown in Figure 3, the initial concept did not meet all design requirements.

This concept would capture the HST keel fitting, but did not have the capability to locate and capture the HST keel fitting in the required capture range. The selected design was an evolution of this concept and is shown in Figure 4. Briefly, it operates in the following manner: The HST keel fitting, with attached spool, is lowered into the capture envelope of the keel latch and, by depressing the t-bar, gives a ready-to-latch indication to the orbiter aft flight deck. The MDU for jaw 1 is turned on and jaw 1 moves toward the locked position. When its deployable bumper makes contact with the HST keel spool, the MDU for jaw 1 cuts off. The MDU for jaw 2 will then be turned on and moves toward the closed position. Jaw 2 continues to close until its stops make contact with the stops on jaw 1 (Figure 5). The spool is then secured by the jaws, but the stops maintain a clearance between the jaws and the spool. This will allow the spool to move in the X direction. To unlatch the HST keel fitting, the MDU for jaw 2 and then jaw 1 will be reversed.

## DESIGN CONSIDERATIONS

The HST keel fitting is designed to provide a low friction mating surface for the orbiter keel latch used during the HST deployment mission. This made it necessary to add an appendage to the HST keel fitting to provide a positive means of resisting the required vertical loads. The shape selected for this appendage was a spool (Figure 6). This spool shape will provide a positive means of resisting the vertical loads imposed on the keel fitting. The internal sloped ends of the spool, in conjunction with the mating slope of the jaws, provide a capture envelope in the vertical direction.

The keel spool is mounted to the HST keel fitting by a spring loaded plunger (Figure 4). A mono-ball is incorporated in the spool mounting to allow for any axis misalignment between the HST and the keel latch. The Belleville spring washers will dampen any shock load as the keel fitting is placed in the keel latch.

Another design requirement of the spool was that it be visible from the aft flight deck by the astronauts, either by direct sight or by use of the orbiter closed circuit television system (CCTV). To make the spool more visible, the spool itself was gold plated.

The HST keel fitting/keel spool is placed in the keel latch capture envelope by an astronaut operating the FSSMP and observing the location of the keel fitting spool. The spool makes initial contact with the T-bar and depresses it approximately 2.54 mm (0.10 in.) (Figure 4). When the T-bar is depressed, redundant microswitches are actuated and will give a ready-to-latch indication on the aft flight deck. The switches are adjusted so that any time the ready-to-latch indication is on, the spool is in the required capture range.

During normal operating conditions, the spool impacts the T-bar with 4.5-22.5 kg (10-50 lb) force. However, a malfunction in the FSSMP could tilt the HST at full rate of 3.2 cm/sec (1.26 in./sec) that causes an impact load of 363 kg (800 lb).

When a ready-to-latch indication is obtained, the jaw 1 MDU is turned on. The MDU bevel drive gear drives a bevel gear at a 2:1 gear ratio. This driven gear has internal splines for mating with the drive screw. The two bevel gears are held in mesh by an EVA nut (Figure 4 and Figure 8). By removing the EVA nut from the driven bevel gear, the gear can be disengaged from the MDU bevel gear; and the drive screw can be rotated without having to backdrive the MDU. This is a safety feature that will allow the drive screw to be rotated in case the MDU malfunctions. The MDU has an internal brake that locks the output shaft if power is removed from the motor.

With the MDU operating, the drive screw will rotate and move jaw 1 away from the stow position. As jaw 1 begins to move, a lever system (Figure 4), will allow a bumper to be extended from the front of jaw 1 by spring force. The entire plate and bumper are moved forward (see Figure 4). Jaw 1 will continue to move until the protruding bumper makes contact with the spool. The bumper will be forced back, exerting only 3.63-4.5 kg (8-10 lb) on the spool. As the bumper is forced back, it will actuate microswitches that will give an indication jaw 1 is in the locked position on the aft flight deck. This will allow jaw 1 to locate the spool and stop whenever the spool is placed in the capture envelope.

The MDU for jaw 2 will then be turned on. Jaw 2 will travel toward the closed position until stops on jaw 2 make contact with stops on jaw 1 (Figure 5). The closing force for jaw 2 is reacted by the jaw 1 stops; no force is exerted on the spool. The MDU for jaw 2 will continue to drive until a 1,134 kg (2,500 lb) preload is applied between the mating stops. When the predetermined preload is reached, jaw 2 MDU is cut off by the power nut being moved in relation to the rest of jaw 2 (Figure 7). The power nut is held in position by four Belleville spring stacks. These spring stacks allow the movement between the power nut and jaw 2.

This preload between the jaws will capture the spool between jaw 1 and jaw 2. The stop lengths are determined at assembly to provide for 0.127 cm (0.005 in.) clearance between the jaws and the keel fitting spool. This allows the jaws to resist keel fitting spool loads in the ±Z and ±Y direction, but will allow the HST keel fitting to move in the X direction to meet the requirement of allowing for thermal expansion and contraction of the HST structure.

The spool is released from the latch by actuating the jaws in the reverse order from which they are latched. Jaw 2 is released first; and when it is no longer in contact with the spool, jaw 1 MDU can be reversed. This order of releasing the spool is necessary because of the spring load that would be applied to the spool by jaw 2 if jaw 1 were released first. When the jaws are 0.95 cm (0.375 in.) from their stowed position, they come in contact with individual preload switches (Figures 4 and 8). These switches serve two functions: (1) They will cut off the operation of the MDU's when they are operated in the reverse direction and the jaws reach their stowed position. (2) The preload switches are also spring loaded so that, when compressed by the jaws while in the stowed position, they will provide stability for the jaws during launch and landing vibration.

## MANUFACTURING PROBLEMS

One of the first problems discovered during assembly operations was that the flange on the drive screw for jaw 2 was galling on the side under pressure when jaw 2 was being closed. This was attributed to the flange flexing during application of the 1,134 kg (2,500 lb) preload. The design solution was to apply only a 227 kg (500 lb) preload; measure the gap between the power nut and jaw 2; machine a spacer 0.51 mm (0.020 in.) thinner than the measured gap (Figure 7) and install it between the power nut and jaw 2. The lesser preload was enough to initially secure the spool and the installed spacer would not allow jaw 2 to move back enough to releasee the spool. Only 227 kg (500 lb) was applied to the flange while it was rotating. No galling has been detected after the spacer was added to the engineering unit.

Another problem discovered during initial assembly was the stops with ramped ends did not provide the necessary dimensional repeatability accuracy for the required gap between the jaws when the jaws were closed. The ramps were initially provided to produce a wedging action between the stops and the tracks they slide in during the latching action. After initial assembly, it was decided to use flat surfaces with a slot on one stop and a mating groove on the opposite stop. This prevents the jaws from racking during locking operations and also provides a positive indexing of the jaws in relation to the spool.

## LUBRICATION

Dry lubricant was used throughout the keel latch except in the MDU and the two ball bearings supporting the MDU bevel gear. These two applications have Brayco 601 grease. External heaters have been provided to prevent freezing of the grease at low temperatures.

NPI 425 dry lubricant was used in all applications where the cure temperature of 302°C (575°F) would not damage the parent metal. NPI 14 was applied to all other sliding surfaces.

The drive screw end bushings are made from Nitronic 60 and the drive screw is made from A-286 stainless steel with NPI 425 applied to all mating surfaces. The keel latch engineering unit has been subjected to approximately 80 cycles and there have been no problems with lubricant break down.

## TESTING PROGRAM

The first test the keel latch engineering unit was subjected to was a proof of concept test conducted in a 6 degrees-of-freedom (DOF) test facility. The test facility was computer controlled and powered by hydraulics. It has the capability to produce motions and forces that simulate the HST being tilted forward into the keel latch capture envelope. It also has the capability to measure forces that are induced into the HST keel fitting by the keel latch during latching operations. Figure 11 shows the keel latch installed in this facility. Equations of motion were developed that considered the mass of the HST, the flexibility of the FSSMP, and the elasticity

of the keel latch support structure. These equations were input to the computer and tests were accomplished which prove, first, that an astronaut could place the keel fitting spool into the keel latch capture envelope; second, the keel latch has the required capture envelope; third, that it would not exert more than the specified loads on the HST keel fitting during a latching operation; and fourth, the keel latch could survive and operate after the specified impact load.

The ability of an astronaut to place the spool in the keel latch capture envelope using the FSSMP manual controls was verified during this series of tests. A direct visual line of sight was available for the initial testing, but later the berthing operation was accomplished by using television cameras only. It was very apparent during this testing that proper camera placement was critical for a satisfactory berthing. It was verified that the FSSMP could position the spool in the required capture envelope and the keel latch could successfully capture and retain the spool over the entire specified capture range. During this series of tests, it was proven that the keel latch could retain the spool when it was subjected to the maximum specified loads in both Y and Z axis.

An impact loads test was also accomplished in the 6 DOF test facility. As stated earlier, for normal operation the force that the spool impacts the keel latch is 4.5-22.5 kg (10-50 lb); but for a malfunctioning FSSMP, the force could be as much as 363 kg (800 lb) for an initial impact and build up to 1,225 kg (2,700 lb) if the power is not cut to the FSSMP. The keel latch sustained no damage during this test.

By observing the motion of the spool in relation to the keel latch and operating the tilt control of the FSSMP in the proper rhythm, the spool can be brought into the keel latch with very little oscillation and very little impact force. It did require some learning on the part of the operator but was easy to accomplish once learned.

During berthing tests it was discovered that the clearance between the spool and the forward part of the keel latch was inadequate. When the spool was being placed in the ready-to-latch position and positioned in the center of the keel latch capture range, the spool clearance at the forward edge (X direction) of the keel latch was 2.29 mm (0.09 in.). This was due to the geometry of the FSSMP and the HST. The spool entered the keel latch on an arc instead of a straight line. A redesign of the keel latch was required to increase this clearance to 3.18 cm (1.25 in.).

The keel latch was then subjected to a vibration test in all three axes. The unit was vibrated in both horizontal axes and operated satisfactorily during post-vibration testing. The unit was then transferred to the vertical test facility and vibrated. Jaw 1 operated satisfactorily, but the MDU for jaw 2 would not cut off.

The engineering unit was disassembled and inspected. It was found that the clearance that provides for microswitch over-travel was less than dimensionally specified. This clearance is required to insure repeatable

microswitch operation. Interference between the power nut and jaw 2 prevented proper mating of the power nut with jaw 2. This condition resulted in the actual over-travel available being less than indicated. The interference problem was corrected by removal of material.

The engineering unit will next be subjected to thermal vacuum and life cycle testing which will complete the required test program.

## STRESS ANALYSIS

The stress analysis of the keel latch was originally begun assuming that the structure was determinate. However, once all the load paths and reaction points were determined, it became obvious that the keel latch was an indeterminate structure.

To solve the system of loads and reactions, a finite element computer model of the latch was built (Figures 13 and 14). A detailed model which would provide stresses was decided against since the keel latch is a fairly complicated mechanism, and there were time constraints. Instead, a more simplified model which would provide reactions was used. Once the reactions were found, stresses for different parts were calcualted by tracing the load paths and using the appropriate reactions for a part and the part geometry.

The Z loads were reacted at the eight rollers that ran in the side plate slots (Figure 4). Each jaw had four rollers, two on the +X side and two on the -X side. The Y loads were reacted at the two drive screw flanges (Figure 4), one on the +Y end and one on the -Y end. Although there were no applied X loads, moments induced into the system by the Y and Z applied loads created X loading. The X loads were reacted by four recirculating rollers (Figure 4). Each jaw had two recirculating rollers, one on the +X side and one on the -X side. Figure 15 shows the reaction points on the computer model.

It can be seen by looking at Figure 15 that the jaw stops were modeled as several skewed bars instead of one straight bar. The reason there are several bars instead of one is that there has to be a grid point at each reaction point, and the bars have to begin and end at a grid point. The reason the bars are skewed instead of straight is that the reaction points don't all fall in line in the XY plane. To avoid getting inaccurate reactions due to the deflection of the skewed bars under load, the bars were made very stiff so as to act like one straight bar.

Several assumptions about the behavior of the keel latch under load had to be made in order to define the proper constraints in the model. The first assumption was that all eight rollers could react at the same time. The second assumption was that both drive screw flanges could react at the same time. The third assumption involves the recirculating rollers, and it had to be approached from a different aspect than the other two assumptions. As stated earlier, the only X loading comes from moments induced by the applied Y and Z loads. After studying the actual keel latch engineering unit, it was decided that when the Y and Z loads were applied, the jaws would form a couple and try to rotate about the Z axis. The reaction to the couple would come

from one recirculating roller on one jaw and one recirculating roller on the opposite side of the other jaw. Therefore, the third assumption was that only two recirculating rollers, one on each jaw, could react at the same time and that they would always be on opposite sides of the jaws from each other. Which two would react was a function of where the external loads were applied. The fourth assumption was that the drive screws would take no bending, therefore, the shear and moment reactions at the drive screw flanges were released.

The next assumption that had to be made in the model was how to incorporate the 227 kg (500 lb) preload between the jaw stops. It was decided that in order to initiate the preload, a forced displacement of one of the drive screw flange ends would be used. By displacing one of the Y-force reaction points in the Y direction, a compression force in the Y direction between the jaw 1 stops and jaw 2 stops was achieved. A dimensionless spring element in the Y direction was placed between the end nodes of either pair of stops in order to detect the amount of compression present for a given forced displacement. The spring elements were dimensionless because the end nodes of either pair of stops were located in the same geometric location in order to represent the hard contact between the stops when the jaws are closed together (Figure 15).

The initial displacement used was a calculated guess based on the spring rate of the jaw stops and the known compression force that was needed. It took only two iterations of holding the spring rate constant, varying the forced displacement, and determining the compressive force in the spring before a 227 kg (500 lb) preload was achieved. Determining the preload case for the model was a very good check for the model because it showed that it was acting symmetrically under the preload, and the actual keel latch acted symmetrically under the preload when it was tested.

Once a method for incorporating a preload had been determined, the worst load case for each reaction point had to be determined. The preload case was considered the first load case, and the other eight load cases contained the preload and the external load. The external loads were applied in four different locations on the model (not simultaneously) (Figure 15) with a +Z and -Z load case at each location for a total of eight cases. The two points identified on each jaw represent the end points of the envelope where the spool could be located when the external forces are applied, and there is an envelope on each jaw because the Y load is fully reversible. It was found that when the external load was applied in all eight cases, the preload was completely relieved, and the worst reactions were a function of only the external load. The load case which was the worst for each reaction point varied.

Two minor design changes were made due to findings from the model and stress analysis. First, the analysis showed that the worst case roller load would fail the side plate slot upper flange. To correct this, the flange was increased to an adequate thickness. Second, the analysis showed that the bending forces on the jaw stops due to the tongue and groove mating at the

ends would fail the stops at a section where the rollers went through the stops. To correct this, the jaw stop material was changed from aluminum, which has a low bending strength, to Inconel, which has a high bending strength.

All the load cases had to be run again when the keel latch was redesigned to solve the clearance problem between the spool and the forward part of the keel latch. The jaw stops were redesigned such that the envelope where the spool could be located when the external forces are applied was increased. When the new loads were determined, the appropriate changes were made in the stress analysis.

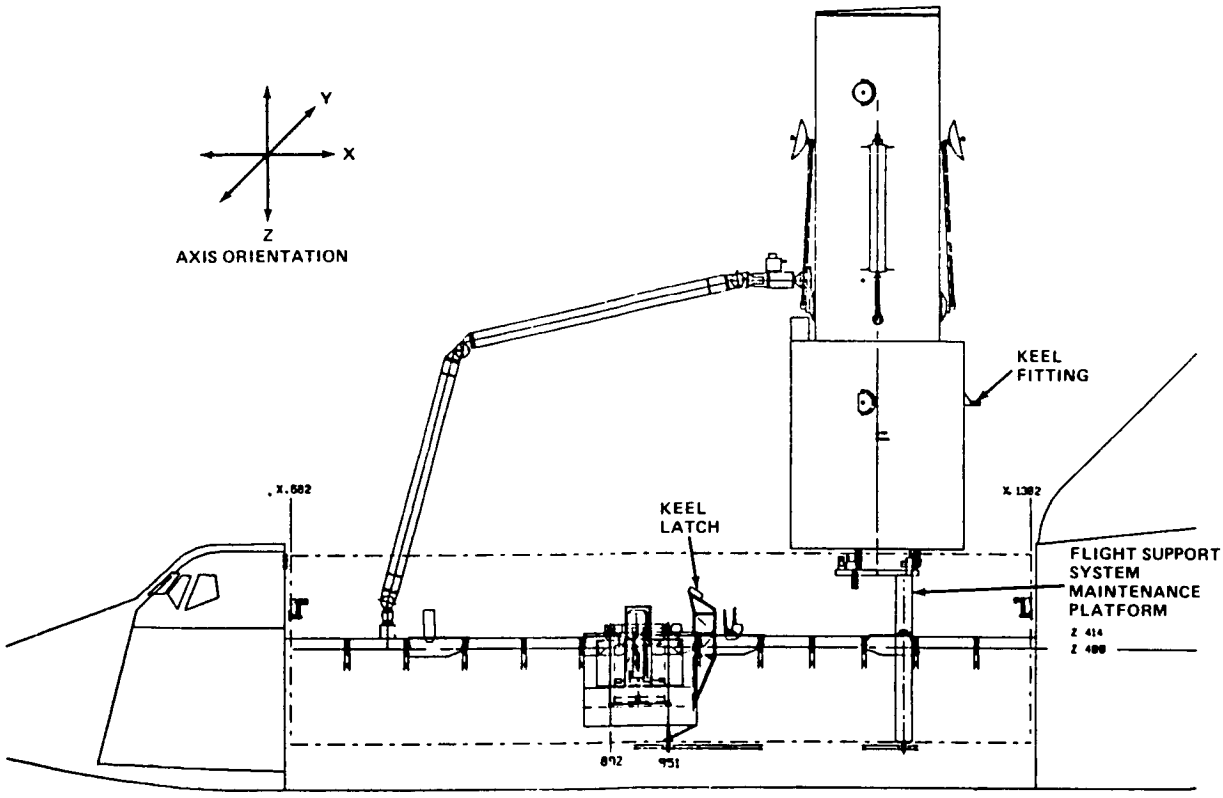


Figure 1. - Berthing configuration.

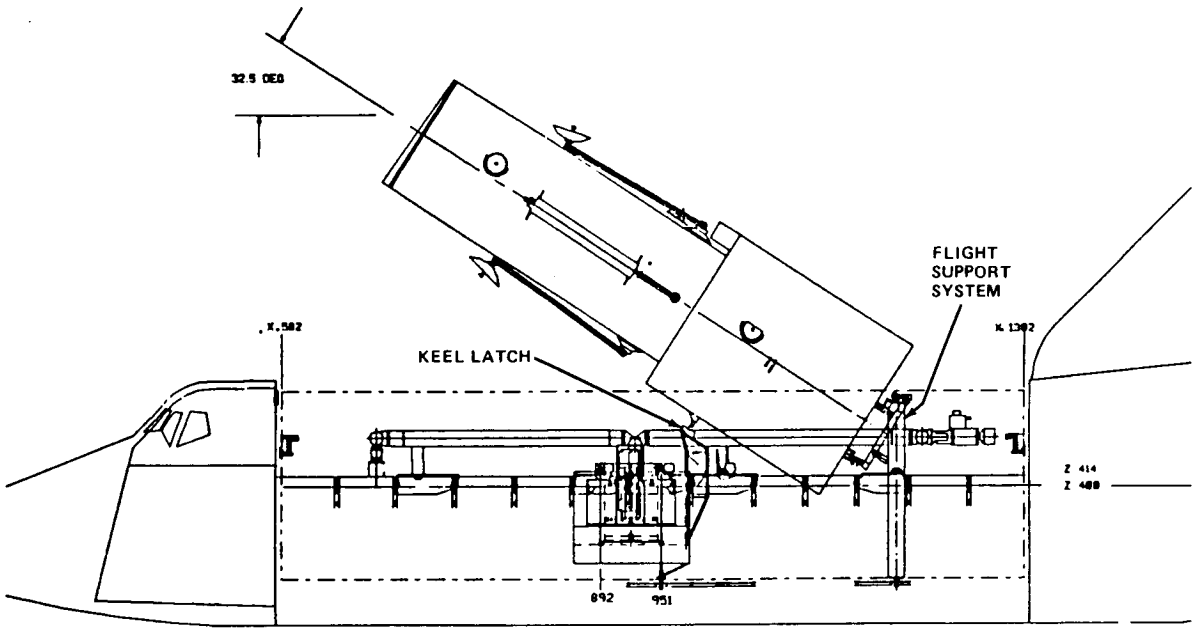


Figure 2. - Stowed/reboost configuration.

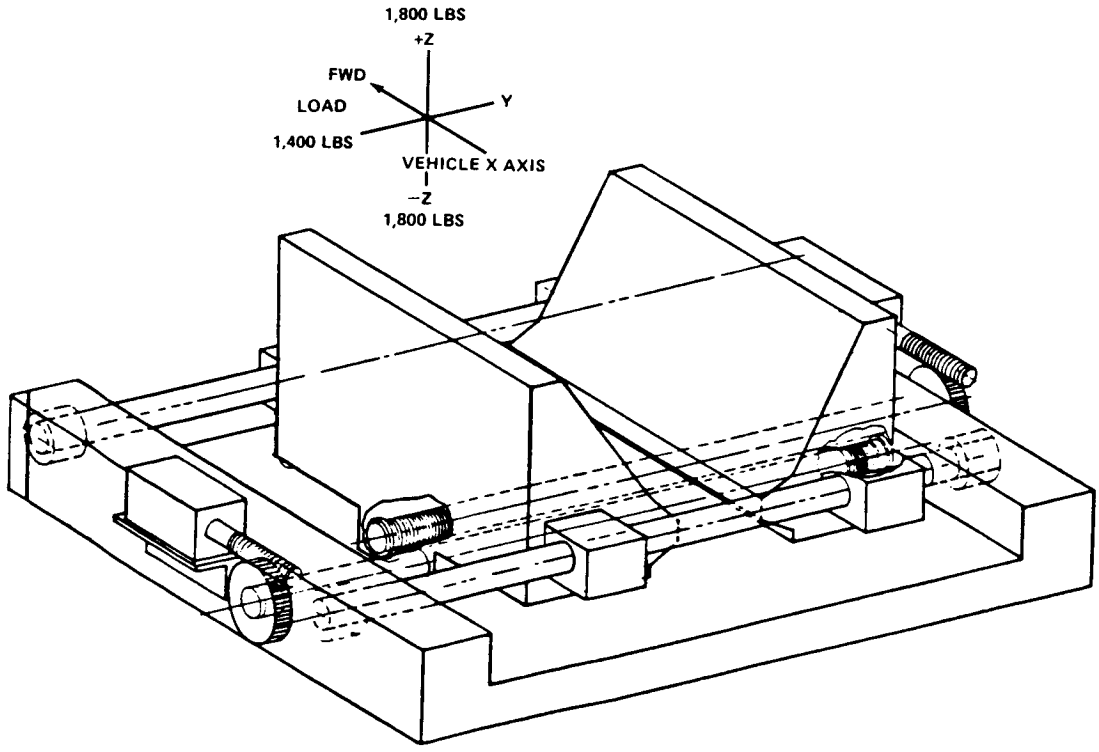


Figure 3. - S. T. keel latch concept.

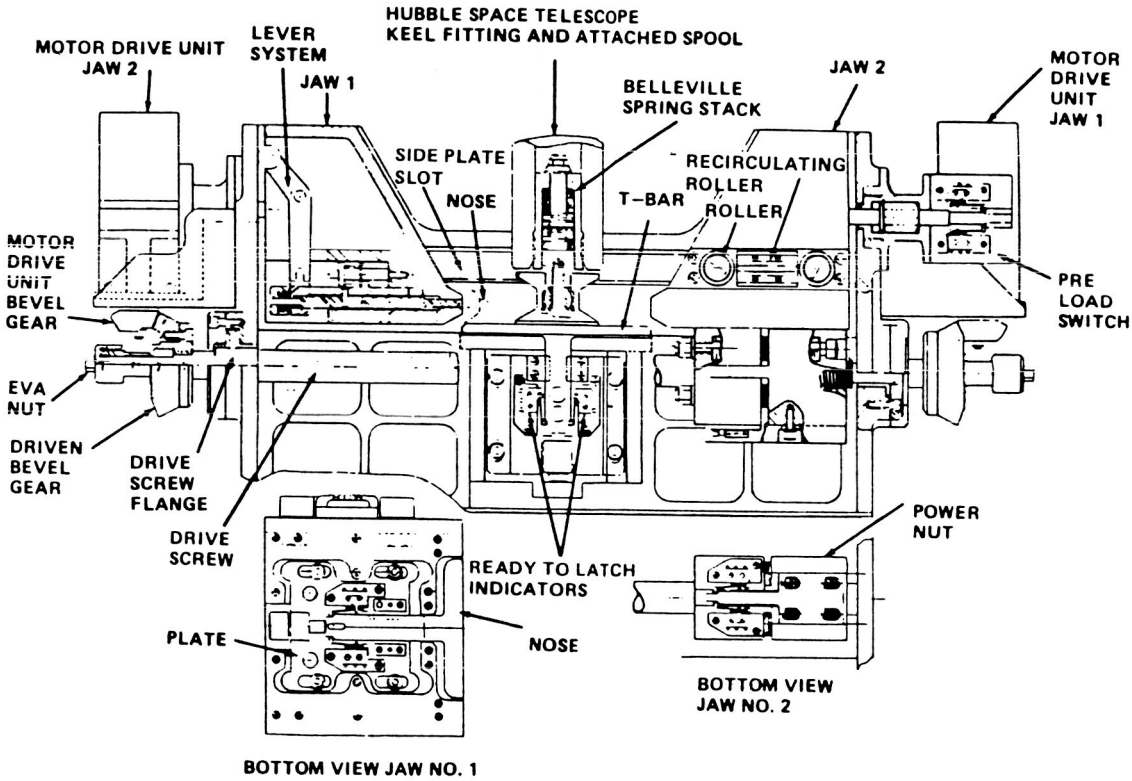


Figure 4. - Keel latch sectional views.

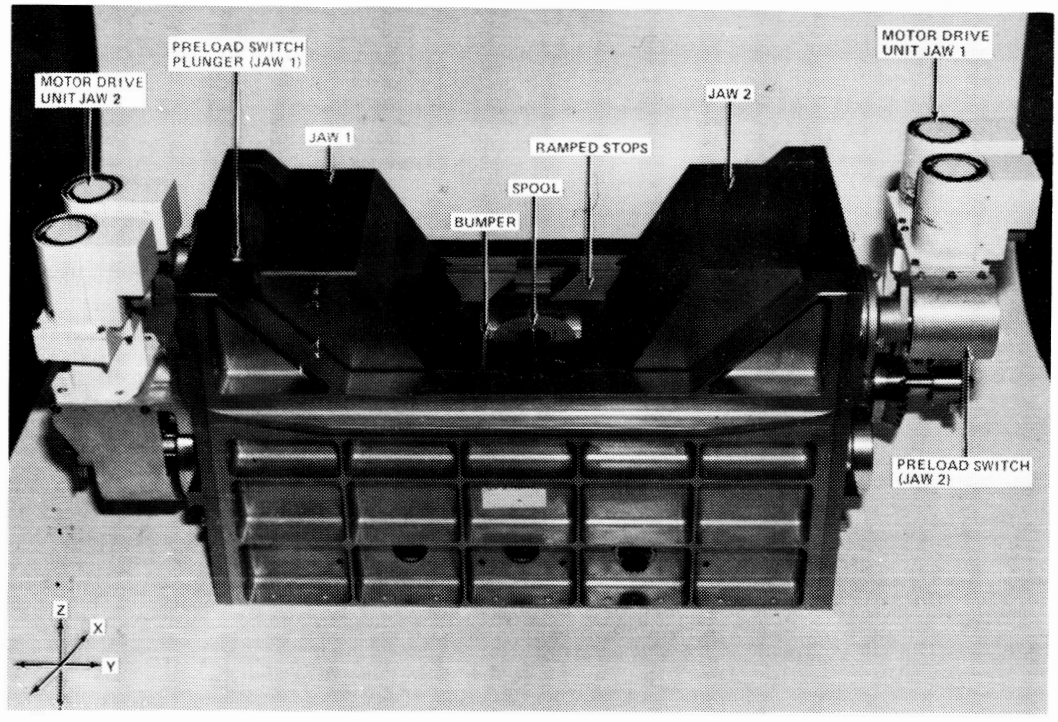


Figure 5. - Side view of keel latch.

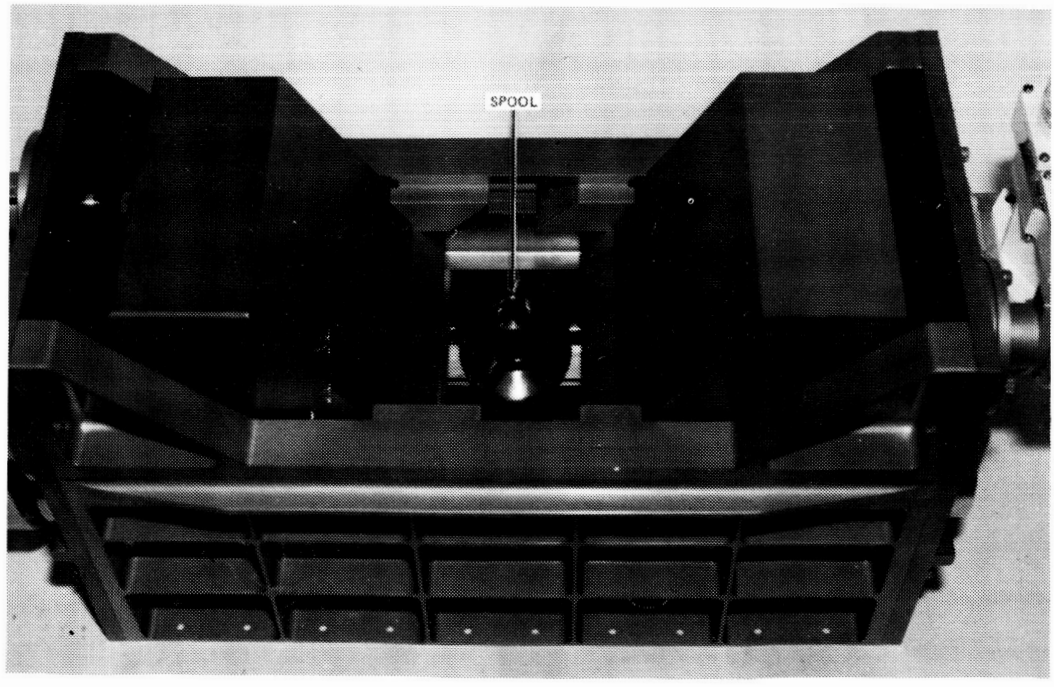


Figure 6. - Keel latch top view.

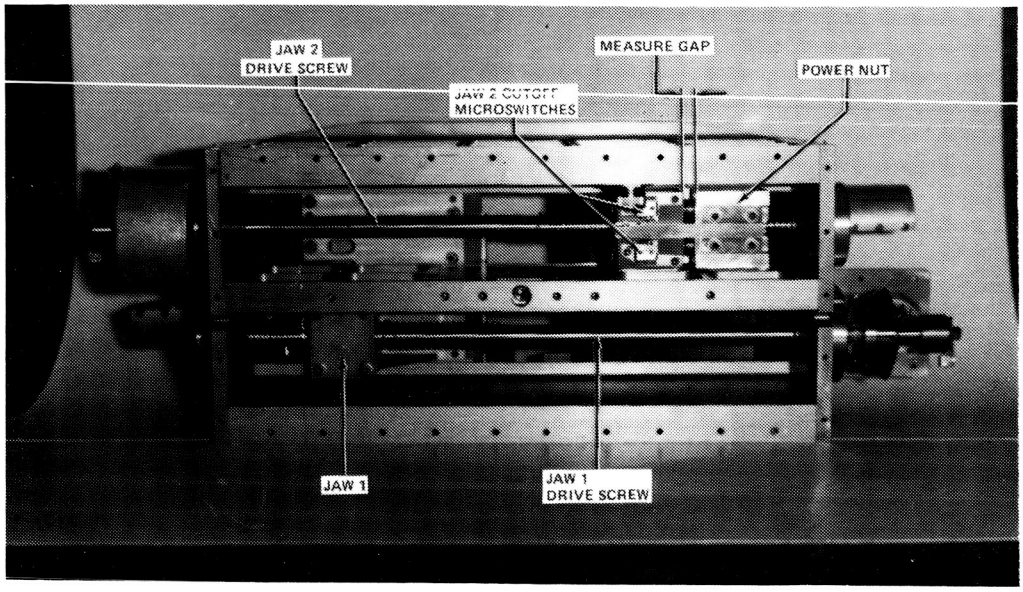


Figure 7. - Bottom view of keel latch.

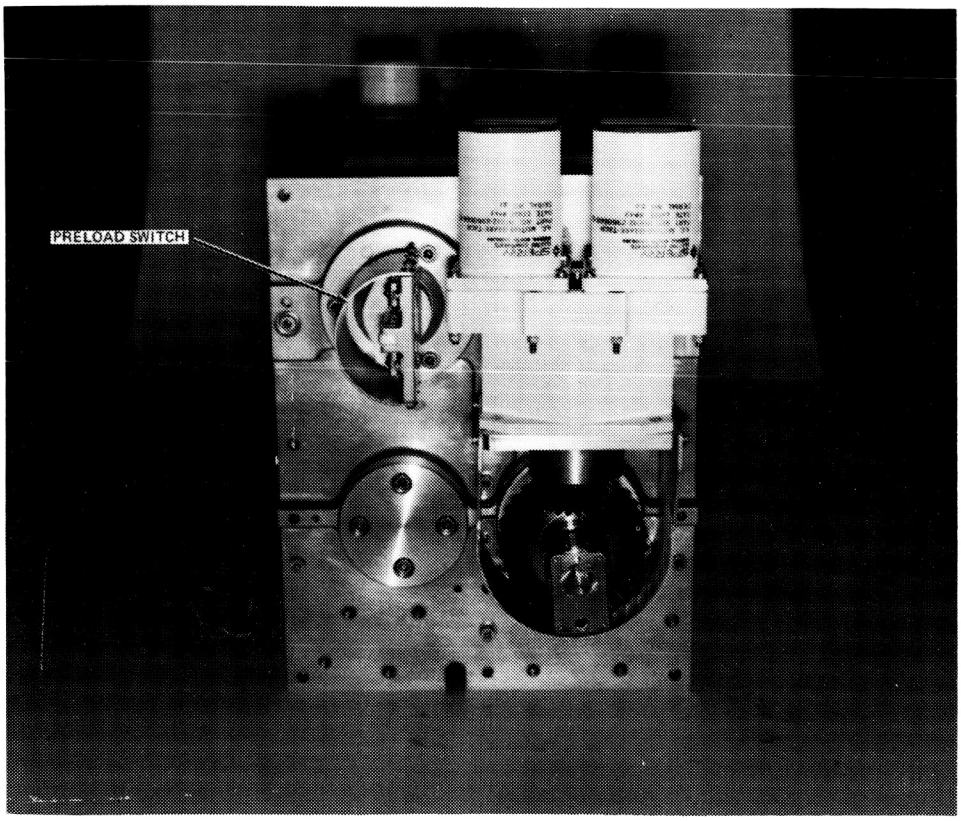


Figure 8. - Keel latch end view.

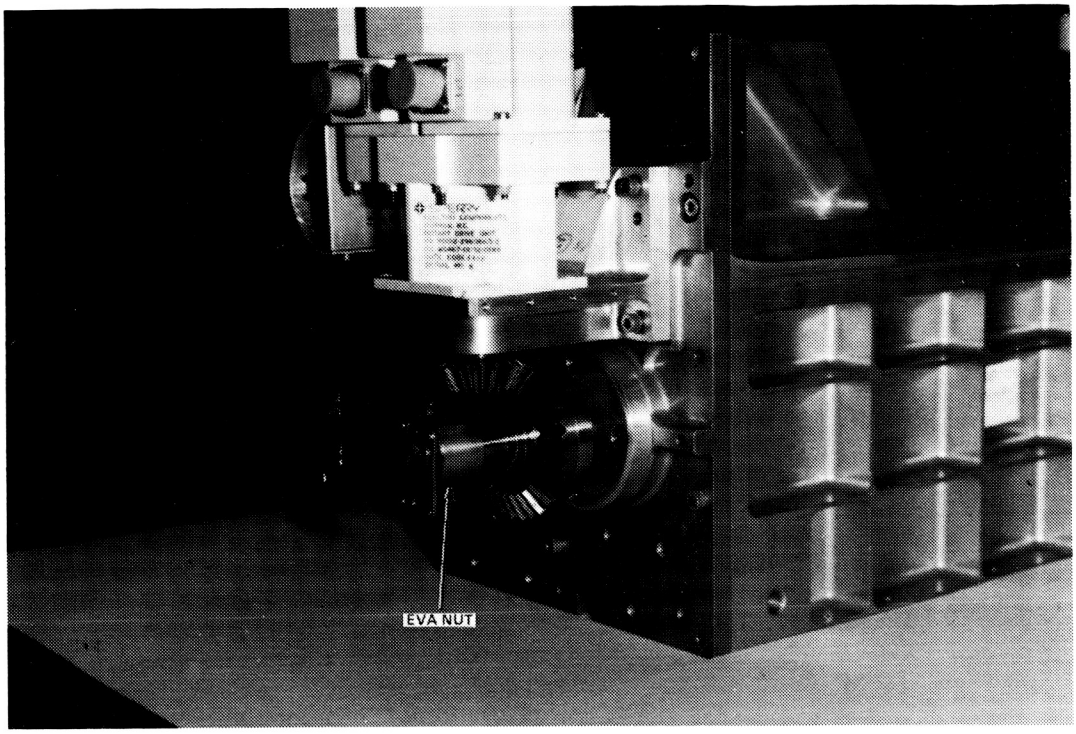


Figure 9. - Keel latch EVA nut detail.

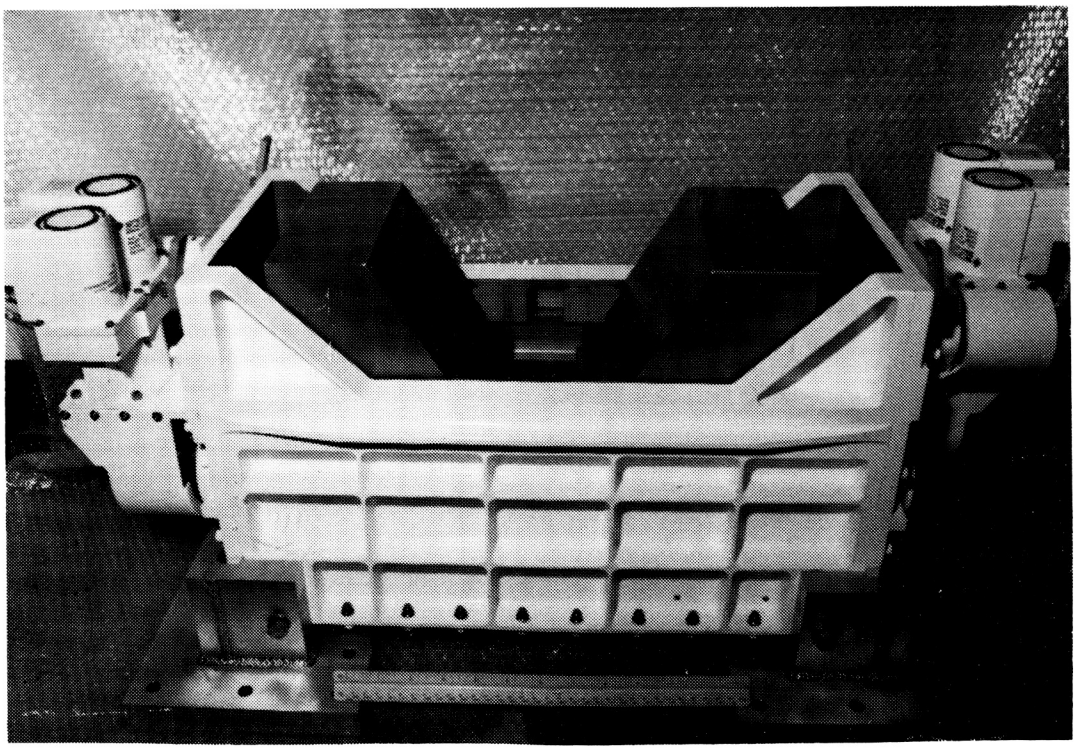

Figure 10. - Keel latch test configuration.

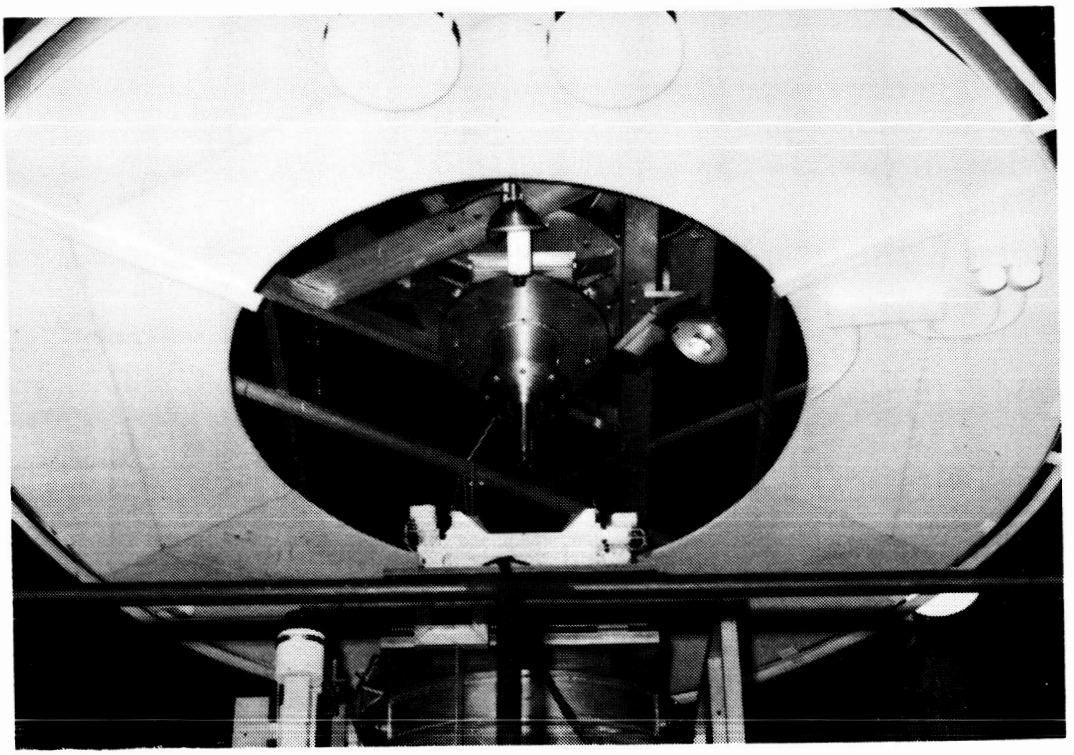

Figure 11. - Six DOF test facility.

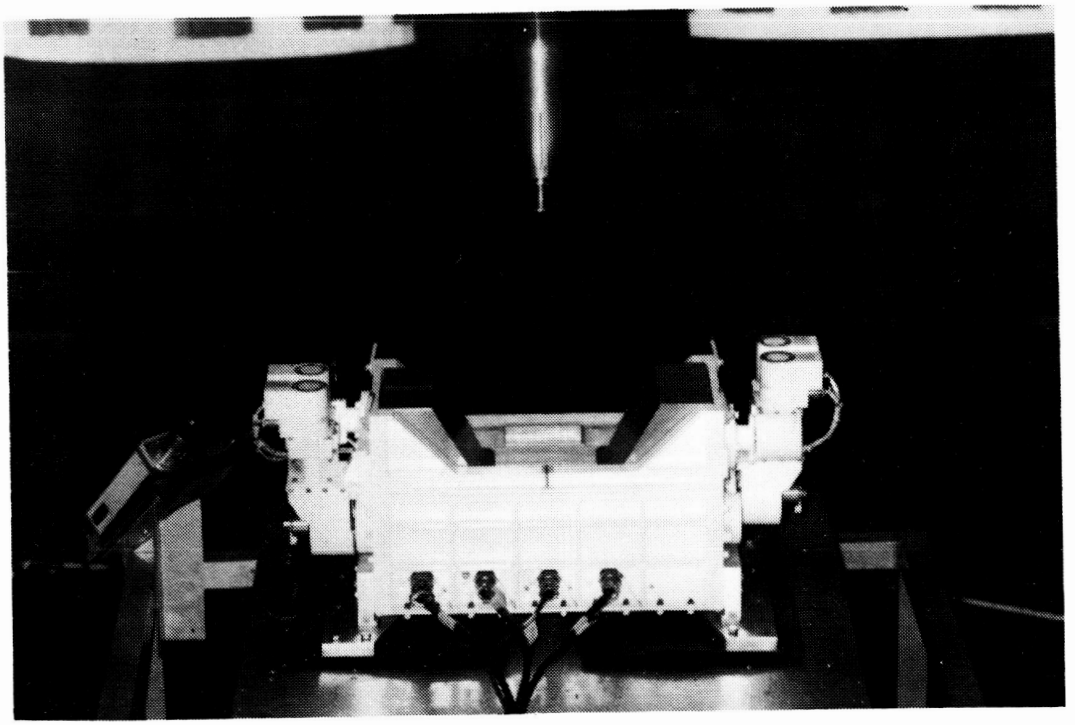

Figure 12. - Six DOF test configuration.

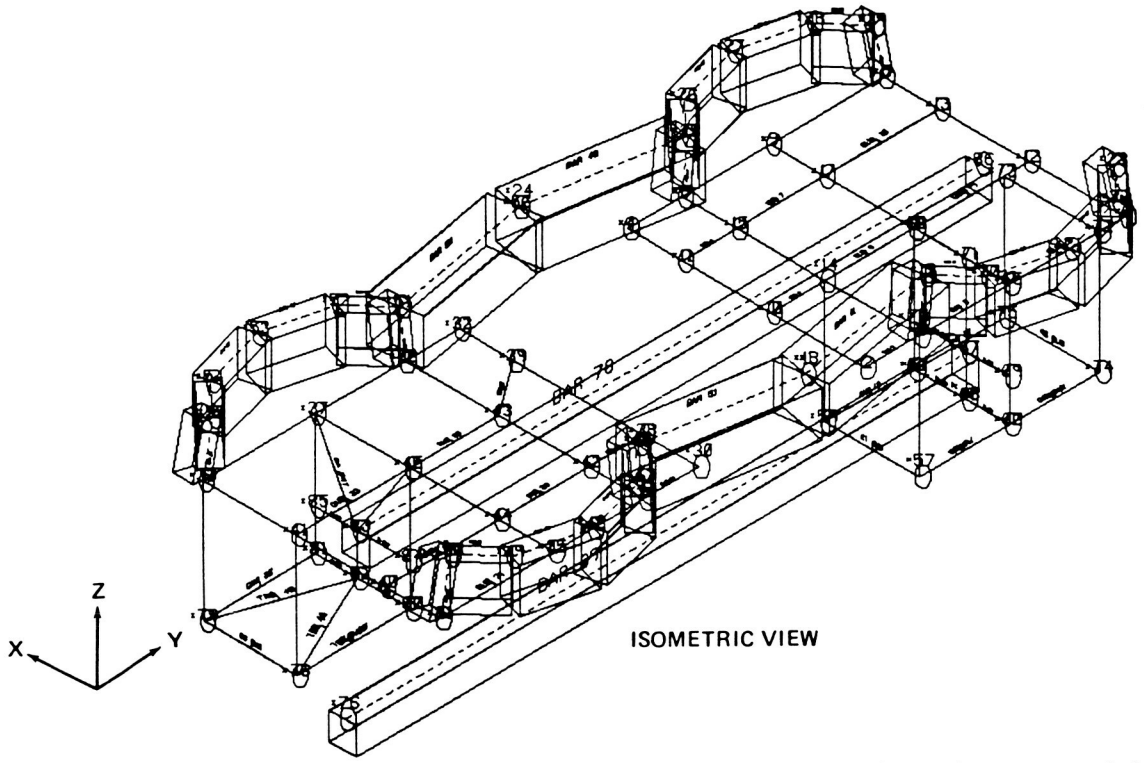


Figure 13. - HST maintenance mission keel latch finite element model.

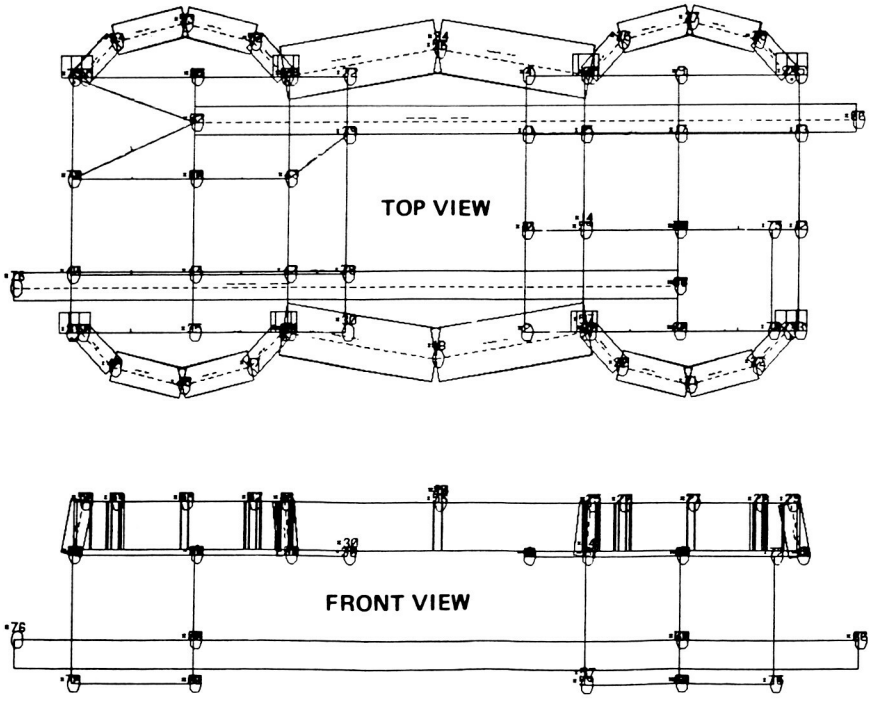


Figure 14. - HST maintenance mission keel latch finite element model.

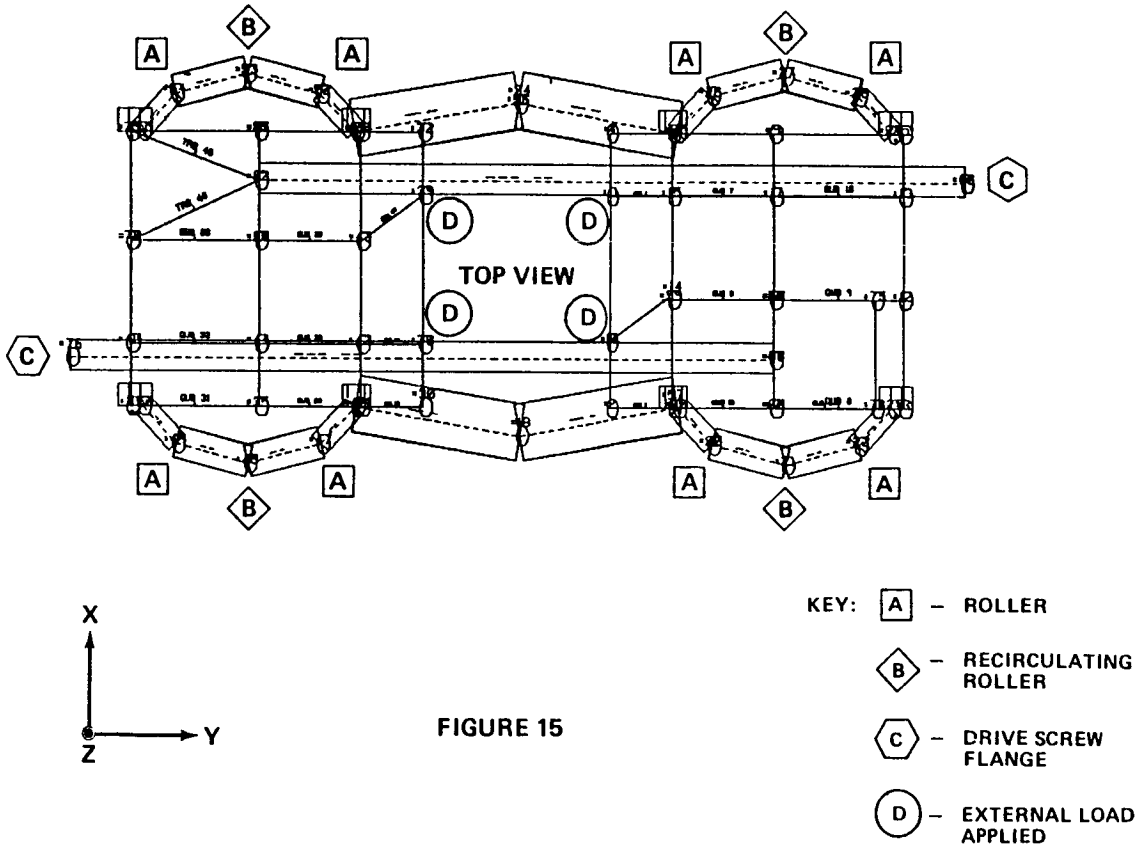


FIGURE 15

Figure 15. - Reaction and load application points.

# A MIRROR TRANSPORT MECHANISM FOR USE AT CRYOGENIC TEMPERATURES

Kenneth W. Stark* and Meredith Wilson*

This report describes the Mirror Transport Mechanism (MTM), which supports a pair of dihedral mirrors and moves them in a very smooth and uniform scanning motion normal to a beamsplitter. Each scan is followed by a quick flyback and repeat.

Included in the report will be material selection, design, and testing of all major components of the MTM in order to meet the stringent performance requirements under cryogenic conditions and survive the launch environment of the shuttle. Areas to be discussed in detail will be those in which failures or performance anomalies occurred and their solutions. Typically, this will include (but not to be limited to) flex pivot failures during vibration testing, excessive dihedral platform sag under one "g" operation, electronic and fiber optic characteristics, and tolerancing considerations.

As of this writing, development of the mechanism has reached the final phase of thermal and vibration qualification. Environmental testing of the complete FIRAS experiment is just beginning.

## INTRODUCTION

The Mirror Transport Mechanism (MTM) is an integral part of the Far Infrared Absolute Spectrophotometer (FIRAS) instrument. The FIRAS measures the spectrum of the 3 K cosmic background radiation, the interstellar dust emission, and any unknown sources in the wavelengths ranging from 100 μm to 1 cm. The FIRAS is a cryogenically cooled (LHe) rapid scan interferometer spectrophotometer. A pair of dihedral mirrors is moved with respect to a beamsplitter, producing the optical path differences which generate an interferogram. Incoming radiation, which is channeled into the interferometer by a skyhorn, is balanced against an internal reference source.

An external calibrator is also provided which when commanded will swing into place in front of the skyhorn at which time the temperature of the internal reference source is adjusted to nearly null the signal. Proper operation requires that the entire instrument be maintained at a temperature below 2 K. Thus, it is enclosed in a large dewar filled with superfluid helium at 1.8 K. Spacecraft orbit is such that complete coverage of the universe requires about 6 months. For double coverage, a lifetime of at least a year in orbit is desired. Since any power dissipated in the dewar increases boil-off of the cryogen, strict limits are placed on the allowable

*NASA Goddard Space Flight Center, Greenbelt, Maryland.

dissipation. The FIRAS power budget is 5 mW. Lifetime in orbit is reduced by about 3 days/mW.

The dihedral mirrors are mounted on the MTM platform and the MTM is designed as a basic 4 bar linkage connected by a set of 8 flexural pivots. These flex pivots are essentially frictionless and provide only a small linear restoring force. Angular rotation is low enough that expected lifetime at normal temperature is infinite. However, the entire mechanism must operate at 1.8 K for more than a year and there is no such previous experience. Flex pivots were fabricated with a special material and life-tested for more than 20 million cycles at LHe temperature and with greater than normal rotation. The MTM is driven by a unique linear motor whose only moving part is completely passive (no contact, no flexing wires). Scan operation is controlled by an optical encoder, which consists essentially of a pair of gratings having 50 lines/mm. Thus, a pulse is generated at intervals of exactly 20 μm. By counting these pulses, the scan motion reverses at the proper position. These encoder pulses are also used to command the A/D converters to sample the detector outputs. Since each pulse is generated at a precise position of the mirrors, data from successive scans can be coadded for greater reliability and noise reduction. Actually data sampling must be at a higher rate than the basic encoder resolution so these pulses are accurately subdivided by a phase lock loop. In normal optical encoder applications of this type, the light sources and detectors for the encoder are located outside the dewar and optical fibers transmit the signals. Launch environment requires rugged caging and locking to prevent damage. The dihedrals are quite large (about 8 in. high) and heavy (about 1.5 lb each) and must withstand launch vibrations. Protection is provided by moving the platform beyond its normal stroke and by locking into a pair of cones and sockets. A latch motor rotates a roller shaft deflecting a leaf spring which forces the cones into the sockets. As further protection, each flex pivot is fitted with a sleeve which limits deflection in the lateral direction.

## REQUIREMENTS

The performance and operational requirements that the MTM was designed to are the following:

(1) Slow scan, 0.228 cm/sec
(2) Rapid scan, 0.342 cm/sec
(3) Flyback, $\geq$1.5 cm/sec
(4) Power dissipation, <5 mW
(5) Dynamic platform tilt (Table I)
(6) Operating temperature, 1.8 K (LHe)
(7) 26-g load vector design criteria
(8) Vibration test specifications (Table II)
(9) Jitter - 40 μsec
(10) Space constraints within FIRAS instrument
(11) Long scan platform travel, -0.4096 to 1.638 cm
(12) Short scan platform travel, -0.4096 to 0.102 cm

All optical and structural components, where possible, are constructed from 6061-T6 aluminum to prevent stresses and distortions upon cooldown to LHe temperatures.

## SELECTION PROCESS

Prior to the selection of the flex pivot mechanism there was an evaluation period in which three basically different mechanisms were investigated. They consisted of a linear ball slide, flexural pivot-four-bar linkage, and a magnetic suspension platform.

The linear ball slide consisted of a platform riding on two parallel shafts through three linear ball bushings. Basically two configurations were built and tested. The first had stainless steel rods without lubrication and the second had aluminum shafts with a hard coat and teflon lubrication burnished onto the shafts. Although the power to drive the platform was low, the noise present on each linear sweep was unacceptable from an optical data analysis standpoint. The stainless steel version was tested first and had the highest noise levels. To try and reduce the noise, hard coated aluminum shafts with a Teflon burnished coating were substituted for the stainless shafts. The noise levels were reduced but were still unacceptable. Another potential problem with this mechanism was that it had to be kept exceptionally clean since contamination on the shafts or bearings would greatly increase power and noise values.

The magnetically suspended interferometer platform (Fig. 11) was designed, built, and tested. Magnetic suspension provides a very smooth, frictionless mounting which can be quite stiff with no restoring force in the direction of motion. Each of three bearing assemblies (Fig. 12) is a square unit with a central hole for the moving shaft. A permanent magnet in each corner sets up flux paths as shown. The flux in opposite air gaps can be differentially changed by winding coils on pole pieces. Depending on current direction total flux at the top gap is increased, while flux in the bottom gap is decreased. The result is a net upward force on the shaft. Coils are also provided on the horizontal poles so that force can be applied in either direction. Two of the magnetic bearings are in line, supporting a single long shaft. These bearings are controlled both vertically and horizontally. The third bearing supports a shorter shaft and is controlled only in the vertical direction.

Although testing of the unit showed good performance, it was not selected for the MTM because the flex pivot design was simpler and would meet the requirements.

The flex pivot mechanism was originally designed as a four bar linkage utilizing six flex pivots (Fig. 1). This mechanism was tested and found to have very smooth operation with extremely low power dissipation (Fig. 2). Because of the excellent operational characteristics and simplicity of design this mechanism was chosen for the MTM. Several design changes were made during the development and testing of this mechanism; however, because of

space limitation only the final version utilizing eight flex pivots will be discussed in detail in this report.

## MECHANICAL DESIGN

The "BASIC DESIGN" mechanism described in this report will be the eight flex pivot four bar linkage (Fig. 3). Briefly this MTM was changed from a six flex pivot design to an eight flex pivot design to increase the rigidity of the dihedral mirror platform support. The original version provided two flex pivots in the movable connecting link which supported the dihedral platform. When the MTM was inverted, as was necessary during certain tests, there was interference with the gratings due to excessive deflections.

This six pivot model was redesigned and reanalyzed utilizing our NASTRAN modeling and analysis program to the present "BASIC DESIGN" MTM, herein referred to as MTM.

The MTM consists of the following major components and subsystems:

(1) Flex pivots, links, and base
(2) Latch mechanism
(3) LVDT and LVT sensors
(4) Fiber optics and grating
(5) Spherical mirror reflector
(6) Linear motor

In Figures 4 and 5 each of the major components is identified. Each of the four links has the holes for the flex pivots line bored so as to provide a true coaxial centerline for the pivot axes, thus eliminating rotational stresses due to misalignment. In addition the center distance of each pivot on corresponding links is located to very close tolerances so as to provide true translational motion of the movable connecting link. This is the link on which the dihedral platform is mounted and as such any rotational motion would be detrimental to the optical performance. The flex pivots are captivated in the links by slotting the bored holes, and with the use of a machine bolt, the hole is clamped about the pivot diameter. This provides a uniform clamping action without distorting the flex pivot. At LHe temperature the $\Delta\ell/\ell$ of aluminum is 0.0043 and that of stainless steel is 0.003; therefore, as the system is cooled the clamping force on the pivot is increased. Tests were conducted to determine whether the clamping force was sufficient to prevent the pivots from moving during vibration or whether we had to consider the use of an adhesive. Measurements taken at $LN_2$ temperatures showed that the push out force was in excess of 2224 N (500 lb) which was above any loads that would be seen during environmental testing. Initially, the pivots were mounted directly in the links; however, because of problems arising out of testing (to be discussed later) close toleranced sleeves are bonded to the pivots which limit the radial excursion and therefore the flexure deflections to a safe level. Another modification that was made was in the material used to fabricate the flex pivots. The standard material is a 400 series stainless steel; however, at LHe temperatures the impact resistance is very low <2.7 N-m (2 ft-lb). To insure a better impact strength at

cryogenic temperatures, INCO 718 was selected for the flex pivots. It has an impact resistance of about 27 N-m (20 ft-lb).

Since this mechanism is essentially frictionless and swings freely, it was necessary to design a latch mechanism that would captivate all moving components during the launch environment and yet be readily uncaged once in orbit and data taking is to begin. In addition it must be positioned such that it will not interfere with the MTM operation when uncaged. As shown in Figure 6 the caging mechanism consists of a 15° stepper motor operating through a 24:1 gear ratio. The output shaft is attached to an arm connected to the shaft at 90° with two special order "V" shaped bearings attached (one on each end). When the motor is engaged, the output shaft rotates and the two bearings each engage a beryllium copper leaf spring (Fig. 4) compressing it approximately 0.051 cm (0.020 in.). This results in approximately 311 N (70 lb) of force which is reacted by the latch cones and sockets (Fig. 7). The surfaces of the cones and sockets are hard anodized to prevent wear debris from forming. In addition, the cone angles were selected such that a self-locking tendency would not be present. Internal to the socket housing, a small spring is incorporated which is designed to give about a 8.9 N (2 lb) unlocking force to the cones so that when the latch motor releases the 311 N (70 lb) holding force the cones are kicked out of the sockets to ensure release. It should be noted here that in order not to have the latch motor assembly interfering with the MTM motion during operation the latch position is slightly out of the MTM operating range. In order to bring the leaf springs close enough to the latch motor for latching purposes, the linear drive motor is used for positioning into the latch cones.

The gear reduction consists of a pinion machined onto the output shaft of the motor, meshing with the two-pass gear system. The large gears are aluminum with a hard anodized surface lubricated with a burnished $MoS_2$ coating. Located within the gear box are two miniature electromagnetic proximity sensors which indicate the latch and unlatch positions.

The motor detent torque of 0.0177 N-m (2.5 in.-oz) is sufficient to prevent the gear box output shaft from rotating during handling environmental testing. For redundancy purposes the motor is constructed with dual windings, any one of which will be able to operate the latch/unlatch sequence.

Because of problems that arose during the tests, which will be discussed later, a third point-constraint was added (Fig. 8). This constrained point prevents the MTM dihedral platform and connecting link from rotating excessively about an axis through the latch cone assemblies.

As part of an overall mechanical analysis of the MTM a NASTRAN model was constructed. It consists of 665 grid points, 449 CQUAD's, 256 CBARS, 6 HEXA, 4 PENTA, and 109 CTRIA elements. The NASTRAN model is shown in Figure 9, which also shows a comparison of NASTRAN modes with measured modes indicating good accuracy of the NASTRAN model.

## ENVIRONMENTAL TESTING AND MODIFICATIONS

Thermally, the MTM must survive launch conditions at LHe temperatures, and once in orbit it must operate at this temperature. Although we were able to performance test the MTM at LHe temperatures, vibration testing could only be done at $LN_2$ temperatures due to the test dewars that were available. The sequence for vibration testing was to perform a room temperature vibration and if everything was successful then an $LN_2$ vibration would follow. The reason for two separate tests was that the room temperature test was out in the open allowing clear visual observation during tests, but the $LN_2$ tests had the MTM mounted inside a dewar where no visibility was possible.

Vibrational testing consisted of (1) a sine burst test at about 20 cps to simulate the steady-state component of the vibration and (2) a random test. These tests were performed separately and in each of three mutually perpendicular directions. The vibration test specification levels used are shown in Table II.

As mentioned previously, there were two major problems that developed during the vibration testing that necessitated significant redesign in the latch mechanism. Loads were developed during testing which caused a rocking motion in the dihedral platform resulting in pivoting motion about the latch cone axis. This placed excessive loads on the pivot flexures causing them to fail.

To reduce this motion a third point latch was developed (Fig. 8) which limited motion to ±0.0051 cm (±0.002 in.). This was arrived at by a compromise of how tight a clearance could be maintained without possible binding and the allowable stress buildup in the flexures at that excursion. The third point latch consists of a slot in the latch motor housing and a tang attached to the rear of the dihedral platform connecting link. The spacing is adjusted so that when the tang is moved into the slot during the latch mode there is a clearance gap on each side of the tang of 0.0051 cm (0.002 in.). This arrangement was retested and worked.

Later in our test program there was a condition in which the MTM was vibrated but because of a misadjustment in the relationship of the latch motor to latch spring, the cones were not seated properly in their respective sockets. This allowed excessive motion at the sockets even though the third point latch was engaged. In effect, the platform could rotate about the third point latch. This caused failure in several pivots. At this point it was decided that the pivots themselves should be protected from excessive loads in case of another overload condition. After an extensive investigation it was decided to enclose each pivot in a sleeve (Fig. 10) that would limit radial movement to an acceptable level. This level was selected at a maximum of 0.0076 cm (0.003 in.) after an analysis showed a stress level of 248 MPa (36 000 psi) was reached with 0.0076 cm (0.003 in.) deflection and that buckling occurred at about 303 MPa (44 000 psi).

Testing in a fixture showed that buckling occurred slightly above 0.0076 cm (0.003 in.) which probably put the stress close to 303 MPa.

The sleeves were designed to have tightly machined tolerances so as to minimize the sleeve to sleeve dimensional variations. Taking into account the tolerances on the pivots, sleeves, and the center shift at 4° (rotation of flex pivot in latch position) of each pivot, a maximum radial clearance of 0.008 cm (0.0032 in.) and a minimum radial clearance of 0.0011 cm (0.00045 in.) are possible. The upper pivot section is bonded to the sleeve. Each sleeve and corresponding pivot have recessed grooves machined into the mating surface to allow for epoxy retention. Subsequent room temperature vibration testing showed no failed pivots.

An $LN_2$ vibration test is planned in early 1986 to verify cold temperature survival.

## ELECTRICAL DESIGN

### Drive and Control of MTM

The MTM operates in a closed-loop velocity mode, in which a velocity sensor feeds into the servoamplifier (Fig. 13). If a constant dc level is applied to the input, the motor will drive at a constant velocity such that velocity sensor output just matches the input. It will continue to move at constant velocity until the input is reversed, after which it will move at constant velocity in the opposite direction until it is again reversed.

Length of stroke is controlled by an optical encoder having 50 lines/mm. The encoder also generates a single zero reference pulse (ZRP) which synchronizes the operation. When the ZRP occurs during forward motion, a converter is set to zero and scan operation begins. Motion continues until the converter reaches 1024 counts. Distance travelled is exactly 20.48 mm, since encoder pulse spacing is 20 μm. When this point is reached, the MTM reverses and flies back at about five times the forward scan velocity.

When ZRP occurs during flyback, a time delay is initiated, after which the direction switches to forward and the cycle repeats. The purpose of the time delay is to ensure that all transients are settled out and operation is smooth by the time ZRP is reached, at which point the next scan begins.

Figure 14 shows the four scan modes which can be selected: LONG FAST, LONG SLOW, SHORT SLOW, AND SHORT FAST. For short scans, forward motion reverses after 256 counts or 5.12 mm. For slow scans, reference voltage is exactly 2/3 the value of FAST scans.

An additional mode of operation is the POSITION mode, in which a position sensor (LVDT) feeds into the servoamplifier and is balanced out by a position-command voltage which can be sent by telemetry. Since this is sent as an 8-bit word, the MTM can be set to any of 256 discrete positions. It will stay in this position until a new value is sent or until operation is returned to the normal SCAN mode.

Drive Motor

The drive motor (Fig. 15) was designed for a stroke of about 30 mm (1.2 in.) and a diametral clearance of about 1.5 mm (0.060 in.). This large clearance provides for the arc movement of the arms and for dimensional changes due to temperature or imperfect alignment.

The moving part, attached to the MTM platform, is completely passive and consists of four powerful rare-earth magnets at each end, forming an annular air gap, north inward at one end, north outward at the other end. A coil at each end cuts these magnetic lines, generating a push-pull force which is essentially linear over its range of travel. The coils are attached to the base, so the lead wires do not flex.

Initial motor design used niobium titanium wire, which becomes superconducting below about 9.5 K. The MTM was tested and operated at 4.5° with a motor of this type. However, some anomalies were noted: an apparent increase in spring constant and a large hysteresis effect. Because of these poorly understood factors, it was decided to redesign the motor, using normal copper wire, if power dissipation could be made low enough.

Since copper has finite resistance it was important to reduce the required current as much as possible by maximizing motor force constant. Redesign included the following:

(1) Samarium cobalt magnets were replaced with neodymium-iron, a newly developed material having about 50 percent higher gauss-oersted product.

(2) The flux return path was at or near saturation. Cross sectional area was increased about 50 percent.

(3) Overall diameter was increased to allow for 30 percent more turns.

Each coil of the final motor design is wound with 2600 turns of number 38 copper wire. With two coils in series (normal coils) there is a total resistance of about 830 ohms at room temperature, decreasing to about 10 ohms at LHe temperature. Redundant coils have the same number of turns, but resistance is 10 to 15 percent higher. The force constant is about 2.6 kg/amp (5.7 lb/amp) and the back EMF is about 27 mV/mm/sec. These same figures apply to either normal or redundant coils.

Optical Encoder

The optical encoder consisting of a scale and a reticle is shown in Figure 17. The scale is mounted on the moving platform and the reticle is attached to the base. Optical fibers are positioned directly below the encoder parts. Those below the scale feed light in from external light sources. A spherical mirror is mounted so that its radius of curvature is in the plane of the gratings. This mirror images the scale pattern onto the reticle, and the fibers below the reticle pick up the fringe pulses and carry them out to external detectors. For reliability, two complete sets of

optics and electronics are provided, only one of which is used at a time. Both F and Z are normal components, $F_2$ and $Z_2$ are redundant.

Both scale and reticle are spring loaded against two edges and the backside since differential expansion between the glass and aluminum due to temperature cycling would result in a position shift.

In conventional encoders, scale and reticle face each other with a small space between. Light passes through the grating patterns and fringe modulation is sensed by a detector. However, spacing between scale and reticle has a large effect on signal output, as shown in Figure 16(a). If nominal spacing is 0.005 in., scale movement of even 0.001 in. can double or halve the peak-to-peak signal. A further disadvantage is that such close spacing between precision glass surfaces is hazardous, particularly in ground handling and testing. Figure 16(b) shows the encoder arrangement used in the MTM. The reticle is separated from the scale and has its pattern in the same plane as that of the scale. Light passes through the scale to a spherical mirror which images the scale pattern back onto the reticle.

The spherical mirror used in the MTM is ground to 1/4 wavelength accuracy and is made of aluminum, as is the tower supporting it. Thus, as distance between mirror and scale (4-in. focal length) contracts due to the cold temperature, the radius of curvature contracts in proportion so that the pattern remains in focus.

Optical Connectors

Three types of connectors are used:

(1) A hermetic feedthrough connector which penetrates the dewar wall

(2) A blind-mating connector to permit installation and removal of the cryo-optical assembly

(3) A connector to permit removal of the MTM from the cryo-optical assembly (see Fig. 17)

Figure 18 shows the hermetic feedthrough connector. A vacuum-tight seal is accomplished by a Koval disc into which glass inserts are fused and then ground and polished to form clear windows. Ground and polished fibers are inserted from each side and butted against the glass windows. Attenuation is about 5 dB/pass through the connector.

The blind-mate connector is a butt joint connector in which one-half is mounted in a floating arrangement and guided by tapered pins into alignment with the other half. Attenuation is about 3 dB/pass.

The MTM optical connector permits separation of the MTM from the interferometer and COA assembly. Alignment pins insure accurate butt connection of fibers. Attenuation is about 3 dB/pass.

## Optical Fibers

The optical fibers selected for this application are large diameter plastic fibers (DuPont Crofon, 1 mm diam). By using such large diameter fibers, the problems in designing and using connectors are greatly eased. These fibers have a high attenuation (about 0.5 to 0.6 dB/ft). However, they are minimally affected by bending, cryogenic temperature, or radiation.

For evaluation of bending and temperature effect, fibers were wrapped around mandrels of successively smaller radius and exposed to cryogenic temperature. The same fiber was used for all the tests, and temperatures were applied by plunging the fiber directly into the cryogen. After wrapping the fiber around each mandrel, it was dipped directly into liquid nitrogen and allowed to stabilize. Attenuation was read, after which it was immersed directly into liquid helium and read again. After warm up to room temperature, it was wrapped around the next smaller mandrel. Figure 19 shows the results. The fibers showed no sign of cracking or crazing.

Radiation received by the fibers during a year in orbit will amount to about 4000 rads. In testing, the fiber was subjected to a total of 80 000 rads with very little adverse effect.

## Optical Preamp Box

Light sources and detectors are housed in the optical preamp box which is located near the dewar and connected to it by optical fibers. The preamp box contains a total of four LED's and four detectors, plus circuitry to control LED current and to amplify the detector signals. Half of these components are for the normal system and half are for the backup redundant system.

The LED's are high-power gallium arsenide diodes which are constructed with a lens. Rated output is 30 mW at 200 mA, although it was decided to limit current to 100 mA for further reliability. The wavelength is 940 nm. Another lens concentrates the output further and an optical fiber is positioned to couple into it as much light as possible. A photo diode monitors a portion of the LED output and feeds into an automatic control circuit to maintain constant output.

## Velocity Sensor (LVT)

The velocity sensor consists of a pair of coils with a permanent magnet core, which generates a voltage when the core is moved axially. Output is proportional to velocity and is essentially linear over its range of travel. To get optimum linearity, core magnets are measured and selected for best uniformity of magnetic field. For reliability, two sets of windings are provided. Sensitivity is about 6 mV/mm/sec for either winding.

Position Sensor (LVDT)

A conventional type linear variable differential transformer is used to measure position. Excitation is about 3.6 kHz and output is converted to dc by a demodulator and op amp. Linearity is about 0.5 percent over its range of 1 in. Redundant windings are provided.

Electronics

Almost all circuitry utilize CMOS devices for two reasons: (1) power requirements are very low, and (2) radiation resistance is adequately high.

TABLE I. - DYNAMIC PLATFORM TILT

| AXIS | P.D.(CM) | ALLOWABLE ROTATION (ARC-SEC) | P.T. (CM) | P.T. (IN) |
|---|---|---|---|---|
| Y | ±.2 | ± 8 | ±.058 | ±.023 |
| | ± 1 | ± 20 | ±.289 | ±.114 |
| | −1 to 5 | ± 204 | −.289 to 1.45 | −.114 to .571 |
| X | ±.2 | ± 16 | ±.058 | ±.023 |
| | ± 1 | ± 40 | ±.289 | ±.114 |
| | −1 to 5 | ± 408 | −.289 to 1.45 | −.114 to .571 |
| Z | NOT SPECIFIED | | | |

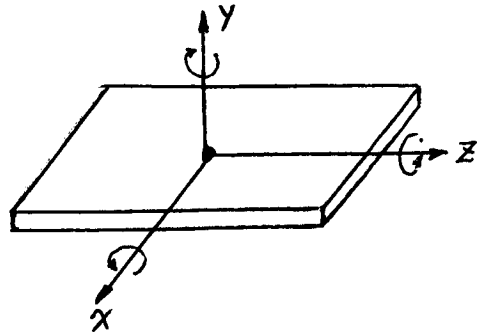


PLATFORM TRAVEL

TABLE II. - VIBRATION TEST LEVELS

| | X | Y | Z |
|---|---|---|---|
| RANDOM (GRMS) | 6.75 | 3.8 | 3.3 |
| SINE BURST (G's) | 10.0 | 10.0 | 10.0 |

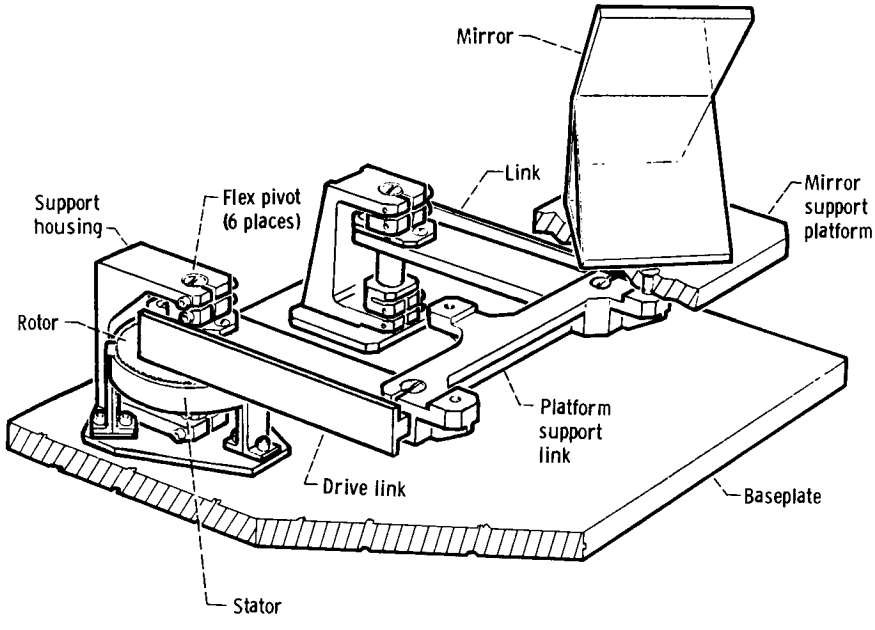


Figure 1. - Original MTM design.

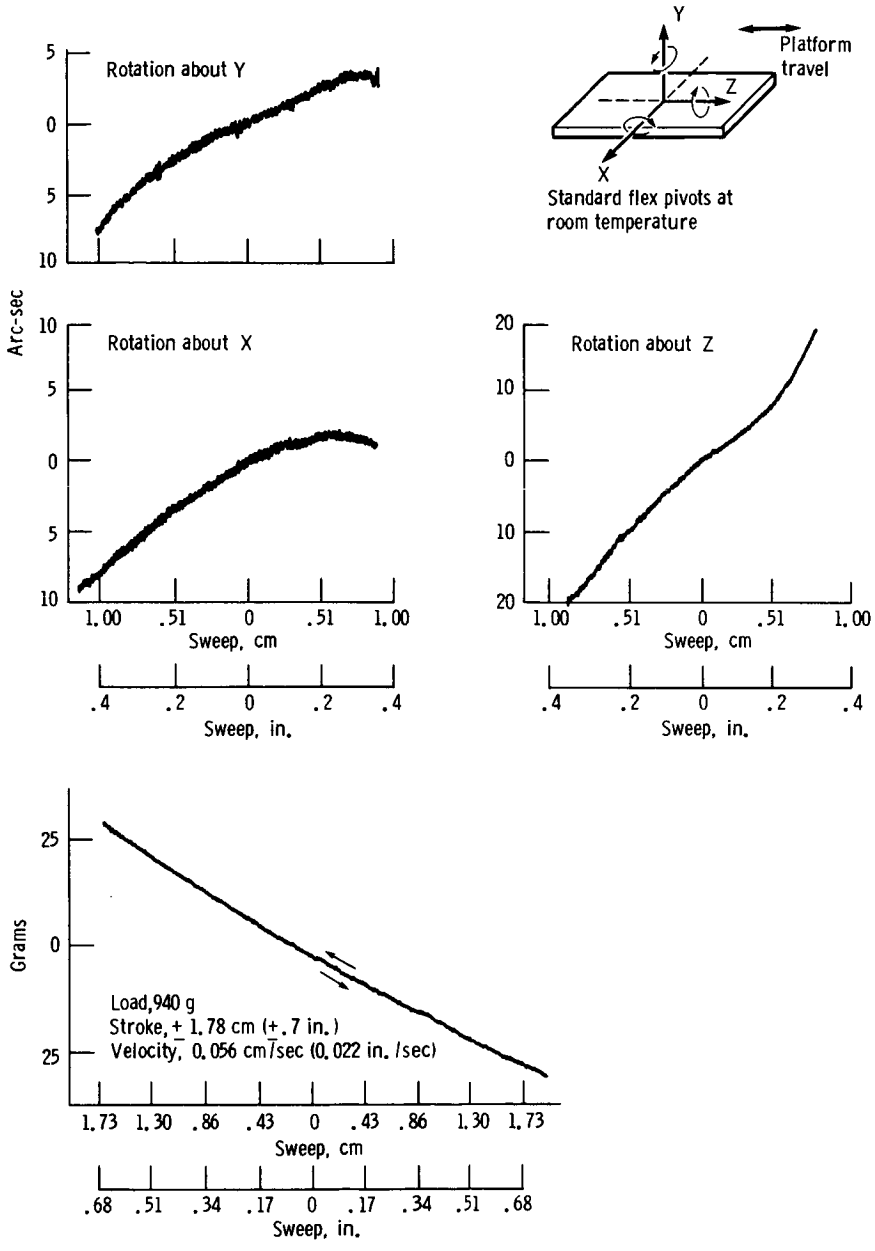


Figure 2. - Flex pivot mechanism operational characteristics.

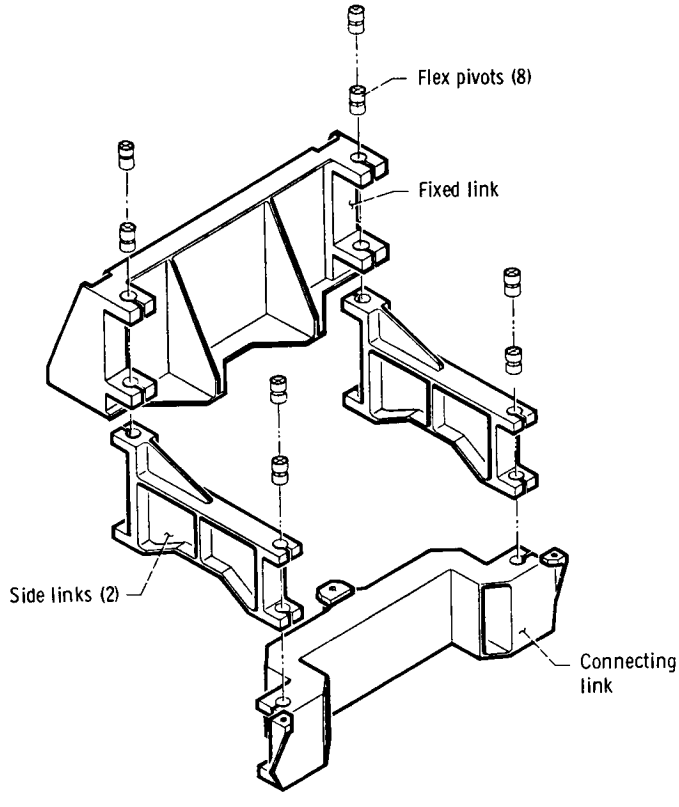


Figure 3. - MTM exploded view.

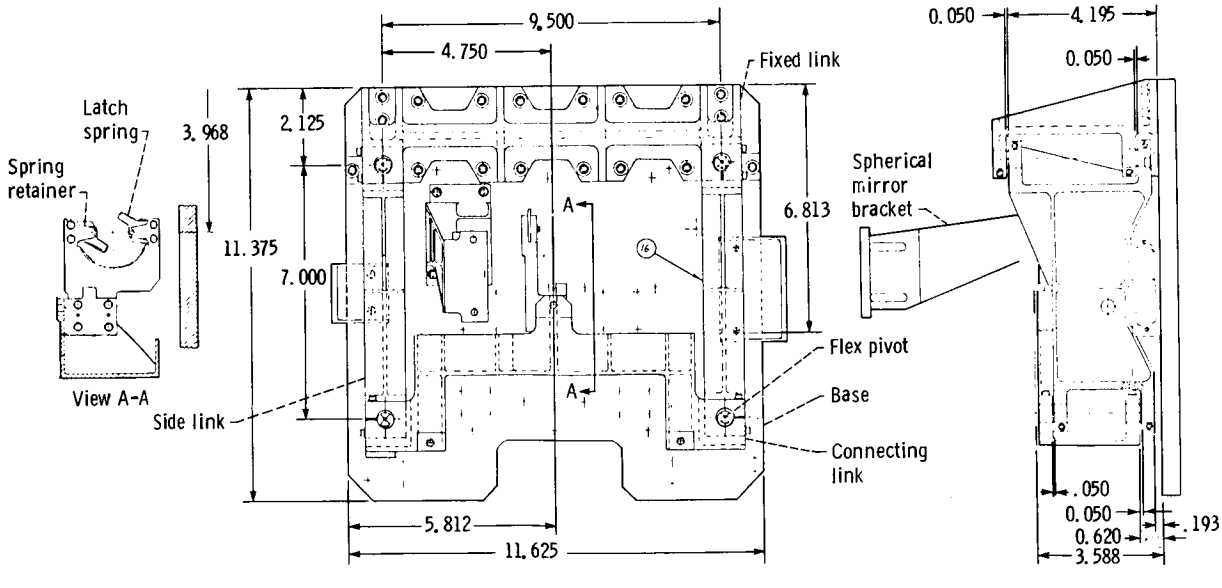


Figure 4. - MTM chassis assembly.

Table A

| Position | Gap |
|---|---|
| At ZPD | .032 min |
| At STOW | .017 |
| At EDT + | .002 |

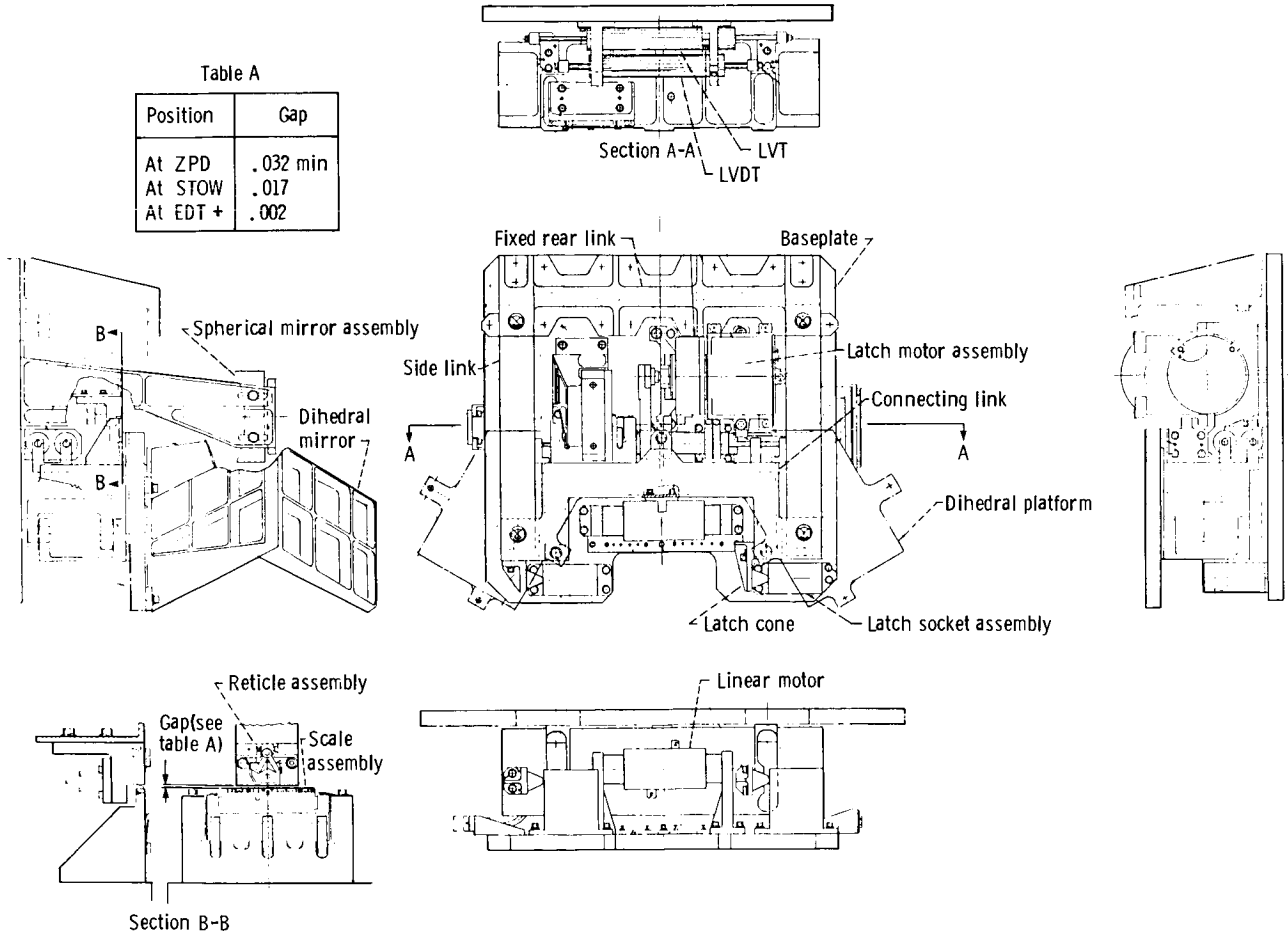


Figure 5. - Mirror transport mechanism assembly.

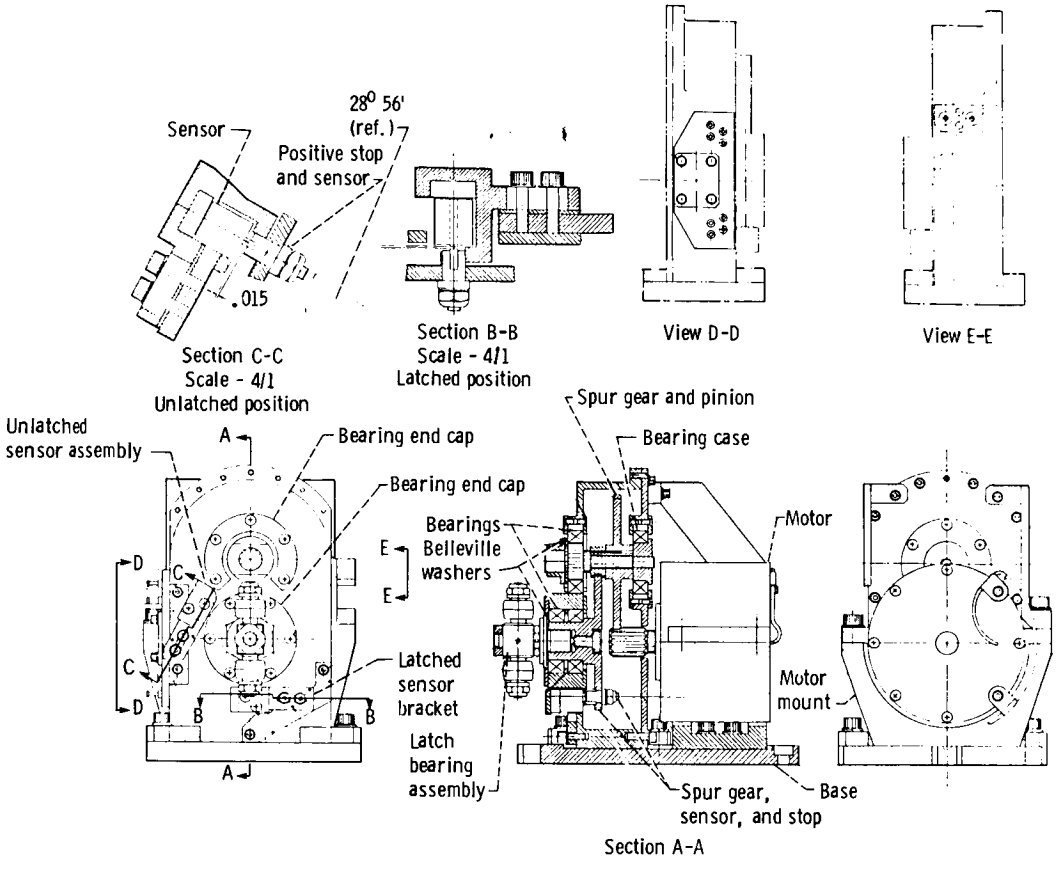


Figure 6. - MTM latch mechanism assembly.

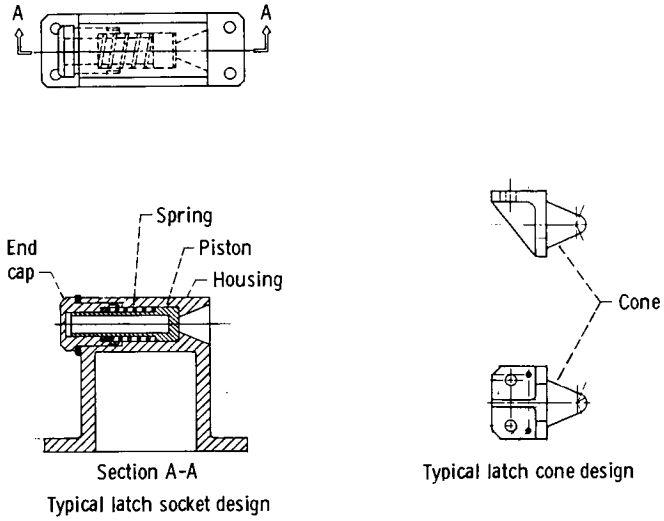


Figure 7. - Passive latch assembly.

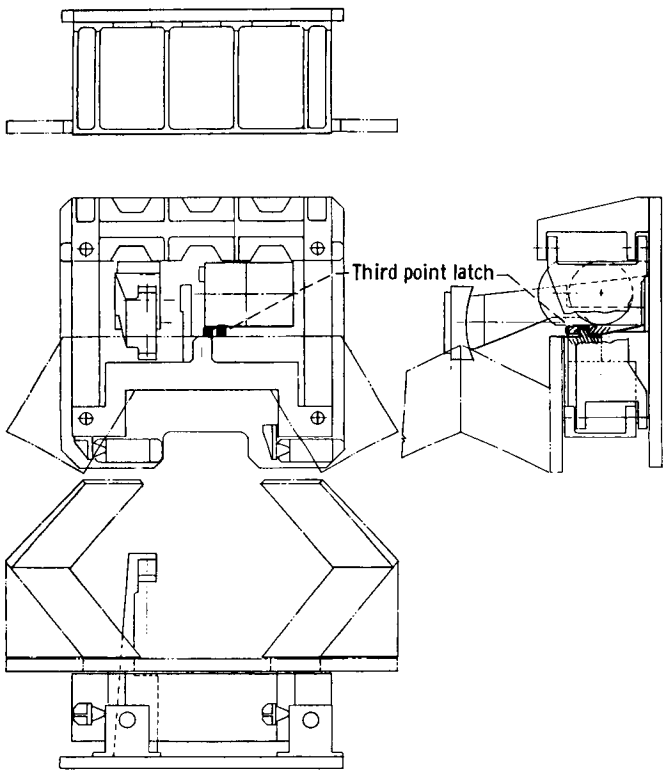


Figure 8. - Third point latch location.

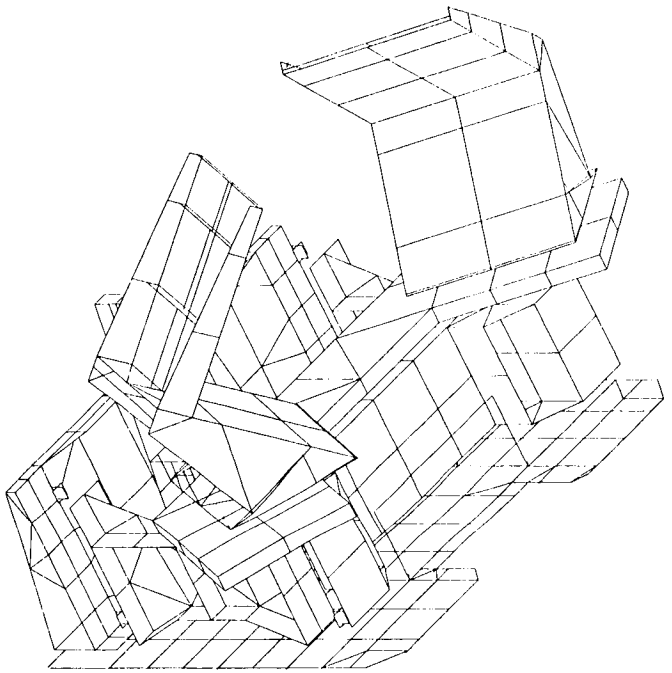

MTM Resonant frequencies

(Baseplate constrained by edges)

| | Modes, Hz | 1 | 2 | 3 | 4 |
|---|---|---|---|---|---|
| Dihedral mirrors | Experimental | .581.63 | 46/49 | --- | --- |
| | Nastran | .477 | 48.1 | 55.5 | 67.2 |

Figure 9. - Nastran model of MTM and correlation with test results.

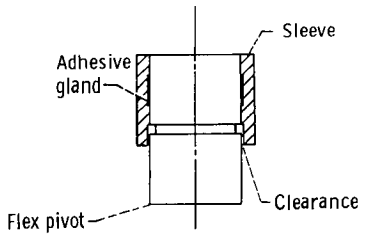


Figure 10. - Flex pivot sleeve assembly.

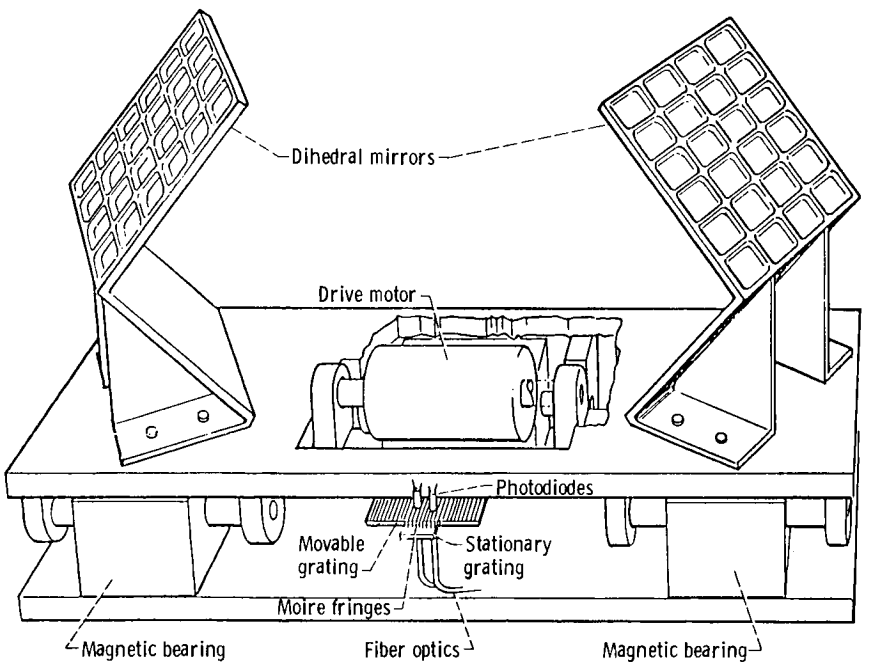


Figure 11. - FIRAS interferometer (magnetic suspension).

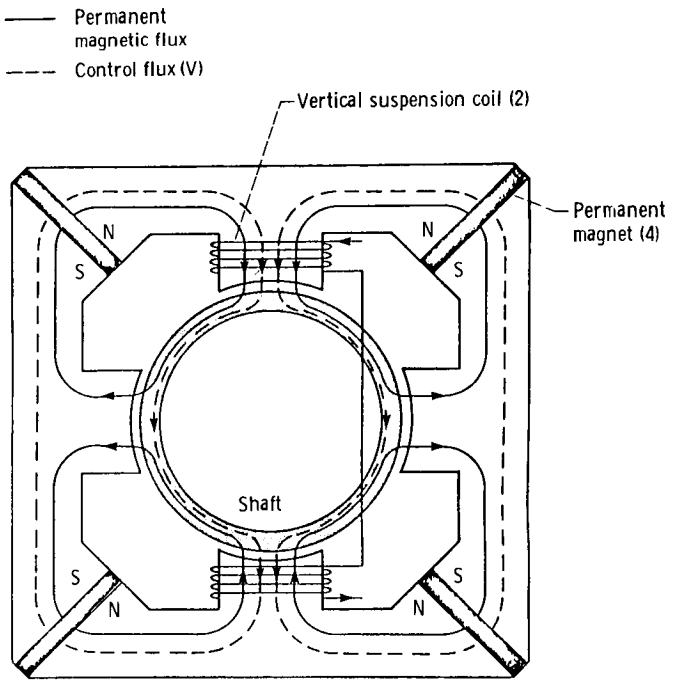


Figure 12. - Magnetic bearing. Current shown drives shaft up.

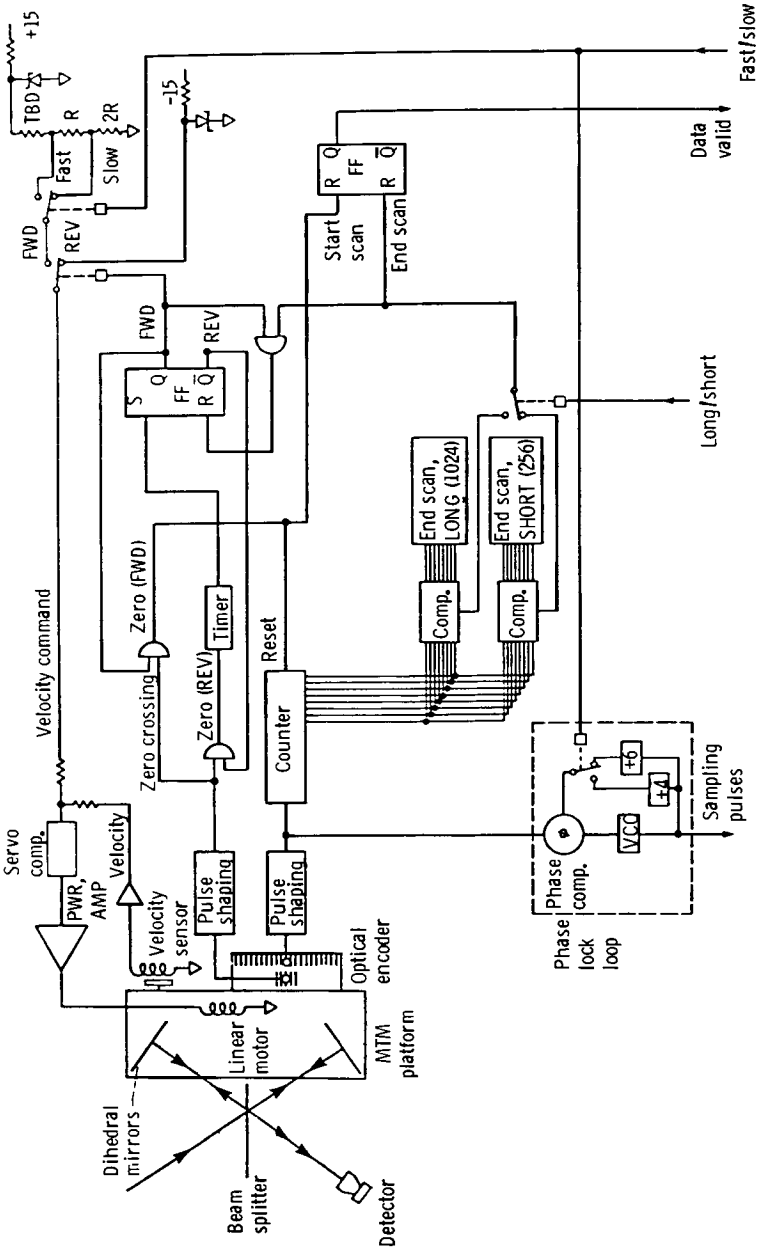


Figure 13. - FIRAS - MTM schematic.

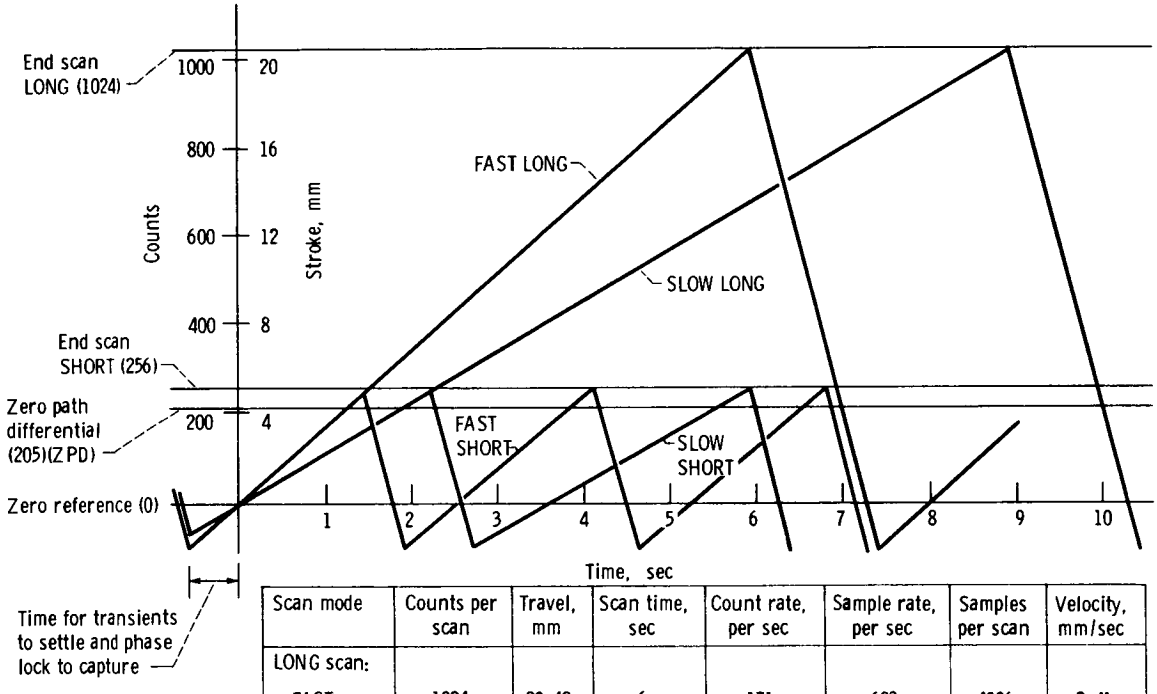


| Scan mode | Counts per scan | Travel, mm | Scan time, sec | Count rate, per sec | Sample rate, per sec | Samples per scan | Velocity, mm/sec |
|---|---|---|---|---|---|---|---|
| LONG scan: | | | | | | | |
| FAST | 1024 | 20.48 | 6 | 171 | 683 | 4096 | 3.41 |
| SLOW | 1024 | 20.48 | 9 | 114 | 683 | 6144 | 2.28 |
| SHORT scan: | | | | | | | |
| FAST | 256 | 5.12 | 1.5 | 171 | 683 | 1024 | 3.41 |
| SLOW | 256 | 5.12 | 2.25 | 114 | 683 | 1536 | 2.28 |

Figure 14. - FIRAS scan modes.

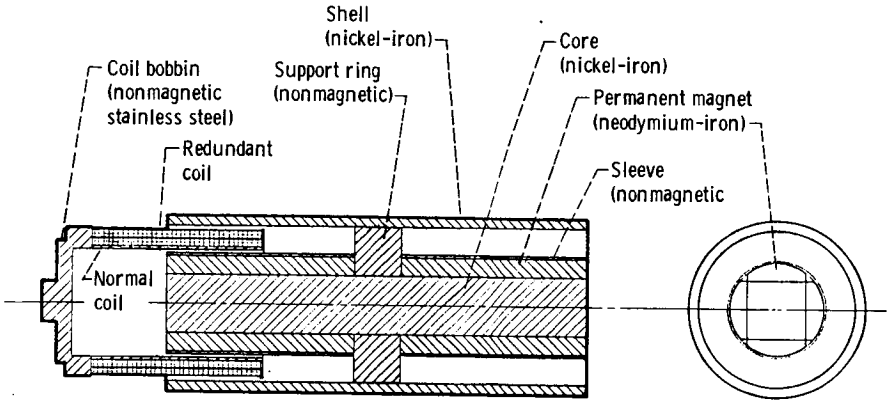


Figure 15. - Linear motor.

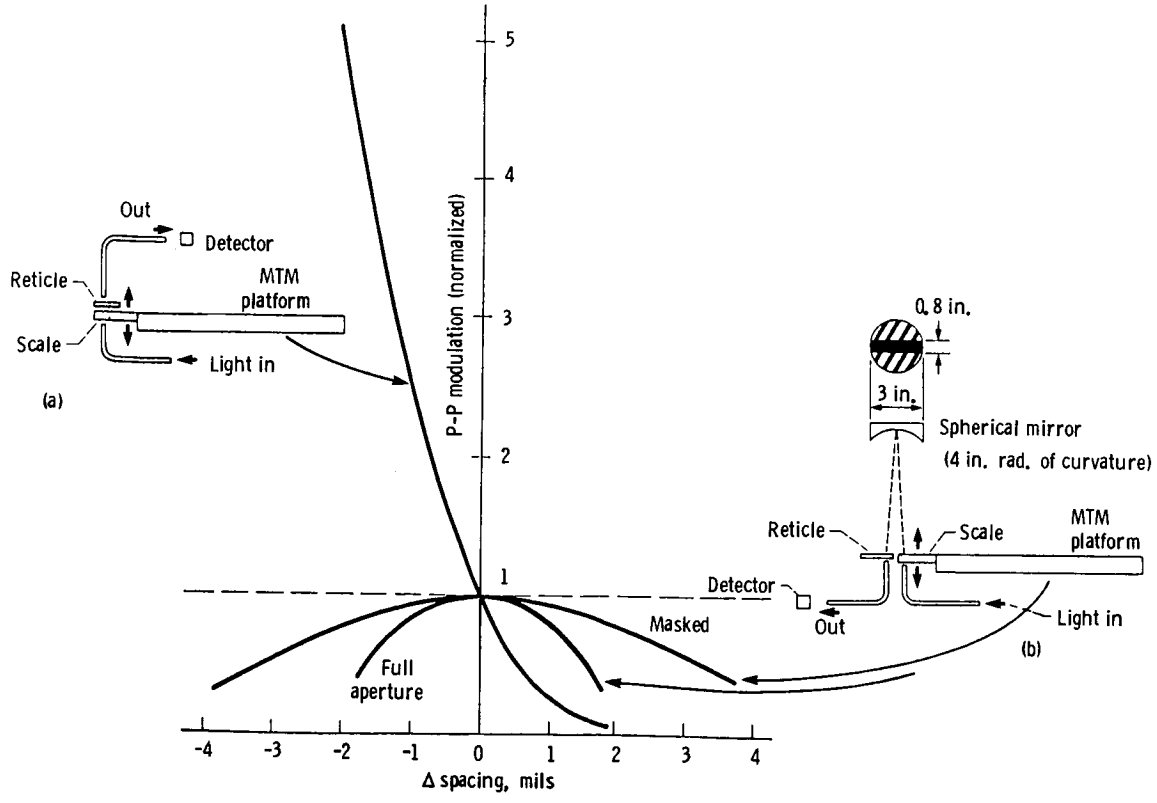


Figure 16. - Effect of grating spacing.

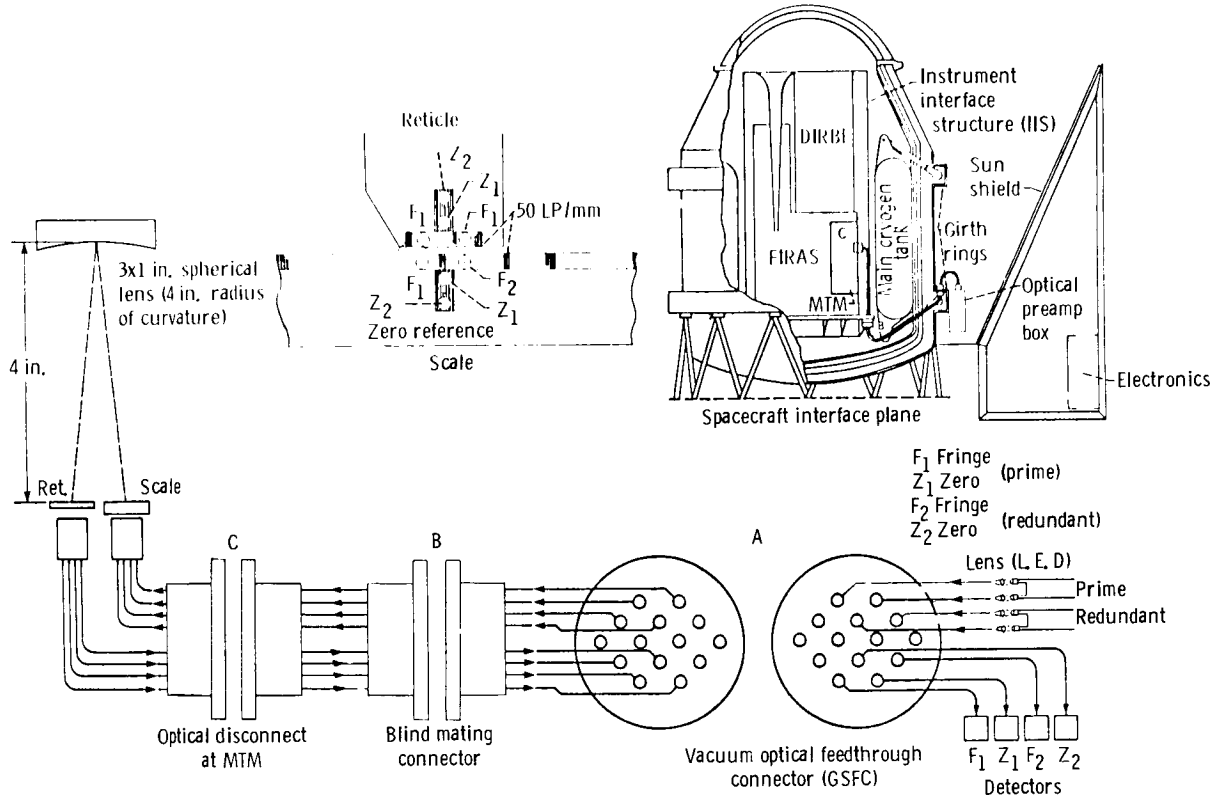


Figure 17. - Optical connectors and fiber optic routing.

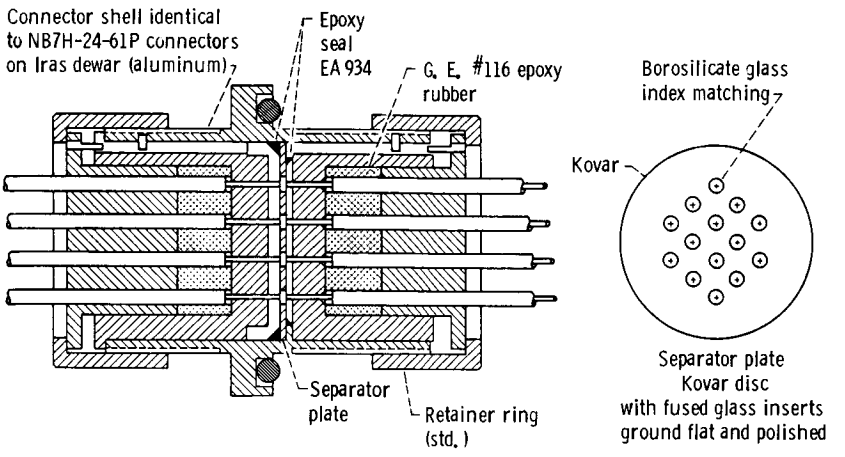


Figure 18. - Vacuum optical feedthrough connector.

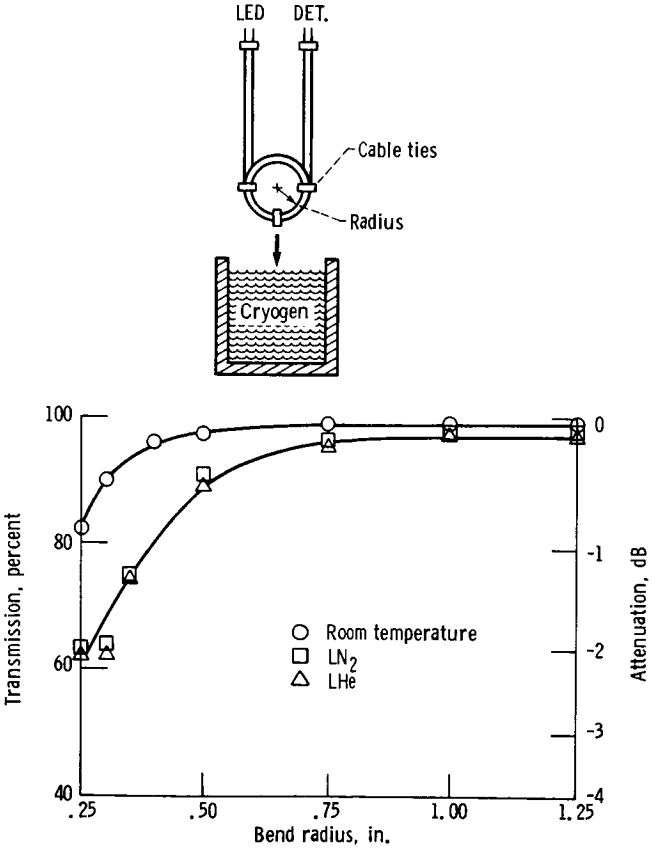


Figure 19. - Optical fiber performance. Fiber, DuPont Crofon OE-1040, 1-mm diameter.

# SHUTTER MECHANISM FOR CALIBRATION OF THE CRYOGENIC DIFFUSED INFRARED BACKGROUND EXPERIMENT (DIRBE) INSTRUMENT

Allen Tyler*

This paper describes the design requirements, the design, the assembly and alignment, and the test program for a shutter mechanism which must operate at cryogenic temperature and draw less than 1.0 milliwatt. The design solution to meet these requirements is a device that positions a mirror with repeated accuracy, has no wearing surfaces, and operates at 2.0°K. The unique feature of this device is the simplicity of the mechanism, thus obtaining high reliability.

## INTRODUCTION

The DIRBE is one of two cryogenic instruments aboard the Cosmic Background Explorer (COBE) spacecraft. DIRBE will measure the diffused radiation of the universe in the wavelength region between 1 and 300 microns. The low signal levels require the use of an instrument whose "self emission" is less than that which is being measured and dictate an instrument operating temperature of 2.0°K. Since the instrument requires in orbit calibration, a requirement became apparent for a shutter mechanism which upon command would move a blade into the first field stop of the optical system, thus blocking the radiation that enters the instrument from space, and simultaneously position a flat mirror which is part of the internal reference source (IRS). This allows the known radiation from this source to be used to calibrate the instrument. Figure 1 shows the arrangement of the optical components within the DIRBE instrument. Highlighted is the field stop that has a square opening that measures 7.9mm by 7.9mm (.311 in. by .311 in.); the shutter mechanism located at the field stop; the IRS, a 32 Hz chopper; and three detector assemblies.

## REQUIREMENTS

The following requirements are summarized and briefly discussed:

a. Provide a radiation seal to the detectors when in the closed position.

b. Reflect radiation from the IRS to the detectors when in the closed position.

*NASA Goddard Space Flight Center, Greenbelt, Maryland.

c. Survive 50,000 actuations (ground test and on orbit).

d. Withstand thermal cycling between room temperature and 2.0°K.

e. Require a maximum power dissipation when energized $\leq$1.0 milliwatt.

f. Provide a fail safe mechanism (electrically fails open).

g. Incorporate dual coil windings and dual electronics for redundancy.

Since the shutter mechanism is required to block out the incoming radiation and simulataneously position a flat mirror to reflect radiation from a known source, the shutter/mirror combination would have to be positioned with repeated accuracy.

The instrument is expected to be calibrated as many as five times per orbit early in the 1 year mission and trailing off to perhaps only once per orbit in the latter part of the mission. The actual number of shutter actuations could be nearly 20,000. The design requirement for 50,000 actuations would be verified with an accelerated life test at liquid helium temperature to demonstrate that this requirement was achieved.

A likely failure mode for a mechanism to operate at 2.0$^{o}$K is the cool down survival itself, in particular the windings. The requirement for dual coil windings will alleviate this potential problem. This mechanism will therefore be exposed to several cool down cycles from room temperature to 2.0$^{o}$K to verify the mechanism's integrity to meet this requirement.

The lifetime of the flight liquid helium dewar is highly dependent upon the heat dissipation within the instrument. The power budget for the DIRBE instrument alloted 1.0 milliwatt maximum power to operate the shutter mechanism.

A shutter that would fail in the closed position would be catastrophic. It is therefore extremely important that in case of an electrical failure (power off condition) the shutter will return to its open position.

## DESIGN

Common motors and solenoids could not be used because of the rigid power and temperature requirements. In addition there existed a tight envelope constraint that had an influence on the final size and shape of the mechanism.

The shutter was designed to move a mirror over a distance of 17.0mm (.67 in) and close off the field stop that has a 7.9 mm (.311 in) square opening. The shutter mechanism designed is essentially a magnetically actuated mechanism (Figure 2). It consists of two curved pole pieces and a metal bobbin manufactured from highly purified iron with low hysteresis and high flux density properties. There is also a flexible tine made of high strength tool steel (SAE 1074 steel) to which an aluminum flat mirror is attached. The bobbin is wound with superconducting wire (niobium titanium wire) which is then vacuum impregnated with FORMVAR to support the windings. The wound bobbin forms two coils which can independently activate the device, thus meeting the redundancy requirement. The wound bobbin is sandwiched between the two pole pieces and the air gap is located at the curved surface. The curve was derived from the equation of a cantilevered beam uniformly loaded in bending. Upon activation, the steel tine is pulled toward the curved pole surface closing the airgap (zipper effect) and taking the shape of the curved pole pieces. To initiate this action, the pull-in current to close the shutter is 45 to 50 milliamps (MA) for a 200 millisecond pulse, but is reduced to 10 MA to hold the tine and shutter in place. To assure release after the current is removed, a small gap is maintained with a .06mm (.002 in) thick plating of a nonmagnetic coating of copper and gold on the contact area of the pole pieces. The spring action of the tine will return it to the open position.

## ASSEMBLY/ALIGNMENT

The two pole pieces and bobbin which are made of pure iron are hydrogen annealed at 1200°K - 1275°K for 4 hours to produce the low hysteresis and high flux density that is required. The bobbin and a spacer sandwiched between the 2 pole pieces accurately locate the 2 curved surfaces with precision. The tine holder with tine attached is mounted to one of the pole parts and is aligned by positioning the tine tangent to the curved pole pieces at the bottom. This condition is achieved by measuring the minimum current required to close the tine. The tine holder is then drilled and pinned at assembly to the pole piece. The shutter mechanism is then mounted to the field stop support. By shimming between the mechanism and field stop support, the shutter blade/mirror is positioned parallel to the field stop with a .076mm (.003 in.) clearance gap (Figure 2). The mechanism is drilled and pinned at assembly to the field stop support. Pinning of the mechanism provides a dual purpose. It prevents movement of the mechanism during launch vibration and it permits disassembly and assembly while maintaining the original alignment.

The minimum achievable gap obtained (.003 in.) will maximize the effectiveness of the photon sealing. For added assurance to block out the incoming radiation, a shutter retainer was added to produce a labyrinth type of seal (noncontacting) along 3 sides of the field stop, which in effect, provides a more tortuous path for photon leakage (Figure 3).

## TEST PROGRAM

The shutter mechanism has undergone a series of tests to verify the following:

- o cool down survival
- o functional performance at 8.0°K
- o thermal cycling survival
- o structural integrity
- o mirror position repeatability
- o photon sealing effectivness
- o 50,000 cycle life test

The mechanism has been cooled several times in a liquid helium dewar to less than 8.0°K and has functioned successfully.

Structural vibration tests have been conducted on the mechanism at room temperature and 8.0°K along three orthogonal axes to the mechanism, to the following levels:

| AXIS | X | Y | Z |
|---|---|---|---|
| quasi-static | 15.0 g's | 15.0 g's | 15.0 g's |
| random | 7.4 grms | 5.5 grms | 5.2 grms |

Verification of the shutter mechanism's capability to accurately repeat mirror position and to block out external radiation to the instrument was accomplished during a complete DIRBE instrument systems test. With the shutter mechanism integrated in the instrument and optically aligned with the internal reference source (IRS), the instrument was cooled to 2.0°K in a liquid helium dewar.

The shutter mechanism was actuated several times during this test, thus blocking out the incoming radiation from a DIRBE external calibrator, a piece of support equipment used to simulate in-orbit radiation from space. Measurements made by the flight detector assemblies within the instrument showed that the shutter, when closed, reduced the incoming signal by greater than 200,000 counts to one. With the shutter closed and the IRS energized, the flight detectors measured the calibrated signal with excellent repeatability each time the shutter was actuated. The data from this instrument systems test was verification that the shutter mechanism met the performance requirements.

A life test is presently being prepared for the shutter mechanism (a second unit) to demonstrate its endurance capability. This test will be an accelerated life test performed at 8.0°K. The shutter mechanism will be actuated once every 5 seconds until 50,000 cycles are reached.

## CONCLUSION

A shutter mechanism was developed to accurately position a mirror, block out the incoming radiation to the instrument, and operate at 2.0°K. This mechanism could be adapted for use with other simular instruments or applications.

## ACKNOWLEDGEMENT

The author wishes to acknowledge the work done by Cornelis de Kramer for the electrical design of the shutter mechanism.

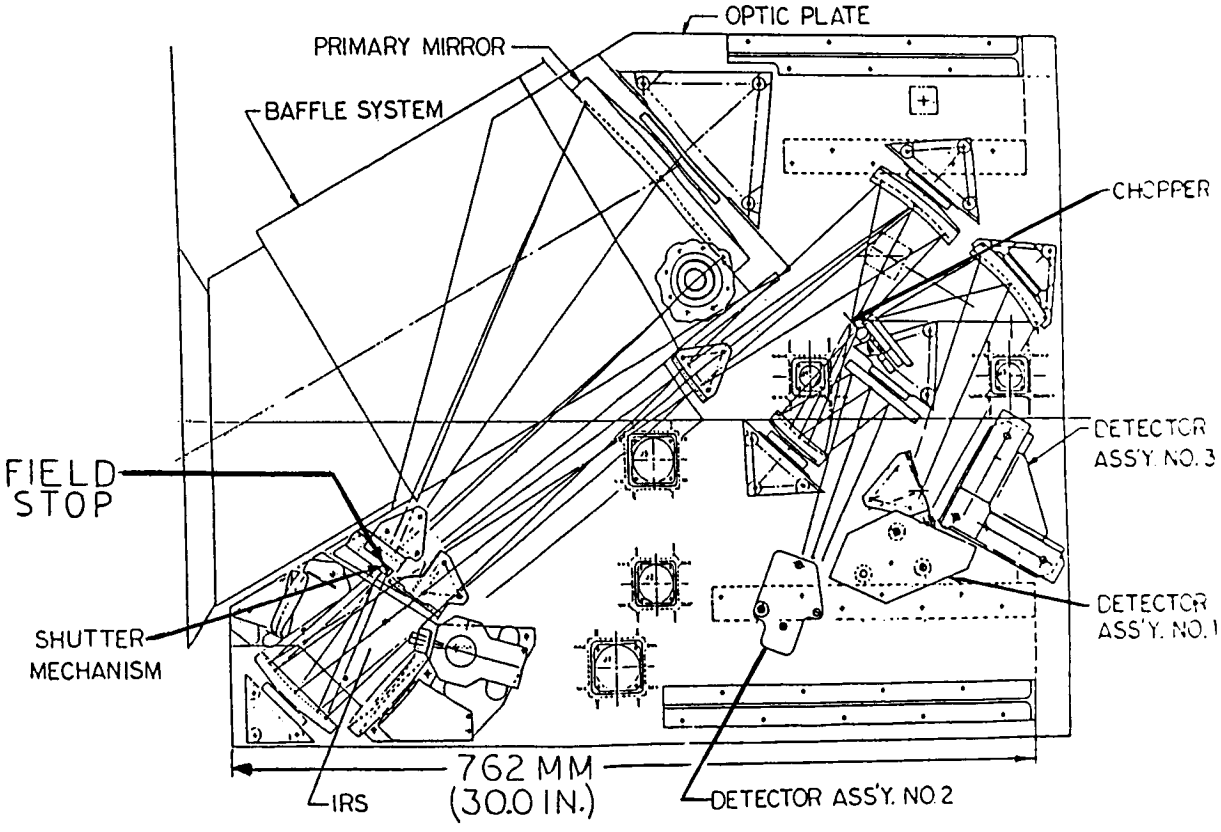


**Figure 1. - DIRBE.**

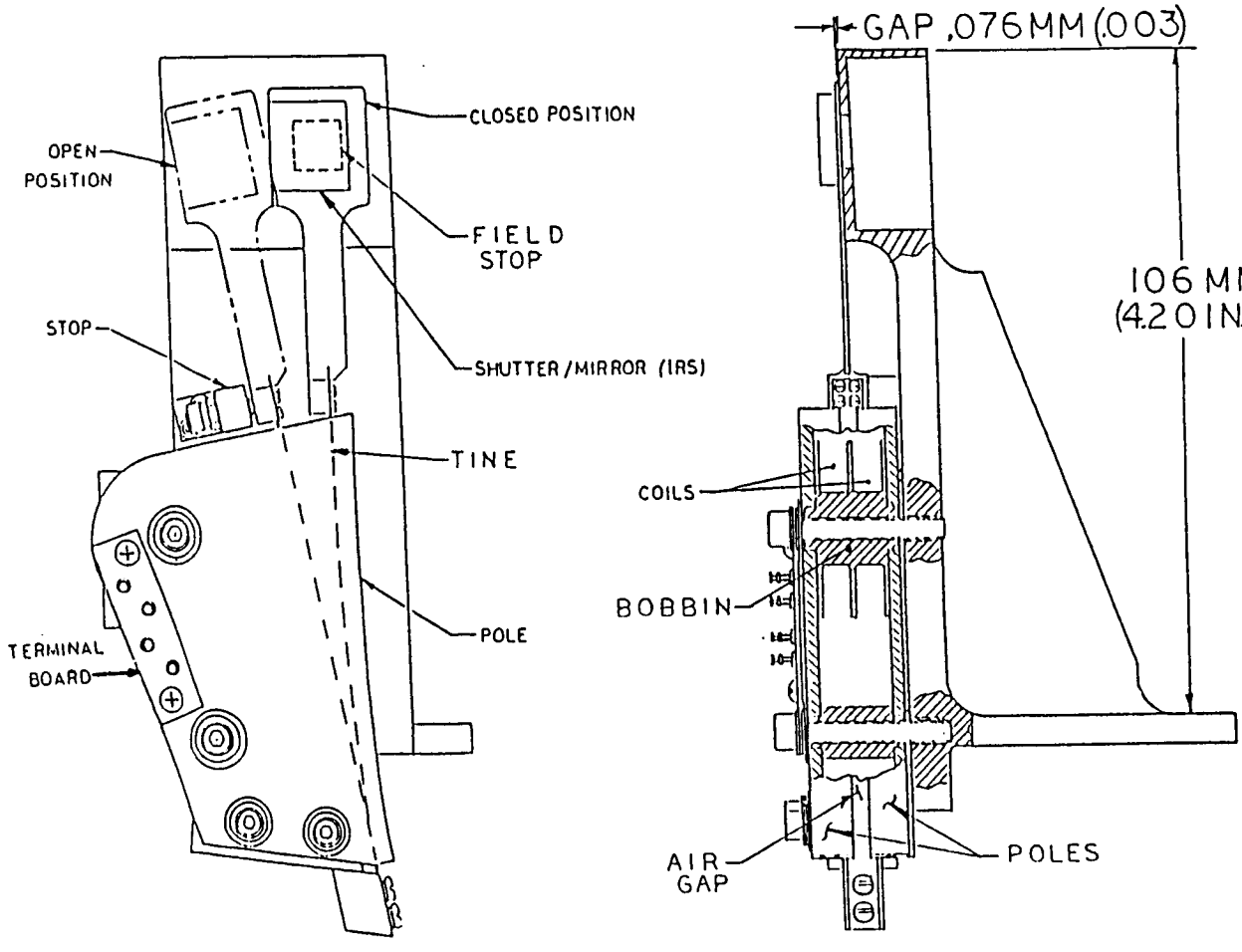


Figure 2. - Shutter mechanism.

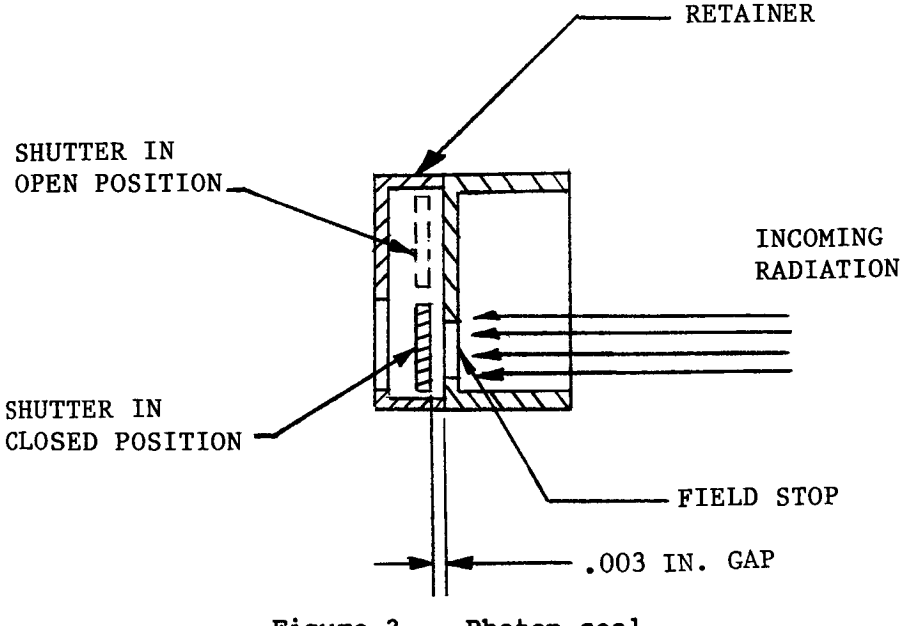


Figure 3. - Photon seal.

# TOWARDS AN OPTIMISED SPUTTERED $MoS_2$ LUBRICANT FILM

E.W.Roberts*

It is shown that the tribological quality of $MoS_2$ lubricant films formed by magnetron sputtering is determined by the choice of sputtering conditions. By selecting the appropriate conditions, films of extremely high lubricity and endurance (in vacuum), which are well suited to many space applications, are obtained. Such $MoS_2$ films, when applied to precision ball bearings, give rise to the lowest torques (for the given test conditions) yet seen in our laboratory. Whilst a remarkably good performance is obtained in vacuum, tests in air show a marked deterioration in lubricating qualities. It is demonstrated that this is attributable to the adsorption of water vapour on $MoS_2$ surfaces and that the degree of deterioration is related to the partial pressure of water vapour present. Analysis of results indicates that the factors relevant to obtaining optimum films are deposition rate and film composition.

## INTRODUCTION

Molybdenum disulphide's efficacy as a lubricant, particularly in high vacuum, is well established. However its application to surfaces by the technique of sputter deposition has only recently come into consideration as a viable process. Interest has grown in this method of application as it offers several advantages over the more conventional techniques of burnishing (of powders) and spray coating (of bonded lubricants). These advantages include:

a) Control over thickness: because the deposition rate is known, thin (sub-micron) films of the required thickness are readily produced. The process is therefore particularly suited to the coating of precision components.

b) Reproducibility: film reproducibility is high provided strict process control is applied.

c) Strong film to substrate adherence: good adherence which is necessary for effective, high endurance lubrication is a characteristic of sputtered films.

d) Coherent films: the lubricant film produced by sputtering is a continuous layer of high coherence.

* European Space Tribology Laboratory, UKAEA, Risley, Warrington, England.

e) Intrinsic films: that is, the coatings are free of materials (such as bonding agents) which are extraneous to the lubricating process.

Though offering these advantages, sputtering is a complex process involving many variables. The conditions necessary to achieve lubricant films having the above qualities must be sought experimentally: this was the aim of the present study. The task was undertaken by sputter-depositing $MoS_2$ films under various conditions of gas pressure and RF power and evaluating the resultant films in air and vacuum using a pin-on-disc apparatus. The sputtering conditions necessary to give the best film (tribologically), once determined, were applied to coatings on ball bearings whose performance was then evaluated.

## MAGNETRON SPUTTERING

Radio frequency sputtering (Ref.1) is brought about by applying RF power between a target (manufactured from the coating material, in our case $MoS_2$) and a substrate (the component to be coated), both target and substrate being located in a low pressure, argon environment. In these circumstances an $Ar^+$ plasma forms and there occurs a build up of charge on the target which gives rise to a negative bias. As a result, argon ions are accelerated towards the target, this bombardment resulting in the emission of target atoms/ions some of which transfer to the substrate. The process is depicted in Fig. 1. The target, in addition to ejecting target atoms, emits secondary electrons which help sustain the plasma but which also bombard the substrate and cause heating. Despite this, sputtering is, in relation to many other deposition techniques, a low temperature process. This is desirable, indeed mandatory, where the temper (i.e annealed condition) of the substrate material must be preserved.

In the present study, film deposition was by means of RF magnetron sputtering. This is an extension of the RF sputtering process described above which offers the additional advantages of:

a) High deposition rates.

b) The virtual elimination of secondary electron bombardment of the substrate and thus lower substrate temperatures.

These are achieved by confining the plasma to an area lying close to the target by means of permanent magnets located behind the target (the actual shape of the plasma is governed by the nature of the electrical and magnetic fields set up within the chamber). An improved ionisation efficiency results which increases the rate of target bombardment and thus gives rise to enhanced rates of deposition. The paths of secondary electrons are constrained by the electromagnetic fields and thus remain in the vicinity of the target.

A disadvantage, however, is that magnetron sputtering gives rise to films of less uniform thickness because the effective source area is smaller than

the target area. A restriction is therefore placed on the size of component that can be coated uniformly.

## RATIONALE OF TESTING

Although simple in concept, sputtering is, as noted earlier, a technically-complex process. This complexity arises as a result of the large number of parameters that collectively determine the conditions of sputtering. These parameters include applied power, gas pressure, target area, target to substrate distance, substrate temperature and substrate bias. Each parameter can influence the quality, in terms of structure, orientation, stoichiometry and adhesion, of the sputtered film (Refs. 2 to 6). Adding to this complexity is the interdependency of several of these parameters.

To simplify the determination of optimum sputtering conditions only the effects of changes in argon pressure and R.F power were examined in the present study: all other parameters being kept constant.

Sputter depositions were carried out at argon pressures of 5, 12.5 and 20 microns (0.67, 1.67 and 2.67 Pa. respectively) and at applied powers of 0.3, 0.6 and 0.9 kW. Thus, in total, nine sputtering conditions were studied.

The values of the remaining parameters were fixed as follows.

Target diameter: 152.4 mm
Target to substrate distance: 56 mm
Substrate bias: zero volts
Substrate temperature: ambient

No bias was applied to the substrate although its potential during deposition would rise naturally to that of the plasma potential. The main intention was to avoid a negatively-biased substrate as this is known to repel sulphur ions and lead to sulphur-deficient films (Ref. 4).

The substrate was water-cooled during etching and film deposition. However substrate temperature rose above ambient (though probably remaining below 70 deg.C) due to heat dissipated by depositing atoms.

## APPARATUS AND TEST SAMPLES

### Sample preparation and sputtering conditions

Depositions of $MoS_2$ were carried out in a Nordiko Vacuum System equipped with NM 2000 Sputtering Modules and an N6-1400 pumping system. High vacuum was achieved by means of an oil diffusion pump. A liquid nitrogen trap, located above the pump, ensured negligible transfer of oil vapour to the sputter chamber.

Coatings were produced, at each of the nine chosen sputtering conditions, on steel (EN31) discs (thrust washers) for pin-on-disc evaluation (see below) and on aluminium stubs for film analysis by EPMA (electron probe micro-analysis). Deposition rates had been measured previously and are reproduced in Fig. 2. Samples were also prepared on glass slides and subjected to freeze fracture so that film morphology could be examined by scanning electron microscopy.

Disc samples were initially cleaned by wiping with cloth soaked in Arklone P solvent followed by three separate ultrasonic cleans in fresh solvent. Prior to sputter deposition the steel discs were sputter etched for 15 mins. at a sputter power of 100 W and at the pressure at which the subsequent deposition was to be carried out (5 to 20 microns Ar) so as to remove loosely bound surface contaminants. The target material was cleaned by sputtering for at least 30 minutes under the intended sputtering conditions of the test.

Tribological assessment-sliding wear tests

Steel discs were coated to a thickness of 1 micron and assessed in high vacuum and air by means of a pin-on-disc apparatus.

The discs had the following specification:

Type: shaft locating thrust washers
Material: EN31 ball bearing steel (52100 AISI)
Hardness: Diamond microhardness 860±10 Vickers
(HRC 58-65)
Surface Finish: Radial 0.15 micron CLA
Circumferential 0.10 micron CLA

The coated discs were spring-loaded to 10 N against three, equispaced, uncoated, EN31 steel balls. A rotational speed of 100 rpm (0.3 m/sec.) was employed for vacuum testing and 10rpm for air tests. The speed was reduced in air so as to reduce rig instabilities which arose as a result of the higher and noisier torque which characterised in-air performance. The apparatus was set to trip when the friction coefficient exceeded 0.3 for 0.5 seconds. Film endurance was defined as the number of disc revolutions completed (or distance travelled) at trip activation. Where film failure did not occur within about $4.5 \times 10^6$ revs. the test was stopped so as to enable completion of the remaining tests within an acceptable timespan. Wear rate calculations were made from measurements of the diameters of the ball wear scars.

## RESULTS

In-vacuo performance

The performance of sputtered $MoS_2$ in vacuum was assessed through measurement of endurance, mean friction coefficient and, where failure did not occur, specific wear rate.

TABLE 1(a) ENDURANCE (x $10^6$ REVS.)

| Ar Pressure (microns) | SPUTTERING POWER (kW) 0.3 | 0.6 | 0.9 |
|---|---|---|---|
| 5 | 0.3 | 0.9 | 1.7 |
| 12.5 | 0.7 | >4.5 | >4.5 |
| 20 | >4.5 | >4.5 | >4.5 |

TABLE 1(b) MEAN FRICTION COEFFICIENT

| Ar Pressure (microns) | SPUTTERING POWER (kW) 0.3 | 0.6 | 0.9 |
|---|---|---|---|
| 5 | 0.021 | 0.024 | 0.017 |
| 12.5 | 0.02 | 0.01 | 0.01 |
| 20 | 0.019 | 0.013 | 0.01 |

TABLE 1 (c) SPECIFIC WEAR RATE ($10^{-19}$ $m^3$/Nm) OF PINS

| Ar Pressure (microns) | SPUTTERING POWER (kW) 0.3 | 0.6 | 0.9 |
|---|---|---|---|
| 5 | - | - | - |
| 12.5 | - | 3.7 | 2.2 |
| 20 | 12.1 | 5.3 | 3.3 |

TABLES 1 (a)-(c) PERFORMANCE OF SPUTTERED $MoS_2$ IN VACUUM

Pin-on-disc tests were continuously monitored by recording the torque output as a function of time. Typically, torque traces were as shown in Fig. 3, curve A. The curve is characterised by a brief running-in period followed by a period of stable performance. Film failure, when it occurred, was seen to be catastrophic, in that it happened suddenly over a relatively small number of disc rotations (Fig. 3, curve A). Because pin wear became rapid in the failure regime, meaningful measurements of wear rates could not be made in those cases where failure occurred within the time available for testing.

Measurements of endurance, friction coefficient and specific wear rates are summarised in Tables 1 (a), (b) and (c). Endurance (Table 1(a)) is observed to be strongly dependent on sputtering conditions with the best films lasting at least fifteen times longer than the worst. It is apparent that film endurance improves with increasing argon pressure and increasing RF power. Friction coefficient, however, is less sensitive to sputtering conditions but nevertheless a similar trend of improved lubricity with increasing pressure and power is discernible. Note that all the films examined gave rise to very low values of friction coefficient (<0.03).

Wear rates of the balls (pins), where measurable, were extremely low, lying in the range 2 to $13 \times 10^{-19}$ $m^3/Nm$.

Selection of Optimum Sputtering Conditions

From the above performance data the sputtering conditions, within the range examined, necessary to produce the best tribological film in vacuum can be determined. In the power/pressure matrix of Table 2 the regions

TABLE 2 OPTIMISATION MATRIX FOR $MOS_2$

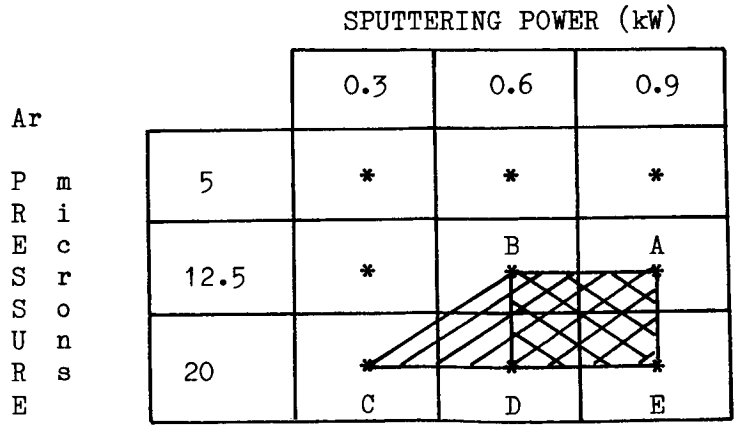


corresponding to films of highest observed endurance (area ABCE) and lowest friction coefficient/wear rate (ABDE), within experimental error, are

shaded. The area where overlap between these two regions exists, and thus the area in which the optimum sputtering conditions lie, is bounded by ABDE. Since films produced under the conditions designated A, B, D and E are of equally high quality then it follows that any combination of R.F power and Ar pressure which lies within the area ABDE will give rise to the best $MoS_2$ film. Based on this reasoning we have chosen as our sputtering conditions for subsequent tribological assessment those values of R.F power and Ar pressure lying at the centre of the area ABDE, that is, 0.75 kW and 16 microns respectively.

Performance of Optimised Film in Air

An $MoS_2$ layer of nominal thickness 1 micron was sputter deposited under the above conditions and assessed on the pin-on-disc apparatus in both air and vacuum. Fig. 4 indicates the changes in friction coefficient that occur on cycling the chamber pressure between high vacuum ($10^{-6}$ torr) and atmospheric pressure. It is apparent from Fig. 4 that on admitting air into the chamber there is a corresponding rise in friction coefficient to about 0.18. On re-establishing high vacuum the friction coefficient decreases to its initially-low value. Thus the effect of pressure on friction coefficient is reversible for brief periods of air-running. If the film is run continuously in air then failure occurs after some 15000 disc revolutions i.e. film endurance is much inferior to that in high vacuum (see, for example, curve B, Fig.3).

The poor performance of sputtered $MoS_2$ in air prompted experiments aimed at determining the factors responsible for film degradation. To determine which of the main constituents of laboratory air (nitrogen, oxygen and water vapour) reduces the lubricity and endurance of $MoS_2$ the following tests were carried out. A test disc was coated with sputtered $MoS_2$ and mounted in the pin-on-disc apparatus. The disc was run-in under high vacuum, until the friction coefficient had become steady at a value of 0.01. The vacuum pump was then isolated and nitrogen bled slowly into the test chamber. The flow of gas was controlled in such a way that the pressure increased incrementally and, at each pressure rise, time was allowed for the torque to stabilise. In this manner it was possible to determine how the friction coefficient varied with changing gas pressure. A similar test was carried out using oxygen. The results of both tests are shown in Fig. 5(a). The introduction of nitrogen has but a small effect on the friction coefficient whilst the influence of an oxygen atmosphere is greater, increasing the friction coefficient from 0.01 to 0.02. A similar test was then conducted using laboratory air (RH=50%, temperature=20.5C) as the test gas. Fig. 5(b) indicates that, upon admission of air, there is a small increase in friction coefficient. This increase , which occurs as the pressure rises from 0.1 torr to 10 torr, corresponds to that seen in the previous tests using nitrogen and oxygen and is presumably attributable to the presence of these gases. Further increases in air pressure up to atmospheric pressure are accompanied by an emphatic increase in friction coefficient, which reaches a value of 0.16. This increase has two components. These can be resolved by differentiating the curve of Fig. 5(b)

to obtain the rate of change of friction coefficient with gas pressure (Fig. 5(c)). Thus the first increase occurs at a pressure of 80 torr and the second, final increase at a pressure of 300 torr. It may be inferred that these two effects are due to the presence of water vapour. Note that these values (80 torr and 300 torr) correspond to partial pressures of water vapour of 0.9 and 3.4 torr (given that the air had a relative humidity of 50 % and a temperature of 20.5 deg.C). If present at these pressures in laboratory air these would give rise to relative humidities of 5% and 19% respectively. This implies that lubricity in air is determined by the dryness of the air: as a guide, best lubricity would be obtained at RH < 5%, intermediate lubricity in the range 5% < RH < 19% and relatively poor lubricity at RH > 19 %.

On re-establishing a vacuum within the test chamber the friction coefficient immediately drops to 0.045. This decrease is the result of the evaporation of some, but not all, of the adsorbed water from the $MoS_2$ lattice. On rotating the disc at 60 rpm there is a further decrease in friction coefficient to about 0.02 resulting from desorption of the remaining water molecules.

Performance of sputter-coated ball bearings

Using optimised sputtering conditions, ball bearings (designation: ED20; type: angular contact) were coated with $MoS_2$ and assessed (at 100rpm) under high vacuum in a pre-loaded (40N) pair configuration. The bearings were fitted with steel (EN31) cages. Two types of test were undertaken. In the first of these all the bearing components with the exception of the balls were coated (i.e. both raceways and EN31 cage). In the second type of test all components of the ball bearing were coated (i.e. including the balls). The coating thickness was nominally 0.5 microns. In each test six bearings were run until the torque reached $8 \times 10^{-3}$ Nm., this corresponding to a sliding (microslip and spin) friction of approximately 0.4.

The manner in which mean bearing torque varied with number of revolutions under vacuum is summarised in Fig. 6. Bearings having uncoated balls exhibited very low mean torque (typically $4 \times 10^{-4}$ Nm) and failed following some one million revolutions. Bearings having all their component parts lubricated showed higher torques (about twice the level seen with bearings employing uncoated balls) though a significant improvement in endurance was observed (typically $4 \times 10^{6}$ revs.).

Thus coating of the balls with $MoS_2$ in addition to raceways and cage brings about, on average, a fourfold increase in endurance though at the expense of a twofold increase in torque. The improvement in endurance may simply be a consequence of the increase in $MoS_2$ -coated area on surfaces which undergo rolling contact (it is proposed to test this notion by coating only the balls). The reason for the twofold increase in torque consequent upon coating balls is as yet unresolved.

Note that, in air, ball bearings with all components coated achieved a lifetime of only about $0.25 \times 10^{6}$ revolutions.

Film Composition and Structure

Analysis of $MoS_2$ by EPMA indicated small deviations from stoichiometry (Table 3): films being either sulphur-rich or sulphur-deficient.

TABLE 3 RATIO OF SULPHUR TO MOLYBDENUM ATOMS IN SPUTTERED $MoS_2$

| Argon Pressure (microns) | SPUTTERING POWER (kW) 0.3 | 0.6 | 0.9 |
|---|---|---|---|
| 5 | 1.67 | 1.69 | 1.75 |
| 12.5 | 2.00 | 2.26 | 2.13 |
| 20 | 1.71 | 2.21 | 2.08 |

Observations of $MoS_2$ films by scanning electron microscopy revealed two types of film morphology. Micrographs of these morphologies which we term Type A and Type B are shown in Fig.7. Type A films are distinguished in section by a columnar structure which gives rise to their distinctive surface appearance whereas the structure of type B films appear more amorphous, their surfaces exhibiting a granular texture. Table 4 indicates the film morphologies resulting from the sputtering conditions examined.

TABLE 4 TYPES OF $MoS_2$ FILM STRUCTURE

| Argon Pressure (microns) | SPUTTERING POWER (kW) 0.3 | 0.6 | 0.9 |
|---|---|---|---|
| 5 | B | A | B |
| 12.5 | B | A | A |
| 20 | B | A | A |

It is apparent from Tables 3 and 4 that the optimised $MoS_2$ film has a type A structure (columnar) and is, to a slight degree, sulphur enriched.

## DISCUSSION

Examination of our results and observations indicates three features common to the best performance films. These are:

a) film compositions are near-stoichiometric and are, to a slight extent, sulphur rich.
b) the films are formed at relatively high deposition rates.
c) the films exhibit type A morphology.

Fig. 8 shows that, within the range of compositions observed, the lubricity of $MoS_2$ films increases with sulphur content. It further appears that deposition rate is a crucial parameter in obtaining the desired stoichiometric or sulphur-rich films. Thus as shown in Fig. 9 high sulphur content is a feature of films deposited at high deposition rates.

This observation is consistent with a view recently put forward by Buck (Ref.7) in which it is proposed that the composition and hence quality of sputtered $MoS_2$ films is governed largely by the level of water vapour in the sputtering chamber during deposition. He derives an equation relating, in effect, a film "quality factor" to the deposition rate of $MoS_2$ and the partial pressure of water vapour. In essence, higher quality films are obtained by maximising the $MoS_2$ deposition rate and minimising water vapour contamination. This is consistent with our observation that the best lubricating films are obtained at the higher deposition rates. Buck also observes that poor-quality $MoS_2$ films are depleted of sulphur. This also is consistent with our findings.

We observe that optimum films exhibit Type A structure. However a strong correlation between film structure and film performance is not proven since some observations were inconsistent with this e.g one film of poor endurance (0.6kW/5 microns) exhibited Type A structure and conversely one film of high endurance (0.3kW/20microns) had a Type B structure (Table 4). Further, these structures are of films deposited on glass substrates and the conditions giving rise to each film morphology on glass may differ from those conditions applying to depositions on steel. It might be expected, for example, that higher substrate temperatures would arise with glass (due to its lower thermal conductivity) and film morphology is known to be dependent on substrate temperatures (see for example Ref.8). Thus, at present, the relationship between film morphology and lubrication is not clearly established.

In air, particularly where motion is of a purely sliding kind, the lubricating properties of sputtered $MoS_2$ are much inferior to those observed in vacuo. Our studies confirm an earlier finding (Ref. 9) that this degradation is attributable to the presence of water vapour. However our observation that the degradation in lubricity is a two stage process which depends on the partial pressure of water vapour gives further insight into this phenomenon. In particular, these observations may indicate that water molecules are adsorbed at two types of surface site. Upon adsorption

of water vapour at the first type of site the friction coefficient increases to about 0.05 and on filling the sites of the second type the coefficient of friction rises to 0.16. Since the second site is readily vacated on reducing the chamber pressure and desorption from the first site requires only a small increase in temperature above ambient (obtained by increasing disc speed), it may be surmised that the heat of adsorption associated with the first type of site is higher than that of the second, though both are low and correspond to heats of adsorption characterisic of physisorption rather than chemisorption. It remains a matter of conjecture as to which sites in the $MoS_2$ lattice correspond to the above. Clearly intercalation sites and edge sites are candidates since adsorption at each type of site would likely affect film lubricity. Indeed there is some evidence that water molecules can penetrate $MoS_2$ layers (intercalation) (Ref.10). However the precise mechanism responsible for lubricant degradation upon physisorption of water is not, as yet, fully understood.

## CONCLUDING REMARKS

It has been shown that, to obtain high lubricity films, high deposition rates are required. Such deposition rates are afforded by RF magnetron sputtering under conditions of relatively high argon pressure and R.F power.

When deposited under optimum sputtering conditions $MoS_2$ films are observed to give rise to very low levels of friction (friction coefficient = 0.01) when measured under conditions of sliding motion (pin-on-disc) under vacuum. This same film, when tested under conditions where motion is principally of a rolling kind (i.e in ball bearings), gives rise to extremely low torque levels. Indeed, these results represent the lowest levels of torque hitherto seen at ESTL, regardless of the lubricant employed, for bearings of this type tested under identical conditions. As an illustration Fig. 10 compares the bearing torques (as a function of rotational speed) obtained in vacuum with various lubricants. These results show that the lubricity of sputtered $MoS_2$ in vacuum is second to none and that the lubricant is well suited to those bearing applications where very low torque and torque noise are required and where the finite film endurance is not a problem.

In air (RH = 50%) $MoS_2$ loses its high lubricity and endurance is reduced very significantly. However, lubricity is recovered on re-establishing vacuum provided operations in air are brief (when compared with endurance in air). The degree to which lubricity is lost is dependent on the partial pressure of water vapour present and occurs in two distinct stages as this pressure is increased. It is recommended that if in-air operation is unavoidable then, where possible, the humidity level should be kept below 5% RH or failing this, below 20% RH.

## REFERENCES


1. Handbook of Thin Film Technology eds. L.I.Maissel and R.Glang, McGraw-Hill, 1970.

2. Spalvins T "Structure of sputtered $MoS_2$ films at various substrate temperatures" ASLE Trans. 17 1, 1-7, 1973.

3. Spalvins T "Tribological properties of sputtered $MoS_2$ films in relation to film morphology" Thin Solid Films 73 291-297 1980.

4. Dimigen H, Hubsch H, P Willich "Lubrication properties of R.F sputtered $MoS_2$ layers with variable stoichiometry" Thin Solid Films 64 221 1979.

5. Christy H I "Sputtered $MoS_2$ lubricant improvements" Thin Solid Films 73 299-307 1980.

6. Christy R I and Ludwig H R "R.F sputtered $MoS_2$ parameter effects on wear life" Thin Solid Films 64 223-229 1979.

7. Buck V "The performance of unbonded $MoS_2$ for space applications" Proc. 2nd European Space Mechanisms and Tribology Symposium, Meersburg, Oct. 1985.

8. Spalvins T "Status of plasma physics techniques for the deposition of tribological coatings" Tribology in the 80s, NASA Conference Publications 2300, Cleveland, Ohio, 1983.

9. Spalvins T "Bearing endurance tests in vacuum for sputtered molybdenum disulphide films" NASA TM X-3193 January 1975.

10. Fleischauer P "Effects of crystallite orientation on environmental stability and lubricating properties of sputtered $MoS_2$ thin films" Aerospace Report No. ATR-82(8435)-1 Aerospace Cooperation March 1983.


## ACKNOWLEDGEMENTS


The author is indebted to the Managing Director, Northern Division, UKAEA, England for permission to publish. The author also wishes to express his thanks to the following UKAEA staff: Mr Frank Goater of ESTL for preparing the test samples and assisting with testing; Ms Margaret Lambert for producing scanning electron micrographs; Mr B. Williams and Mr M. Craven for undertaking film analyses. ESTL is indebted to ESA for financially supporting this project.

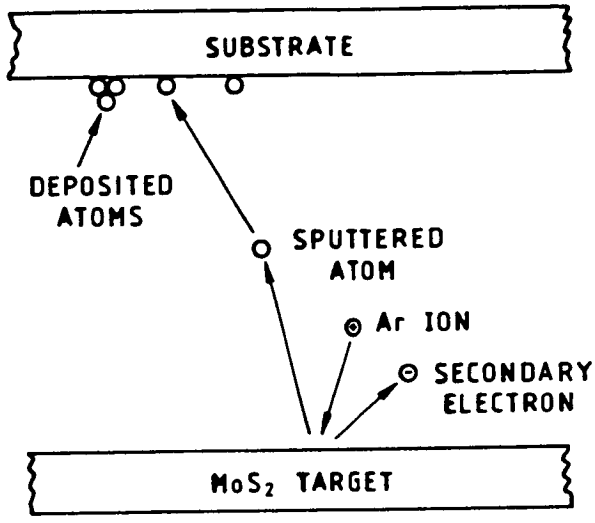


Figure 1. - Sputtering process.

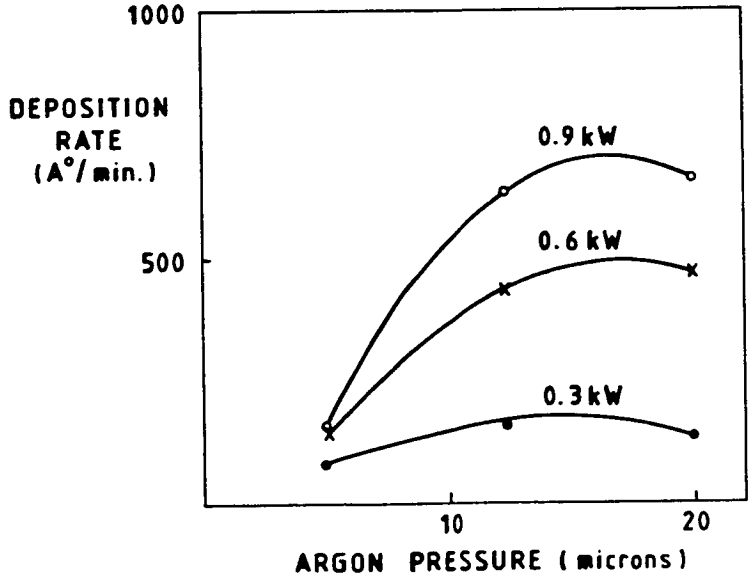


Figure 2. - Deposition rate of sputtered molybdenum disulphide as function of argon pressure.

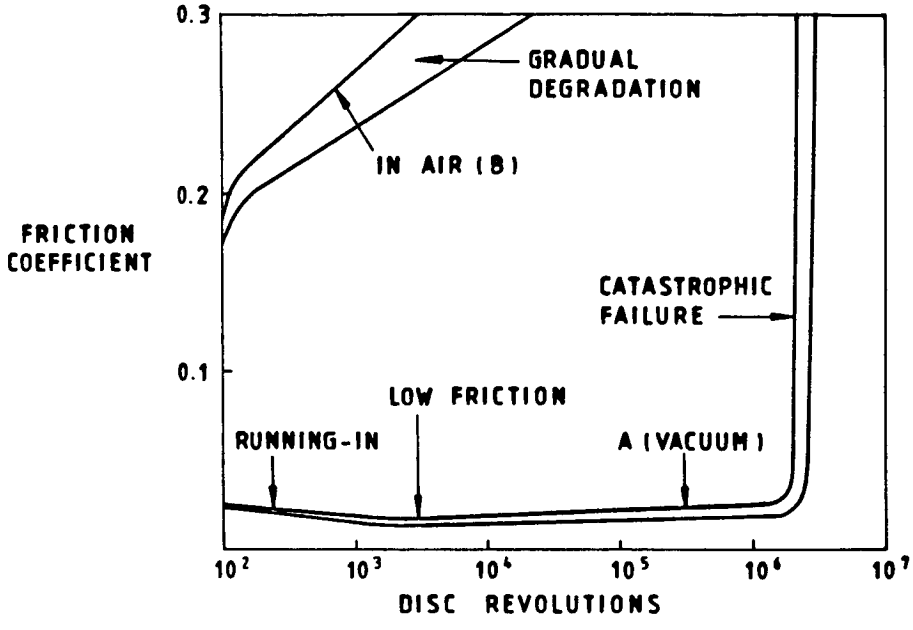


Figure 3. - Failure modes of sputtered $MoS_2$ under sliding motion.

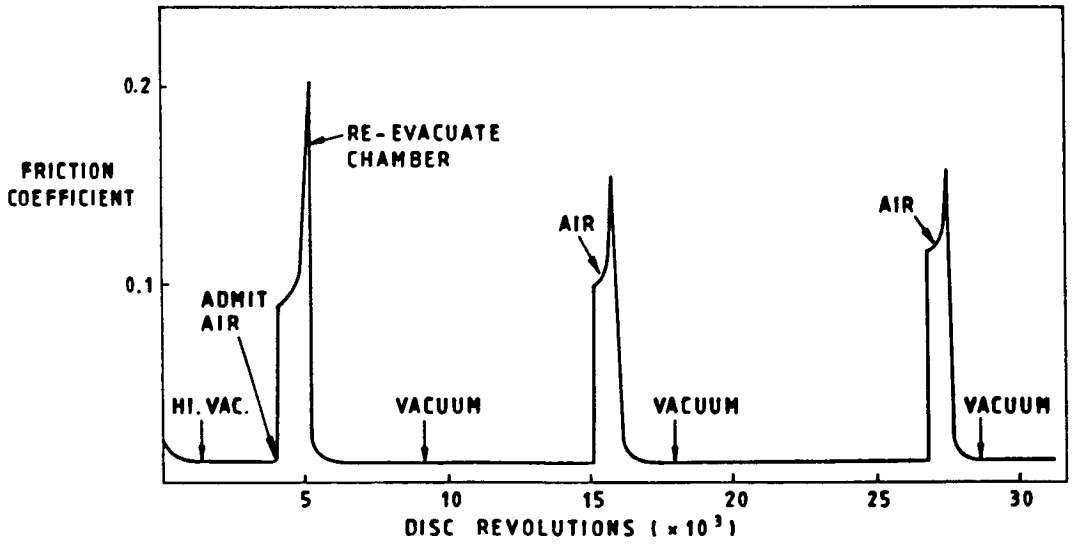


Figure 4. - Effect on $MoS_2$ lubricity on alternating environment between high vacuum and laboratory air (RH = 50 %, T = 20.5 °C).

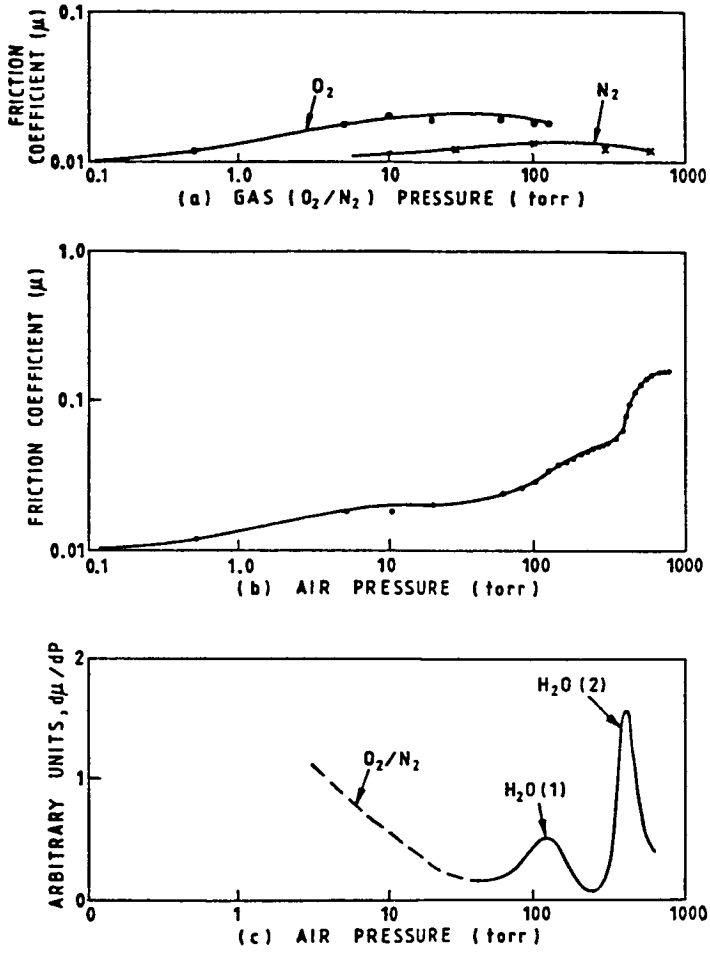


Figure 5. - Effect of gas pressure on friction coefficient of sputtered $MoS_2$.

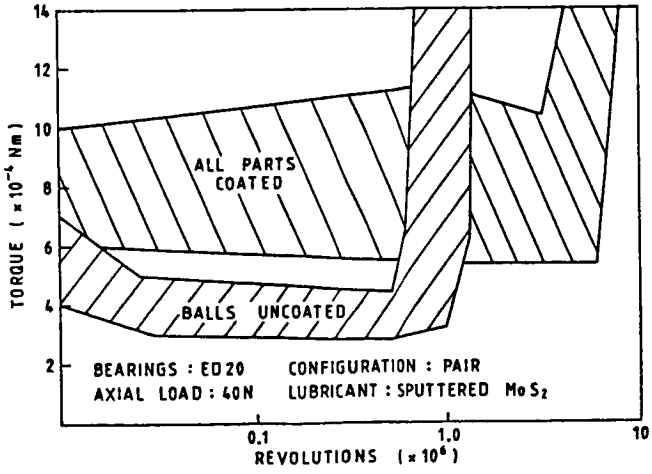


Figure 6. - Bearing torque vs. revolutions (in vacuum).

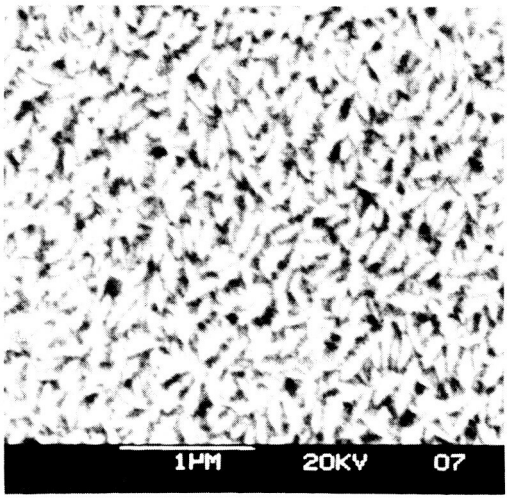


SURFACE

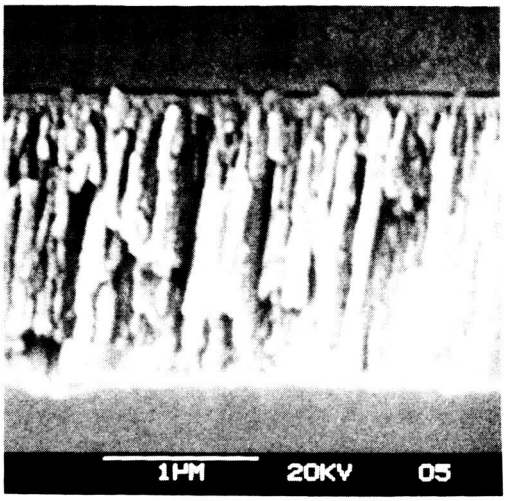


SECTION

TYPE A FILM

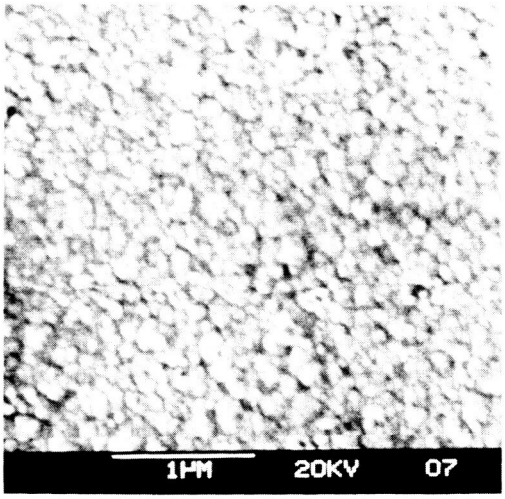


SURFACE

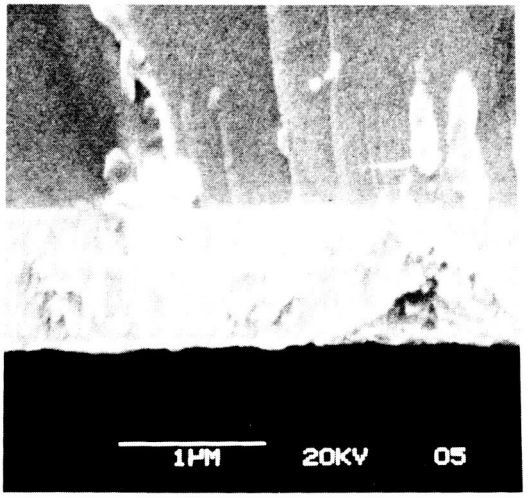


SECTION

TYPE B FILM

Figure 7. - SEM micrographs of sputtered $MoS_2$ films.

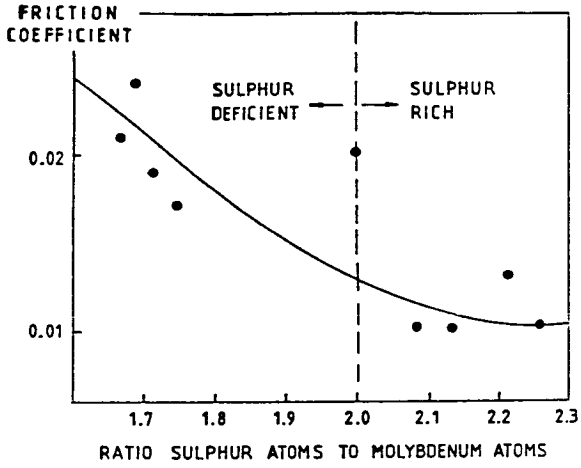


Figure 8. - Friction coefficient of $MoS_2$ films as function of sulphur content.

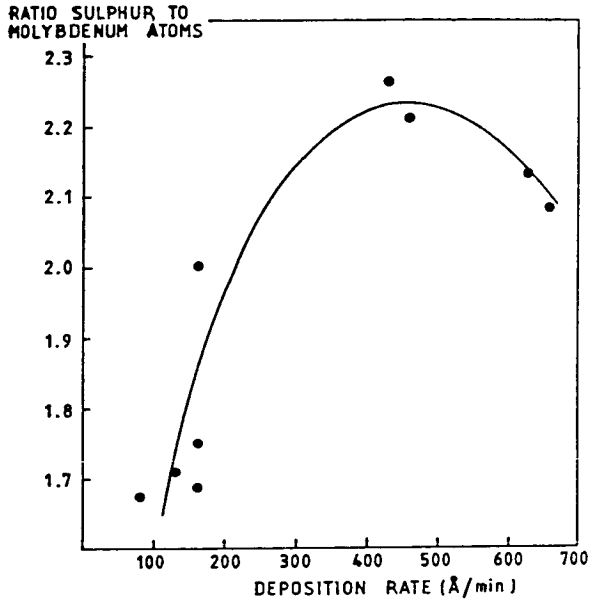


Figure 9. - Sulphur content as function of deposition rate.

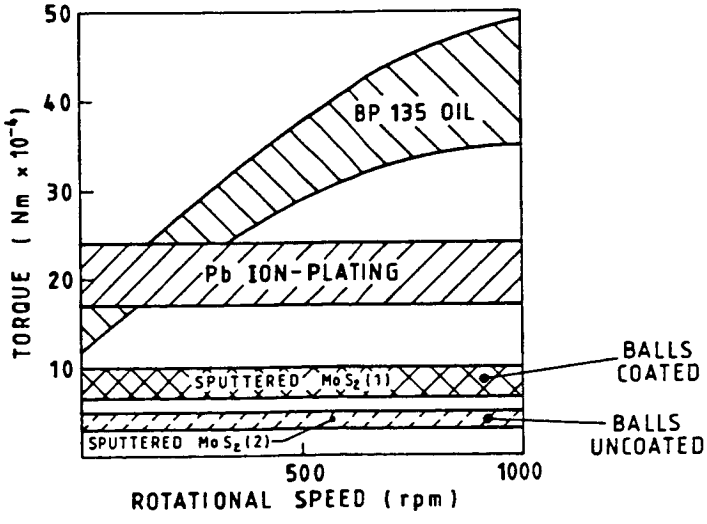


Figure 10. - Torque vs. rotational speed of ED20 bearing pairs employing different lubricants (under vacuum).

# ROLLING ELEMENT BEARINGS IN SPACE

J. W. Kannel* and K. F. Dufrane*

The paper discusses some of the advances in tribology that have been associated with aerospace mechanisms. The needs of aerospace have been the dominant forces leading to improvements in understanding and applying tribology technology. In the past two decades improvements in understanding bearing torque, elastohydrodynamic lubrication, lubricant distribution, cage stability, and transfer film lubricants have been made. It is anticipated that further developments will be made in response to future aerospace requirements.

## INTRODUCTION

The development of aerospace mechanisms has required considerable advances in the science of friction, wear, and lubrication (tribology). The aerospace industry has been the dominant driving force in tribology and has given tribology the popularity and respectability it now enjoys. Further, many of the tribology techniques developed for aerospace have been applied to mechanical components for non-aerospace systems and have been a benefit to all technology. Figure 1 shows a qualitative chart which illustrates the growth of tribology problems with aerospace and the advances that have been made. Despite significant advances in tribology, the insatiable demands of aerospace systems seem to grow faster than the solutions.

Major tribology advances have been made in several areas, with rolling element bearings being a particularly important example. Without the advance made in rolling-bearings or alternative concepts, many of the space systems would not be possible. The paper discusses a small part of their advances and how these advances can be applied to assist design. The paper discusses bearing torque for small and medium sized bearings, cage stability, lubricant distribution, and transfer film lubrication. The paper does not deal with the emerging area of high temperature tribology, which is an area needing major advances to permit the practical use of engines and mechanisms at high temperatures.

## TRIBOLOGY DEVELOPMENT

### Gyroscope Bearing Lubrication

Early in the space program the need for special lubricants for precision gyroscope systems became apparent. The most popular lubricant soon became KG-80, which was a replacement for the original fluid Teresso V-78. Interest in fluids at various viscosity levels prompted the development of

*Battelle Columbus Division, Columbus, Ohio.

the Super Refined Gyroscope (SRG) lubricants. These SRG fluids represent a homologous group that allows the users to select a specific viscosity, and the researchers to vary viscosity, in controlled experiments with a reasonable degree of confidence. Selecting the proper viscosity involves several important considerations depending on the application.

Operating torque is one important consideration in selecting the viscosity. Typical viscosity-temperature data are given in Figure 2 for the SRG fluids. Several experiments have been conducted with an R-6 bearing to define the torque and lubrication capabilities of the SRG lubricants. Figure 3 shows torque as a function of viscosity. This bearing was lubricated with a few milligrams of the selected lubricant by using a Freon carrier. The Freon evaporates and leaves a residual film of lubricant. The torque is related to the shearing of the viscous layer between the balls and races. Figure 3 clearly shows the torque penalty associated with increasing the viscosity of the bearing lubricant.

One advantage of increasing viscosity is illustrated in Figure 4. Lift-off speed is defined as the speed at which a lubricant film is formed that completely separates the balls and races in the bearing. The lubricant film condition is monitored by an electrical continuity approach. The dynamic electrical resistance of the bearing is interpreted in terms of percentage of lubrication, i.e., the percentage of the time no electrical shorting occurs. At a temperature of 60 C the R-4 bearing would generate a good elastohydrodynamic (ball race) lubricant film at a speed of 80 rpm if a KG-80 fluid were used. If an SRG-40 fluid were used, the speed required for good lubrication would be 160 rpm. The higher viscosity fluid would be preferred if the primary bearing operating speed was to be in this range. However, if the operating speed is much higher, the lower viscosity lubricant may be preferable because of the associated lower operating torque.

The lubricant viscosity is also a factor in evaporation rates, which can be important for vacuum applications where extended life is desired. In general, evaporation rates for a given type of fluid decrease as the viscosity is increased. For example, Table 1 presents measured evaporation rate data for two different lubricants at different viscosities. For long-life applications the lower loss rates associated with higher viscosities are desirable, but the high viscosity lubricants have the accompanying disadvantage of higher operating torques.

Cage Stability

Gross bearing torque can be controlled by proper selection of the lubricant and lubricant quantity in the bearing. However, bearing torque variations are much more difficult to control. Small torque variations in a gyroscope of a despun antenna support in space can result in intolerable errors in positioning and control. One major source of torque variation is erratic motions of the cage separating the balls. Under ideal conditions the cage simply rotates with the balls. However, under some conditions the

cage incurs rapid secondary motion, which is known as cage instability. Cage instability generates erratic friction in a bearing, which is observed as erratic torque. Figure 5 is an example of torque fluctuation measured in a bearing operating in an unstable mode.

The key to cage stability lies in the tangential stiffness of the ball-race interfaces and the rate at which energy can be absorbed at these interfaces. When the cage strikes a ball, the ball will slip and generate a reactive force against the cage. If the slip occurs easily, such as when the balls and races are completely separated by a film of low viscosity fluid, the reaction force is small. Under such conditions the cage energy is absorbed by shear losses in the lubricant film. Conversely, if the ball and races are separated by a highly viscous fluid, the ball slippage will be small, the shear losses much less, and the cage motion will be undamped. Depending on the parameters of the particular bearing, cage instability can be a serious problem.

A cage stability criterion is given by:

$$Dp = \frac{32C_{\mu}^{2}}{M\,C_{sl}} \tag{1}$$

where

$C_{\mu}$ is a ball-race traction parameter inversely related to film thickness
$C_{sl}$ is the ball-cage spring rate (linearized)
M is the cage mass

$$C_{\mu} \approx \mu_{avg} A/h \tag{2}$$

where

$\mu_{avg}$ is the average contact zone viscosity ($\sim 10^{6}$ Cp for a mineral oil)
A is contact area
h is film thickness

As h gets small or $\mu_{avg}$ gets large, $C_{\mu}$ gets large.

The larger the value of Dp the higher the likelihood the cage will be unstable. An approximate criterion for cage stability is given in Figure 6. To check stability, values of the ball-cage friction coefficient, f, and a factor $e_f$ must be known, where:

$$e_f = \exp\,(-\pi/Dp-1) \tag{3}$$

An accurate assessment of cage stability requires analyses of the cage motions using comprehensive computer models.

Lubricant Distribution

Large spacecraft starting with Skylab have brought a new set of tribological problems. Smaller spacecraft could be stabilized by spinning the spacecraft or by the use of control jets. The large extended mission spacecraft require large control moment gyroscopes (CMG's), which are capable of handling large slew loads resulting from astronauts moving around the crafts and from changing the orientation. The large CMG's have considerable weight and operate at high speeds. Small bearings using lubricant-impregnated retainers no longer suffice for these units; positive lubrication of large bearings is required. The lubrication has to be highly reliable, but extremely compact to meet weight and space requirements.

One major tribological challenge is insuring that the lubricant gets into the bearing to lubricate the ball-race interfaces. Devices such as centrifugal oilers attached to the rotating shaft were successfully used in some applications. However, positive lubricators in space require a hard look at how lubricant migrates around the bearing cavity in a vacuum environment. Typical results of creep tests are shown in Figure 7.

A drop of lubricant approximately 0.5 mm in diameter was positioned on a polished steel plate in a 10 mPa ($10^{-5}$ torr) vacuum chamber. The spreading of the drop was monitored over a period up to 400 hours. For the two lubricants shown in Figure 7, the rate of creep would decrease over an extended time period. The higher viscosity fluid, SRG 160, tended to creep much more slowly than the low viscosity fluid, SRG 60. The lubricants would not creep around sharp edges or over a debris track of Synthane. Lubricant tended to creep in the direction of a thermal gradient of 4C, as shown in Figure 8. Lubricant would not creep against the thermal gradient. These results demonstrated that the lubricant must be resupplied directly to the ball tracks on the races or to the balls themselves. Since the quantity of make-up lubricant is very small, the delivery system must be arranged for the centrifugal force field to permit direct impingement on the races, as opposed to controlling the direction through a jet. The tribology technology developed for large CMG's permitted the design of automatic lubricators that functioned for extended missions.

Transfer Film Lubrication

One major key to the success of the NASA space efforts has been the use of highly efficient systems and the minimization of weight. Large tribology devices cannot be tolerated and every effort must be given to optimizing system performance. In some applications, such as the liquid oxidizer and fuel pumps in the Space Shuttle main engine, the bearings must be cooled and lubricated with the cryogenic fluid. Cryogenic fluids tend to be good for bearing cooling, but are poor lubricants. One method to lubricate bearings in this environment is by transfer film lubrication.

Transfer film lubrication implies that the lubricating cage material is transferred to the ball and, in turn, to the races, Transfer film technology is in its infancy as a tribological science and little is known about materials or operating conditions required to optimize this type of lubrication. In most applications, transfer films are difficult to achieve and even more difficult to substantiate. Enough is known about transfer films to realize both their importance and their limitations.

Figure 9 shows the results of transfer film studies with Rulon-A and 5 percent $MoS_2$. A 440C ball (Figure 10) was loaded against an oscillating 440C cylindrical ring. A Rulon-A wiper was loaded against the ball to create a transfer film for the ball-race interface. As the load (contact stress) between the ball and ring was increased, the roughness of the ring wear track decreased slightly. At a mean stress level of 1.38 GPa (200,000 psi) the transfer film was insufficient to prevent roughening of the surfaces. The experiments imply that there is a limiting stress for effective transfer film lubrication.

The traction associated with solid surface films can be computed using elasticity theory for the traction of surface layers, as shown in Figure 11. The smaller the value of $\gamma$ in the Figure, the lower is the surface film elasticity. Values of $\gamma$ of 0.01 might be associated with $MoS_2$, and values of $\gamma$ of 0.002 would be indicative of a PTFE coating. The traction-slip curves are, in many respects, similar to those for liquid lubricants. An effective viscosity for a transfer film can be expressed:

$$\mu_{eff} = \frac{2p_o h}{3V} \frac{C_T V}{\Delta V} \qquad (4)$$

where

$p_o$ is the maximum contact pressure
$C_T$ is the traction coefficient
$h$ is film thickness
$V$ is rolling velocity
$\Delta V$ is slip velocity

For a solid-film-lubricated bearing, Equation 4 in conjunction with Equations 1-3 show the factors affecting cage stability. Large values of the traction coefficient, for a given value of slip, can product an unstable cage. The lower the resilience of the surface film, the greater the probability for cage unstability.

## CONCLUSIONS

Numerous tribology problems have been encountered in the development of aerospace mechanisms. These problems have led to research activities which have not only yielded solutions to the problems but have also aided in overall technology development. Examples of aerospace tribology advances include better understanding of bearing torque, elastohydrodynamic lubrication, lubricant distribution, cage stability, and transfer film lubrication.

There are several tribology related problems currently facing industry and specifically the aerospace industry. For example, lack of tribology materials and lubricants are major limitations to high temperature engine development. Lack of low temperature lubricant technology is a limitation to cryogenic lubrication. Bearing precision is a limitation to very accurate mechanical control devices. The research required to address these and other problems promises to insure a productive future in tribology.

TABLE 1. EFFECT OF VISCOSITY ON EVAPORATION RATE OF TWO LUBRICANTS IN A 0.133 MPa ($10^{-6}$ TORR) VACUUM

| Fluid | Published Viscosity at 40C, $10^{-6}$ $m^2/s$ | Weight Loss Rate at 40C $mg/cm^2$-hr |
|---|---|---|
| Super-refined Paraffinic Mineral Oil (SRG 30) | 14 | 18 |
| Super-refined Paraffinic Mineral Oil (SRG 40) | 27 | 13 |
| Perfluoro Ether | 8 | 2.2 |
| Perfluoro Ether | 28 | 0.19 |
| Perfluoro Ether | 357 | 0.0002 |

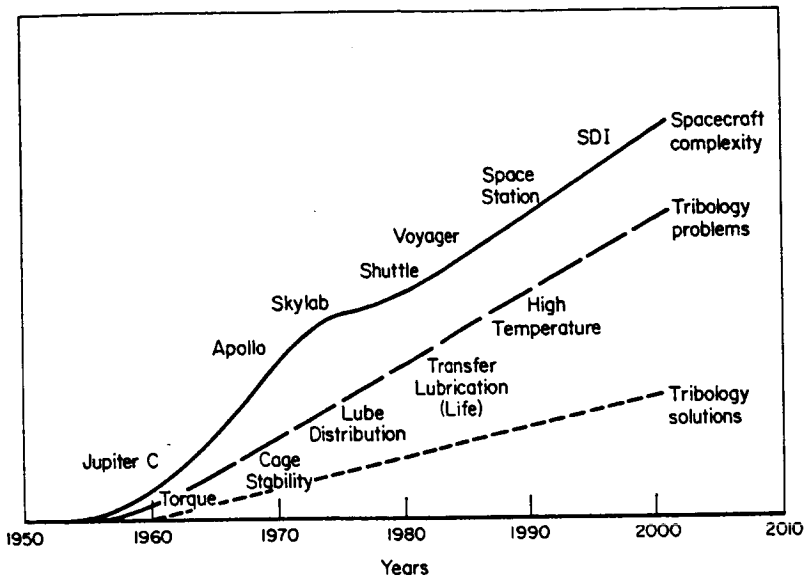


Figure 1. - Tribology challenge.

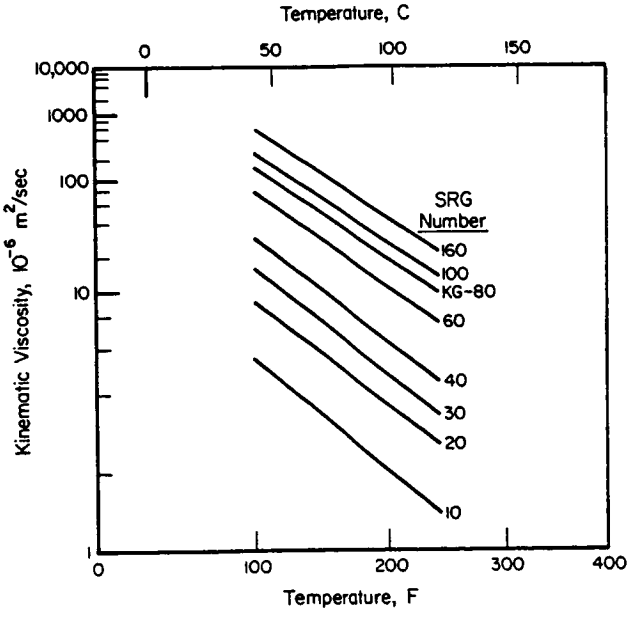


Figure 2. - Viscosity versus temperature for a homologous series of super-refined mineral oils.

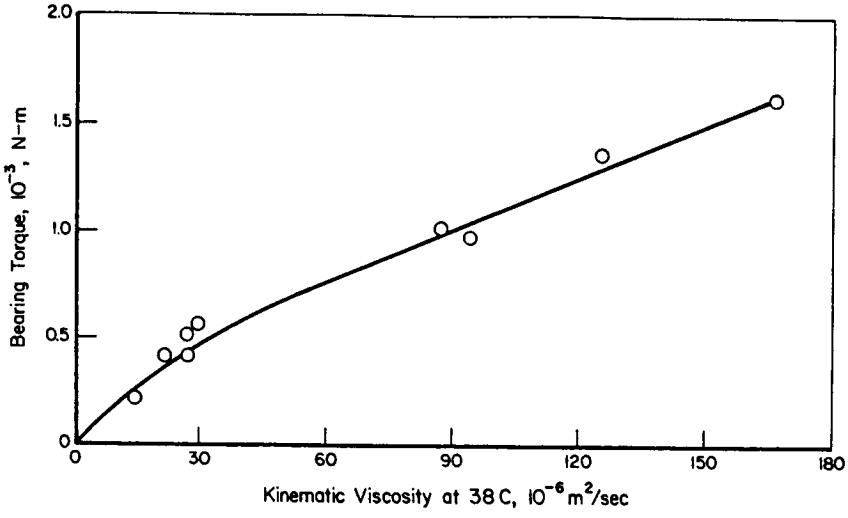


Figure 3. - Measured bearing torque as a function of lubricant viscosity for various lubricants at 25C for an R-6 bearing at 480 rpm.

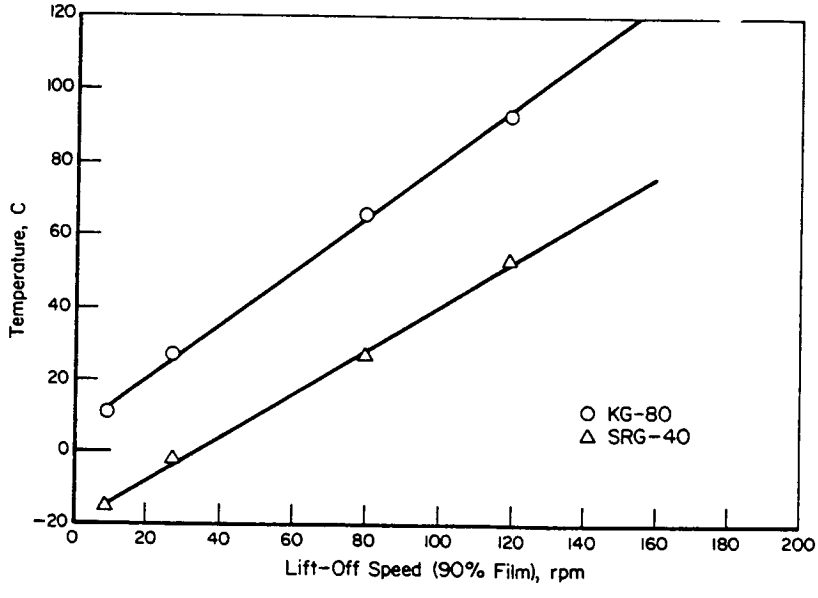


Figure 4. - Lift-off speed as a function of temperature for an R-6 bearing loaded to 980 $MN/m^2$ maximum Hertzian contact stress (inner race) and lubricated with two superrefined mineral oils.

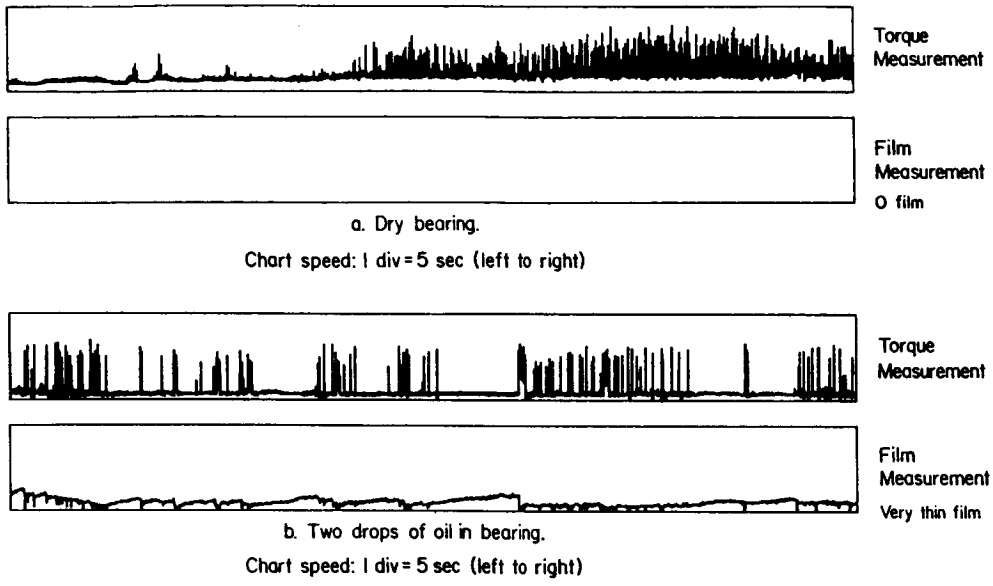


Figure 5. - Bearing torque and film thickness measurement with no lubricant and meager lubricants. Torque spikes imply instability.

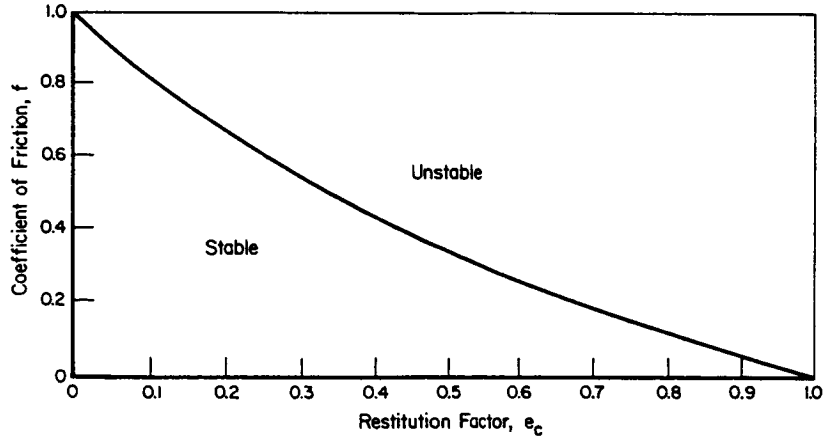


Figure 6. - Quick check of cage stability.

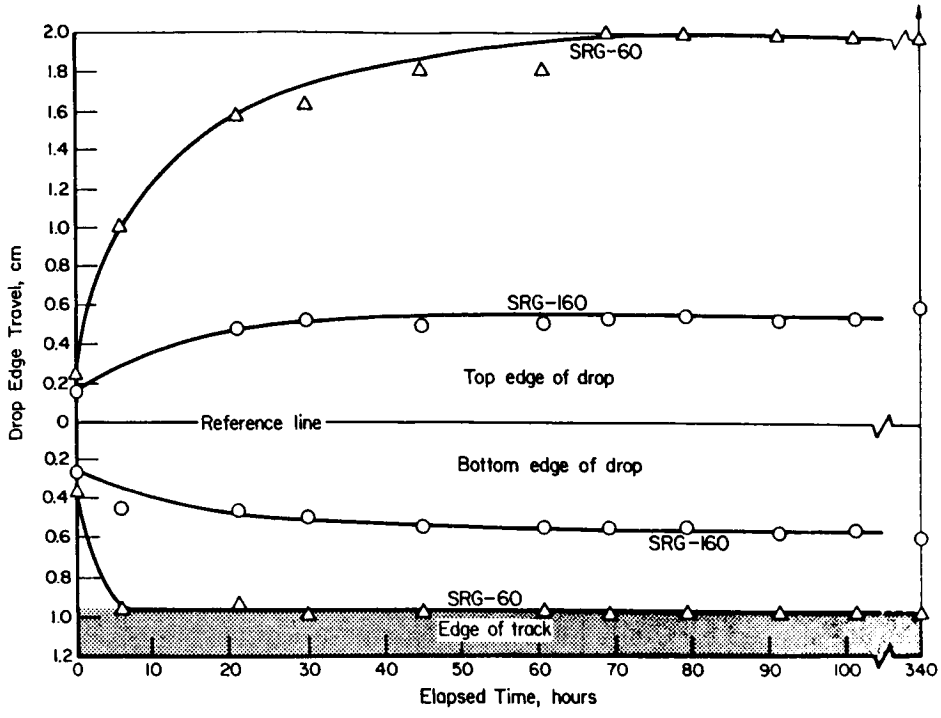


Figure 7. - Results of creep experiments in presence of a synthane transfer film SRG-60 and SRG-160 oils.

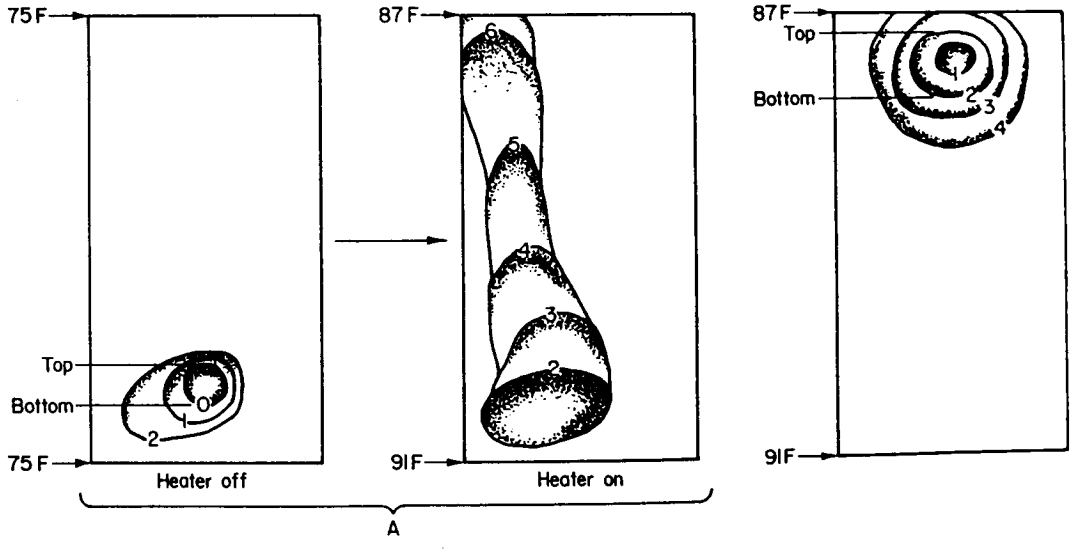


Figure 8. - Sketch showing migration patterns of KG-80 in the presence of a 4 F thermal gradient.

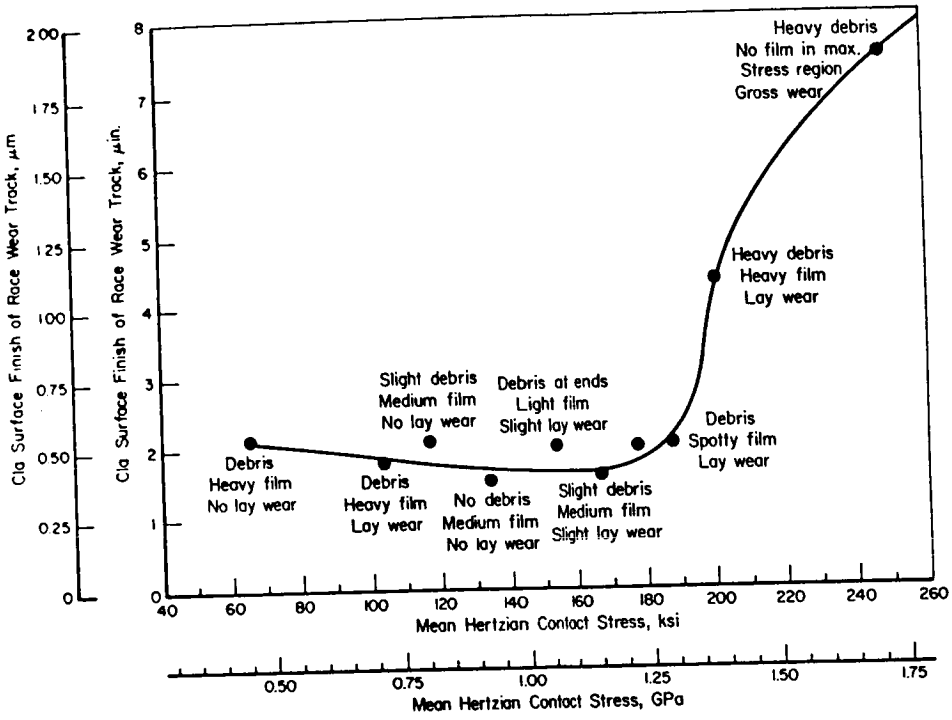


Figure 9. - Relationship between race wear track surface finish and ball-race contact stress for a race lubricated with a rulon-A + 5 percent $MoS_2$ transfer film.

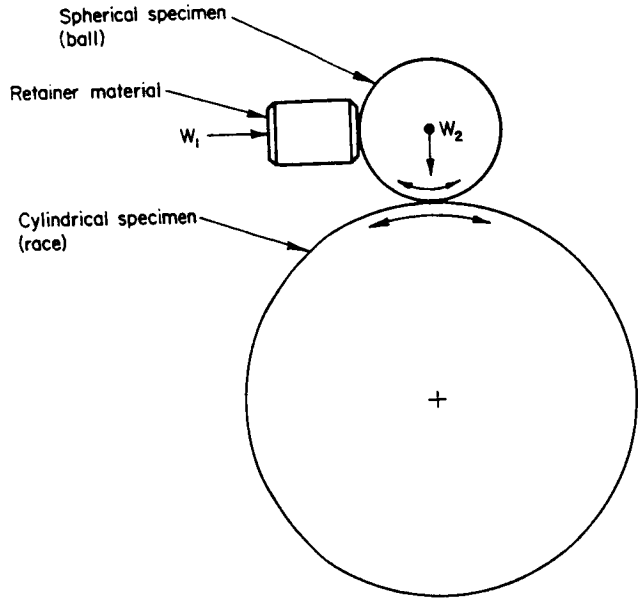


Figure 10. - Schematic drawing of apparatus for transfer analysis.

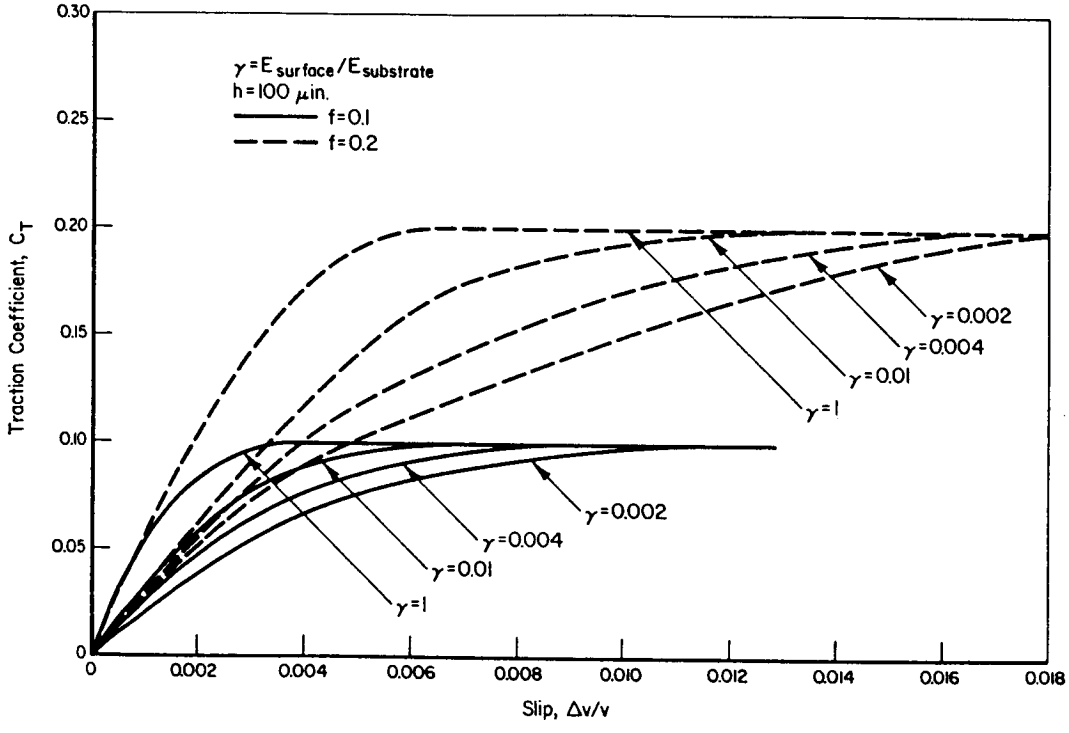


Figure 11. - Theoretical traction slip curves for various coatings.

# DUTY CYCLE TESTING AND PERFORMANCE EVALUATION OF THE SM-229 TELEOPERATOR*

Robert S. Stoughton** and Daniel P. Kuban+

This paper contains the first known experimental studies and analyses of teleoperator performance for specific duty cycles. The results are presented in two distinct areas as position usage patterns, and as three-dimensional power grids. The position usage patterns are a valuable means to assess the available motion range. The power grids are a unique concept for evaluating joint performance. Final conclusions contain recommendations to upgrade the teleoperator for optimum performance.

## INTRODUCTION

This paper summarizes the results of work performed for the Consolidated Fuel Reprocessing Program at the Oak Ridge National Laboratory. An experimental analysis was conducted of the duties of a force-reflecting teleoperator system applied to a series of tasks. These tasks are typical for operations in a remote hazardous environment. The teleoperator system studied is one used in many applications in this country, the TeleOperator Systems (TOS) Model SM-229. In this experiment, the joint positions and motor currents were recorded at a rate of 10 Hz over 50 h of operation. This work provides general information about teleoperators that was previously unavailable, and that is useful in determining design parameters for improved systems. They provide insight into proper motor sizing, gear ratios, and drive configurations. The resulting analysis technique is generalized and shown to be a valuable tool for design analysis of operating and future systems.

*Research sponsored by the Office of Spent Fuel Management and Reprocessing Systems, U.S. Department of Energy, under contract No. DE-AC05-840R21400 with Martin Marietta Energy Systems, Inc.

**University of California, Santa Barbara.

+Oak Ridge National Laboratory Engineering Division, Oak Ridge, Tennessee.

## EXPERIMENTAL SYSTEM

The experimental work described here was carried out in the Remote Systems Development Facility (RSDF) located at Oak Ridge National Laboratory (ORNL). This facility provided a realistic working environment for evaluating remote maintenance equipment. The design and makeup of this facility have been described previously.[1] A remote test area with the teleoperator slave arms, an operator control station, and a PDP 11/34 data acquisition system are the major components of the RSDF. The remote test area (Fig. 1) contains equipment for a variety of manipulation tasks considered to be the generic subtasks of more complex remote operations. The slave manipulator arms are mounted on the end of a telescoping hoist of a three-axis transporter, allowing the arms to travel anywhere within the remote cell. The operator control station (Fig. 2) contains the master arms, television screens for viewing the remote test area, and controls for the cameras, transporter, and auxiliary functions.

The teleoperator used was a TeleOperator Systems (TOS) Model SM-229, a force-reflecting system with a lift capacity of 10 kg per arm. The master arms and slave arms (Fig. 3) are kinematically identical. Figure 3 also shows the reference configuration of the manipulator, with the upper arm and end effector horizontal and forward, and the forearm vertical.

The shoulder pitch and roll motions are driven by two motors through a geared differential. This differential drive configuration allows the two motors to share equally the load in a pure pitch (or pure roll) motion. However, simultaneous pitch and roll loading results in unequal duty cycles in the two motors. The elbow pitch is gear driven by a single motor. The wrist yaw (or elbow roll) is driven by a single motor via metal tapes. The wrist pitch and roll are driven by two motors through a differential with the torque transferred via metal tapes passing over idlers in the elbow. The wrist yaw, wrist pitch/roll, and tong motors are mounted on the shoulder roll and the motors provide the mechanical counterbalance for the forearm. Gears in the elbow pitch drive rotate this motor package to balance the forearm.

Position data for the joints were measured by potentiometers within the arms, and motor current data were measured by precision shunt resistors within the control boxes. These signals were recorded with a PDP 11/34 at 10 Hz while operators performed selected manipulation tasks. Data were sampled for the right slave arm only, so all results presented pertain to the right slave arm. It was determined[2] that the right arm is used significantly more than the left, so this limitation was not considered detrimental.

## EXPERIMENTAL TASKS

Five manipulation tasks were previously selected as being generic representations of remote maintenance operations:[1]

1. Removal/installation of an in-line instrument package. Using an impact wrench, loosen the clamp retaining the instrument package and disengage the pin connector from the instrument package.

2. Removal/installation of a 1/4-hp motor. Remove the motor with a lifting bale (see Fig. 4), assisted by an overhead hoist.

3. Removal/installation of a 76-cm pipe flange. Remove flange mounting bolts with the impact wrench and use the hoist to lift the flange (see Fig. 4).

4. Removal of a tubing service jumper with three horizontal connectors. Loosen the clamps with the impact wrench and remove the jumper.

5. Removal of a 15-cm pipe flange with two horizontal captured bolts. Loosen the captured bolts with the impact wrench and remove the flange.

Because the geometry and activity of tasks four and five are similar, this study considers their averaged data as one task. Tool-changing time is included in the task analysis, particularly the motion and time required to access the impact wrench.

Four experienced manipulator operators performed each task at least ten times. Data recording started when the operator began the task and ended immediately upon completion of the task or upon any equipment malfunction. A total of about 50 h of operational data were recorded in this manner.

The results presented here can be applied with certainty only to the specific tasks studied. Teleoperators perform a wide range of complex, unstructured tasks which cannot all be represented by the tasks that were studied here. The mobility of the transporter system does reduce some of the task-dependent effects because the operator can use any desired approach to the work site, and can use transporter movements to eliminate long reaches.

It was apparent that the wrist-pitch degree-of-freedom (DOF) was severely torque limited because just holding the impact wrench required nearly all of the available torque. This constraint made reassembly of the 15-cm pipe flange impossible because there was not enough torque remaining to manipulate the flange.

Full stall torque from the motors was not always available because of equipment limitations and drift in the analog control system (the brakes would energize when the position error of any joint exceeded a safety limit). The averaged torque that was available without exceeding this limit was measured daily. The available torque averaged for all seven motors was only about 75% of the full stall torque.

## EXPERIMENTAL DATA AND DISCUSSION

The recorded data were compiled into arrays of joint positions and motor currents for each DOF, relative to the amount of time spent at that position and at that current. The position data were also transformed from joint position to wrist position and orientation in cartesian coordinates. The velocity data were derived from the position measurements relative to time, and the motor-current measurements were converted to motor torque. The three-dimensional mechanical power grid was developed to describe how the joint was exercised during the experiment. This plot shows torque and velocity combinations versus their total duration time normalized to the longest duration combination.

As each task had more than one trial, the arrays were accumulated to obtain a composite average of the trials. These data were then converted to percentages of total time. The data arrays for all five tasks were then averaged with equal weighting to obtain the final results. A complete discussion of the test procedures and equipment, and the results can be found in Ref. 3.

The first area that will be discussed is that of joint position usage. Figures 5 through 7 are histograms showing how the operators used the available motion range for some of the joints. The angular range of each plot corresponds to the motion range of that joint, and the radius of each "pie slice" is proportional to the percentage of total time that the operator stayed in that part of the motion range. To visualize the wrist roll histogram (Fig. 7), one must consider the tong to be holding a pin or bar such that it is vertical in the reference configuration. The plot represents the orientation of that pin with respect to the wrist.

These figures (5 through 7) also provide very useful data for analyzing usage. Of more general interest is the working volume of human-controlled manipulation as applied to the generic tasks. These data are given in Figs. 8 through 10 as histograms of the position of the wrist pivot in cartesian coordinates. Figure 11 combines the histogram data of the wrist pitch and yaw as wrist orientation. In each plot, the darkest blocks are the most frequently used areas. Progressively lighter areas are less frequently used (geometric progression of 0.6), and the lightest shades represent blocks in which the wrist position was less than 1% of the time spent in the most used block.

Table 1. Mean Positions in Joint Coordinates

| JOINT | MEAN OPERATING POSITION | REFERENCE POSITION (Figure 3) |
|---|---|---|
| Shoulder pitch | -9.8° (down) | 0° |
| Shoulder roll | -13.0° (left) | 0° |
| Elbow pitch | 5.1° (forward) | 0° |
| Elbow roll | 42.5° (left) | 0° |
| Wrist pitch | -17.7° (down) | 0° |
| Wrist roll | 4.0° (CCW from behind) | 0° |

Table 2. Mean Position in Cartesian Coordinates Measured From Shoulder Pivot

| DIRECTION | MEAN WRIST POSITION (cm) | REFERENCE WRIST POSITION (Figure 3) (cm) |
|---|---|---|
| Vertical | 10.77 (down) | 10.63 |
| Forward | 8.74 (forward) | 10.04 |
| Transverse | 1.88 (left) | 0.0 |

The second area of discussion is that of how each joint was exercised. The three-dimensional mechanical power grids (Fig. 12, typical) were developed as an aid for analyzing the gear reductions and motor sizings. These grids were developed from the measured data and are valid only for this teleoperator configuration, and these specific tasks. The independent variables on these grids are the components of mechanical power: velocity and torque, scaled to the no-load speed and stall torque, respectively. Each variable is divided into 25 increments (4% of range) to form a 25 by 25 grid. The dependent variable is the log of the total operation time, scaled to the most used grid block. Thus, the height of each crosshair of the grid represents the log of the total operation time spent simultaneously within the velocity and torque ranges corresponding to that crosshair. Note that when the velocity and acceleration are in the same direction, the diagonal connecting stall torque and peak velocity is a physical limitation of the motor. Time can be spent above this diagonal only when the velocity and acceleration are in opposite directions.

This representative data collected from a working teleoperator system allows immediate understanding of the design margin and limitations within each joint. Figure 12 presents an idealized mechanical power grid for teleoperator joints. The most time is spent at 0 to 4% velocity and torque because the teleoperator is not moving and has no load, while the operator moves the transporter or adjusts the cameras. The grid represents desirable features by its symmetry about its main diagonal (good balance of speed and torque) and by reaching zero usage time just below 100% of torque and velocity capability (avoiding saturation). In an ideal power grid, the motor and gear reduction are adequate to meet all demands, but they are not significantly oversized.

The degree of symmetry in the grid provides a quantitative evaluation of the gear reduction. Figure 13 illustrates actual data from the wrist pitch DOF with the grid shape indicating a gear reduction that is too small. This gear reduction gives the joint a no-load speed in excess of that required and yet reduces the available stall torque to a level that hinders performance. In this DOF, high (% of max) velocities do not occur, while high torques occur regularly, as shown by the grid being skewed toward the torque axis. The opposite occurs when the gear reduction is too large. The joint could support torques greater than required but would be limited in velocity, shown by the grid being skewed toward the velocity axis.

The volume beneath the normalized grid and the points where the grid reaches zero along each axis provide data to evaluate motor sizing. Figures 14 and 15 show the grid shapes corresponding to a proper gear reduction, but with an oversized and undersized motor, respectively. These grids represent actual data from the shoulder roll and elbow pitch, respectively. When the motor is too large, the capacity in both torque and velocity is considerably greater than required, and the grid reaches zero at well below full capacity

with a small enclosed volume. Conversely, an undersized motor often operates at peak capacity in velocity or torque (the zero crossing is extrapolated beyond 100%) and the normalized grid encloses a large volume.

The power grid scales for the shoulder and wrist are special since they are driven by differentials. The torque/velocity capacity for one DOF in a differential drive varies with the simultaneous torque/velocity of the other DOF. The torque/velocity grids are scaled to the maximum possible values (i.e., when both motors drive the same DOF). The scaling causes the shoulder power grids to appear to be the result of oversized motors. The shoulder roll power grid (Fig. 14) is relatively symmetrical but reaches zero at well below full capacity. If simultaneous pitch and roll torques/velocities could be avoided, smaller motors could be used. The elbow pitch power grid (Fig. 15) encloses a relatively large volume with significant times spent at near 100% of torque and at near 100% of velocity. A motor 10 to 15% larger is required to allow both needs to be met. The wrist pitch and roll power grids (Figs. 13 and 16) are each skewed toward the torque axis and high velocities are never used. The time at high torque is particularly significant because of the differential drives. The high torque indicates that large gear reductions are needed, but this is limited by the load capacity of the metal tapes.

In the past, teleoperator joint gear reductions have been determined using the concept of effective radius, which is the direct-drive lever arm at which the stalled motor torque will support the design capacity. For example, a motor with a stall torque of 4 N·m used to support an 80-N capacity has an effective radius, $\rho$, of 0.05 m. The gear reductions for the joints are determined by dividing the maximum joint length, L, by the effective radius and the number of motors, N, that are driving that joint (i.e., two for differentials):

$$R = L/\rho N$$

Past designs have consistently used this formula for all joints but the results of this report indicate that some design revisions are now appropriate. Table 3 presents the joint lengths and gear reductions based on an effective radius and the suggested improved gear reductions based on the experimental evaluation. This would be of tremendous value if this evaluation was made on a prototype unit and then implemented on the production units.

The improved gear reductions are based on matching the zero crossings on the torque and velocity axes. In some cases, the measured zero crossings had to be extrapolated beyond 100%. For the wrist pitch, a somewhat larger increase than the stated 40% may be needed, as the wrist pitch was incapable of supporting the torque needed to reassemble the 15-cm flange.

Table 3. Joint Lengths and Gear Reductions

| JOINT | LENGTH AT FULL EXTENSION (cm) | ACTUAL GEAR REDUCTION BASED ON $\rho$ [a] | IMPROVED GEAR REDUCTION BASED ON EXPERIMENTAL DATA |
|---|---|---|---|
| Shoulder pitch[b] | 142 | 40 | 43.3 |
| Shoulder roll[b] | 58 | 29.4 | 30.6 |
| Elbow pitch | 84 | 43.5 | 39.6 |
| Wrist yaw | 15 | 8 | 8.9 |
| Wrist pitch[b] | 15 | 3.9[c] | 7.7 |
| Wrist roll[b] | 12 | 3.3 | 5.1 |

[a]90-N capacity, $T_{stall}$ = 1.71 N•m (continuous) $\rho$ = 1.9 cm.

[b]Differential drive.

[c]Select worst case for differential; second gear reduction is then adjusted for actual gear selection by choice of differential output gear.

## CONCLUSIONS

The duty cycles of a human-controlled manipulator have been experimentally measured. The time-use histograms of the kinematic range reveal specific improvements can be made in the joint motion ranges of the TOS Model SM-229. The working volume of the teleoperator can be applied to the design of all human-controlled manipulators. The mounting configuration of teleoperators must be designed to optimally fit the volumetric coverage to the working volume, and the drive configurations must operate most effeciently within the working volume for the anticipated tasks.

A graphical method for optimizing joint velocity and torque capabilities has been developed. This method, based on three-dimensional time-use histograms of mechanical power usage, was applied to the measured duty cycle data to determine optimal motor sizing and gear ratio selection for this human-controlled system.

REFERENCES

1. M. Clarke, W. Hamel, and J. Draper, "Human Factors in Remote Control Engineering," pp 8-16 in Proceedings 31st Conference on Remote Systems Technology, American Nuclear Society, 1983.
Nuclear Society, 1983.

2. J. V. Draper and M. M. Clarke, personal communication, October 1983.

3. R. S. Stoughton, "Kinematics and Duty Cycles of the SM-229 Force Reflecting Servomanipulator," M.S. thesis, The University of Tennessee, Knoxville, 1985.

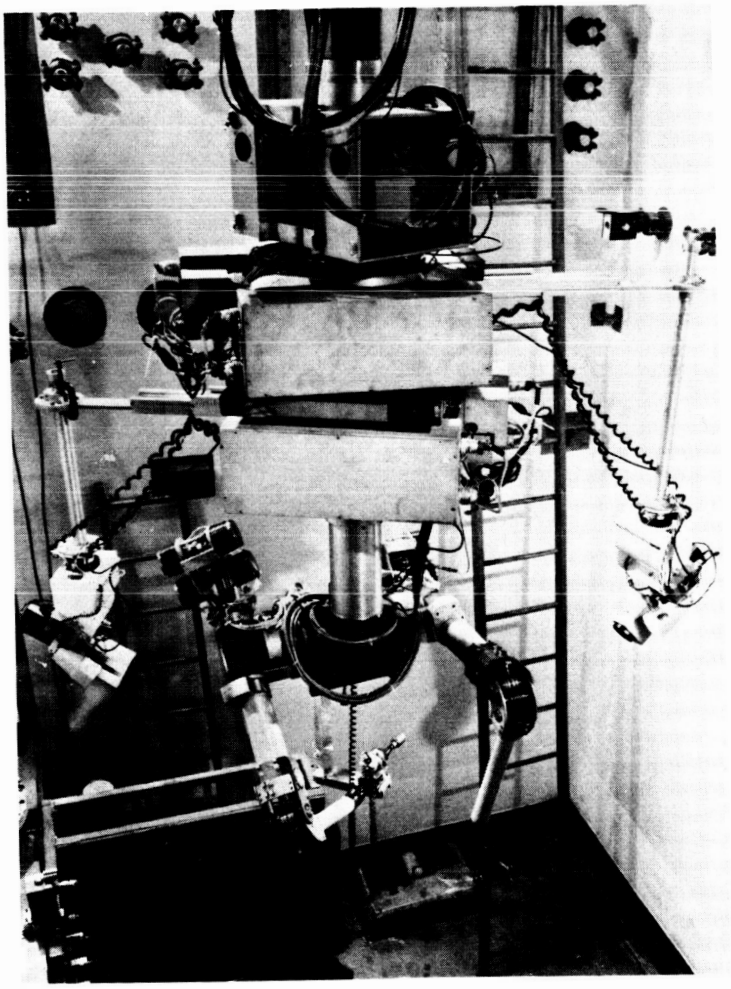

Figure 1. - Slave manipulator arms and remote cell.

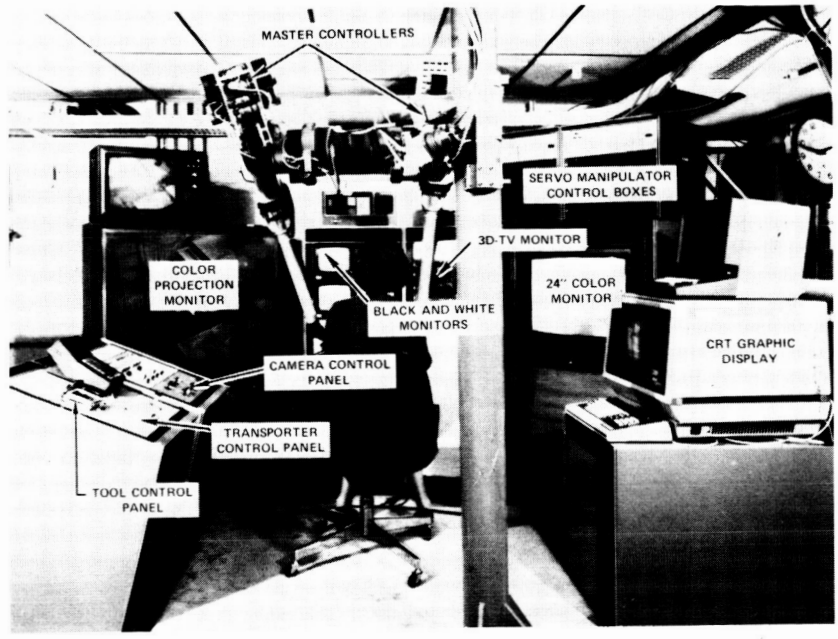


Figure 2. - Operator control station.

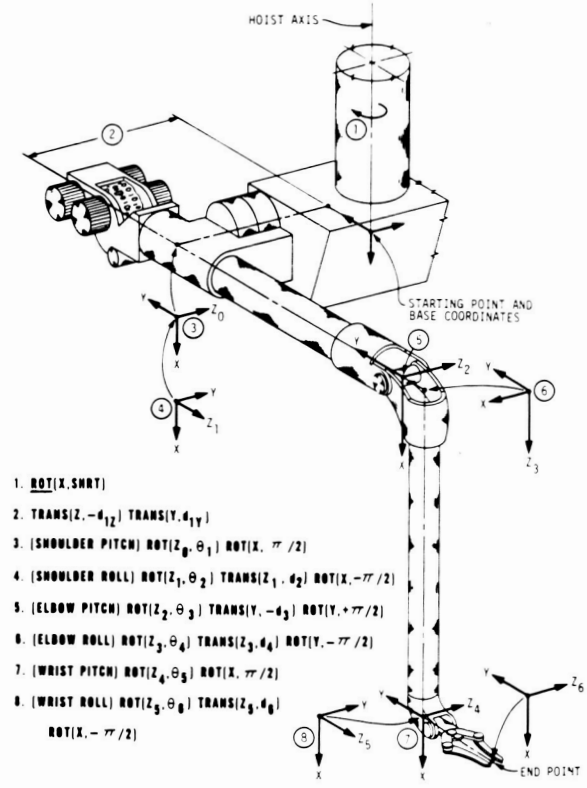


Figure 3. - Manipulator kinematics.

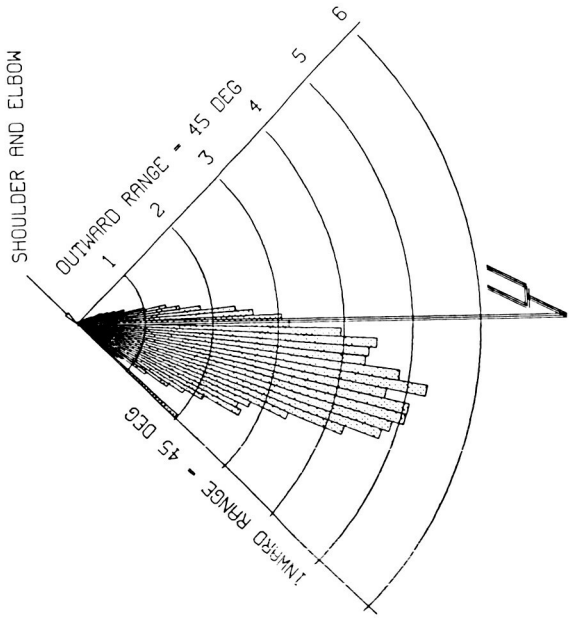


Figure 5. - Range of shoulder roll position usage.

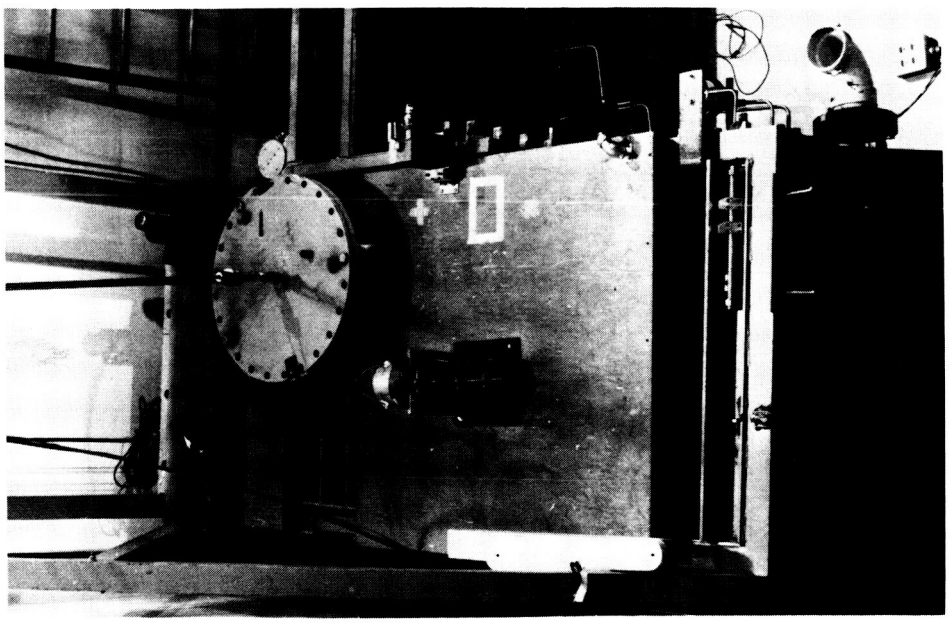

Figure 4. - Motor mount and 76-cm pipe flange.

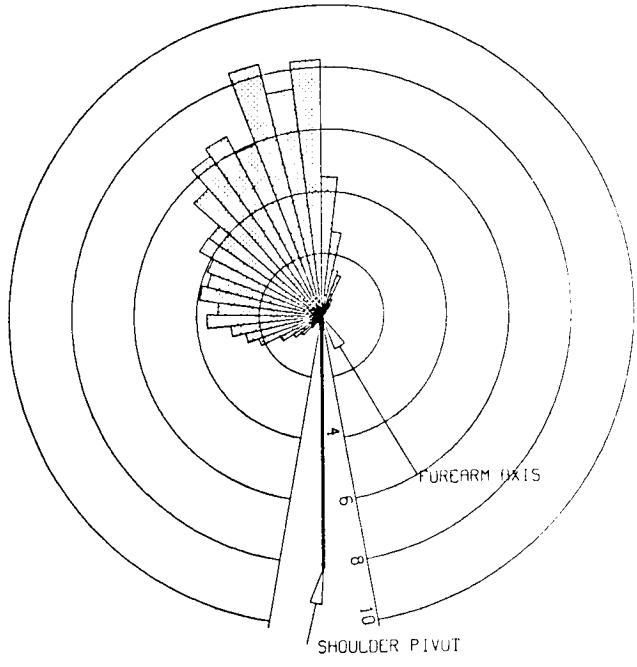


Figure 6. - Range of elbow roll (Yaw) position usage.

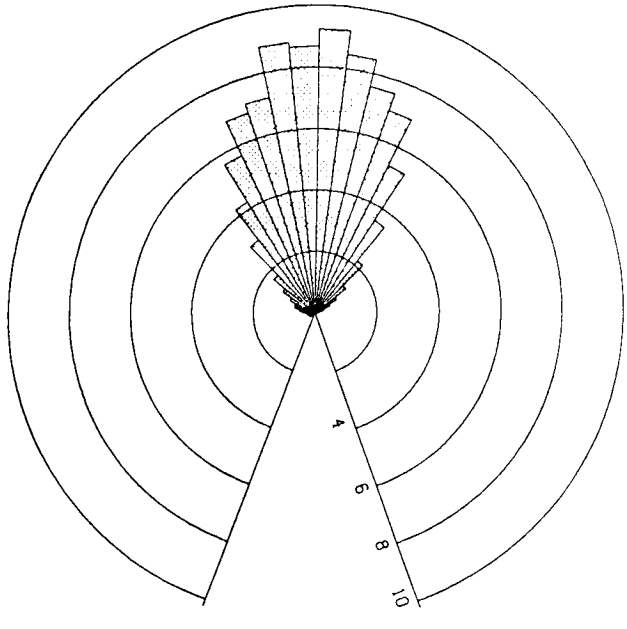


Figure 7. - Range of wrist roll position usage.

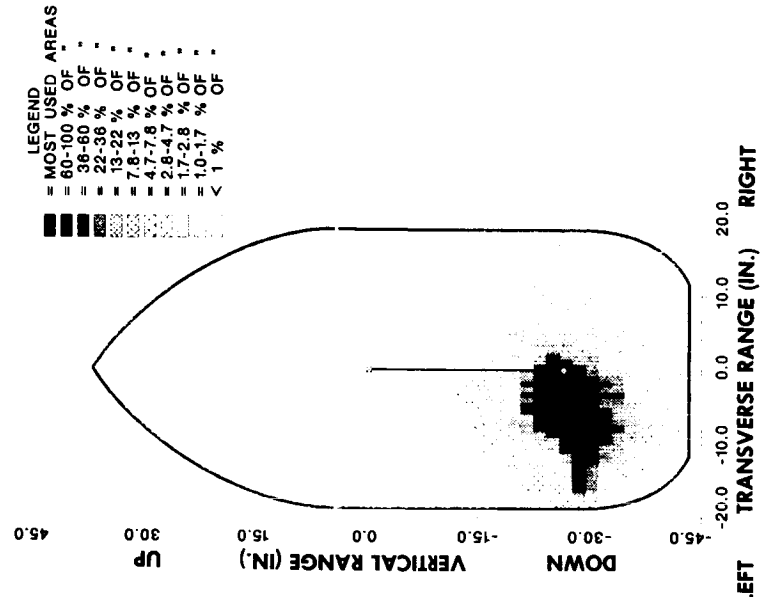


Figure 9. - Wrist position grid--back view.

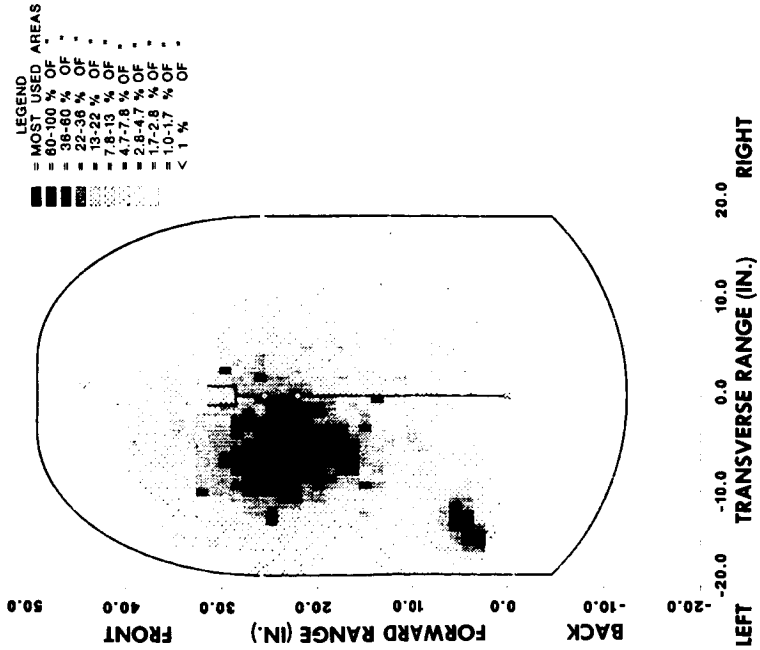


Figure 8. - Wrist position grid--top view.

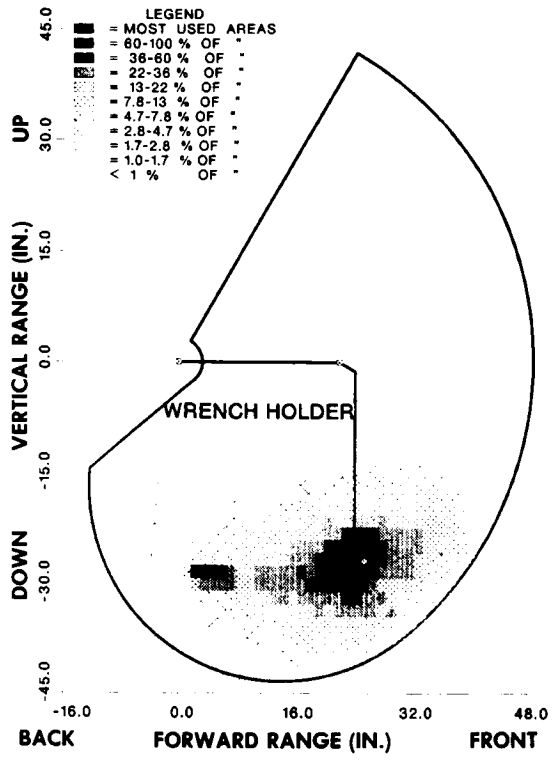


Figure 10. - Wrist position grid--
right side view.

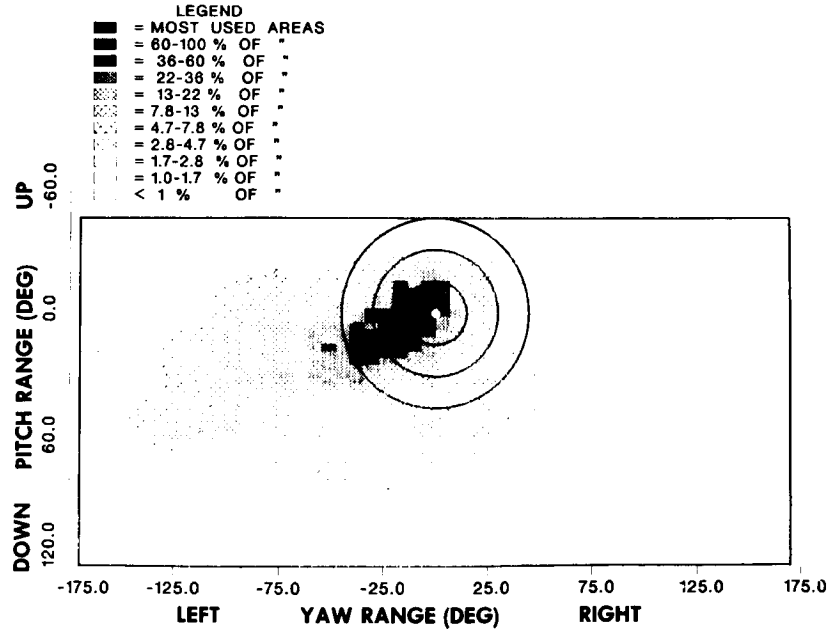


Figure 11. - Wrist orientation grid.

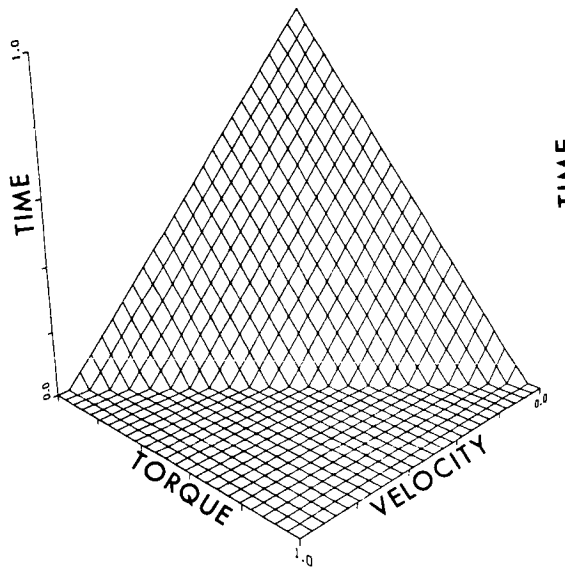


Figure 12. - Ideal mechanical power grid for teleoperators.

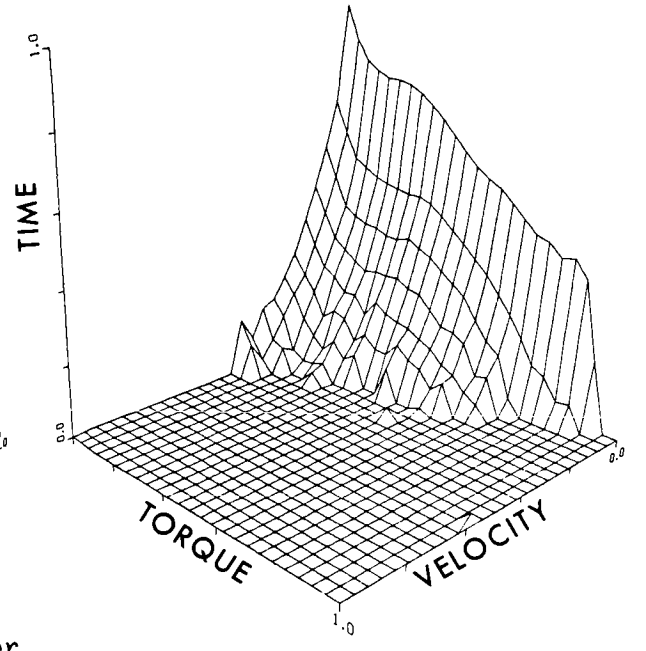


Figure 13. - Mechanical power grid for wrist pitch.

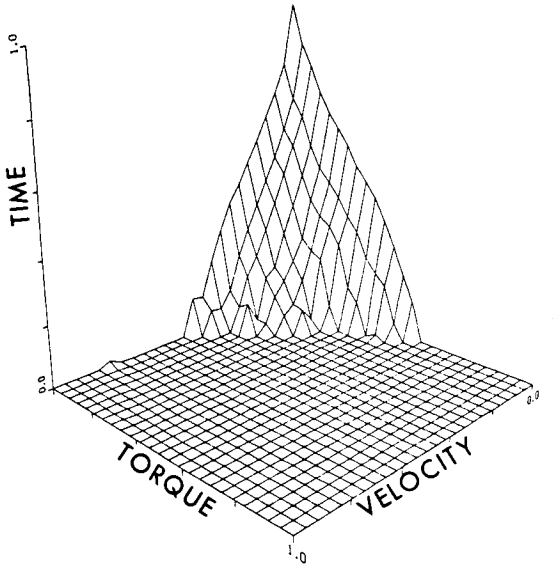


Figure 14. - Mechanical power grid for shoulder roll.

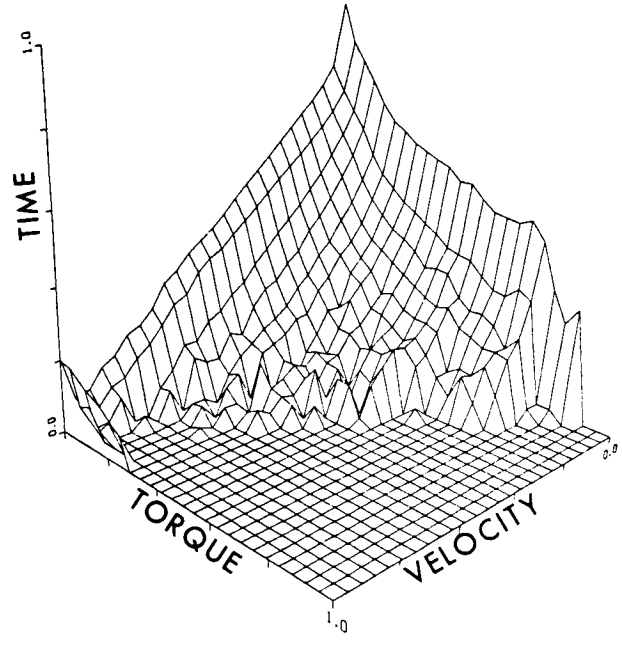


Figure 15. - Mechanical power grid for elbow pitch.

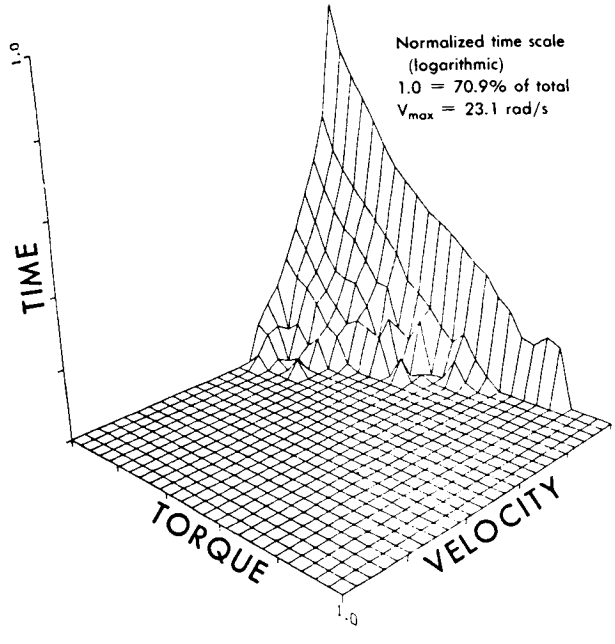


Figure 16. - Mechanical power grid for wrist roll.

# PSEUDO-PROTOTYPING OF AEROSPACE MECHANICAL DYNAMIC SYSTEMS WITH A GENERALIZED COMPUTER PROGRAM

Vikram N. Sohoni
and
Milton A. Chace

## 1. INTRODUCTION

Mechanical system CAE is a distinct, relatively new field of computer-aided mechanical engineering. It is complimentary to neighboring fields such as geometrical or solid modelling, finite element stress analysis and vibration analysis. The functional distinction of the field is that it determines the time-dependent behavior of entire interconnected systems of parts and other elements, ranging through angular displacements which may be sufficiently large to require non-linear solution.

Engineers responsible for mechanical design are particularly assisted by mechanical system CAE, since this technology enables them, accurately and early, to predict the behavior of machinery or vehicles for many variations in design. Behavior assessment can be done even before the first prototype exists, or in compliment to prototype or product testing. The assistance for aerospace design is especially compelling due to extreme requirements for reliable performance, and the difficulty of providing a zero gravity environment for physical testing.

For many years machine designers appraised the performance of devices such as four-bars, slider-cranks and cam-follower mechanisms, utilizing the assumption of kinematic behavior. Solutions were essentially geometric and were usually performed graphically. The first computer implementations were limited to kinematics. Two early programs were KAM [1] (Kinematic Analysis Method, 1964) and COMMEND [2] (Computer Oriented Mechanical Engineering Design, 1967). Both programs were created by IBM. KAM solved for displacement, velocity, acceleration and reaction force of a limited number class of spatial linkages, notably vehicle suspensions. COMMEND was a planar program particularly intended for computer-aided engineering of IBM's mechanical products.

The original version of DRAM was completed in 1969, at The University of Michigan [3, 4, 5] through the efforts of Professor Milton Chace and Michael

*Mechanical Dynamics, Inc., Ann Arbor, Michigan.

Korybalski. At that time it was named DAMN (Dynamic Analysis of Mechanical Networks). It was historically the first generalized (type-variant) program to provide time response of multifreedom, constrained, mechanical machinery undergoing large-displacement behavior. Major improvements and additions were made to the program by D.A. Smith in his doctoral thesis work over the period of 1968 to 1971 [6]. Since then, DRAM (Dynamic Response of Articulated Machinery) has undergone continuous improvement particularly through the efforts of John C. Angell [7, 8].

The ADAMS (Automated Dynamic Analysis of Mechanical Systems) program was originally completed in 1973 as doctoral thesis work by Nicolae Orlandea [9, 10]. ADAMS was designed as a three-dimensional, large-displacement dynamic program, without however some of the capabilities for impact and surface-to-surface contact possessed by DRAM. ADAMS also utilized a different coordinate scheme than DRAM and involved sparse matrix methods in the equation solutions. Again, major improvements and additions have been made to the original ADAMS code; most of them by J. Angell, R. Rampalli, and T. Wielenga. An important adjunct to ADAMS, ADAMS/MODAL, has recently been completed by V.N. Sohoni and J. Whitesell [11]. ADAMS/MODAL performs automatic linearization of mechanical systems (this of course requires circumstances of small-displacement), then proceeds to determine the system modal characteristics and time dependent response.

In this paper the scope and analytical methods involved in ADAMS are reviewed, followed by a discussion of some aerospace examples. ADAMS and DRAM are intended for direct use by engineers and senior designers. For this reason much effort has been devoted to facilitating ease of use. The programs self-formulate all of the relations described in the following sections of the mechanical system. Computer graphics is utilized to provide output in a flexible, comprehensive form.

ADAMS and DRAM are provided as proprietary software by Mechanical Dynamics, Inc., 3055 Plymouth Road, Ann Arbor, Michigan.

## 2. MODELLING OF MECHANICAL SYSTEMS

ADAMS is a general, fully three-dimensional code. For a given mechanical system, each rigid part is represented by six coordinates. A local part reference frame is attached to each part. The translational displacements of each part are measured as displacements of the local part reference frame origin along the three global coordinate axes. To orient the part in space, three Euler angles are employed.

Interactions between parts in a mechanical system can generally be classified into the following three categories.

1. Kinematic
2. Compliant
3. Elastic

## 2.1 Kinematic Connections

Two parts can be connected by a kinematic connection or joint. These connections are such that they only allow certain types of relative motions between the connected parts. The equations representing the relationships implied by the joint are formulated as non-linear algebraic equations in terms of the coordinates of the two parts connected and the geometry of the joint.

To illustrate the formulation of these algebraic relationships consider parts i and j as shown in Figure 1. These two parts are connected by a spherical joint, for example, at markers[1] $i_k$ and $j_k$ on parts i and j, respectively. The spherical joint constraint requires that these two markers be coincident at all times. Writing the vector equation around the loop 0, $0_i$, $0_j$, 0:

$$\underline{R}_i + \underline{T}_i \ \underline{r}_{i_k} + \underline{p} - \underline{T}_j \ \underline{r}_{j_k} - \underline{R}_j = 0 \qquad (2.1)$$

where

- $\underline{R}$ = Position vector to the origin of the local part reference frame from the global origin, relative to the global frame.
- $\underline{T}$ = Transformation matrix from local part reference frame to global reference frame.
- $\underline{r}$ = Position vector between points in a part relative to the local part reference frame.
- $\underline{p}$ = Vector from marker $j_k$ to marker $i_k$, relative to global reference frame.
- i,j = Part numbers being connected by the joint.
- $i_k$,$j_k$ = Indices of the markers being connected by the joint

Since markers $i_k$ and $j_k$ are always coincident

$$\underline{p} = 0$$

From equation 2.1

$$\underline{R}_i + \underline{T}_i \ \underline{r}_{ik} - \underline{T}_j \ \underline{r}_{jk} - \underline{R}_j = 0 \qquad (2.2)$$

Equation 2.2 is a vector equation, equivalent to three scalar equations. Parts i and j have twelve degrees of freedom. However, the presence of three scalar algebraic constraint equations reduces the degrees of freedom to nine. In a similar manner, using vector equations, the constraint equations for all other possible physical joint types have been derived and are automatically invoked by ADAMS, depending on the mechanism example input.

[1] The term "marker" denotes the combination of a point (indicating translational position) and a triad of unit vectors (indicating orientation).

In general the algebraic equations representing joints can be written as

$$\underline{\phi}(\underline{q}, \underline{\dot{q}}, t) = 0 \tag{2.3}$$

where

$\underline{\phi}$ = Vector of constraint equations
$\underline{q}$ = Vector of n coordinates
$t$ = Time
$\underline{\dot{q}}$ = Vector of Velocities

Because of the generality of this form, user specified constraints can also be included, such as the interaction between variables due to controllers. ADAMS has a large library of kinematic joints. Some of these are:

1. Spherical
2. Rotational
3. Translational
4. Universal
5. Cylindrical
6. Gear

## 2.2 Compliant Elements

The second type of interaction between parts is through compliant elements. These do not reduce degrees of freedom. However, the forces developed in compliant elements are functions of the displacement and velocities of the parts on which these compliant elements act. Consider two parts i and j as shown in Figure 2. These parts are connected by a compliant element C at markers $i_\ell$ and $j_\ell$ in parts i and j, respectively. Force $\underline{f}$ developed in the compliant element acts with equal magnitude but opposite direction on markers $i_\ell$ and $j_\ell$.

The simplest compliant element is a linear spring-damper. The force developed in such an element can be written as

$$\underline{f} = [k(l - l_0) + cv]\underline{p} \tag{2.4}$$

where

$\underline{f}$ = force vector due to compliant element
$k$ = spring constant
$l_0$ = free length of spring
$l$ = distance between points pi and pj
$c$ = damping coefficient
$V$ = velocity of marker $j_\ell$ with respect to marker $i_\ell$ along the line connecting them
$\underline{p}$ = unit vector along the line from marker $i_\ell$ to $j_\ell$

Force f acts at marker $i_\ell$ and an equal and opposite force -f at marker $j_\ell$. The resulting moments on the two parts are

$$\underline{M}_i = \underline{r}_i \times \underline{f} \tag{2.5}$$

and $\underline{M}_j = \underline{r}_j \times -\underline{f}$

where

M = moment acting on respective part
$\underline{r}$ = position vector of marker in local part reference frame
i,j = parts being connected by compliant element

In a similar manner equations for other compliant elements can be developed. Some of the standard compliant elements that are available in ADAMS are:

1. Translational spring-damper element (three directional force)
2. Rotational spring damper element (one torque)
3. Bushing element (three forces and three torques)
4. Action only forces
5. Bistop (impact)

The characteristics of elements can be specified as linear or can be invoked from an extensive library of standard non-linear functions. These functions can be combined using arithmetic operators to conveniently formulate more specialized affects.

In general equations representing compliant elements can be written as

$$\underline{F}(\underline{q}, \dot{\underline{q}}, \underline{f}, t) = 0 \tag{2.6}$$

where

$\underline{f}$ = vector of force in compliant elements
$\underline{F}$ = vector of equations defining the compliant forces

## 2.3 Elastic Elements

Elastic elements are a further generalization of compliant elements. While with the compliant element, force in the element is defined to be along the line defined by markers between which the element is connected, this is not generally required for an elastic element. An example of an elastic element is a beam element. The forces applied on the two parts connected are functions of the beam stiffness and damping matrices and the relative displacement and velocity of the two parts. The standard stiffness and damping matrices are the 6x6 matrices as for a beam element with clamped-clamped

boundary conditions. Non-standard stiffness and damping matrices can be specified. Under this category, multi-dimensional elements such as tires can also be considered. The equations for representing elastic elements are also given by Equation (2.6).

## 2.4 Equations of Motion

In ADAMS the equations of motion for parts in the system are written as second order Lagrange's equations of motion in the constrained form [12].

$$d/dt\{\partial T/\partial \underline{\dot{q}}\} - \partial T/\partial \underline{q} - [\partial \underline{\phi}/\partial \underline{q}]^T \underline{\lambda} = \underline{f} \qquad (2.7)$$

where

$T$ = System kinetic energy
$\underline{\lambda}$ = Vector of Lagrange multipliers corresponding to the equations of constraint
$\underline{f}$ = Vector of conservative and non-conservative "generalized" forces

# 3. ANALYSIS PROCEDURES

Mechanical systems can be modelled in ADAMS using the various entities described in the preceding section. These models can then be analyzed in any one of the following modes:

1. Static
2. Quasi-static
3. Kinematic
4. Transient dynamic
5. Modal

The first three modes of analysis are described only briefly. In the static mode, starting from an initial estimate of position, ADAMS computes the position of static equilbrium. The quasi-static mode allows the system to be stepped through time while computing static equilibrium at output time steps. The system velocities and accelerations are ignored in this analysis. The kinematic mode, works from only the constraint conditions to determine position and orientation of all parts in the mechanical system. The velocity and acceleration of all parts, if requested, can also be computed. Forces in compliant and elastic elements and joint reaction forces can also be obtained.

## 3.1 Transient Non-linear dynamics

In the transient dynamic mode the mechanical system is presumed to be multifreedom and its transient performance is to be determined by numerical integration of the governing system equations (2.3), (2.6), and (2.7). In general the governing equations can be written as a mixed system of second order differential and algebraic equations as:

$$\underline{H}(\ddot{\underline{q}},\dot{\underline{q}},\ \underline{q},\underline{\lambda},\underline{f},t) = 0 \tag{3.1}$$

In order to utilize a standard numerical integrator, the second-order differential equations have to be reduced to the first-order form by introducing velocities as solution variables. In the first order form the governing equation is given as

$$\underline{g}(\dot{\underline{y}},\underline{y},\underline{f},t) = 0 \tag{3.2}$$

where

$$\underline{y} = \begin{bmatrix} \underline{q} \\ \dot{\underline{q}} \\ \underline{\lambda} \end{bmatrix}$$

There are two integrators available in ADAMS at present.

1. Non-Stiff Integrator (Adams-Moulton)
2. Gear's multi-step Stiff Integrator

The non-stiff integrator is only used for systems considered to be "non-stiff" [13]. However, since most mechanical systems are considered to be 'stiff' [13], (i.e. have widely separated eigenvalues) the Gear multi-step stiff integrator is generally applicable.

The Gear stiff integrator formula is a predictor-corrector formula. The prediction for the system state at a point ahead in time is made by an explicit predictor formula not presented here. The corrector for the system is given by the following implicit formula (orders of the dependent variable y (n+1) occur in different terms).

$$\underline{y}^{n+1} = -h\beta_0\dot{\underline{y}}^{n+1} + \sum_{j=1}^{k} (\alpha_j\ \underline{y}^{n-j+1} + h\beta_j\dot{\underline{y}}^{n-j+1}) \tag{3.3}$$

where

h = Integration step size
$\alpha,B$ = Gear integration constants

As can be seen, this formula is of the implicit type. Repeated application of this formula about a fixed point in time can reduce the integration error further. This, however, is not a numerically stable procedure. A numerical stable procedure is to solve the non-linear governing equations by employing the Newton-Raphson interative procedure. This procedure requires the initial corrected state of the system to be computed by substituting predicted values on the right hand side of equation (3.3). Sucessive corrections to state vector can then be made by the following Newton-Raphson equation.

$$\{\partial \underline{g}/\partial \underline{y} + (-1/h\beta_0)\partial \underline{g}/\partial \dot{\underline{y}}\}\ \Delta \underline{y} = -\underline{g} \tag{3.4}$$

In a compact form

$$\underline{J}\Delta \underline{y} = -\underline{g} \tag{3.5}$$

where the Jacobian matrix

$$J = \{\partial \underline{g}/\partial \underline{y} + (-1/h\beta_0)\partial \underline{g}/\partial \dot{\underline{y}}\}$$

$\Delta \underline{y}$ = Correction in $\underline{y}$

The numerical integration procedure starts by computing y from equation (3.3) on the basis of the history of y and $\dot{y}$ over the preceding k time steps. The residual of the governing equations, obtained after evaluation, using predicted values of y is reduced by repeated application of the Newton-Raphson formula of equation (3.4). The iterative procedure is stopped when the convergence criterion is satisfied. An important observation to be made about the Jacobian is, that while the governing equation for the system may consist of a large number of equations, the Jacobian matrix is extremely sparse (less than ten percent non-zero entries). This permits use of sparse matrix algorithms for the rapid repetitive solution of Equation (3.4).

## 3.2 Linearized Analysis of Mechanical Systems

Recent developments in the ADAMS software now allows determination of natural frequency and mode shapes for linear circumstances of systems which are normally non-linear. The governing equations of the mechanical system, equation (3.2), can now be linearized about an operating point

$$\underline{y}^* = (\dot{\underline{y}}_0, \underline{y}_0, \underline{f}_0, t_0) \tag{3.6}$$

to give

$$\delta \underline{g} = \underline{A}\big|_{\underline{y}^*}\delta \underline{y} - \underline{B}\big|_{\underline{y}^*}\delta \dot{\underline{y}} + \partial \underline{g}/\partial f\big|_{\underline{y}^*}\delta f + \partial \underline{g}/\partial t\big|_{\underline{y}^*}\delta t = 0$$

where $\underline{A} = \partial \underline{g}/\partial \underline{y}$ and $\underline{B} = \partial \underline{g}/\partial \dot{\underline{y}}$

If we assume that the mechanical system represented by equation (3.2) is in a state of equilibrium (or other state such that matrices A and B are time invarient) then

$$\partial \underline{g}/\partial t = 0$$

Furthermore since the modal characteristics are independent of system applied forces,

$$\delta \underline{f} = 0 \tag{3.7}$$

In this case we may express

$$\delta \underline{y} = e^{\sigma t}\underline{z} \tag{3.8}$$

Equation (3.8) may be differentiated with respect to time to give

$$\delta\dot{\underline{y}} = \sigma e^{\sigma t}\underline{z} \tag{3.9}$$

The resulting eigenvalue problem is

$$\underline{A}\ \underline{z} = \sigma\underline{B}\ \underline{z} \tag{3.10}$$

To construct the eigenvalue problem of equation (3.10) requires that matrices A and B be constructed. From equation (3.4) it can be seen that these are the very same matrices constructed for the corrector formula of the integration procedure. Therefore, at a given operating point, the Jacobian matrix computed in ADAMS is sufficient information to construct the eigenvalue problem. However, the presence of algebraic equations in the governing equations causes the eigenvalue problem to take on non-standard characteristics. Matrix B is inherently singular due to the absence of any derivatives of Lagrange multipliers in the governing equations. The large eigenvalue problem of equation (3.10) is not well posed.

It is possible to reduce this large ill-conditioned problem to a well-conditioned standard problem. The procedure involves recognizing that the form of the algebraic equations allows us to represent a set of variables as being a linear function of another independent set of variables. This fact can be used to reduce this large eigenvalue problem to one that has a size of 2 x the number of degrees of freedom. That is the smallest size to which a first order problem can be reduced. This procedure is embodied in the ADAMS/MODAL linear analysis software. The details of this procedure are described in reference [11].

## 4. EXAMPLES

Two examples are now described illustrating the application of ADAMS to aerospace mechanical system problems.

### 4.1 Example 1 - Boom Docking

The first example is that of an ADAMS simulation of a boom docking maneuver to couple two satellites. As shown in Figure 3, the target and chaser satellite are maneuvered to within one meter of one another. The target vehicle is equipped with a funnel that has a latching mechanism at its base. The chaser vehicle has a telescoping boom that can be extended or retracted as desired. The object is to extend the boom so that its tip reaches into the base of the funnel on the target satellite. Once this is accomplished the latching mechanism at the base of the funnel is tripped and latches onto the tip of the boom. The chaser satellite then begins to retract the boom, thus pulling the two vehicles together. In the ADAMS model the boom is represented by a number of parts that slide with respect to one another. The entire boom is elastically connected to the chaser satellite.

Figures 3 to Figure 7 show a sequence of snapshots of the docking maneuver. In the first snapshot, Figure 3 the two vehicles are separated by about one meter. The chaser satellite now begins to extend the boom as shown in Figure 4. The tip of the boom makes contact with the funnel, Figure 5, and is guided towards the base of the funnel. Impact and surface geometry of the tip and the funnel is modelled by user supplied subroutines in ADAMS. The next snapshot, Figure 6, shows the tip of the boom extended beyond the base of the funnel. The latching mechanism at the base of the funnel attaches onto the tip of the boom. The chaser satellite now begins to retract the boom, causing the two vehicles to move closer. The final snapshot, Figure 7, shows the two satellites coupled together.

Output can be requested from ADAMS in a tabular or graphical form. The output could consist of displacements, velocities, and accelerations at any point on any of the parts. The forces acting in various elements of the model can be obtained. The forces acting on the tip of the boom when it comes in contact with the funnel can be obtained.

Since all the parameters necessary to perform this simulation were not available, parametric studies had to be performed to obtain acceptable values for certain parameters in order to produce the desired docking maneuver. Initially it was found that the velocity with which the chaser satellite approached the target was too high. This caused the target to spin away when the funnel was impacted by the boom. The parameters related to the latching mechanism at the base of the funnel had to be adjusted to achieve a rapid latching of the boom. Initially the latching mechanism was not quick enough, thus the boom tip that ran into the latching mechanism was retracted by the chaser before the mechanism latched.

## 4.2 Example 2 - Satellite Docking Using Clamp Mechanisms

A second example is a satellite docking maneuver using a clamp mechanism. In this simulation it is assumed that the chaser satellite can be steered to within fifteen centimeters in front of the target. As shown in Figure 8 the chaser has four locking handles. Correspondingly the target vehicle has four claws with spring loaded levers. When the handles come to within seventy millimeters of the base of the claws the locking levers on the claws are triggered to cause the handles to be pulled into the claws.

In the ADAMS model the levers are connected to the claws by means of revolute joints. The clamping action of the lever is caused by a torsional spring of linear characteristics. The claws are themselves mounted on the target by an elastic connection.

Figure 8-12 shows a sequence of snapshots of the two satellites during simulated docking. In the first snapshot, Figure 8, the two vehicles are at some distance from one another and have some angular misalignment. As can be seen all the claws on the target are open. As the two vehicles approach, one of the handles on the chaser vehicle gets close enough to the claw to

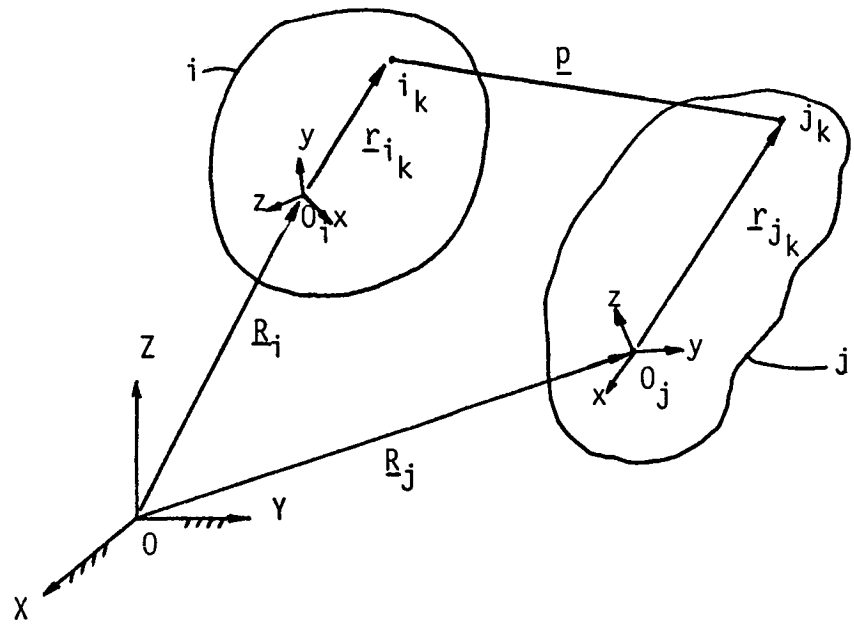


Figure 1. - Two parts connected by kinematic joint.

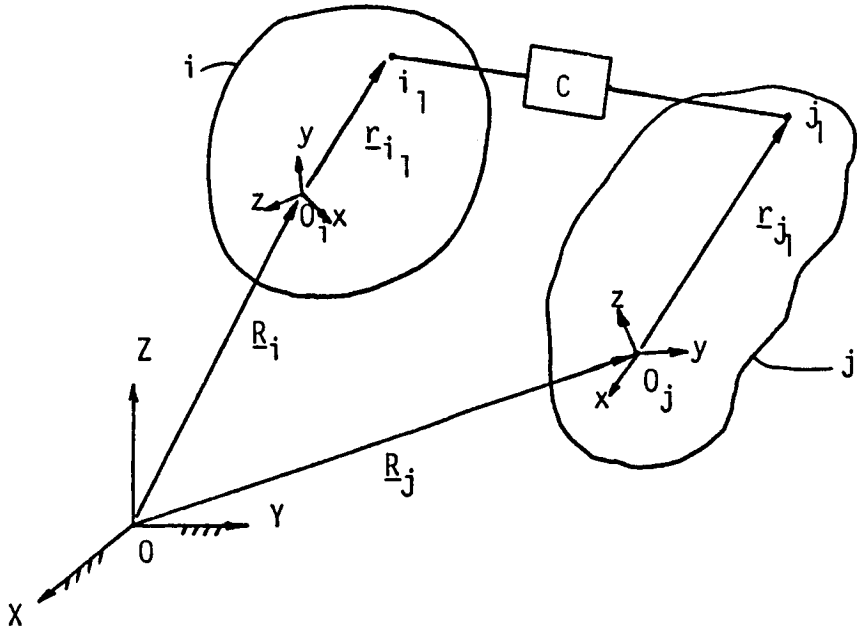


Figure 2. - Two parts connected by compliant element.





159 - 160

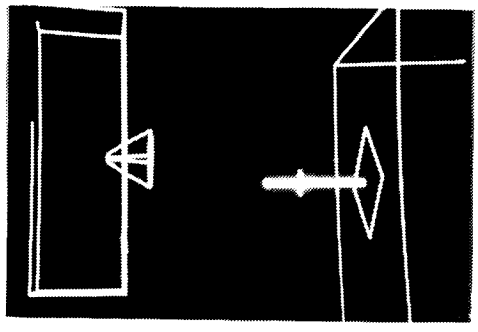

Figure 3

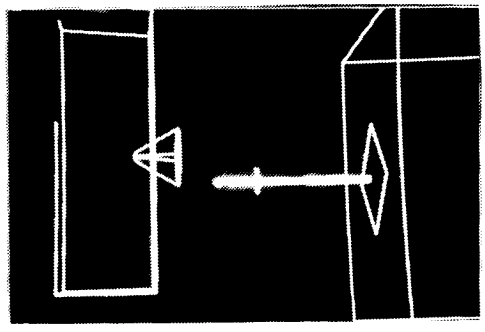

Figure 4

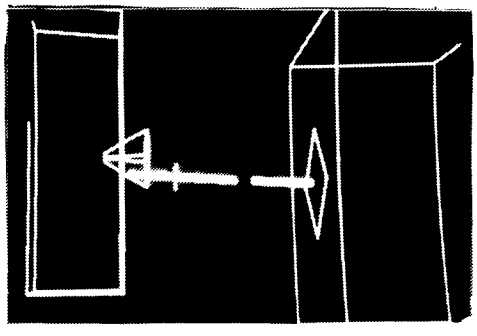

Figure 5

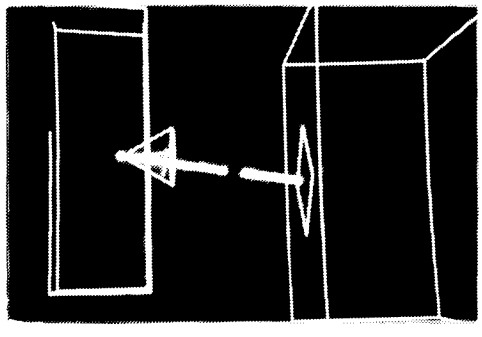

Figure 6

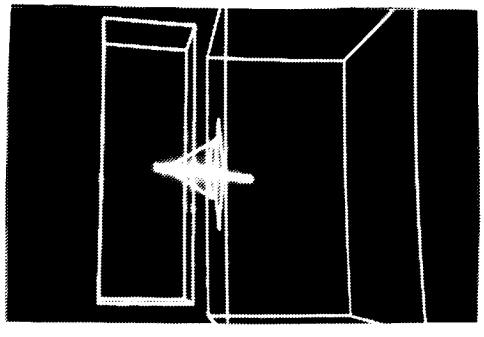

Figure 7

Figures 3 thru 7. - Snapshots of boom docking maneuver.

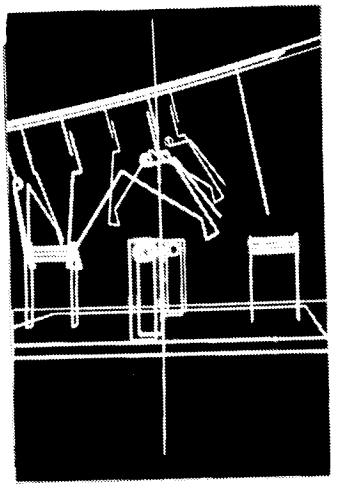

Figure 8

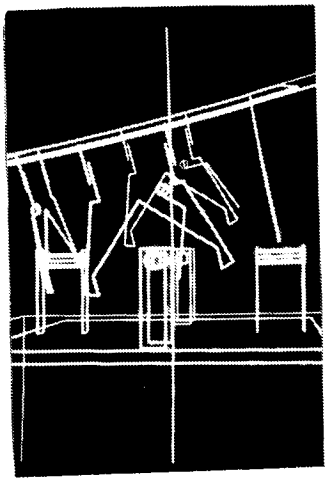

Figure 9

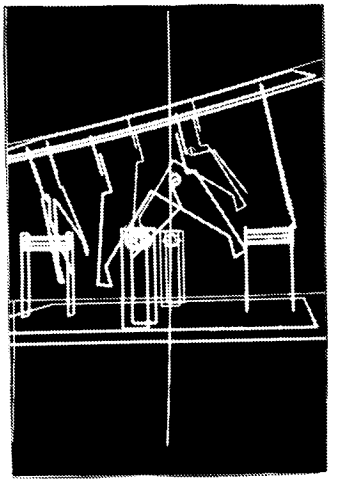

Figure 10

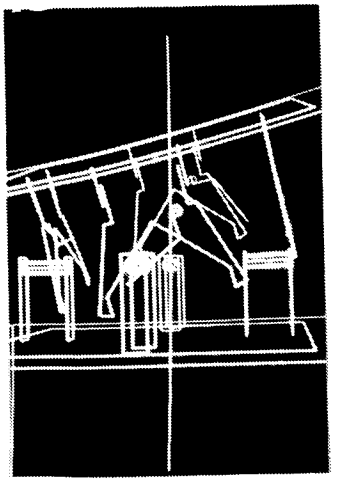

Figure 11

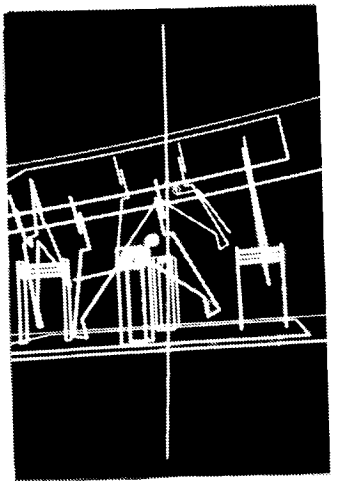

Figure 12

Figures 8 thru 12. - Snapshots of satellite docking with clamp mechanism.

# DUAL WOUND DC BRUSH MOTOR GEARHEAD

Barrie W. Henson*

This paper describes the design requirements, the design, development tests and problems, the qualification and life test and the findings of the strip examination of a dual wound DC brushed motor gearhead. At the time of writing it is the only space qualified dual wound DC brushed motor gearhead in Europe.

## INTRODUCTION

The dual wound DC brushed motor gearhead which is described herein was developed under the auspices of the ESA Space Telescope Solar Array Project. Moore Reed & Co. Ltd., Andover designed and manufactured the motor and OTM Servomechanism Ltd., Staines was responsible for the gearhead.

Brush motors have been a cause for concern with regard to reliability of the brush/commutator interface. However, they do have advantages over stepper and brushless types, in particular simplicity of electronics and lower costs. This unit has also demonstrated that a long life and reliable performance can be obtained.

## REQUIREMENTS

The unit was designed especially to fulfill the requirements and interfaces of a drive unit in the Hubble Space Telescope Solar Array. However, it is suitable for general use on space projects. It was necessary for the unit to be compatible with the existing electronics and, therefore, the motor had to be a direct current "brushed" type. A picture of the unit is shown in Figure 1.

The specification defined by ESA identified the following key aspects :

1. Performance parameters:
   The unit should operate at a nominal Voltage of 28 vdc.
   The design rating should be 1.5 Nm output torque with a shaft speed greater than 30 r.p.m.
   Note: The qualification and life test was performed at a torque of 1.27 Nm (180 oz.in) based on the project requirement.

*European Space Agency, Noordwijk, Holland.

2. Interface requirements:
The mounting interfaces at the front and back should facilitate mounting in a tube with access from one end.

3. Configuration:
To provide electrical redundancy the motor design should comprise a dual wound armature with a commutator at each end.
The motor power should be routed via terminal posts mounted in the rear end cap. Provision should be made to facilitate purging with inert gas if required for the brush material.

4. Special aspects:
The brush material, bearings and lubrication should utilise space qualified materials, parts and techniques.

5. Environment:
The following qualification levels should be demonstrated:
. Vibration : 10g Sine, 19.5 g(rms) Random
. Temperature : Survival + 95°C to - 60°C.
Operational + 80°C to - 45°C.

In addition to the basic performance parameters above, the unit had to be capable of being backdriven to enable astronaut manual over-ride.

## DESIGN

### Motor

The motor is a two pole permanent magnet device in a frame size 18. A fundamental feature of the unit is the dual wound armature with a commutator at each end. This arrangement provides electrical redundancy using a common armature, shaft, housing and magnet system. The configuration is shown in Figure 2.

The principal electrical system is duplicated to provide redundancy in the event of winding or connection failure. The two windings are radially separated and electrically isolated in the armature stack by wrapping the respective windings in Melinex slot liners. The winding layout is shown in Figure 3. The inner winding (redundant) is connected to the front commutator and the outer winding (prime) is connected to the rear commutator.

The armature wire size has been carefully chosen to give the same torque from each winding and the number of turns per winding is identical to ensure the no-load speed is equal. The resulting performance per winding is higher than a normal size 11 motor and the stall torque is approximately double.

Two ceramic magnets are bonded to the stainless steel housing. They are made of barium ferrite which was chosen because it has a good resistance to demagnetisation. This permits the rotor to be removed and replaced without affecting the performance. Although the magnetic characteristics of the material exhibits a knee in the BH curve, it is not possible to demagnetise the motor under normal operations or by reversing the motor whilst running at ambient temperature.

The commutators are made of copper and are comprised of eleven segments set in a moulding. A pair of spring loaded brushes are located in a holder adjacent to each commutator. The wires from the front brush assembly pass through a tube located in the gap between the magnets and exit through the rear end cap where terminal posts are provided for external connections.

The brush material is Boeing compound 046-45. The material is supplied in a compact form and comprises mainly molybdenum disulphide. It has a low rate of wear in vacuum but has the disadvantage that it requires purging when used in air. Because it has a high $MoS_2$ content the commutator film has a relatively high and variable resistance which influences the performance characteristics at low voltages and loads. In normal operation these effects disappear. For this reason the motor run-in tests are made at 28 Volts and a torque of 100 gcm. The motor shaft is supported on Bartemp dry lubricated bearings. Lubrication is achieved by transfer from a sacrificial cage made of a PTFE/$MoS_2$/glass fibre composite.

## Gearhead

The gearhead is manufactured entirely from stainless steel. It has a conventional spur gear and layshaft configuration and has a ratio of 160:1. There are five layshafts and each one is mounted on miniature ball bearings. This arrangement results in a high overall efficiency ($\sim$90%) and permits the unit to be backdriven. A cross-section of the gearhead is shown in Figure 2. The bearings used are mainly the caged type with shields, but in two cases different bearings had to be used to accommodate the loads and envelope constraints. All bearings are lubricated with Braycote 601 grease.

All the gears and layshafts are hardened by a diffusion process known as "Tufftriding". This is a proprietary type of nitriding process and is used to improve the wear characteristics. It also improves the fatigue life.

## Motor Gearhead Assembly and Mounting Arrangements

The motor-gearhead interface comprises a spigot location with a screw fixation and the motor shaft pinion meshes directly with the first layshaft gear in the gearhead. Locking of the interface is achieved by four small spots of adhesive.

Performance of the unit with one winding powered at 28 Volts is shown below and is illustrated in Figure 4.

| | |
|---|---|
| No load speed (r.p.m.) | : 38 - 43 |
| No load current (mA) | : 50 - 100 |
| Speed at 1.5 Nm (r.p.m.) | : 30 - 34 |
| Current at 1.5 Nm (mA) | : 300 - 420 |

The performance with both windings powered is very similar to Figure 4 but the speed at rated torque is slightly higher and of course the total current is shared between the two windings. The torque required to backdrive the unit is less than 0.7 Nm (100 oz.in.).

The purpose of the two windings is to provide redundancy rather than to increase the torque capability. The gearhead is designed for the rated torque of 1.5 Nm and has a factor of safety of 2 based on static loads. The motor gearhead should not be operated above the rated torque.

In the specific application for which it was designed the motor gearhead is mounted inside a tube. This is achieved by using a special collar at the front end and a Delrin spider at the rear end as shown in Figure 5. Various alternative methods of mounting may be considered but they should always provide support at the front and rear.

## DEVELOPMENT PROGRAMME

### Choice of Lubricant

Previous experience indicated that Braycote 601 grease (formerly 3L38RP) was the preferred lubricant for the gearbox bearings. However, for the gears, it was decided to make a comparison test with Braycote Y Vac 3 grease, because of its reported good behaviour in an industrial application.

Two identical gearheads, size 18 with a 100:1 ratio, fitted to a size 11 motor were evaluated at ambient temperature and in vacuum over a temperature range of + 85°C to - 45°C with a torque load of 0.7 Nm (100 oz.in).

The main difference in the performance of the two gearheads was at low temperature (-45°C) when the gearhead containing Y Vac 3 grease required a significantly higher motor current than the one with 601 grease for the same output torque. This was attributed to the increased viscosity of the base oil (Fomblin Y 140) in the Y Vac 3 which has a pour point of - 25°C and therefore was semi-solid in this test. Thus considering the required environmental range Braycote 601 was chosen because its low pour point ensured consistent performance even at - 45°C.

## Choice of Brush Material

Many types of material have been considered by engineers for use in DC brushed motors. The ideal solution has still to be found as most materials have some disadvantage when operation in both air and vacuum is required. Normally the most critical problems occur in vacuum (often at low temperature) when high wear rates are observed.

The motor used in the gearhead lubrication tests was fitted with brushes made from a material designated Sperry 318 E. The motor gearhead performed very well but after 95 hours (33 hours in vacuum) the motor stopped. Investigation revealed that the brushes were completely worn out, a length of some 6 mm being consumed. Consequently the commutator area was full of powder. This result persuaded us to return to a known material, namely Boeing compound 046-45, because previous experience indicated that it had good wear resistance.

## Bearing Failures

The first 160:1 gearhead tested was coupled to a size 11 motor. The unit was subject to thermal vacuum testing and a life test. After 39 hours operation a gearhead failure was observed. Investigation revealed that a bearing on the third layshaft had collapsed although the rest of the gearhead was in good condition. This was an unexpected failure mode and from a brief examination it was considered to be a random failure.

The second 160:1 gearhead was coupled to a dual wound size 18 motor. The unit was subject to sine and random vibration at qualification levels. Subsequent derivation of Q factors due to fixture design and mounting resonances indicated that the unit was subject to random levels of the order of 100 g(rms). To improve this situation for future vibration tests a new fixture was designed. The unit was then subject to thermal vacuum testing and life testing. A total of 82 hours running time had been accomplished when the unit failed. Investigation revealed that the identical bearing on the third layshaft had collapsed. The gearhead was generally in good condition, but the appearance of the grease had deteriorated and some evidence of debris existed. This failure eliminated the "random" bearing failure theory previously supposed.

A detail design assessment of the gearhead was initiated. This resulted in the following conclusions:

- drawing dimensions allowed axial pre-load to occur under worse case tolerance conditions.
- dimensions of the third shaft resulted in the bearing being under an axial pre-load and induced a small angular misalignment of the bearing.
- the failed bearing had higher loads than all other identical bearings in the gearhead and these were not conducive to a long life.

Resolution of these difficulties was achieved by implementing the following design changes: -

- Revision of axial dimensions to ensure clearance existed under all tolerances.
- Inclusion of a double bearing in the failed location on the third shaft.
- Application of the Tufftride process to the gears and shaft. This change was made to reduce wear debris which could promote breakdown of the grease and become a source of contamination in the bearings.

To ensure that these changes had eliminated causes of the bearing failure a modified gearhead was subject to a 200 hour life test. This test was completely successful.

Shaft Failure

The gearhead which had accomplished 200 hours operation was still running smoothly and it was decided to continue the test to obtain more confidence. At 240 hours a catastrophic failure occurred. The third layshaft fractured at a change in the cross-section from a gear face to the bearing spigot. This formed an almost square corner, less than 0.125 mm (0.005") radius to facilitate seating of the bearing.

A thorough metallurgical examination revealed that during final machining the Tufftride layer had been ground away on the bearing spigot. Thus at a critical change of section with a sharp radius attracting a stress concentration factor of about 4 the material properties also changed. The section and surface structure are shown in the scanning electron microscope picture, Figure 6, and the fracture line is shown in Figure 7.

The running time equated to approximately 3 million revolutions of the shaft, i.e. some 6 million stress reversals. Analysis of the load/fatigue curve indicated that the 'expected' life had been reached. Whilst the running time was some 5 times more than required for the intended application, it was considered essential to initiate design and process changes to improve the product in view of the wide variations associated with fatigue failures. The changes required were quite straightforward, viz.:

1) increase the blend radius from 0.125 mm (0.005") to 0.250 mm (0.010"), and thus reduce the stress concentration factor from 4 to 1.5.
2) finish grinding the bearing spigot prior to applying the Tufftride process because the growth in size due to the Tufftride process is insignificant.

These changes were consequently incorporated in the Qualification and Life Test model for formal testing.

## QUALIFICATION AND LIFE TESTS

The planned test programme comprised:

- performance tests at motor level.
- performance tests at motor gearhead level.
- vibration tests.
- performance tests at ambient and in thermal vacuum.
- a 100 hour life test at ambient and in thermal vacuum.

The life tests were extended to 250 hours because performance remained satisfactory and time permitted.

The performance tests at motor and motor gearhead level confirmed that the unit complied with its specification.

### Vibration

The motor gearhead was mounted using the collar and spider shown in Figure 5.
The qualification level vibration test comprised:

a. Sinusoidal

| | |
|---|---|
| 5 - 20 Hz | : 20 mm peak to peak |
| 20 - 100 Hz | : 16.3 g. |
| Duration | : 1 sweep per axis at 2 octaves/min. |

b. Random

| | |
|---|---|
| Level | : 19.5 g(rms) |
| Spectrum | : See Figure 8 |
| Duration | : 3 minutes per axis |

During these tests the actual level on the motor was also monitored. It was noted that a substantial degree of cross-coupling occurred even with the new fixture. Q factors up to 3 resulted in levels up to 60 g(rms) on the motor. Post vibration function tests confirmed that the unit was still in good working order.

### Thermal Vacuum

The thermal vacuum and life tests were performed at the European Space Tribology Laboratory, Risley U.K.

The motor gearhead was subject to function tests at a torque of 1.27 Nm (180 oz.in) at ambient temperature with a nitrogen purge and in vacuum over a temperature range of + 80°C to - 45°C. The unit was also subject to temperature survival tests at + 95°C and - 60°C. Performance was nominal throughout the tests and all motor configurations were demonstrated.

Life Tests

The planned life test comprised of operations on each winding at a torque of 1.27 Nm (180 oz.in) at ambient and in vacuum over a temperature range of + 50°C to - 30°C. During the initial phase of the ambient life test the winding 1 current trace became noisy and the shaft speed reduced. After some brief checks of no-load speed, start voltage and breakaway torque measurements, the performance reverted to nominal. It was concluded that the temporary anomalous performance was caused by a brush fragment. The motor gearhead continued to function well for the planned duration of 100 hours, 50% of which were in vacuum.

Extended Life Test

Due to the satisfactory performance obtained, the life test was extended until a total running time of over 250 hours had been accomplished. Fifty percent of this testing was in vacuum and the motor gearhead was still giving a nominal performance.

## STRIP EXAMINATION AND ANALYSIS

The motor gearhead was progressively stripped and subject to a full examination. The main observations were:

- the motor condition and general appearance was good.
- the gearhead condition and general appearance was clean and good with adequate grease coverage.
- the brushes were in good condition but had worn slightly unevenly, at least 50% of their length remaining.
- the commutators were showing slight wear as expected.
- some brush debris was evident in various places, obviously having been blown around by the gaseous purge used when operated in air.
- insulation resistance had reduced to values of 10 KΩ and 80 KΩ . It is believed this was due to tracking across debris paths possibly formed by centrifugal deposition of $MoS_2$.
- all gears were in good condition and there was no evidence of wear.

## SUMMARY

The motor gearhead has performed extremely well and completed a life test far in excess of that originally planned. The development problems encountered were very instructive and indicate the care and detail consideration that needs to be taken in the construction of reliable motor gearheads.

ACKNOWLEDGEMENT

The author wishes to thank the following personnel for their contributions towards this successful project.

Mr. R. Smith, Mr. A. Flew - Moore Reed and Company Ltd.
Mr. A. Yardley - OTM Servomechanism Ltd.
Mr. J. Anderson - European Space Tribology Laboratory, (ESTL), Risley, U.K.
My colleagues at the European Space Agency, Noordwijk

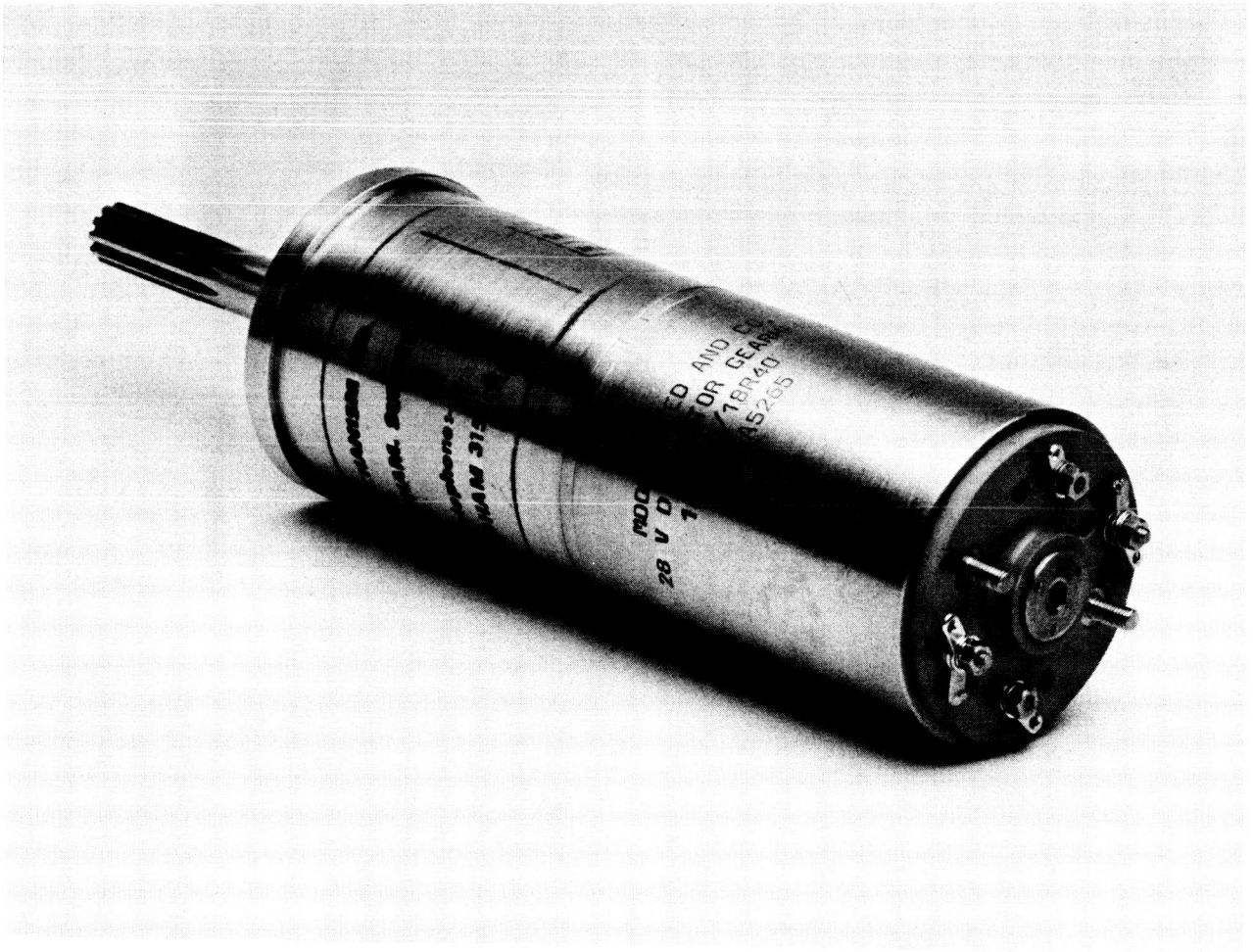

Figure 1. - Dual wound motor gearhead.

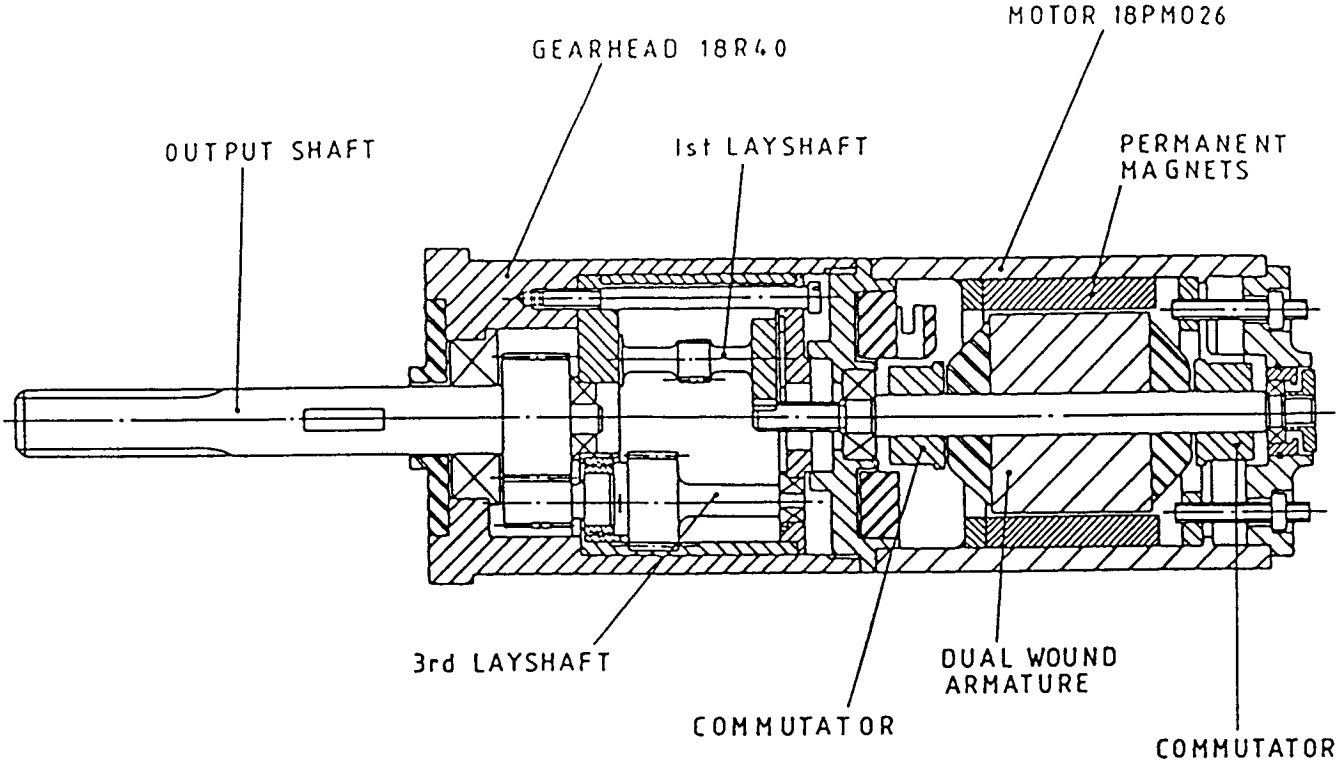


Figure 2. - Section view of dual wound motor gearhead. Note second layshaft omitted for clarity.

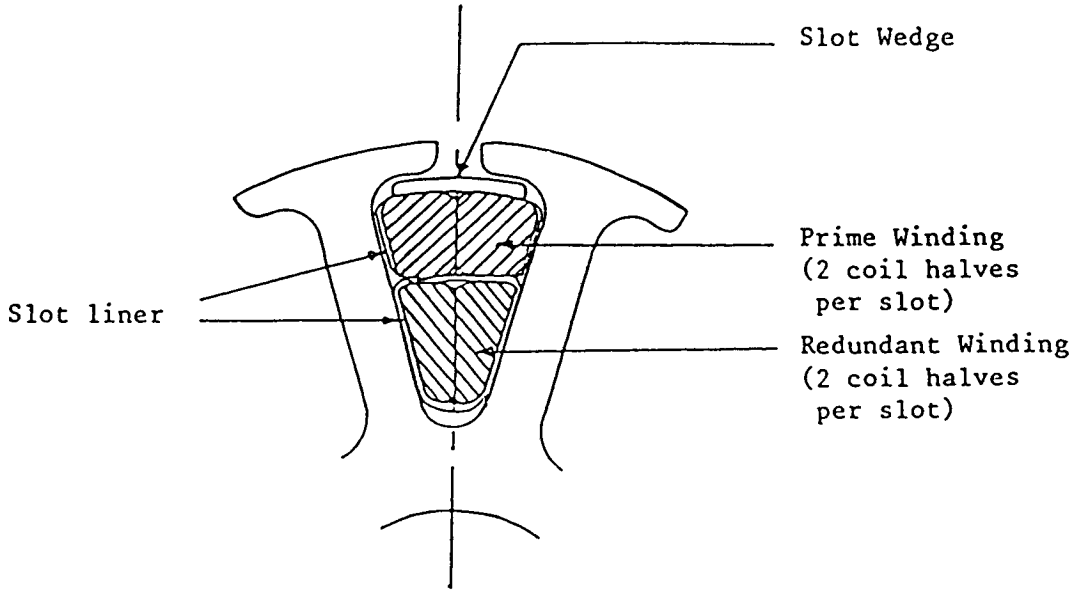


Figure 3. - Winding layout.

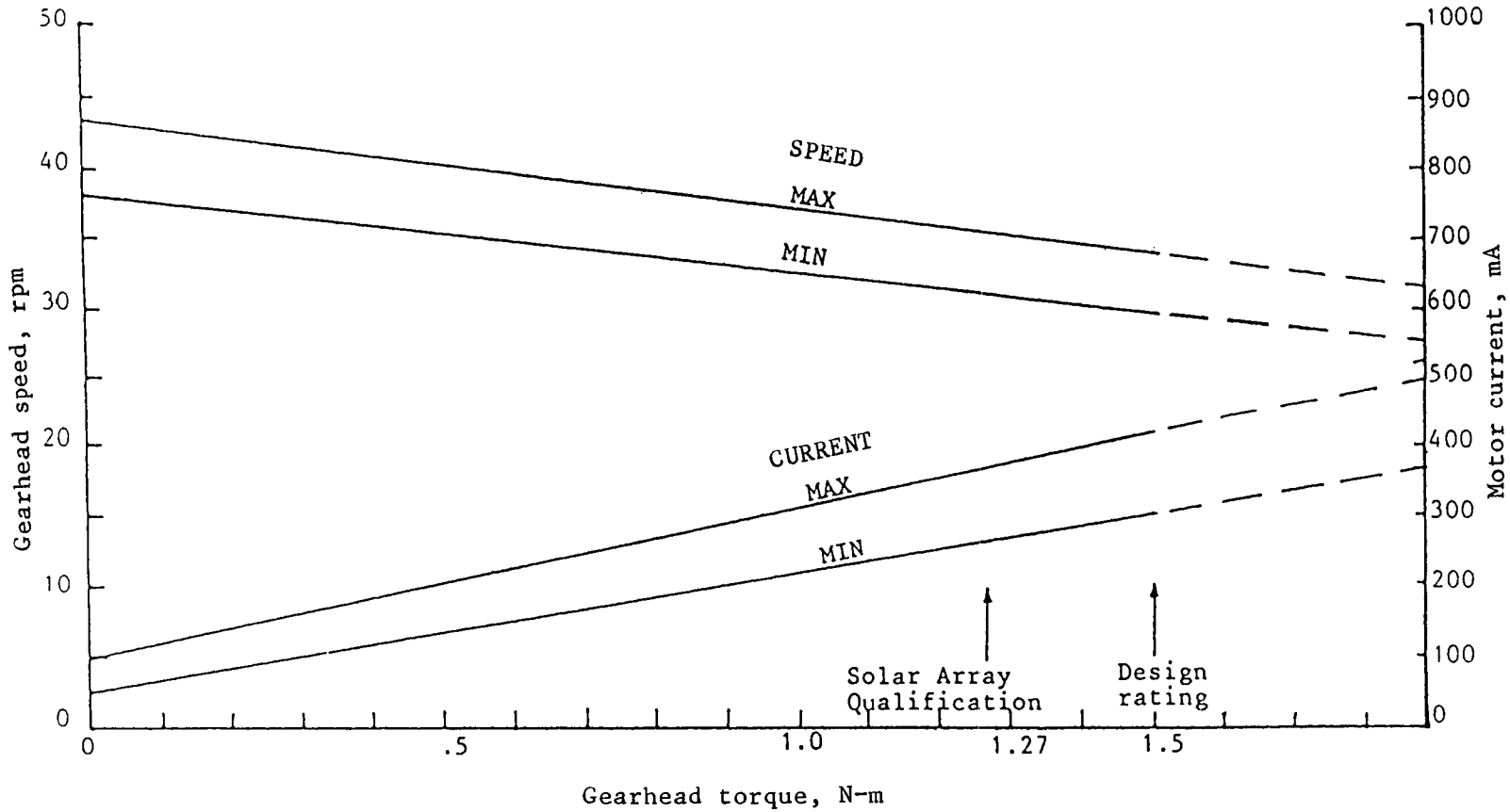


Figure 4. - Gearhead torque as function of gearhead speed and motor current. One winding powered at 28 volts.

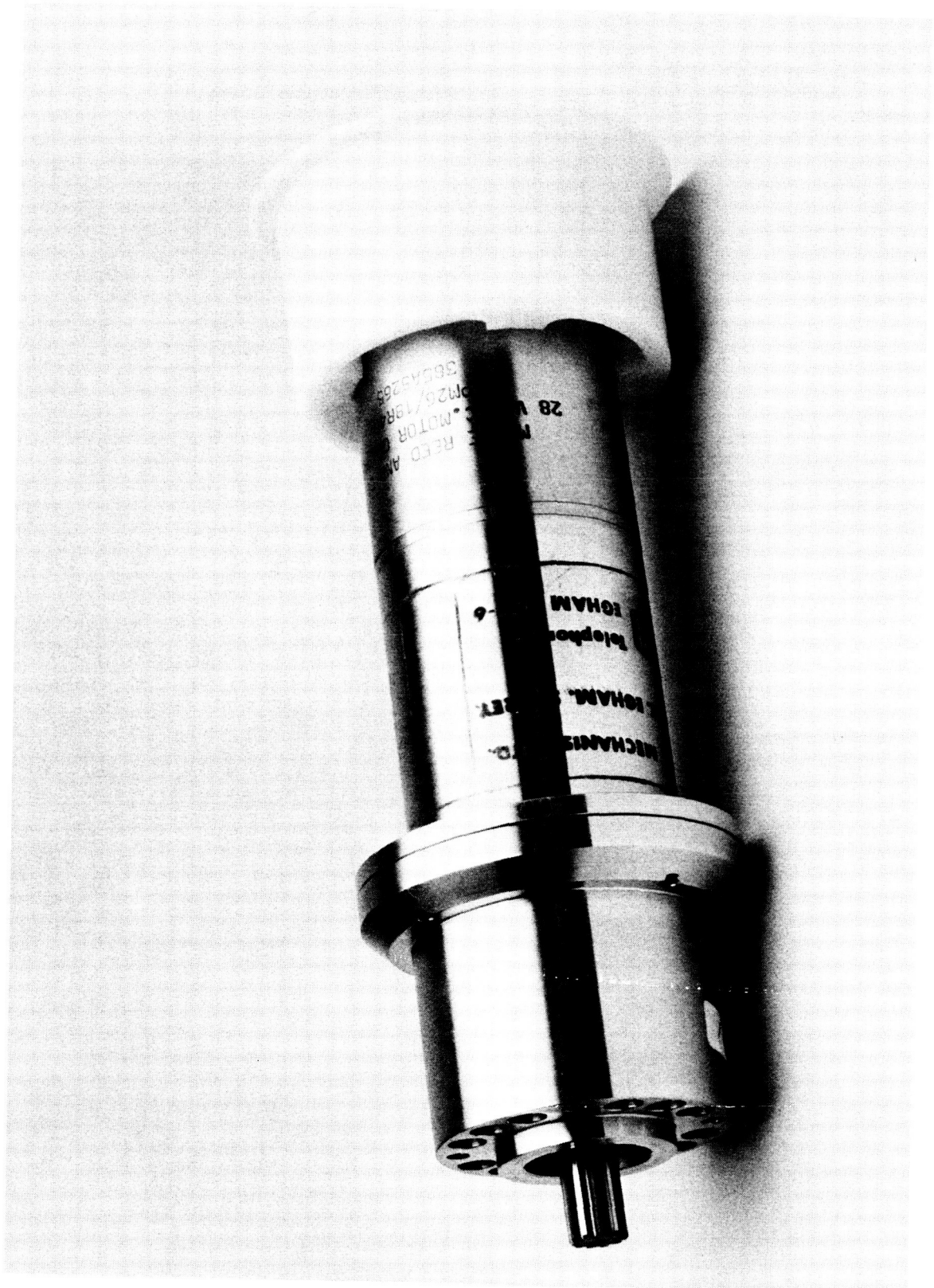

Figure 5. - Dual wound motor gearhead mounting arrangement.

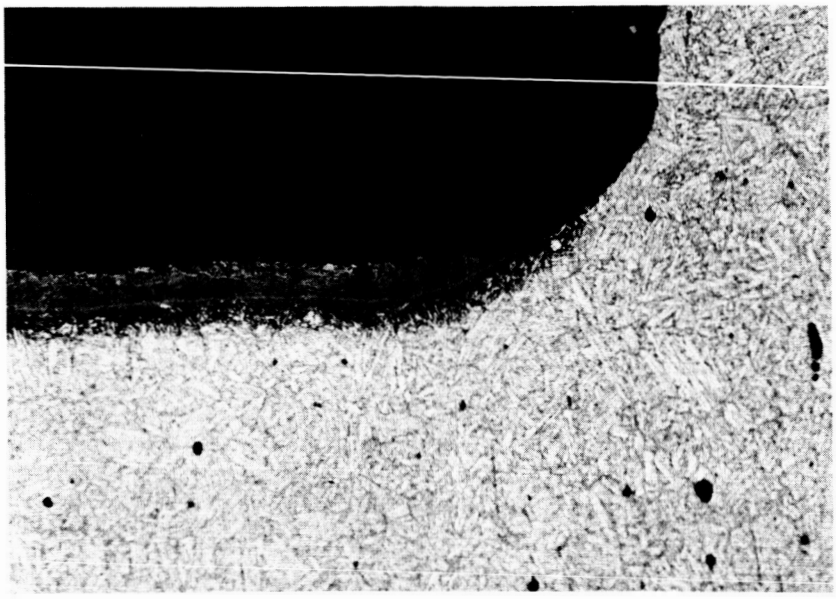

Figure 6. - Cross section of gearhead shaft.

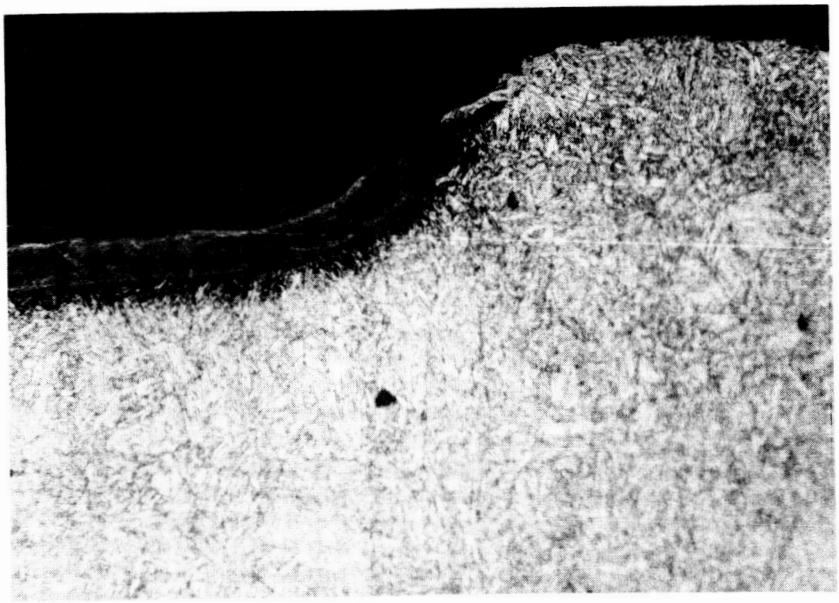

Figure 7. - Cross section of fracture line.

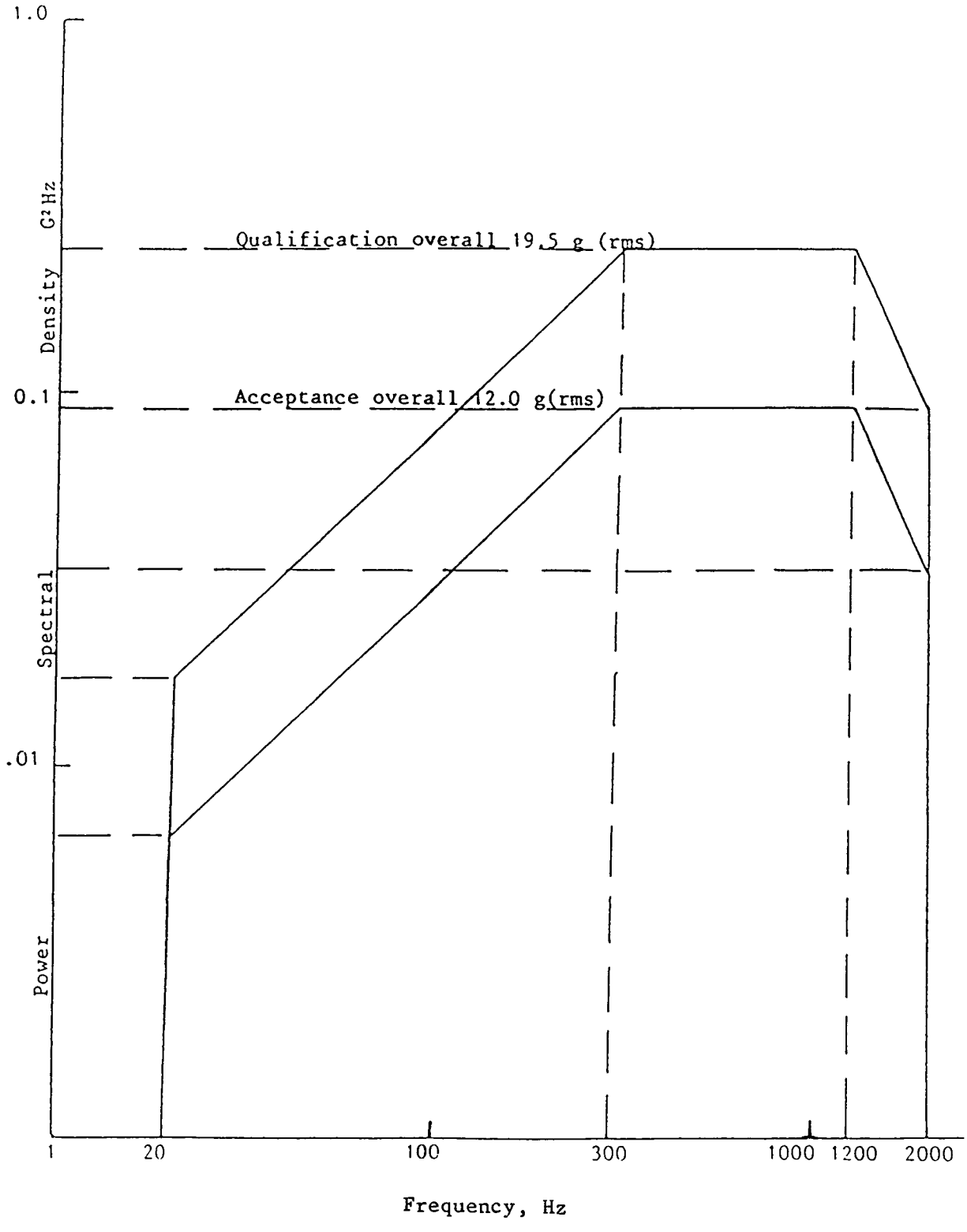


Figure 8. - Random vibration test requirements.



C-3

# REDUNDANCY FOR ELECTRIC MOTORS IN SPACECRAFT APPLICATIONS

Robert J. Smith and Alastair R. Flew*

This paper identifies the parts of electric motors which should be duplicated in order to provide maximum reliability in spacecraft applications. The paper describes various common types of redundancy and gives the advantages and disadvantages of each. The principal types are illustrated by reference to specific examples. For each example, constructional details, basic performance data and failure modes are described, together with a discussion of the suitability of particular redundancy techniques to motor types.

## INTRODUCTION

The question of redundancy in electric motors for space applications is fascinating if nothing else because of the large number of ways in which redundancy can be achieved. This paper will describe some of these techniques, all the data being from real applications.

It will be noted that the redundancy techniques described are not restricted solely to one type of electric motor. To illustrate this point examples are given of both Stepping motor and D.C. motor applications using the same redundancy technique. The redundancy techniques described have been used in many different applications including solar array drive mechanisms, deployment mechanisms, antenna pointing mechanisms and motorised hinges.

There is of course no universally accepted or right approach to the question of redundancy in electric motors. The decision on which technique should be used is usually a compromise between reliability, criticality of application, mass, cost, physical size, performance and many other factors, not least of which is the personal preference of the mechanism designer.

Despite, however, these apparent problems we have attempted to draw comparisons between the various methods available and these appear in the form of selection charts shown in Tables 1 and 2. We hope this will be useful for future reference and we certainly expect it to generate further discussion on what we find to be an interesting aspect of electric motor design for space application.

*Moore Reed and Company Limited, Andover, England.

## TYPES OF REDUNDANCY

There are basically five different types of redundancy which are applicable to electric motors. These range from total system duplication to zero redundancy and are discussed in detail below.

For clarity, that part of the system which is normally energised under no-fault conditions is referred to as the Prime system and the back-up system (normally unpowered) is referred to as the Redundant system. In the event of a failure in the Prime system, it is necessary to:

a) de-energise the Prime system

b) energise the Redundant system.

Because any such failure represents a major event in the life of a motor system, the changeover from Prime to Redundant system is not normally automatic but is instead initiated by ground commands. In this way due consideration may be given to the mode of operation which caused the Prime system to fail and a decision made as to whether continuing operation in this mode could lead to a similar failure of the Redundant system.

### Type 1 Redundancy - Two motors geared to a common shaft

Under this arrangement, a pair of similar, non-redundant motors are coupled to the driven shaft, often by means of reduction gears. One motor is normally energised and the other (the Redundant motor) is de-energised and normally back-driven by the Prime motor.

It is therefore important that either motor operating alone is capable of driving the load and back-driving the Redundant motor. Effects such as the bearing friction and magnetic detent torque of the Redundant motor will be magnified by the gear ratio, whilst rotor inertia will be reflected as the square of the gear ratio.

Under fault conditions, if the failure mode is open-circuit, operations may continue using the Redundant motor with no decrease in overall system performance. If, however, the failure mode is a short-circuit, the retarding torque of the failed motor will increase - possibly substantially - depending on the type of motor and the severity of the fault.

In order to overcome these problems both motors must be larger and more powerful than if a non-redundant system were used. The gear mechanism must be strong enough to withstand operation in the presence of maximum retarding torque due to a failed motor.

If high positional accuracy of the driven shaft is required, backlash in the reduction gearing may cause difficulties when changing from Prime to Redundant motors.

Type 2 Redundancy - Two motors and differential gearbox

Using this system, the speed of the output shaft of the gearbox is proportional to the difference in speed of the two input shafts. Drive can thus be transmitted from either motor whilst the other remains stationary. The differential unit has internal losses which represent a retarding torque and the motors must each be capable of overcoming this in addition to the load torque. As it is not necessary to be able to back-drive a failed motor, the motors need not be as large and powerful as if Type 1 redundancy were employed.

Type 2 redundancy therefore gives good protection against both open-circuit and short-circuit failure modes. Its principal disadvantage lies in the mass and complexity of the differential unit, which is in itself a non-redundant element.

Type 3 Redundancy - Tandem motor

Under this type of redundancy, two motors are effectively combined into one unit, that is, two stator assemblies in a common housing, and two corresponding rotor assemblies on a common shaft. Fig.1 shows this type of redundancy applied to a frameless Stepping motor. The Prime and Redundant parts of the motor are electrically and mechanically isolated, but the additional detent torque of the Redundant system acts to reduce the overall output torque of the Prime system. As with Type 1 redundancy, full protection is given against open-circuit failures, but any form of short-circuit failure results in increased retarding torque of the affected system. However, with Prime and Redundant elements mounted on a common shaft, there is no magnification factor and any retarding torque is transmitted on a 1:1 basis.

Each half of a tandem motor can, therefore, be smaller than an equivalent non-redundant motor under Type 1 redundancy. Mass will also be less than for two separate motors as only one set of bearings and end frames is required.

One obvious disadvantage of the tandem motor is its extra length and this type of redundancy should not be considered unless the basic rotor and stator elements are themselves short and compact. For instance, cylindrical-armature D.C. motors do not lend themselves to the tandem-motor configuration, whereas "pancake" style motors are well suited. Even so, it may prove necessary to provide an auxiliary rear support to the motor if it is required to survive in a severe vibration environment. On machines with small radial air-gaps (e.g. Stepping motors) it is also necessary to ensure that the shaft is sufficiently rigid and well supported to avoid rotor-stator contact.

Type 4 Redundancy - Dual-wound Motor

Only the windings, electrical connections and leadwires are duplicated with Dual-wound redundancy. All the other parts remain as for a non-redundant motor. However, since it is invariably the windings and/or lead connections where the probability of failure is highest, this type of redundancy is entirely acceptable and valid. The Prime and Redundant windings are normally separated from each other by Mylar or Melinex insulators. Fig. 3 shows the technique applied to a housed Stepping Motor. Because only half the normal slot area is available for each winding, the performance of a dual-wound motor is inevitably less than for a comparable non-redundant motor operating under similar conditions. Detent torque and mass are approximately the same as for a non-redundant motor.

On certain types of motor it is difficult to achieve complete physical separation between Prime and Redundant windings. This is particularly true of brush D.C. motors where there are a large number of coil end-to-commutator connections which tend to overlap or cross one another. Also, because the Prime and Redundant windings are in closer proximity than with other types of redundancy, there is a possibility of thermal interaction between the two windings.

With the Prime and Redundant windings sharing a common magnetic circuit, a degree of transformer action occurs when alternating current flows in one winding. With a short-circuit fault on one winding, the machine behaves like a transformer on load and the input current rises to supply the secondary current. This current, flowing in the failed winding, also creates a retarding torque, so the overall output torque of the motor is degraded. For obvious reasons, the effect is only apparent in Stepping motors operating at high stepping rates; at low step rates, or when using D.C. motors, the effect is negligible.

Like the other types of redundancy so far discussed, dual-winding gives complete protection against open-circuit failure modes.

Type 5 Redundancy - No duplication

Although not strictly a redundancy method, zero duplication must at least be considered as an option. From the foregoing, it might be inferred that wound electrical components have inherently poor reliability. However, this is not the case and the main reason for providing redundancy is that electrical actuators are often used in highly critical applications where a failure, however remote the possibility, could have a catastrophic impact on the success of the mission. This is particularly true of mechanisms designed for continuous operation of up to 10 years duration on geo-synchronous spacecraft. However, there are many applications (such as pay-load experiments) where non-redundant motors are completely acceptable. Motors can be designed so that known failure modes are reduced or eliminated.

For instance, the use of ultra-fine winding conductors can generally be avoided, as can the common practice of pressing a winding to form it into a more compact shape. Performing solder joints to space-approved standard and minutely examining joints (before and after insulation) for compliance with these standards, are further examples of how the quality of manufactured items is maintained. During testing, exposure of all Flight units to acceptance-level vibration and subsequent electrical testing, further ensures that the motors are as free as possible from any design or manufacturing defect.

So, by applying an appropriate level of product assurance, the reliability of even a non-redundant motor can be significantly improved over that of a commercial-standard motor.

## FAILURE MODES

Potential failure modes applicable to most types of electric motor are:

- Bearing Failure
- Air gap contamination
- Demagnetisation
- Open-Circuits
- Short-Circuits
- Insulation breakdown to chassis.

In addition, there are generally other failure modes specific to the particular motor under consideration. These invariably relate to the mechanical configuration of the motor and must be considered on an individual basis. The above principal failure modes are now discussed under separate headings.

### Bearing Failure

The various failure modes of ball bearings are well documented and are not within the scope of this paper. However, ball bearings are invariably non-redundant components and any increase in bearing friction will reduce the overall torque capability of the motor. Only Type 2 redundancy gives protection against motor failures of this nature.

### Air gap contamination

For obvious reasons, motors having small air gaps (such as Stepping motors) are more susceptible to air gap contamination than other types. Fortunately, by adopting stringent cleaning procedures at component level and performing final assembly operations under clean room conditions, contamination from sources within the motor can be made to be an extremely unlikely event.

Because most motors used in spacecraft applications employ permanent magnets in either the stator or the rotor, any ferrous debris which does occur inside the motor (or which is subsequently introduced into the motor) will tend to be attracted into the air gap region. There is thus an obvious possibility of increased frictional torque or even rotor jamming. As with bearing failure, only Type 2 redundancy gives protection against this type of motor failure.

Demagnetisation

The performance of most Permanent Magnet materials is subject to both reversible and irreversible changes. Reversible changes normally occur as a result of high or low temperature operation, with the highest flux density occurring at low temperatures and vice versa. Normal magnet performance is restored on return to room temperature. This normally affects both Prime and Redundant systems equally and should be considered as a motor characteristic rather than a failure mode as such.

Irreversible demagnetisation is a more severe effect because it can only be restored by remagnetisation. It can happen if a motor is overdriven by, for example, operating on too high a supply voltage, or by instantaneously reversing the polarity of the supply to a D.C. motor. Certain magnetic materials (e.g. ferrites) are more susceptible to irreversible demagnetisation at low temperatures.

The effect of irreversible demagnetisation on a motor is to reduce its output torque for a given supply current and (in the case of a D.C. motor) to increase the gradient of the speed versus torque characteristic. This type of failure can be accommodated by switching to the Redundant system where Redundancy Types 1, 2 or 3 are used. Type 4 redundancy (dual-winding) does not give protection against this failure mode because both Prime and Redundant windings share a common magnetic circuit.

Provided the specified power supplies are not exceeded, a correctly designed motor should be capable of operating at all points within its specified temperature range, under any load conditions, without irreversible demagnetisation.

Open Circuits

Open-circuits can be induced by vibration or by adverse thermal conditions, or by a combination of both. Under hard vacuum conditions, it is often difficult to provide adequate paths for thermal power dissipation, particularly when the power is supplied to the rotating component such as a D.C. motor armature. Localised temperature rises can, therefore, be quite significant. If the motor is also required to operate under high ambient temperature conditions, there is a possibility of solder joint failure if

temperatures exceed about 180°C. The integrity of the various insulation systems cannot normally be assured above this temperature. Motor operational constraints are often introduced for this reason and it is important that these are observed. The effect of an open-circuit is mis-stepping in the case of a Stepping motor, and reduced torque and speed in the case of a D.C. motor.

There are two types of open-circuit failure specific to brush D.C. motors. One is brush failure: a brush which fails to make contact with a commutator, or a broken brush connector, can result in total motor failure. The second type of failure is a broken conductor-to-commutator joint. This failure, whilst not so severe, can cause a significant decrease in performance.

There is also a range of drive, wiring, and connector faults which, occurring externally to the motor, can give the same effect as an open-circuit within the motor.

All the open-circuit failure modes above can be overcome without penalty by switching to the Redundant part of the system, irrespective of the type of redundancy used.

Short-circuits

The worst case short-circuit is a terminal-to-terminal short which in most cases can only occur due to a fault external to the motor. Most internal short-circuits originate in the same way as for open-circuits. It is possible for two open-circuits to combine to form a short-circuit. The short-circuit failure is always more severe than an open-circuit in that motor performance, even when operating on the Redundant winding, is less than when operating under no-fault conditions on the Prime winding. Only Type 2 redundancy offers the possibility of full protection against this sort of failure.

Insulation breakdown to chassis

This can be thermally or vibration induced, as for open-circuits or, in machines fitted with brushes, insulation breakdown can occur as a result of brush debris accumulation. Motors are normally manufactured so that all electrically active components are fully isolated from the structural parts of the machine. Because of this, a single insulation breakdown is unlikely to have any noticeable effect on motor performance, unless it affects the operation of the drive circuits. Two insulation breakdowns in the same winding will, however, produce a short-circuit. If the electronic drive components are configured such that even a single insulation breakdown can cause fault current to flow in the winding, then this will also produce a short-circuit.

## RECENT EXAMPLES OF MOTORS HAVING REDUNDANCY

### Tandem Stepping Motor

The motor to be described is a frameless, size 23, 2 phase, $1.8^{o}$ step motor designed for operation on bipolar drives in full step or ministep mode. The motor was designed for continuous running in a Solar Array Drive Mechanism. Basic constructional details are shown in Fig. 1 from which it can be seen that the unit comprises identical Prime and Redundant motors.

On the Stator, each motor consists of a stack of corrosion resistant iron laminations carrying copper conductors in insulated slots. The Prime and Redundant windings are separated from each other at the closest point by means of a PTFE insulation ring. On the Rotor, each motor consists of a pair of Stainless steel pole pieces and a $SmCo_5$ magnet mounted on a common, non-magnetic shaft.

The motor has the following dimensions:

- Diameter 57 mm
- Length 76 mm
- Mass 900 g

The basic performance of either the Prime or Redundant motors is:

- Holding Torque .28 Nm
- Detent Torque .07 Nm
- Power input for peak torque 3.6 W
- D.C. Resistance 10.0 $\Omega$

Features of the motor include accurate alignment between Prime and Redundant motors to enable the use of either motor without significant loss of positional accuracy. This also enables both motors to be energised simultaneously to give approximately double the single motor torque if necessary. However, a disadvantage of aligning the motors in this way is that the detent torque also doubles, which reduces the overall torque capability of the motor. Had the requirement for accurate Prime and Redundant alignment not been a design criterion, it would have been possible to offset the Redundant motor by half a step from the Prime motor such that the Prime and Redundant detent torques would cancel leading to more useable driving torque.

The dynamic performance of the motor is shown in Fig. 2 where the pull-out torque (curve (a)) and the power input (curve (c)) are shown as a function of supply frequency. The drive used was full-step bipolar,

providing 600 mA maximum to either phase. The performance curves exhibit the usual frequency-dependent decrease of torque and input power which occurs with Stepping motors when the conduction period is short compared to the electrical time constant of the motor.

To simulate operation after one winding has developed a worst-case short-circuit failure, the leads from one phase of the redundant motor were connected together whilst the Prime motor was driven using the same drive as previously. Torque measurements made on the unit resulted in curve (b) shown in Fig. 2. It can be seen that the magnitude of the retarding torque (i.e. the difference between curves (a) and (b) is largely independent of supply frequency. This is attributed to the fact that Prime and Redundant windings share a common electrical time constant and thus the waveform of the fault current varies with time in the same way as the waveform of the supply current.

It should be observed that for any given frequency, the input power remains unchanged regardless of whether or not a fault is present on the Redundant winding. This is to be expected since the Prime and Redundant motors are electrically independent: the retarding torque of the failed motor is seen by the healthy motor purely as an increase in mechanical load.

Dual-wound Stepping Motor

This motor is a housed, size 23, 2 phase, $1.8^{o}$ step motor designed for intermittent operation in an Antenna Pointing Mechanism. The rotor and stator assemblies are mechanically identical to either the Prime or Redundant element of the Tandem motor described above. The general arrangement is shown in Fig. 3. The Prime and Redundant windings are insulated from the stator stack by slot liners and from each other by Mylar slot dividers inserted between the two windings from either end of the stack. The two windings are thus physically separated from each other at all points.

The motor has the following dimensions:

- Diameter 57 mm
- Length 51 mm
- Mass 620 g

The basic performance using either the Prime or Redundant winding is:

- Holding Torque .24 Nm
- Detent Torque .035 Nm
- Power input for peak torque 3.6 W
- D.C. Resistance 17.0 $\Omega$

With both windings sharing a common stator stack, the changeover from one winding to the other can be accomplished without any variation in rotor position. This also means that both windings may be energised simultaneously to give increased torque capability. However, since this effectively doubles the power dissipation in the same stack, simultaneous operation should be performed with caution to avoid overheating the winding. Also, using both windings, it is easy to drive the magnetic circuit into saturation. Thus, rather less than double the torque is available; on the unit under consideration, an increase in Holding Torque of only 50 % is achieved with both windings energised.

The pull-out torque and power input characteristics of the motor are shown respectively, by curves (a) and (b) in Fig. 4. A full-step bipolar drive was used, providing up to 470mA to either phase. The winding on this motor is designed to provide approximately the same performance as for the Tandem motor for the same power input and this can be verified from the performance data.

To simulate a worst-case short-circuit fault, the leads from one phase of the Redundant winding were connected together whilst the Prime winding was driven as previously. Torque and input power measurements made on the unit gave the results indicated by curves (c) and (d) of Fig. 4. By comparing curves (a) and (c), it can be seen that the retarding torque due to the fault current is approximately 50% greater than for the Tandem motor and is frequency independent above 50 Hz. However, examination of curves (b) and (d) shows that the power input under fault conditions increases significantly as supply frequency increases.

Both the above effects are due to the inductive coupling between the Prime and Redundant windings; there is a significant transformer effect. At low frequencies (less than 25 Hz) electrical rise time is insignificant; the drive pulses are square waves and quasi D.C. conditions exist. There is little transformer action between the two windings and the fault current which flows is due only to the motion of the rotor. Power input under these conditions is the same as for no-fault conditions and the retarding torque is similar to that of the Tandem motor. At high frequencies (greater than 250 Hz) the transformer effect predominates. Current circulating in the failed winding acts to reduce the mutual flux density and this increases the difference between the emf induced in the Prime winding and the supply voltage. Hence the supply current and input power increase significantly and the additional fault current creates extra retarding torque. At intermediate frequencies, a combination of the two effects is present. The dual-wound Stepping motor is, therefore, very inefficient if operating at high speeds under fault conditions.

Dual-wound D.C. Motor

This motor is a housed, size 18, permanent magnet brush D.C. motor having redundant windings, brushes and commutators. It is designed for short term operations in a Deployment Mechanism. Constructional details are

shown in Fig. 6. The Redundant winding is fitted in the bottom of the armature slots, with connections brought out to the front commutator. The Prime winding is inserted on top of the Redundant winding and connected to the rear commutator. Within the armature stack, the windings are separated from each other and from the stack by Melinex insulators. Due to the large number of commutator connections which are required, it is not practical to separate the two windings in the overhang region at either end of the armature. The two sets of brushgear are supported by moulded plastic brushblocks.

The motor has the following dimensions:

- Diameter 44 mm
- Length 70 mm
- Mass 440 g

Using a 28 V supply, the performance using either Prime or Redundant windings is as follows:

| | | | |
|---|---|---|---|
| Stall torque | 58 Nmm | No-Load speed | 6500 rev/min |
| Stall current | 1.5 A | No-Load current | 75 mA |
| Rated torque | 12 Nmm | Torque constant | 40 Nmm/A |
| Rated speed | 5000 rev/min | | |

Due to the large difference between rated torque and stall torque it may well be necessary to operate using a current limited power supply to avoid damage to other parts of the mechanism. However, if this is not a constraint, then it is possible to energise both motor windings simultaneously to double the stall torque. On the particular motor under consideration, this could be achieved without saturating the magnetic circuit.

The application for this motor required it to be able to operate at very high armature temperatures. This, combined with the high rotational speed, gave concern over the integrity of the solder joints between the commutator and coil ends. However, failure of one or more of these joints would result in an open-circuit condition from which complete recovery is possible using the Redundant winding.

A short-circuit failure between two adjacent coils was simulated by connecting together two adjacent commutator segments on the unpowered winding. The resulting performance is shown by the dotted lines in Fig. 5. For any given output torque, the motor speed is decreased by approximately 12% from the no-fault value. Being a D.C. machine there is no transformer effect and fault current is entirely due to rotational emfs. Retarding torque, and hence additional input power, are therefore greatest at high speeds and zero at the stall point.

The same condition occurs in the event of a terminal-to-terminal short-

circuit, only here the effect is drastic with no-load speed reduced to less than 50% of the no-fault value. This is indicated by chain-dotted lines in Fig. 5 . Fortunately, this could only result from a harness failure or other external fault.

## CONCLUSIONS

Although there are five basic types of redundancy at mechanism level, there are only three motor options: non-redundant, dual-wound or tandem. At motor level, non-redundancy gives smallest size, lowest mass and highest performance. At the other extreme, tandem motors can provide performance very close to that of non-redundant motors, but at the expense of almost doubling volume and mass.

An attempt has been made to compare the merits of the three types of redundancy and the results are shown in Table 1 for stepping motors and Table 2 for D.C. motors. It should be emphasised that the data given in the tables is intended for guideline purposes only. It is always necessary to consider specific requirements in detail to enable an optimum solution to be reached.

TABLE 1 COMPARISON OF REDUNDANCY METHODS FOR STEPPING MOTORS.

| Motor parameter | Redundancy method | | |
|---|---|---|---|
| | Non-redundant | Dual-wound | Tandem |
| Length | L | L | L x 1.9 |
| Diameter | D | D | D |
| Mass | M | M | M x 1.8 |
| [a] Holding Torque | $T_H$ | $T_H$ x 0.7 | $T_H$ |
| [a] Detent Torque | $T_D$ | $T_D$ | $T_D$ x 2 |
| [b] Effect of open circuit | - | No effect | No effect |
| [b] Effect of short circuit | - | Torque reduced as frequency increased | Reduced torque |
| Increase in input power due to short circuit | - | Power increased as frequency increased | None |

a. Comparisons made at same power input
b. When fault occurs on unpowered winding

TABLE 2 COMPARISON OF REDUNDANCY METHODS FOR D.C. MOTORS.

| Motor parameter | Type of redundancy | | |
|---|---|---|---|
| | Non-redundant | Dual-wound | Tandem |
| Length | L | L x 1.2 | L x 1.9 |
| Diameter | D | D | D |
| Mass | M | M x 1.2 | M x 1.8 |
| [a] Stall Torque | T | T x 0.7 | T |
| [a] No-load speed | N | N x 1.4 | N |
| [b] Effect of open circuit | - | No degradation | |
| [b] Effect of short circuit | - | Operating speed reduced | |
| Increase in input power due to short circuit | - | Inversely speed dependent | |

a. Comparisons made at same power input at stall
b. When fault occurs on unpowered winding.

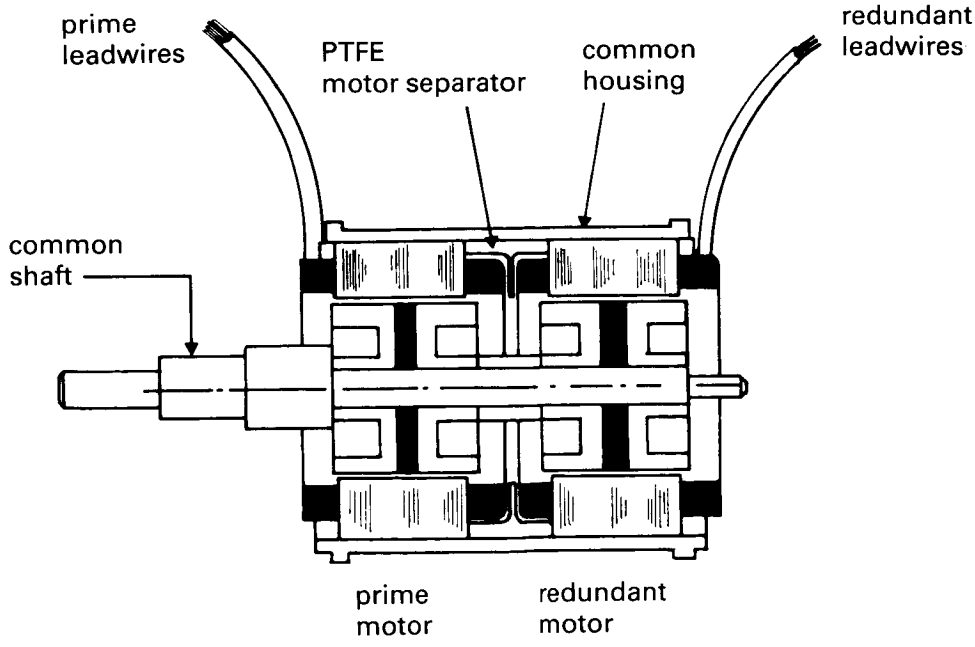


Figure 1. - Construction of tandem stepping motor.

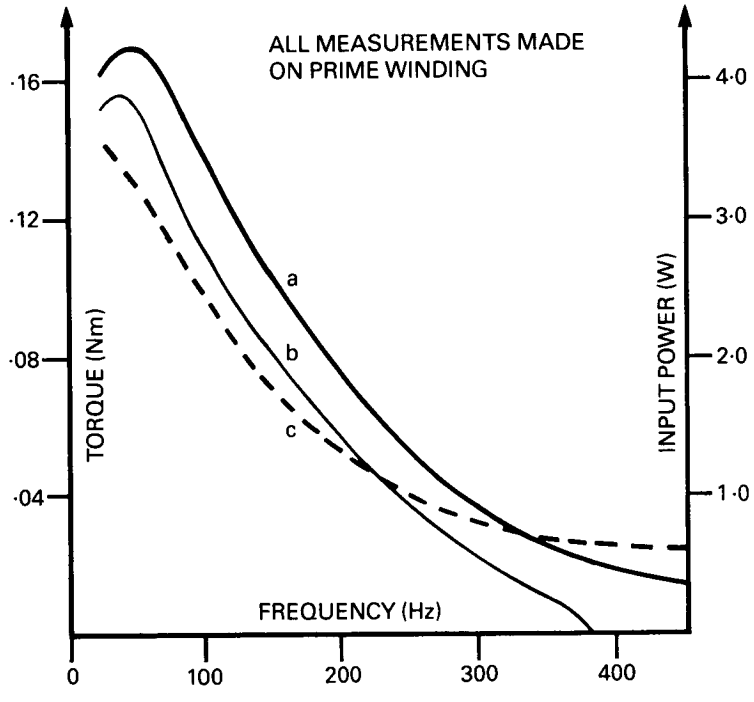


a: No-fault torque characteristic
b: Torque characteristic with short circuit on redundant winding
c: Input power corresponding to (a) and (b)

Figure 2. - Performance of tandem stepping motor.

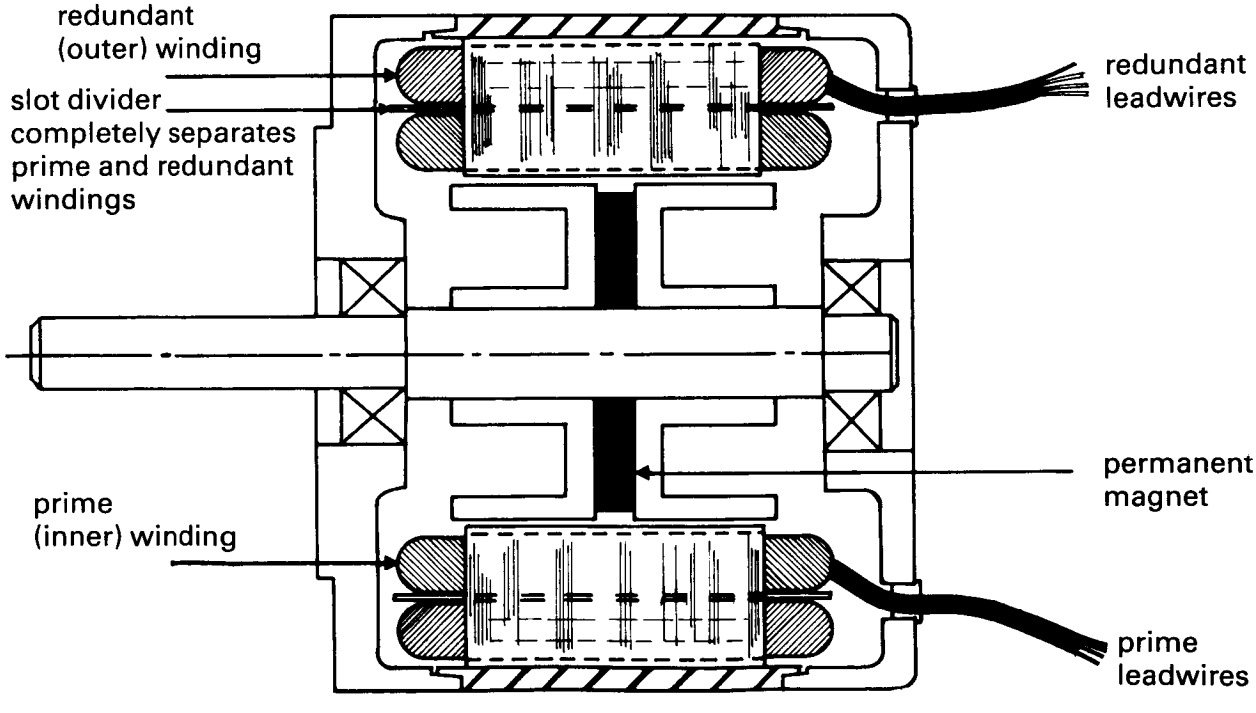


Figure 3. - Construction of dual-wound stepping motor.

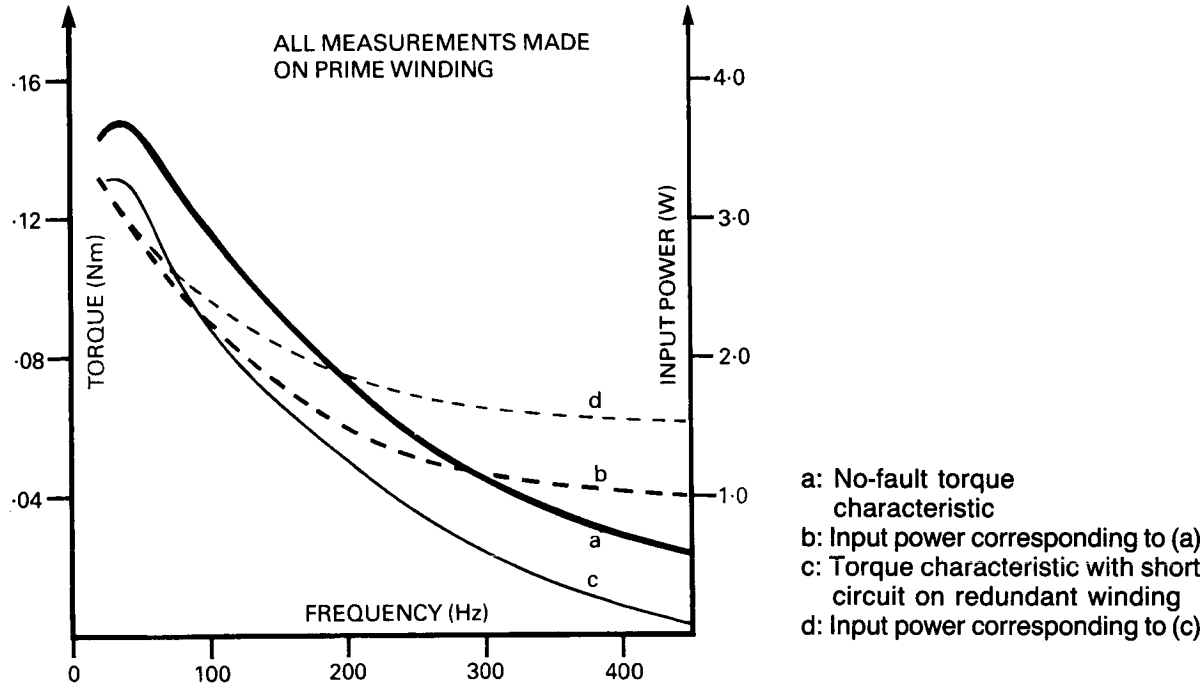


Figure 4. - Performance of dual-wound stepping motor.

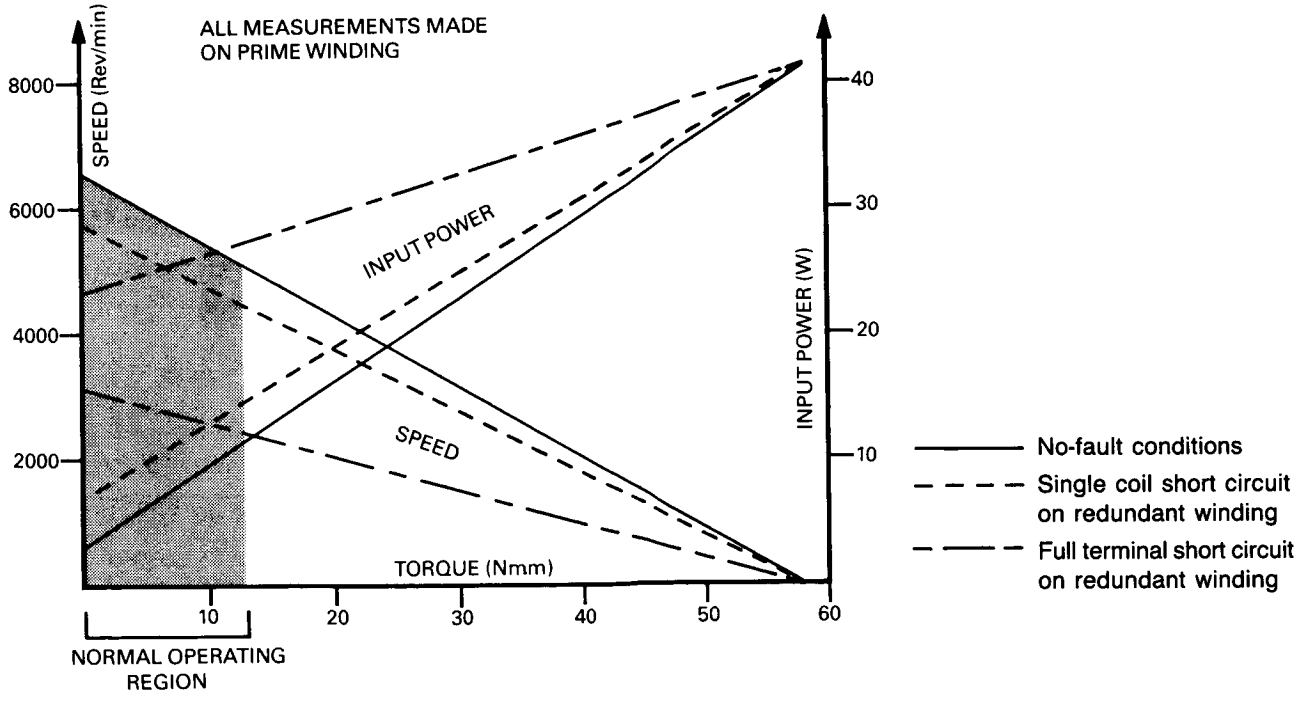


Figure 5. - Performance of dual-wound D.C. motor.

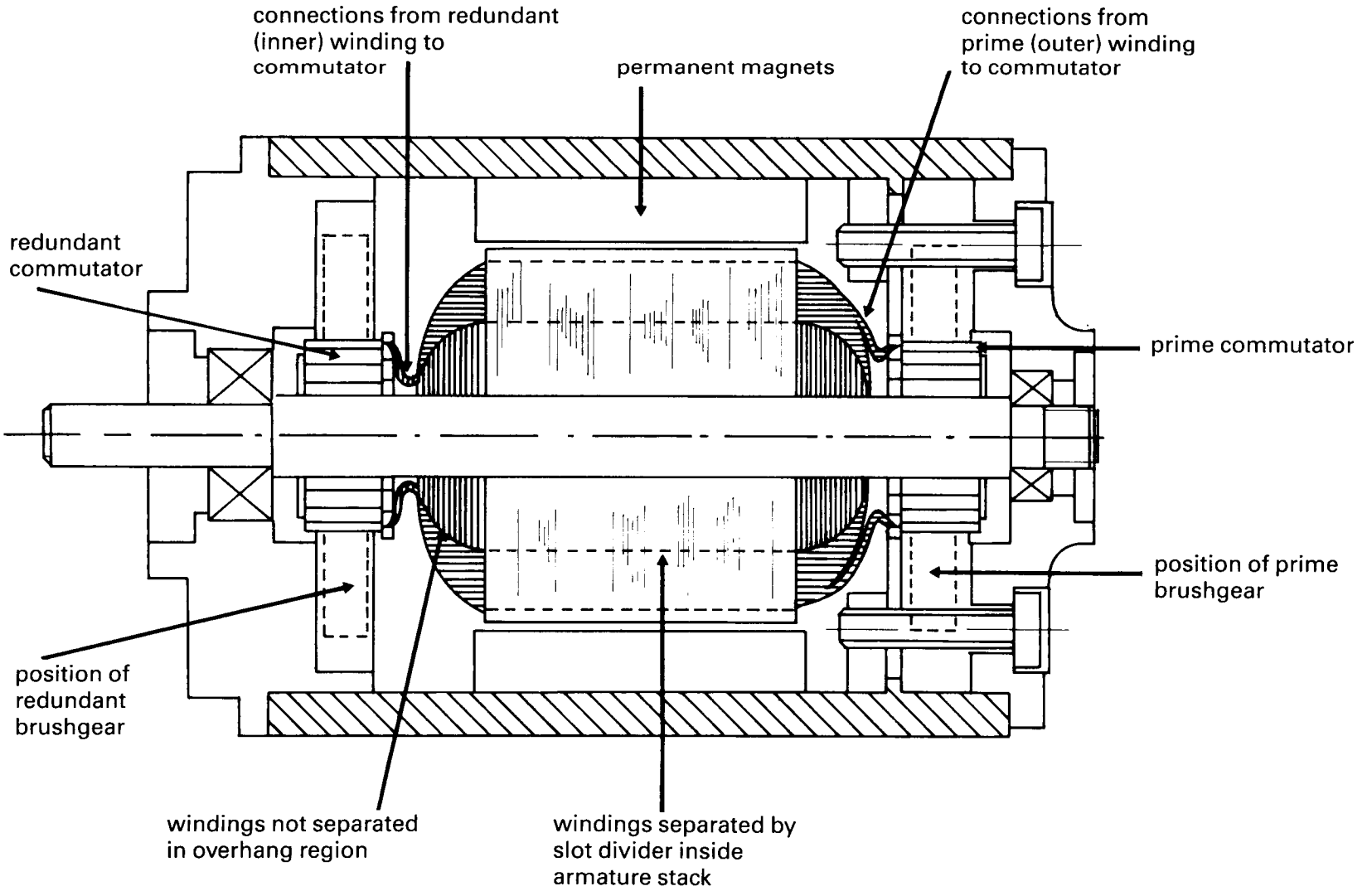


Figure 6. - Construction of dual-wound D.C. motor.

# RF SWITCH POSITIONER FOR COMMUNICATIONS SATELLITE NETWORK

A.G. Storaasli, H.P. Griesser, R.W. Grant*

The RF switch positioner is a simple, lightweight, redundant positioning mechanism used to reconfigure the antenna beam on the INTELSAT VI satellite. It simultaneously rotates approximately 100 squareax waveguide switches through a full 360°.

## BACKGROUND

INTELSAT VI is a geosynchronous communications satellite designed and built by Hughes Aircraft Company's Space and Communications Group for the INTELSAT consortium.** Five satellites are to be placed in orbit over three major regions: the Atlantic (AOR), Pacific (POR), and Indian (IOR) oceans. The system is designed to operate in any of the three ocean regions. If a satellite has to be moved, its communication payload must be reconfigured in orbit to operate in the new ocean region.

The 4 and 6 GHz zone coverage beams (see Figure 1) must be reconfigured to direct the maximum RF energy where needed (i.e., populated areas). The zones are reconfigured by changing the relative amplitudes and phases in the antenna feed network (Figure 2); the connection of each horn to the proper network is enabled by devices called squareax switches (Figure 3). The three switch conditions are affected by rotation of a crank shaft. Figure 3 shows the squareax switch in the Atlantic condition; the 120° rotation of the

*Hughes Aircraft Company, Space and Communications Group, El Segundo, California.

**The INTELSAT VI spacecraft is being developed and built by an international team of contractors lead by Hughes Aircraft Company for the International Telecommunications Satellite Organization (INTELSAT), the nonprofit cooperative of 110 countries that owns and operates the global communications satellite system used by countries around the world for international communications and by more than 27 countries for domestic communications.

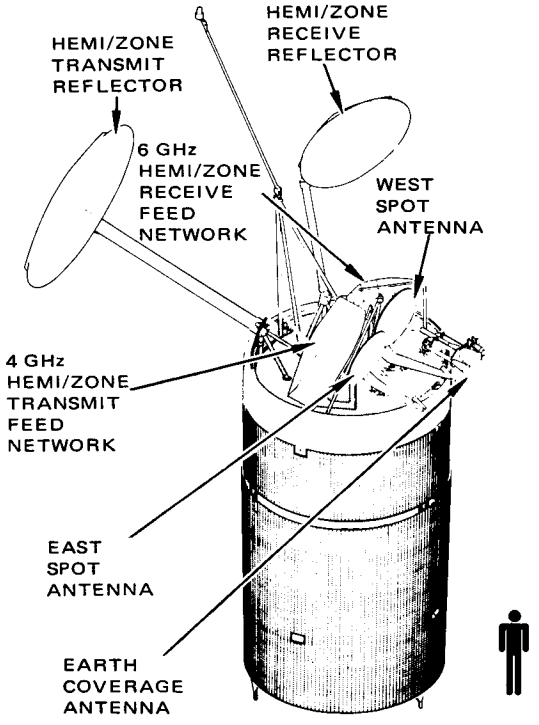


Figure 1. - Antenna farm configuration for INTELSAT VI.

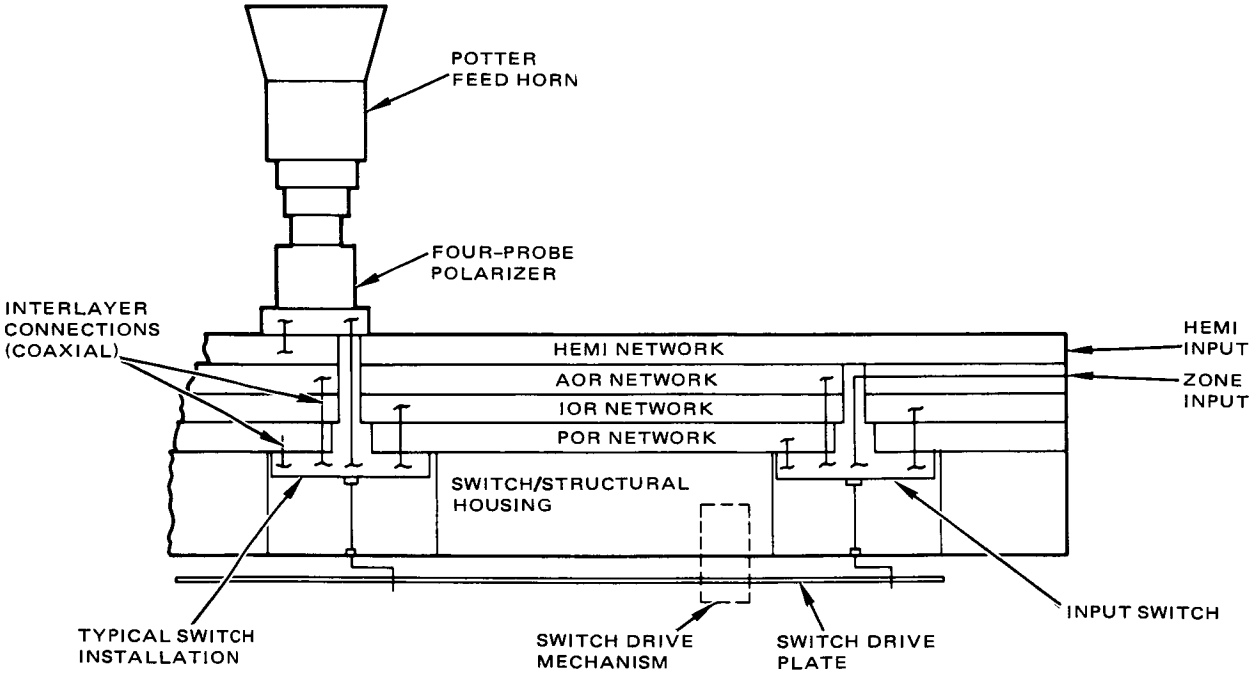


Figure 2. - Hemi/zone squareax network implementation.

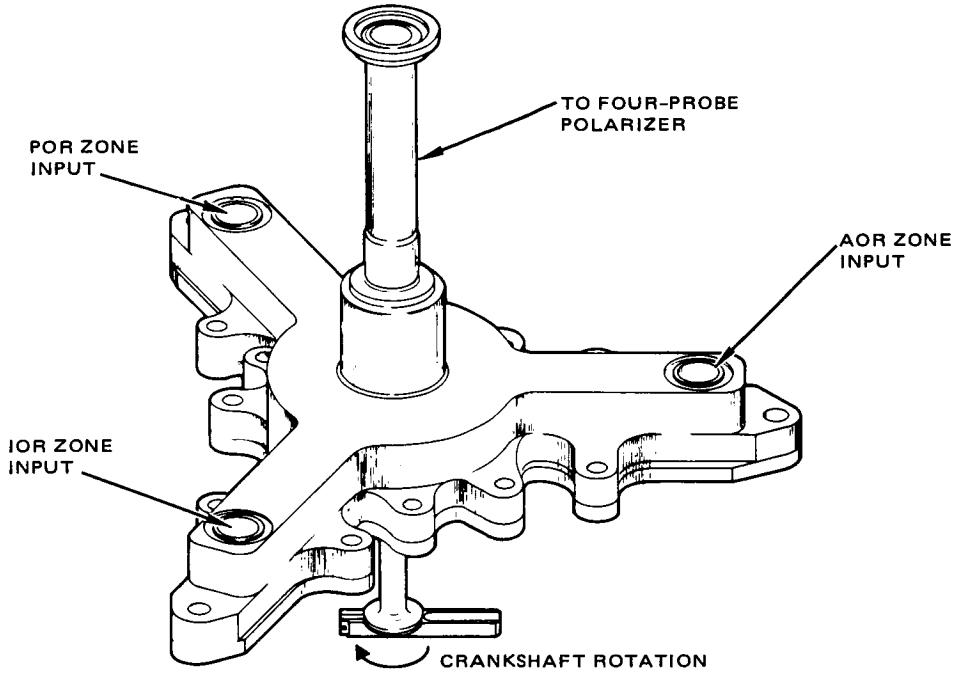


Figure 3. - Squareax switch.

crank provides connection for the POR or IOR zone, depending on the direction of travel.

Ninety-two such squareax switch/horn sets are on the transmit feed network and 91 on the receive feed network. Proper reconfiguration requires that all switch cranks on a network be rotated 120° (switches must be in the predetermined location at launch). The RF switch positioner performs the function of driving the 92 (or 91) cranks in unison.

## APPROACH

An early concept considered was to use a long belt to turn pulleys (sprocketed or nonsprocketed) on each shaft (Figure 4). It appeared simple and lightweight, but serious design limitations became evident: maintaining belt tension, cumulative error buildup, and the need to deal with a mix of CW and CCW rotations.

The final solution was to use the swashplate arrangement shown in Figure 5. A lightweight plate is driven in an orbiting motion by cranks connected to the plate such that they are caused to rotate. By controlling the orbit of the plate, all switch cranks are simultaneously stopped at the proper 120° location.

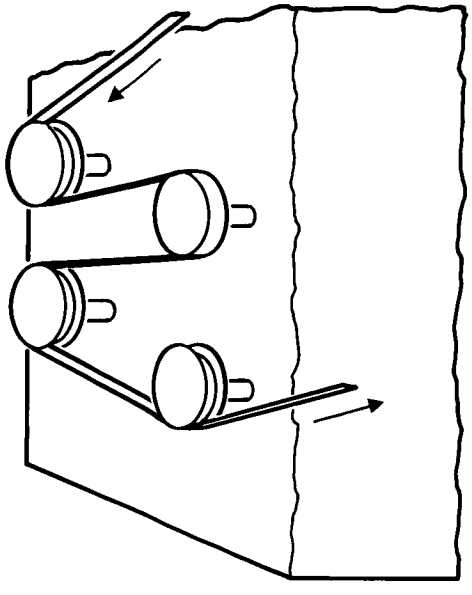

Figure 4. - Early belt drive concept.

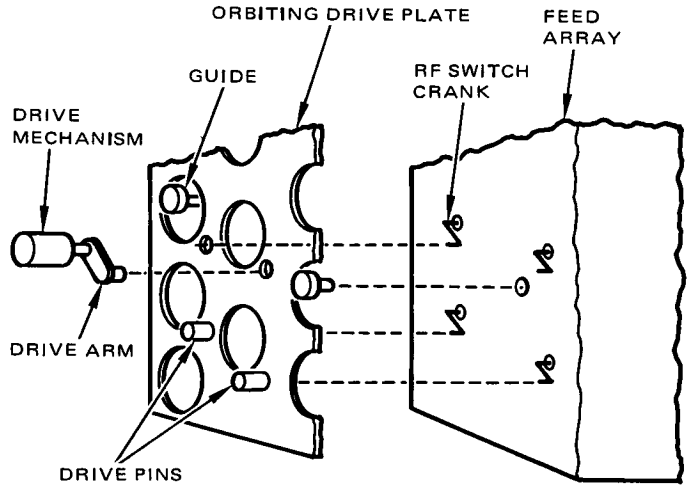


Figure 5. - RF switch positioner concept.

Detailed Description

Implementation of the design proved challenging considering the size of the feed networks, the number of switches, and the need to avoid mismatches between the plate and switches that may cause rotational errors or jamming.

Figure 6, a production honeycomb plate, was sized in thickness such that it could be held in place by a reasonable number of "mushrooms" in the launch vibration environment. The mushrooms, attached to the feed substrate, retain the plate laterally by their snug fit at respective plate lightening holes. The redundant motor set provides one rotational link; two passive links are located elsewhere to ensure proper orbiting motion. The cranks have slotted engagements so jamming cannot occur from tolerance buildups or thermal distortions.

Drive redundancy was a design baseline. Motor/gearhead pair plus differential gearing seemed a likely choice, however a more simple design was found. The Figure 7 design consists of two motor/gearheads connected by the mesh of respective output spur gears. Rotation of drive A pinion causes drive B (including plate) to orbit around drive A axis (drive B must be locked). Alternatively, if the redundant drive B is driven, its pinion will walk around drive A in the same orbital motion.

Redundant pots located on the base, connected by a similar crank, sense the orbital position. A tradeoff was performed on motor type dc versus stepper. The dc motor is workable, but the stepper motor was chosen since

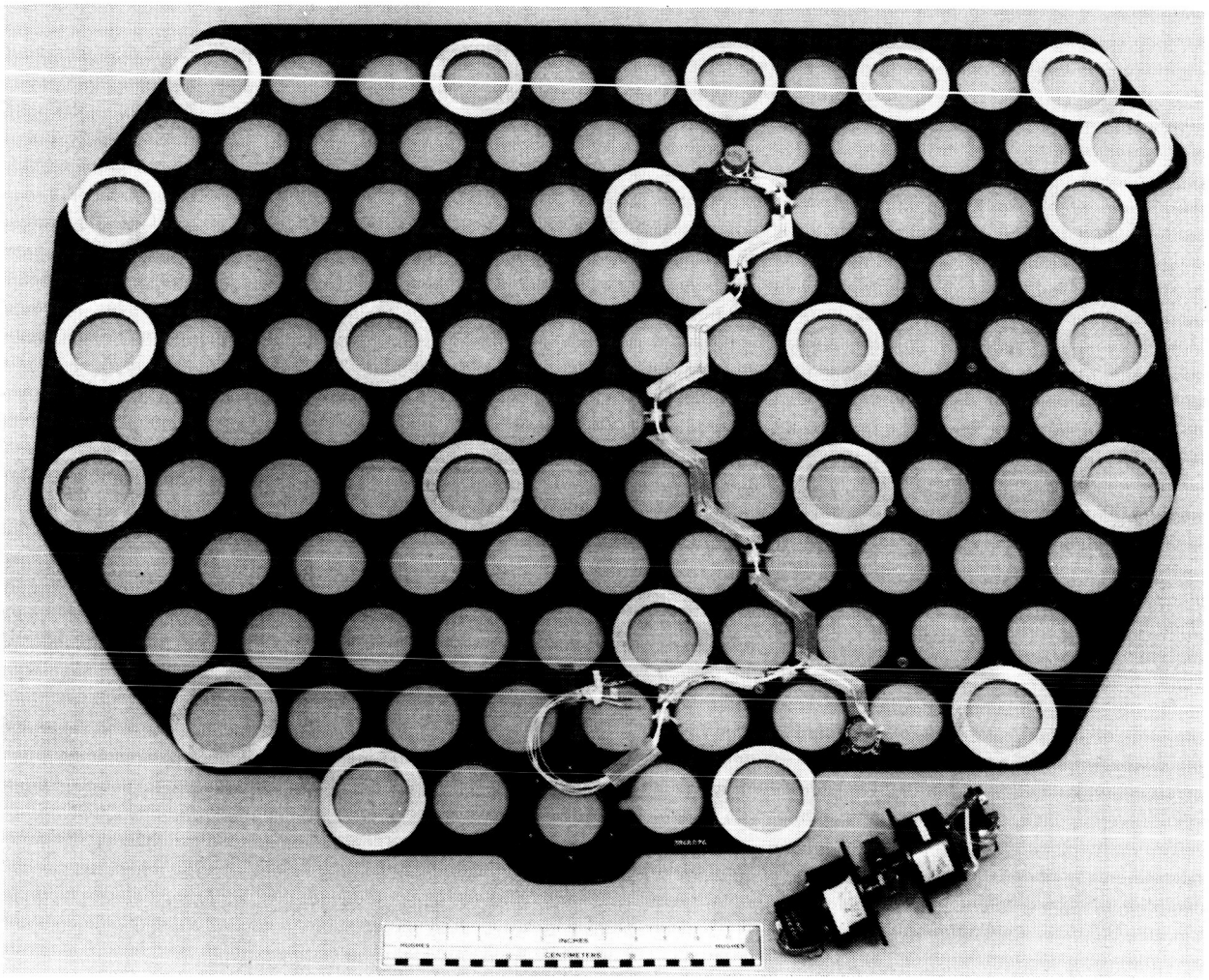

Figure 6. - Aluminum honeycomb plate and drive.

stepper motor drive electronics are being used in other areas of this spacecraft. Another advantage of stepper drive is that a predetermined step count can be used for accurate positioning. Each drive consists of a 45° size 11 stepper and 4126:1 gearhead. Figure 8 shows a production set of redundant motor geardrive and pots.

Table 1 lists the salient positioner characteristics. The 2° accuracy was not overly difficult to meet. The chief contributors were pot readout, manufacturing tolerance, and thermal gradients. The 4126:1 gear ratio was selected to give high torque margin, yet move the 120° at an acceptable rate.

## Development and Testing

Engineering model testing performed early in the program proved helpful in locating some design problems or errors. It also gave some insight to

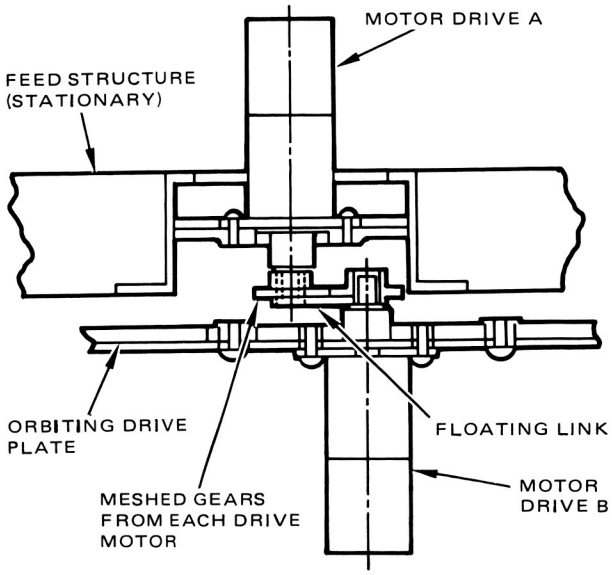


Figure 7. - Redundant drive configuration.

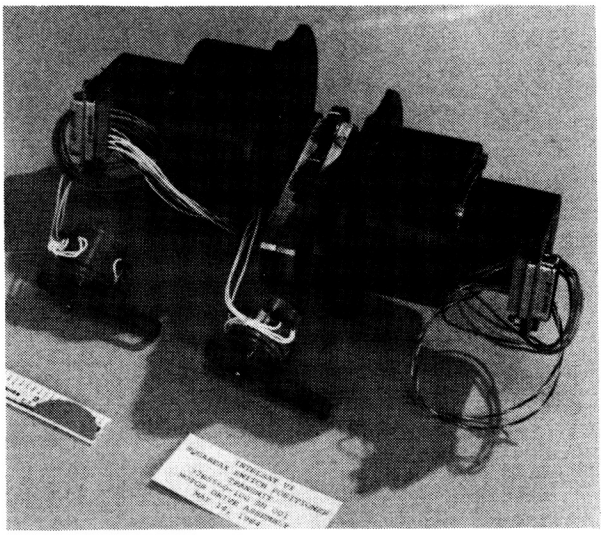

Figure 8. - Redundant motor gear drive and pots for one RF switch positioner assembly.

TABLE 1. RF SWITCH POSITIONER CHARACTERISTICS

| | |
|---|---|
| POWER CONSUMPTION | 15 W |
| ACCURACY | $\pm 2^{o}$ |
| POSITION INDICATOR | REDUNDANT POTENTIOMETERS |
| RANGE | $0^{o}$ to $240^{o}$ |
| SWITCHING TIME | 20 MIN AT 25 STEPS/SECOND |
| GEAR RATIO | 4126:1 |
| POSITIONER TORQUE | >4.13 N.m (FACTOR OF 3 OVER WORST CASE OF TORQUE) |
| WEIGHT | |
| TRANSMIT UNIT | 3.22 kg |
| RECEIVE UNIT | 2.35 kg |

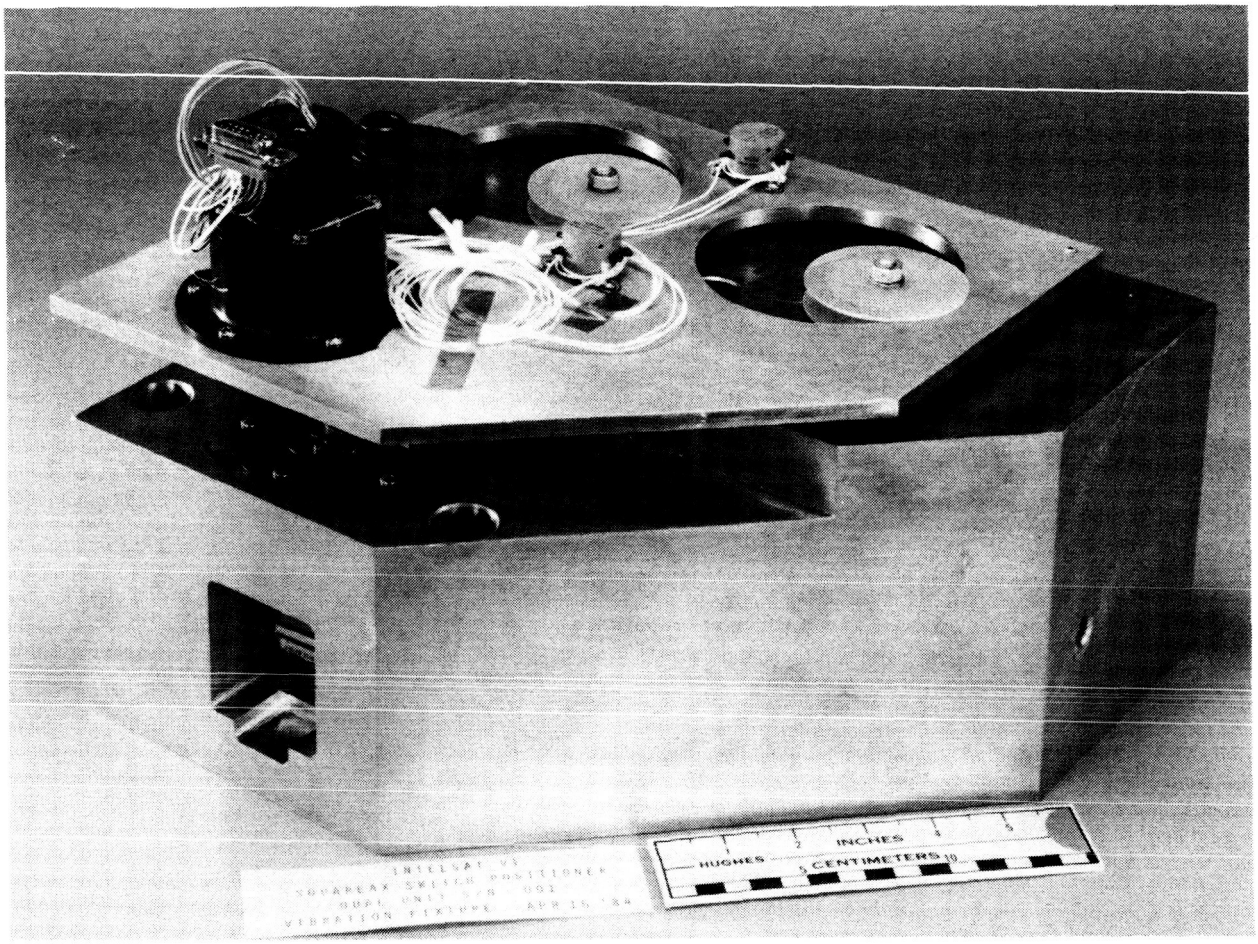


Figure 9. - Qualification unit with dummy plate section.

the lateral vibration nature of the plate which was a major concern because of the difficulty in analyzing such a plate.

Qualification testing consisted of random vibration and thermal-vacuum tests along with functional tests. To make the testing manageable, unit level testing consisted of the drive, idler cranks, pins, and plate section. Figure 9 shows the qualification level vibration setup. This is a reasonable screening test; additional testing takes place after installation to the actual feed assembly.

Only two anomalies were encountered in qualification testing. One idler link was damaged in vibration testing which was diagnosed as a setup problem resulting in unrealistic acceleration amplification.

The second anomaly took place during thermal-vacuum. To verify drive margin, clamp devices are installed to provide worst case frictional torque. Motor voltage is then reduced below the 28 Vdc nominal until the starting voltage is determined. During operation at the low temperature

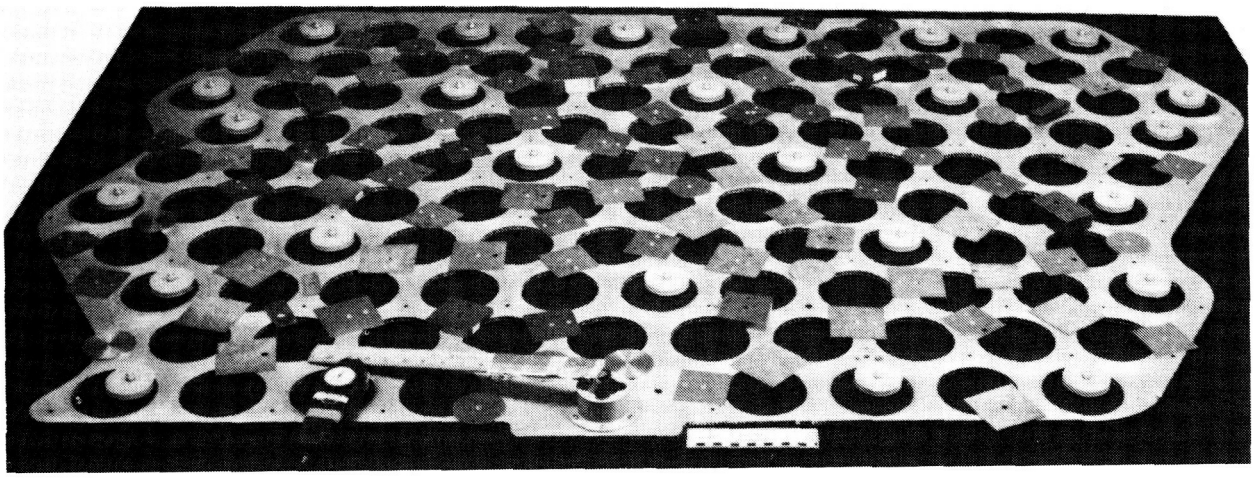

Figure 10. - Simulated thermal gradient test setup.

cycles the starting voltage was erratic although within specification. It was determined that the clamp experienced stiction, and was not a unit problem. The flight test setup now uses a magnetic particle brake to produce more consistent drag torque.

The aluminum honeycomb is susceptible to thermal gradients even though the area is covered with a thermal blanket. A special test was conducted to determine torque effects due to thermal gradient across the width of the plate.

The test setup (Figure 10) consisted of a full sized, aluminum honeycomb, transmit drive plate installed on the mushroom positioners. The positioners were mounted on a 1 inch thick plywood sheet and arranged in the flight configuration. A gear on a shaft replaced the front of the outer drive motor. The inner drive motor was mounted to the plywood substrate, and a link was provided to constrain the gears to orbit around each other.

The equivalent motor torque required to move the plate was measured with a torque watch. Larger torques were measured by attaching a moment arm to the shaft and driving it with a force guage as shown in Figure 10. The actual drive plate torque was twice the motor torque because of the 2:1 reduction of the gear linkage ratio.

The distortion due to a thermal gradient across the width of the plate was simulated by a uniformly distributed load on the plate face. The plate was mounted horizontally, and various weights were uniformly arranged upon it.

A $1^{o}C$ gradient across the width of the plate has been predicted as the worst case. This gradient will cause a 0.30 cm deflection at the plate's center. The force this deflection will generate on the positioner disks can be simulated by distributing 3.6 kg uniformly across the plate. Margin can then be demonstrated by applying additional weights.

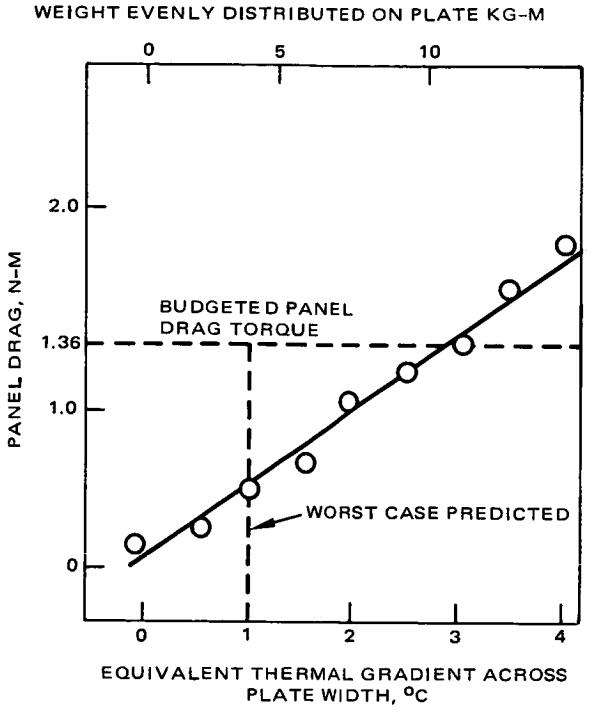


**Figure 11. – Panel drag versus plate thermal gradient.**

The results of the tests are shown in Figure 11. Data was taken in eight increments from 0 to 14.5 kg. The panel drag was linear with respect to the thermal gradient as expected. The panel drag exceeded the budget only at a 3°C gradient, three times the predicted worse case.

This test shows that the thermal gradient across the width of the plate will not impede the motion of the switch positioner. The low panel drag is primarily due to the low friction coefficient between the plate and the positioner disks and the low stiffness of the plate. A relatively small force is needed to hold the plate straight against thermal distortion.

## CONCLUSIONS

The RF switch positioner has been space qualified and has performed to expectations in conjunction with the feed networks in range testing.

# EVALUATION OF A HIGH-TORQUE BACKLASH-FREE ROLLER ACTUATOR

Bruce M. Steinetz* and Douglas A. Rohn*

and

William Anderson†

The results are presented herein of a test program that evaluated the stiffness, accuracy, torque ripple, frictional losses, and torque holding capability of a 16:1 ratio, 430 N-m (320 ft-lb) planetary roller drive for a potential space vehicle actuator application. The drive's planet roller supporting structure and bearings were found to be the largest contributors to overall drive compliance, accounting for more than half of the total. In comparison, the traction roller contacts themselves contributed only 9 percent of the drive's compliance based on an experimentally verified stiffness model. The drive exhibited no backlash although 8 arc sec of hysteresis deflection were recorded due to microcreep within the contact under torque load. Because of these load-dependent displacements, some form of feedback control would be required for arc second positioning applications. Torque ripple tests showed the drive to be extremely smooth, actually providing some damping of input torsional oscillations. The drive also demonstrated the ability to hold static torque with drifts of 7 arc sec or less over a 24 hr period at 35 percent of full load.

## INTRODUCTION

Roller traction drives have found their way into a variety of industrial applications ranging from low-power, elastomer-coated rollers in paper handling equipment to 100 kW variable-speed pump drives. As power transmissions, few mechanical drives match their low-noise, smooth-torque-transfer characteristics and speed-regulating accuracy. However, their suitability as servodrive mechanisms is just starting to be appreciated. Absence of "backlash" and "cogging" (low-velocity errors) are two notable qualities.

Recent examples include a traction roller servosystem for part positioning on an ultraprecise single-point lathe (ref. 1) and an advanced technology propeller pitch control mechanism (PCM) for future large turboprop aircraft

*NASA Lewis Research Center, Cleveland, Ohio.
†Nastec, Inc., Cleveland, Ohio.

(ref. 2). The traction feed system built by Lawrence Livermore Laboratories, which used a drive roller against a translating traction bar, had a positioning repeatability of 0.005 μm (0.2 μin.) under thrust loads to 1300 N (300 lb) using laser interferometry feedback (ref. 1).

A promising approach for meeting the demanding PCM requirement is an all electromechanical system incorporating a multiroller 210:1 hybrid traction drive for a Mach 0.8, 150 passenger turboprop commuter aircraft (ref. 2). This torsionally stiff system can vary the pitch of 4 m diameter propellers carrying up to 10 000 kW. With the proposed low-friction mechanism coupled to a high-resolution digital controller, blade position accuracies of better than 3 arc min of a degree are projected, well within synchrophasing (precise speed control) allowances of a multiengine aircraft of this size. This 1500 N-m (1100 ft-lb) actuator would also be suitable for other high torque applications such as tank turret aiming and missile tracking mechanisms.

In this investigation, a 16:1 ratio, 430 N-m (320 ft-lb) output torque roller actuator (fig. 1) was evaluated experimentally to determine its potential suitability as a space vehicle, high-torque actuator, such as for a control moment gyro (CMG) gimbal drive. Analytical predictions of the torsional stiffness of the drive are compared with static torsional stiffness measurements. Data on the drive's zero backlash, torque ripple, starting friction, and hysteresis characteristics were also obtained as well as data on its positional accuracy performance and ability to attenuate some drive system torque ripples.

## BACKGROUND

Traction drives in their simplest form are just two smooth, unequal-size wheels in driving contact. As a minimum, a preload system is required to maintain sufficient normal load to prevent the rollers from slipping over one another. Drives can be designed with either a fixed or variable preload depending on the particular application. Unlike gear meshes, the roller contact due to its low sliding nature can be designed to operate for extended time periods without liquid or grease lubrication for low-power applications. This can be accomplished by either using high-traction solid-film coatings such as ion-plated gold or silver or using advanced, low-wear, high-traction polymers such as certain polyimides or polyamide-imides. The elimination of depletable liquid lubrication is a decided benefit for spacecraft mechanism applications.

Furthermore, rollers, unlike gears, have the ability to slip harmlessly at predetermined traction limits. This overtorque, release-clutch tendency can prevent catastrophic damage if jamming should occur at some point in the mechanism drivetrain.

Light-duty (up to about 10 kW) variable ratio traction drives have been commercially successful in industrial applications for many years. Due to their inherent smooth torque transfer characteristics and potential for cost

reductions, traction drives have been investigated as replacements for geared drives for fixed ratio power transmissions and mechanisms.

Unlike a simple gear mesh, the normal load imposed on a traction contact must be several times higher than the transmitted traction force to prevent slip. Thus, to achieve high-power (or torque) density, the traction drive should be constructed with multiple, load-sharing roller elements which can reduce the contact unit loading. Planetary roller drives have multiple contacts and ensure that the normal contact loads are reacted internally by the ring roller rather than by bearings. However, because of planet roller-to-roller interference, a single row planetary drive is limited in speed ratio.

The drive system devised by A.L. Nasvytis in the early 1960's (ref. 3) used the sun and ring-roller of contemporary planetary traction drives but replaced the single-row of equal diameter planet rollers with two or more "stepped" or dual diameter planets. With this new multiroller arrangement, practical speed ratios of up to 250:1 could be obtained in a single stage with three planet rows. Furthermore, the number of planets carrying the load in parallel could be greatly increased for a given ratio. This resulted in a significant reduction in individual roller contact loading with a corresponding improvement in torque capacity. The Nasvytis type drive evaluated herein achieves a 16:1 ratio in a single stage using two rows of stepped planet rollers (fig. 1).

A novel geometric arrangement that combines traction rollers with gears in parallel was also devised by Nasvytis (ref. 3). In the roller-gear drive, as it is termed, the center portion of the roller is replaced with a spur gear. The rollers not only serve to transmit a portion of the torque but also provide a support bearing function since their diameters are equal to the pitch diameter of the gear. The rollers which share torque in parallel with the gears eliminate the effects of backlash and help minimize breakaway torque while adding substantial stiffness to the drive system.

The performance of a 26:1 ratio, 540 N-m (400 ft-lb) CMG rotary actuator, which incorporated a roller-gear drive (fig. 2) in combination with a brushless dc motor, was evaluated in reference 4. In this drive, the rollers share 25 percent of the torque in parallel with the gears. Static output torsional stiffness values of $680 \times 10^3$ N-m/rad ($500 \times 10^3$ ft-lb/rad) or greater were measured at the zero torque crossing point. Breakaway or starting friction varied from 0.4 to 2.5 percent of rated torque. While no backlash was detected, a small degree of lost motion (hysteresis) was measured that ranged from 2.9 to 4.7 arc sec up to 25 percent of maximum torque. Tests of a similar, but smaller, 106 N-m (78 ft-lb) torque, 15:1 ratio roller-gear/brushless dc motor servodrive were conducted in reference 5.

## ACTUATOR DESIGN

### Specifications

The need for a backlash-free, high-torque, low-torque ripple actuator was identified for a large space vehicle application. Critical system requirements included a minimum drive torsional stiffness of 340 000 N-m/rad (250 000 ft-lb/rad) at the output, a low weight, and a minimum design life of 1600 hr. Maximizing the drive's torsional stiffness while minimizing the drive weight consistent with the achievement of required life were the paramount considerations guiding the design. Structural design tradeoffs and material selections were consistent with flight hardware requirements.

Maximum input speed to the drive is 275 rpm and maximum input torque is 27 N-m (20 ft-lb), which is equivalent to 0.78 kW (1.05 hp). These conditions exist only when the actuator must reposition its driven element from point A to point B, which is only 6 percent of the total duty cycle. Most of the time the mechanism is hunting or "dithering" around a desired set point.

Two drive designs were generated, one based on lubrication with a high-traction vacuum oil and one based on dry operation. The overall configuration and dimensions were identical except for the preload mechanism which provided higher normal loads in the wet drive to transmit the same torque with a 40 percent less available traction coefficient. The rolling-contact fatigue life of the lubricated drive was well in excess of the required 1600 hr. Since dry lubrication has advantages in space, the dry configuration was chosen for evaluation.

This drive was designed to operate without liquid lubrication with a design traction coefficient of 0.1, 20 to 100 percent below the maximum available traction coefficient of the gold-ion-plated sun rollers against their mating steel first-row planet rollers (ref. 6). Gold was ion plated onto the sun roller surface with a thickness of 0.2 μm (7.8 μin.) as a dry film lubricant between the sun and first-row planet contact to prevent the rollers from cold welding in the vacuum environment. Life limitation in this design is one of wear of the gold layer. Based on sliding friction data (ref. 7), the gold thickness was determined for a minimum 1600 hr of operation.

### Geometry

The drive is nominally 25 cm (9.84 in.) in diameter by 22 cm (8.66 in.) in length and weighs 10 kg (22.1 lb) (fig. 1). This compact Nasvytis planetary drive packages well in the tight required design envelope. The servomotor-driven input shaft transmits torque to the two halves of the sun roller through two sets of torque loader balls. The sun roller, in turn, drives five stepped first-row planets which are in contact with five second-row planets. These outer planets carry the torque to the ring roller attached to the output shaft. Because of the double end geometry of the rollers, ten, twenty, and ten parallel contact paths occur, respectively, at successive contacts. The number of

planet rollers per row, number of rows, and relative step sizes are design parameters to be optimized for a given application.

The torque loading mechanism increases the normal load between rollers in direct proportion to the applied torque. The potential for slip is not only eliminated by incorporating a roller loading mechanism, but also the normal loads on the rollers do not have to be set at maximum at all times. Thus, the system's fatigue (wet lubricated drive) or wear (dry drive) life is extended and frictional losses are minimized.

The torque loading mechanism consists of six 0.64 cm (1/4 in.) diameter balls contained in ramp-shaped pockets equally spaced circumferentially between the sun roller flanges and thrust collars. The sun roller surfaces are crowned cones that mate with the first-row planet rollers with their slightly conical (4°) surfaces. When torque is applied to the drive above some predetermined preload setting (ranging from 10 to 50 percent of maximum torque), the sun roller thrust collars will advance circumferentially relative to the sun roller flanges. This will cause the balls to roll up their ramps, squeezing the two sun roller halves together axially. The axial clamping force, in turn, produces a radial loading on the roller cluster through the sun's tapered contact with the first row planets. The two sun halves are synchronized to move together by means of a series of interlocking fingers on each roller. The ratio of tangential force to normal force imposed on the traction drive contacts for a given torque; in other words, the applied traction coefficient can be varied by simply changing the slope of the ramp-shaped pockets. This applied traction coefficient is always designed to be less (at least 20 percent less in this case) than the maximum available traction coefficient to provide sufficient safety margin against slip.

## TRACTION DRIVE ANALYSIS

### Torsional Stiffness

High drive actuator system torsional stiffness is generally important for a variety of reasons. The most important reason for this application was to increase the system's bandwidth (response rate limited by natural system resonance). To achieve high bandwidth, the design philosophy was to make each structural/traction element as stiff as possible while minimizing rotational inertias ($J_{Drive}$ = 0.055 kg-m$^2$ at output) consistent with the other requirements of the drive. The requirement for high torsional stiffness had the greatest influence on the design of the torque loader, the second-row planet bearings, and the spider cage/roller support housing. The torque loader system was integrated in the sun roller instead of at the optional ring roller position, since the effective Hertzian compliance of the loading balls is significantly reduced by the square of the drive speed ratio.

Cylindrical roller bearings modified to essentially zero-mounted radial clearance (less than 2.5 μm (0.0001 in.)) were used as second-row planet support bearings rather than ball bearings. The aluminum spider cage/roller support housing was fabricated from a solid piece with cutouts for the second

planets rather than a bolted-up structure that could sacrifice stiffness at the connections.

The components within the drive which contribute to stiffness (or its reciprocal, compliance) were analyzed. The main contributors included the spider cage, planet bearings, input shaft and torque loader system, roller support housing backing plate, traction contacts, outer housing, bearing post depression in backing plate, and the output shaft. In analyzing each of these components it should be noted that their individual stiffness values must be adjusted by the appropriate speed ratio factor to relate their contribution to an effective overall torsional stiffness of the drive, typically (in this paper) at the output shaft.

The predicted effective stiffnesses at the low-speed shaft of each major drive component are listed in table I at zero torque (startup) with an initial contact preload set at 50 percent of maximum. This zero torque stiffness is critical to the response rate of a positioning mechanism that continuously adjusts about a new set point. The components have been ranked according to their percent of compliance contribution, which helps to identify the components that require the most improvement for maximum drive stiffness. The maximum available traction coefficient between the gold sun and steel first row planet contacts was conservatively assumed to be $\mu = 0.12$, and the maximum available traction coefficient for all remaining steel components was conservatively taken as $\mu = 0.2$. The overall predicted output shaft torsional stiffness was initially 670 000 N-m/rad (490 000 ft-lb/rad).

Compliance calculations for the input shaft and torque loader system, outer housing bearing post depression in backing plate, and output shaft were idealized and treated with a normal strength of materials approach. The spider cage was modeled as a repeated frame structure of aluminum support and steel bearing posts connected by a rigid link, the carrier ring, pinned to their ends (ref. 8). The cylindrical roller bearings were modeled with a 5 μm (0.0002 in.) diametral clearance using the method of reference 9. The roller support housing backing plate for the planet bearing posts was modeled as a disk with torque applied at the inside diameter and reacted at the outside diameter as described in reference 10. The traction contacts were analyzed using the comprehensive technique developed in reference 11; this technique is summarized in the appendix. A computer program, which was written using this approach, calculates traction contact compliances at each of the roller contacts and relates them to the output shaft. The roller contacts theoretically contribute only 9 percent of the drive's compliance (see table I).

When the component stiffnesses $k_i$ are expressed as equivalents at the output shaft, the components can be treated as torsional springs in series. The total stiffness $K_{T,Drive}$ is given by

$$K_{T,Drive} = \left( \sum_{i}^{n} k_i^{-1} \right)^{-1}$$

Other Considerations

Traction roller contacts can have a broad variety of available maximum traction coefficients, normal loads, contact ellipticity ratios, and applied loading. The relative effects of these variables are important to the designer of a traction drive mechanism that requires a certain level of torsional stiffness. For a given application, usually defined in terms of driven torque load and overall ratio requirement, each parameter described in the appendix can be adjusted, though not totally independently, to achieve the desired stiffness. Holding other parameters constant contact torsional stiffness increases with an increase in normal load and available traction coefficient but decreases with an increase in transmitted traction force. Large variations in stiffness can be achieved through the choice of roller-contact geometry. Contacts with a high ellipticity ratio (wide in the direction perpendicular to rolling) have higher stiffnesses. Roller size has the strongest stiffness effect, as shown in reference 11, if just static windup without rolling contributions is considered. In general, contact stiffness $k_t$ is related to tangential force $F_x$, normal load $N$, ellipticity ratio $a/b$, maximum available traction coefficient $\mu$, torque $T$, and the ratio $F_x/N$ as follows:

$$k_t \propto (\text{size})^{7/3} \quad \text{at constant} \quad F_x,\ N,\ a/b,\ \text{and}\ \mu$$

$$k_t \propto (\text{size})^{2} \quad \text{at constant} \quad T, F_x/N,\ a/b,\ \text{and}\ \mu$$

The foregoing cases show that contact torsional stiffness will approximately double for a 40 percent increase in roller sizes.

Roller coating effects. - In the roller actuator reported herein, the sun roller was ion plated with a 0.2 μm coating of gold to provide protection against wear and cold welding of the steel rollers in a vacuum. The effects this roller coating had on torsional deflections were determined using the analysis of reference 12. In that study, it was shown for a specific pair of steel rollers that a 30 percent increase in deflection over noncoated rollers would result with a 2.5 μm coating of material (having an elastic modulus 100 times less than steel) under a static traction force one-fifth the normal load. For the roller drive evaluated in this investigation, the gold coating was thinner (less than one-tenth the thickness of the previous case) with an elastic modulus much higher (one-third instead of one-hundredth that of steel) under a static traction force one-tenth the normal load. Thus, it was concluded that the gold coating had a negligible effect on torsional stiffness. It should be noted that the stiffness of a roller mechanism design with a relatively thick polymer or elastomer coating would probably be less than with a gold coating.

Ratio effects. - Static torsional stiffness is also dependent on the ratio of the drive and number of planets as shown in figure 3. This plot was generated for a simple, single-row planetary roller drive having the sun as input and ring as output. Suitable ring diameter and input shaft, output shaft, planet bearing and support structure stiffnesses were chosen for a maximum output torque of 170 N-m (1500 in.-lb). For this plot, output torque, ring diameter, contact ellipticity, available and applied traction coefficients,

input shaft stiffness, and output shaft stiffness were held constant. For a simple planetary, there exists a maximum ratio for each number of planet rollers without planet roller-to-roller interference. Also, there is a practical limit to speed ratio (approximately 7) in a simple planetary above which the size of the sun roller relative to the ring roller becomes so small as to unfavorably overload the sun roller contact for appreciable torque transfer.

In general, effective stiffness increases most rapidly with ratio when planet bearings and support posts are stiff (upper set of curves in fig. 3). This is because the input shaft stiffness becomes more dominant (proportional to ratio squared at output) when the bearings and supports are stiff. Thus, in maximizing drive stiffness or comparing drives of different stiffnesses, ratio, individual component stiffnesses, and sizes must all be considered.

Comparison with gears. - A comparison of the theoretical stiffness of equally sized gear and traction roller pairs made of steel showed that traction contacts were typically two or three times stiffer than gears under comparable loads (ref. 13). Figure 4 shows the stiffness of traction contacts relative to comparably sized and loaded gears plotted as a function of gear tooth size (diametral pitch). The method used to analyze gear stiffness considers the local Hertzian normal compliance and tooth beam bending. It also considers standard undercut and fillet bending and shear as well as foundation flexibility (ref. 14).

It is apparent from figure 4 that gear mesh stiffness is relatively insensitive to the number of teeth (diametral pitch) or the torque level and that fluctuations between two relatively discrete levels occur as the load is transferred between single-tooth and double-tooth contact. This stiffness fluctuation contributes to velocity fluctuations in a loaded gear train, in addition to fluctuations from normal geometric tooth (unloaded) errors. In contrast, the stiffness of a traction drive contact is essentially constant for a given load, although some degradation with increased transmitted torque will occur as shown.

## RESULTS AND DISCUSSION

### Verification of Compliance Model

Simple contact rig. - Data that can verify a compliance analysis of torsionally strained contacts are few in the literature. To corroborate the analysis used, tests on a simple configuration were conducted at NASA Lewis Research Center. The apparatus used consisted of a 7.6 cm (3.0 in.) diameter crowned roller loaded against a flat (0.05 μm surface finish) plate (see sketch in fig. 5). Normal loads up to 4450 N (1000 lb) could be applied by spherical roller bearings on the roller's support shaft. Torque was applied to the shaft by an arm and weight system. Linear displacement probes and dial indicators measured the circumferential deflections of an arm fixed to the roller. Preliminary compliance measurements showed that test rig flexibility had to be measured and subtracted from the deflections of the traction roller.

Contact stiffness. - Comparison of predicted and measured compliance for the roller/plate contact is shown in figure 5 for a normal load of 4450 N (1000 lb). The slope and thus the roller contact stiffness of the data agree well with the theoretical predictions. Stiffness is relatively constant up to the normal maximum torque operating limit set by the normal loading mechanism. Of course, without an autoloading mechanism, stiffness dramatically drops as the slip torque is reached as indicated by both the data and the theoretical model. The 5 to 6 arc sec scatter between the data and the theory in the mid-torque region is believed to be due to a presently unaccounted for nonlinearity in rig flexibility at the arc second level.

## Roller Actuator Stiffness

Test setup. - Static torsional stiffness measurements of the drive with the sun roller (input) locked and torque applied to the output shaft were performed. Torque was applied to the transmission through a calibrated torque meter using a smooth hydraulic piston loading system. Angular displacements of the output shaft were measured using an eddy-current proximity transducer mounted at a 14 cm (5.5 in.) radius. The effects of rig mounting flange flexibilities were minimized by mounting the position transducer directly to the housing mounting flange. Output shaft displacements were corrected electronically for small windups noticed at the input shaft using a second eddy-current probe mounted at the input shaft. On the average this correction amounted to only 4 percent of the output shaft rotation. The angular resolution of the measurement system was 1.9 arc sec. Output shaft torque and angular deflection traces were recorded on an x-y chart recorder revealing drive stiffnesses and hysteresis.

Experimental results. - The torque-angular deflection trace of the drive preloaded to 50 percent rated torque capacity (fixed at the sun shaft) is shown in figure 6. These traces were obtained by repeatedly cycling (2 cycles shown in figure) over positive and negative torque values. Inelastic displacements from contact microslip resulted in some hysteretic (microslip) loss during torque reversals. However, the slope of the torque-angular deflection curve is constant across the zero torque line, thus indicating no "backlash" is present. Backlash would appear in this trace as a horizontal or "zero stiffness" line. This inherent, backlash-free behavior of traction rollers is a decided benefit for mechanism control systems that typically must position a load around a desired set point.

Torsional stiffness was graphically determined from the torque-angular deflection trace at the zero torque crossing point and was found to be 230 000 N-m/rad (170 000 ft-lb/rad) ±10 000 N-m/rad. This is roughly one-third the initial predicted value. Drive stiffness was relatively constant with applied torque for the 50 percent preload case up to 40 percent design torque. However, a significant loss in stiffness occurs at torques above the preload setting due to rotation of the loading mechanism. This is normally not a serious problem with most positioning mechanisms since stiffness at the torque crossing is most critical. Stiffnesses with drive roller normal loads set to 75,

100, and 125 percent rated torque capacity were found to be 210 000, 240 000, and 250 000 N-m/rad, respectively.

Individual stiffness measurements of key drive components were made to investigate the discrepancy between the measured and predicted drive system stiffnesses. The two largest contributors to drive compliance are the spider cage support structure and the second-row planet support bearings. In conducting each of these tests, loading conditions were imposed which closely duplicated those in the drive. The stiffness of the spider cage was measured while installed in the drive by measuring the angular deflection of the spider cage about the center line of the drive using a similar eddy-current probe setup as described earlier. The measured linear stiffness reflected to the output shaft was 990 000 N-m/rad (730 000 ft-lb/rad), approximately half that predicted analytically using the simple beam model. Evidently, a detailed finite element model would be needed to provide better stiffness estimates for the relatively complicated spider cage (see fig. 1).

Radial stiffness measurements of four of the drive's cylindrical roller planet bearings were made in a specially designed loading fixture with the same setup that exists in the second-row planet rollers. Two bearings were loaded in tandem with a calibrated test machine fixture (fig. 7). Displacement measurements were made of the inner race relative to the outer race with a differential electronic indicator system with a resolution of 0.1 μm (5 μin.). Data for one of the bearing tests, typical of the load-dependent stiffnesses for each of the four bearings tested, are shown in figure 8. Comparing these data to those predicted by theory of reference 9, assuming a nominal 5 μm (0.0002 in.) diametral clearance shows a significant difference in the slopes or radial stiffnesses near zero load. The measured radial stiffness is approximately 30 percent of that predicted near zero load, approaching 60 percent of the predicted value at higher radial loads. The test data reveal a "settling-in" region as the load is first applied; this behavior is not reflected by the bearing deflection model.

The measured stiffnesses of the bearings and the spider cage were much less than the initial predictions indicating areas where drive stiffness was sacrificed. For comparison purposes, the measured stiffnesses of these two components were used in place of their original predictions (table II) to recalculate an overall predicted drive stiffness at zero-torque load. This stiffness of 370 000 N-m/rad (270 000 ft-lb/rad) is now 60 percent higher than that measured for the drive system.

When analyzing the contribution of the planet bearings to drive stiffness, both theoretically and using actual bearing data, it was assumed that all planet bearing supports shared the load equally. Due to manufacturing tolerances for bearing post locations, the bearings on the test drive are likely to be out of perfect position. Thus, at initial load application only one or two of the supports may be, in fact, loaded. In view of this nonideal load sharing, a decrease in the effective planet bearing system stiffness would be expected. For instance, if it were assumed that only two of the five bearing supports were active at the initially applied torques, then the effective bearing support compliance would increase by a factor of 2.5, resulting

in a recalculated drive stiffness of 230 000 N-m/rad (170 000 ft-lb/rad). This stiffness agrees exactly with that measured.

It is clear that structural component and bearing compliance dominate the overall stiffness of the drive. Even doubling or tripling compliance of the traction drive contacts themselves would be expected to have only a relatively minor overall effect.

Based on these results, drive stiffness improvements resulting from a redesign of the second-row planet support structure were analytically considered. Machining the spider cage from beryllium with more rigid connections for planet bearing posts would be expected to improve this component stiffness by 90 percent. Using preloaded or line-to-line fit cylindrical roller bearings would remove the initial "settling in" behavior observed in the bearing radial stiffness measurements, giving appreciable higher stiffness at zero load (zero drive torque).

## Torque Ripple/Breakaway Torque

Apparatus. - Tests were conducted to determine (approximately) the torsional ripple/attenuation characteristics of the roller actuator. A variable-speed dc motor drove the high-speed shaft of the actuator. Steady torsional loads were applied to the output shaft through a pulley/weight system by lifting dead weights. The steady-state (or dc) component as well as the fluctuating (or ac) component input and output torque signals were measured using torque meters and were recorded on a strip chart recorder. The roller actuator normal loads were set for 50 percent maximum torque capacity. System calibration was required because of unavoidable torsional ripples caused by the variable-speed motor input and a mild resonant vibration on the cable-mass system at about 4 Hz. Calibration was carried out using a "dummy" shaft directly coupled between the input and output torque meters with the roller drive removed.

Torque ripple test results. - The variations of roller actuator input and output torque signatures for one complete output shaft revolution are shown in figure 9. The actuator was driven at 10 and 20 percent of maximum speed and at three torque levels corresponding to 15, 25, and 31 percent of maximum torque at 50 percent preload. Data for both input and output torque are presented with the ripple shown as a percent variation (plus/minus) of the noted steady-state torque for the 10 percent speed case. Data collected at 20 percent speed showed virtually the same trends. The figure shows that the input torque varied approximately 7 to 8 percent while the output torque varied on the order of 0.3 percent. If no attenuation (damping) was present, then input and output torque percent fluctuations would be expected to be about the same. This suggests that the drive does not excite or amplify torsional oscillations but, in fact, helps to attenuate vibration through Coulombic damping. The traces appearing in figure 9 were taken with prerun rollers having less than perfect surface condition. Thus, these traces are considered to represent a conservative view of the smooth torque transmitting capability of the test drive.

In contrast, gearing must be of high precision to minimize the torque ripple produced by kinematic errors from inherent tooth spacing inaccuracies and flexible tooth bending under load. However, even very precise gears will produce some meshing excitations as the transmitted load is passed from single tooth to double tooth contact and back.

Breakaway torque. - Static frictional torque, or the minimum torque applied to the input shaft necessary to rotate the drive without any load, was measured for various drive preload settings early in the test program. This relatively small breakaway torque is present at any drive speed and makes up a part of the rolling power losses. Breakaway torques at the input ranged from 12 oz-in. at 35 percent preload to 21 oz-in. at 56 percent preload. For all of the measured preload settings up to 100 percent, breakaway torques were less than 1.9 percent of maximum allowable torque. A tradeoff between low breakaway torque and loss in stiffness due to loading mechanism travel must be made by the designer in setting the proper preload.

## Positional Accuracy

Apparatus. - A simple test was devised to determine the positional accuracy of the test drive under load in an open-loop control mode. Tests were conducted by driving the input precisely 64 revolutions under four steady torque load levels by raising a weight at a constant speed. The system was then "unwound" by rotating the input shaft back to its initial position while maintaining torque in the same direction. Accuracy measurements in terms of the difference in output shaft angular position before and after rotation were made using a micrometer/lever arm system that could easily resolve angular positions to within 8 arc sec of a degree. Starting and ending positions of the input shaft were precisely reregistered using an indexing arm that contacted against a precision machined surface.

Accuracy results. - Data collected for average angular positional error shown as a percentage of total rotation are given for various output torque loads in figure 10. The percent angular positional errors of the output shaft were calculated by dividing the difference between output shaft starting and ending positions by the four revolutions made. As shown in figure 10, the angular error increased with applied torque load ranging from 0.08 percent under 5 percent load to a maximum of 0.98 percent at 31 percent of maximum allowable torque while drive normal loads were set at 50 percent of the maximum value.

These small errors in reproducing commanded input position are caused by two unavoidable characteristics of roller drives. The phenomenon of rolling creep under torque loads is the major contributor to open-loop positional inaccuracy. As each pair of rollers roll over each other under a steady torque, there is a small relative speed difference which is seen at the output as lost motion. The creep or positional error shown in figure 10 increases with torque as predicted by equations (2) and (4) of the appendix. At low torques, or when the drive operates unloaded, very small kinematic errors due to imperfectly ground rollers (diameter tolerance, out-of-roundness, lobing,

waviness, etc.) can be present. Hence, for critical point-to-point (PTP) positioning applications the control system must be closed loop in order to feedback output position when using roller actuators. This is not uncommon for such precision positioning mechanisms.

### Long-Term Holding Ability

In some critical mechanism applications, the ability to position and then hold a load in that fixed position without a brake mechanism is a decided benefit. Though not a critical design requirement of the roller actuator, the drive's long-term holding ability was tested for three steady torques (25, 50, and 70 percent maximum design torque) using the same loading and measurement systems as described in the Roller Actuator Stiffness section. Drive roller normal loads were set at 75 percent of maximum. Total drive output shaft rotation was measured for 24 hr with the input shaft locked (fig. 11). Initial drive torsional windup due to load application is shown at time zero.

The additional rotation (drift) shown is mainly attributed to the tangential, time-dependent yielding or plastic creep of the heaviest loaded interlocking surface asperities. This deformation, greatest just after startup, asymptotically approaches a steady-state value as stress-strain equilibrium is reached.

## SUMMARY AND CONCLUSIONS

Operating characteristic tests were conducted on a high-torque roller drive suitable for a space vehicle actuator application. Analysis and test results are presented for a 16:1 ratio 430 N-m (320 ft-lb) output torque drive having two rows of stepped planet rollers. This drive operates without liquid lubrication using traction rollers ion plated with 0.2 μm of gold. Estimated service life for the prescribed duty cycle is at least 1600 hr for this thickness of gold. The drive is nominally 25 cm in diameter by 22 cm in length and weighs 10 kg. The output torsional stiffness of the drive was measured by torsionally loading the output shaft while the input shaft was locked. Theoretical calculations of the drive's torsional stiffness were made and agreed within 60 percent of the measurements at low torque when including the effect of the measured compliance of the second-row planet support structure and bearings. The method of calculating traction contact torsional stiffness as a function of normal load, applied traction force, and roller dimensions among other variables was reviewed. Torsional ripple tests were conducted at 10 and 20 percent speed for torques up to 31 percent of allowed torque at 50 percent fixed preload. Open-loop positional accuracy of the drive's output shaft was also measured as a percent error of total rotation as a function of driven torque. Based on these findings, the following results were obtained:

1. Planet bearings and support structure cause the greatest loss in drive stiffness, accounting for more than 50 percent of total.

2. Traction contacts are very stiff contributing just 9 percent to system compliance based on an experimentally verified traction compliance model.

3. Drive exhibited zero backlash but displayed a small hysteresis displacement of 8 arc sec.

4. Torque ripple was extremely small. Coulombic damping attenuated torque oscillations from 7 to 8 percent at input to 0.3 percent at output.

5. Open-loop positional accuracy of drive degraded with transmitted torque. A closed-loop control system is needed for arc second positioning applications.

6. Drive demonstrated ability to hold torque for extended periods of time with drifts in position of the order of arc seconds.

## - APPENDIX -

## CONTACT TORSIONAL STIFFNESS ANALYSIS

When two elastic bodies, such as traction rollers, are brought into contact and loaded under a system of forces, deflections occur. When the load is a normal force, the deformation and contact area are given by the classical theory of Hertz. Adding a tangential force produces a relative deflection of the bodies in the tangential direction. A magnified cross-sectional view of the contacting bodies under these conditions is shown in figure 12. If the bodies are rollers or balls which are allowed to rotate under these forces, fresh unstrained material passes through the effective contact region which increases the relative displacement of the bodies. The analysis of reference 11 as it relates to traction roller contacts will be briefly reviewed herein.

Analytically, contact compliance is treated as a boundary value problem in elasticity with several conditions to be satisfied. In simplified terms, the first constraint is that the addition of a tangential force to the contact does not alter the Hertzian normal pressure distribution. Second, all the assumptions inherent to the Hertzian solution are retained, including nonwarping of the contact surface, bodies not too closely conforming in the contact area, body radii large in comparison with contact dimensions, and like elastic properties of the two bodies. Third, the contact region is divided into two zones: one with "microslip" or relative motion between the mating surfaces, and one where the two surfaces are "locked" together. In the slip region, the applied shear stress (traction force per unit area) is assumed to reach its limiting value, proportional to a constant traction coefficient $\mu$ times the local normal pressure in accordance with Coulombic fiction. Within the locked region, the applied shear stress is less than $\mu$ times the normal pressure. Outside the Hertzian contact area, traction is zero. The local deflection of a point on the surface with respect to a distant point in the body is constant over the locked region and varies over the slip region and outside the contact area. Far away from the contact, the strain is zero.

These considerations apply equally to two cases: static loading and rolling under an applied tangential load. Deformation in a steady rolling contact is viewed from a stationary coordinate system with the origin at the center of contact. Material of each contacting body flows through the contact region under a strain field which is invariant with time. The static case, which is static only in the sense there is no rolling (forces and deflection can vary with time), consists of torquing two contacting rollers and allowing only the motion due to contact compliance to occur.

### Static Roller Compliance

For a pair of contacting static rollers under equal and opposite normal loads and proportional and opposite torque loads, the static torsional compliance $C_t$ of <u>one</u> roller was found in reference 11 to be

$$C_t = \frac{1}{2\pi G a r^2}\left(1 - \frac{T}{\mu N r}\right)^{-1/3} \Gamma \qquad (1)$$

where

r rolling radius of roller under consideration

G shear modulus of the material

a Hertzian semiwidth of elliptical contact area (perpendicular to direction of rolling)

T applied torque

$\mu$ available traction coefficient

N normal load

$\Gamma$ contact geometry parameter which depends only on Poisson's ratio and contact ellipticity ratio a/b

Alternately, the torsional stiffness $k_t$ of a traction roller is defined as the reciprocal of the compliance (or $c_t^{-1}$). It can be seen from the previous equation that torsional stiffness is not linear with torque. It should be noted that compliance (or stiffness) is defined as the slope of the deflection versus torque (or torque versus deflection) curve for each particular roller contact.

## Rolling Contact

The foregoing analysis treats the static case where the rollers' contact point remains fixed in space under the line of centers between the rollers' centers. The only motion is equal and opposite circumferential deflection. However, as explained in reference 11, even a simple roller pair, with a locked output shaft will see some rolling. Under certain conditions rolling motions will alter the contact torsional compliance. Thus, rolling contact effects are included in the stiffness analysis as summarized here.

In drives where one or more pairs of contacting rollers are in series with a driver and driven, there are essentially three sources of rolling motion which affect the contact torsional compliance and are superimposed on the static compliance. The first is gross rotation of the driven element. In a slewing operation, steady-state rotation and associated creep do not affect the roller contact torsional stiffness. However, in a system where torque is applied and the driven inertia accelerates from rest, the early motions can affect the contact stiffness. The second source is downstream torsional compliance. Even if the driven element is fixed so that no gross rotation occurs, the components coupling it to the roller drive will have finite stiffness. Similarly, in a multistage drive, each roller contact has a finite stiffness.

Thus, each roller contact will see the motion produced by deflections downstream. The third source of rolling motion is the rotation induced by the static compliance of the rollers themselves which causes some very small rotation. This motion tends to sweep roller surface material in and out of the contact as if it were rolling.

Two contacting bodies which are rolling with a globally steady velocity and tangential load will experience a small, relative velocity difference known as creep. This velocity difference is due to the state of the elastic strain in the surfaces as the roller material is swept through the contact region. Material is tangentially stretched and compressed, or vice versa, and the surface traction forces which locally exceed the coefficient of friction cause areas of microslip which relieve the strain without gross sliding. Creep is of great engineering importance because the product of creep and tangential force is a measure of the power loss.

Several theoretical models of creep have been proposed and evaluated. The expressions for determining the value of creep for a dry contact chosen in reference 11 were

$$\frac{\Delta U}{U} = \frac{3\mu N}{G\pi ab}(1 - \nu)(1 - K) \tag{2}$$

where

$\nu$ Poisson's ratio
b Hertzian semiminor contact width (in direction of rolling)

and

$$\frac{\Delta U}{U} = \frac{(U_1 - U_2)}{(U_1 + U_2)/2} \tag{3}$$

where

$U_{1,2}$ solid-body surface speed of rollers 1 and 2

K dimensionless measure of the locked portion of the rolling contact determined from

$$\frac{F_x}{\mu N} = 1 - \frac{3}{2}\left\{\left(2K - K^2\right)^{1/2}\left[1 - \frac{2}{3}K + \frac{1}{3}K^2\right] - (1 - K)\sin^{-1}\left[\left(2K - K^2\right)\right]^{1/2}\right\} \tag{4}$$

where

$F_x$ tangential force in rolling direction

To calculate the motion due to rolling creep, the motion itself is desired rather than the rate of motion by which creep is normally defined. As shown

in reference 11, creep at constant torque can be expressed as angular motion $\theta$ over some small time interval $\Delta t$ by

$$\frac{\Delta\theta}{\theta} = \frac{X_1/r_1 - X_2/r_2}{(X_1/r_1 + X_2/r_2)/2} \tag{5}$$

where

$X_{1,2}$ solid-body surface motion of rollers 1 and 2

$r_{1,2}$ radii of rollers 1 and 2

To utilize this analysis, loads are applied incrementally. At each small torque increment, values of K, creep rate, and angular motion are calculated for each of the simple contacts. The resultant rolling contribution is combined with the static deflection obtained in that torque increment using the principle of linear superposition. Appropriate values of motion are found using this incremental approach for each roller contact which include the effects of structural deflection.

The direct superposition of rolling and static compliance is not strictly correct since the surface stress fields and microslip regions are not the same. However, as was shown in reference 11, this method provides a reasonable approximation of roller contact stiffness, especially for positioning mechanisms which spend much of their time "hunting" for position about the zero torque crossing region.

## REFERENCES


1. Bryan, J.B.: Design and Construction of An Ultraprecision 84 Inch Diamond Turning Machine. Precis. Eng., vol. 1, no. 1, Jan. 1979, pp. 13-17.

2. Steinetz, B.M., et al.: An Advanced Pitch Change Mechanism Incorporating a Hybrid Traction Drive. AIAA Paper 84-1383, June 1984.

3. Nasvytis, A.L.: Multiroller Planetary Friction Drive. SAE Paper 660763, Oct. 1966.

4. High Torque CMG Rotary Actuator. (ACS-10357, General Electric Co.;NASA Contract NAS5-20298) NASA CR-122458, 1972, p. 2-1.

5. Auclair, G.F.; and Seminski, R.B.: Roller-Gear Drive Development. (ACD-10104, General Electric Co.; NASA Contract NAS8-26213) NASA CR-103057, 1971, p. 4.

6. Spalvin, Talivaldis; and Buzek, Bruno: Frictional and Morphological Characteristics of Ion-Plated Soft Metallic Films. Thin Solid Films, vol. 84, 1981, pp. 267-272.

7. Spalvins, T.: The Structure of Ion Plated Films in Relation to Coating Properties. NASA TM-87055, 1985.

8. Roark, R.J.; and Young, W.C.: Formulas for Stress and Strain, 5th ed., McGraw-Hill, 1975.

9. Harris, T.A.: Rolling Bearing Analysis, Wiley, New York, 1966, pp. 166-171.

10. Nestorides, E.J.: A Handbook on Torsional Vibration, Cambridge University Press, Cambridge, Eng., 1958, pp. 98-99.

11. Rohn, D.A.; and Loewenthal, S.H.: An Analysis of Traction Drive Torsional Stiffness. J. Mech. Trans. Automation Des., vol. 107, no. 4, Dec. 1985, pp. 573-581.

12. Kannel, J.W.; and Dow, T.A.: Analysis of Traction Forces on a Precision Traction Drive. ASME Paper 85-TRIB-45, Oct. 1985.

13. Loewenthal, S.H.; Rohn, D.A.; and Steinetz, B.M.: Application of Traction Drives as Servo Mechanisms. Nineteenth Aerospace Mechanisms Symposium, NASA CP-2371, 1985, pp. 119-139.

14. Cornell, R.W.: Compliance and Stress Sensitivity of Spur Gear Teeth. J. Mech. Des., vol. 103, no. 2, Apr. 1981, pp. 447-459.

TABLE I. - THEORETICAL STIFFNESS (FULLY REFLECTED TO OUTPUT) OF THE TEST TRACTION ROLLER DRIVE AT ZERO TORQUE AND 50 PERCENT INITIAL PRELOAD

| Element | Stiffness, N-m/rad (ft-lb/rad) | Compliance, rad/N-m (rad/ft-lb) | Percent of total compliance |
|---|---|---|---|
| Spider cage/bearing and aluminum support posts | $2.00\times10^{6}$ ($1.50\times10^{6}$) | $.50\times10^{-6}$ ($.667\times10^{-6}$) | 33 |
| Planet bearings-cylindrical roller (203) diametral clearance = 5 μm (assumed) | $2.80\times10^{6}$ ($2.11\times10^{6}$) | $.357\times10^{-6}$ ($.474\times10^{-6}$) | 23 |
| Input shaft and torque loader system (bearing balls) | $3.80\times10^{6}$ ($2.79\times10^{6}$) | $.263\times10^{-6}$ ($.358\times10^{-6}$) | 18 |
| All traction contacts ($\mu_{gold} = 0.12; \mu_{steel} = 0.2$) | $7.90\times10^{6}$ ($5.80\times10^{6}$) | $.127\times10^{-6}$ ($.172\times10^{-6}$) | 9 |
| Roller support housing backing plate (aluminum) | $8.63\times10^{6}$ ($6.37\times10^{6}$) | $.115\times10^{-6}$ ($.157\times10^{-6}$) | 8 |
| Outer housing (aluminum) | $17.1\times10^{6}$ ($12.6\times10^{6}$) | $.058\times10^{-6}$ ($.079\times10^{-6}$) | 4 |
| Bearing post depression in aluminum backing plate | $19.4\times10^{6}$ ($14.30\times10^{6}$) | $.052\times10^{-6}$ ($.070\times10^{-6}$) | 3 |
| Output shaft | $29.4\times10^{6}$ ($21.7\times10^{6}$) | $.034\times10^{-6}$ ($.046\times10^{-6}$) | 2 |
| Total drive | $.670\times10^{6}$ ($.494\times10^{6}$) | $1.506\times10^{-6}$ ($2.023\times10^{-6}$) | 100 |

TABLE II. - COMPARISON OF PREDICTED AND MEASURED STIFFNESSES (FULLY REFLECTED TO OUTPUT)

| Element | Predicted stiffness, N-m/rad (ft-lb/rad) | Measured stiffness, N-m/rad (ft-lb/rad) |
|---|---|---|
| Spider cage-bearing and aluminum support posts | $2.00 \times 10^6$ ($1.50 \times 10^6$) | $.99 \times 10^6$ ($.730 \times 10^6$) |
| Planet bearings- cylindrical roller (203) diametral clearance = 5 μm (assumed) | $2.80 \times 10^6$ ($2.10 \times 10^6$) | $.770 \times 10^6$ ($.570 \times 10^6$) |
| Total drive | $.670 \times 10^6$ ($.494 \times 10^6$) | $.230 \times 10^6$ ($.170 \times 10^6$) |
| Total drive[a] | $.370 \times 10^6$ ($.270 \times 10^6$) | ---------- |
| Total drive[b] | $.230 \times 10^6$ ($.170 \times 10^6$) | ---------- |

[a]Drive stiffness recalculated based on the measured planet bearing and spider cage component stiffnesses.
[b]Drive stiffness recalculated based on measured planet bearing and spider cage component stiffnesses assuming nonideal load sharing of second-row planet bearings.

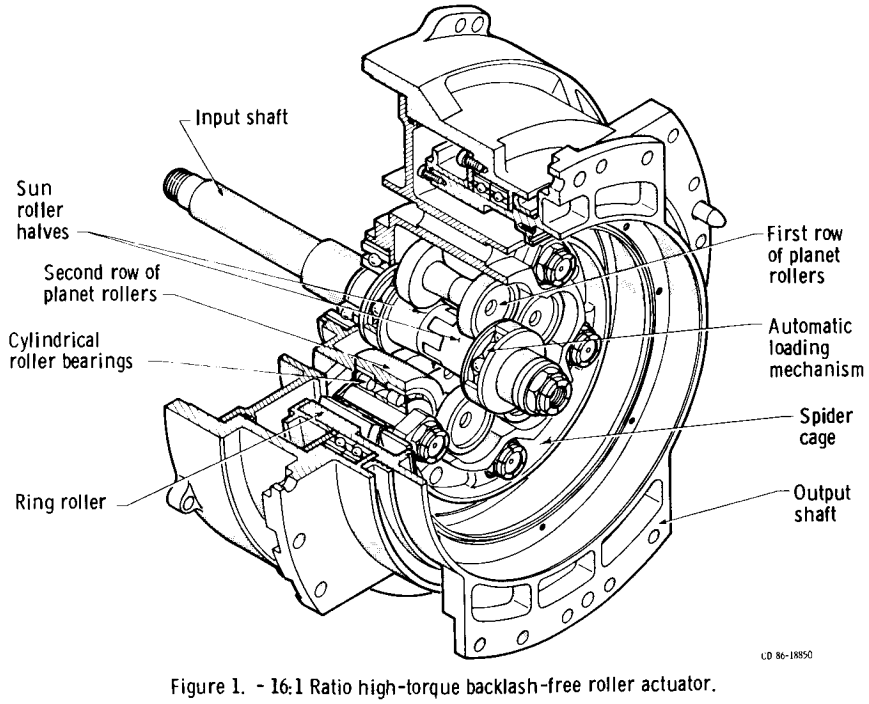


Figure 1. - 16:1 Ratio high-torque backlash-free roller actuator.

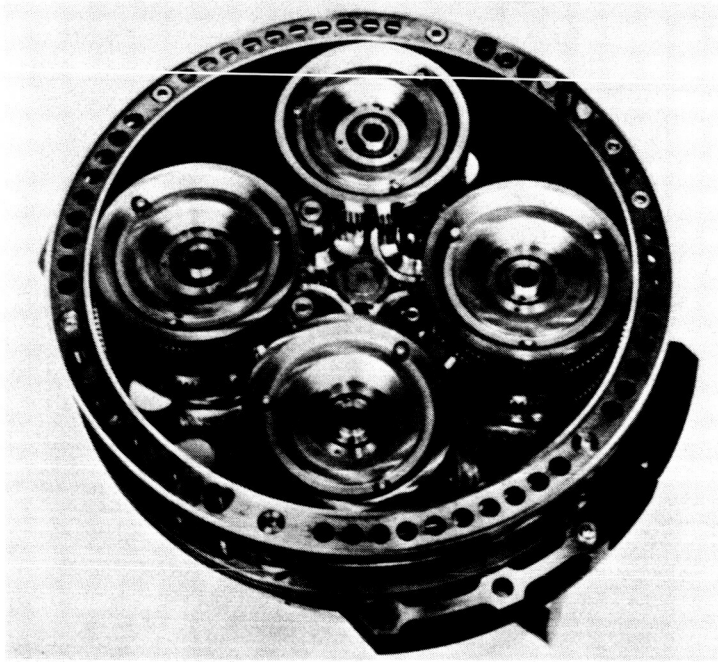

Figure 2. - 26: 1 ratio control moment gyro roller gear drive.

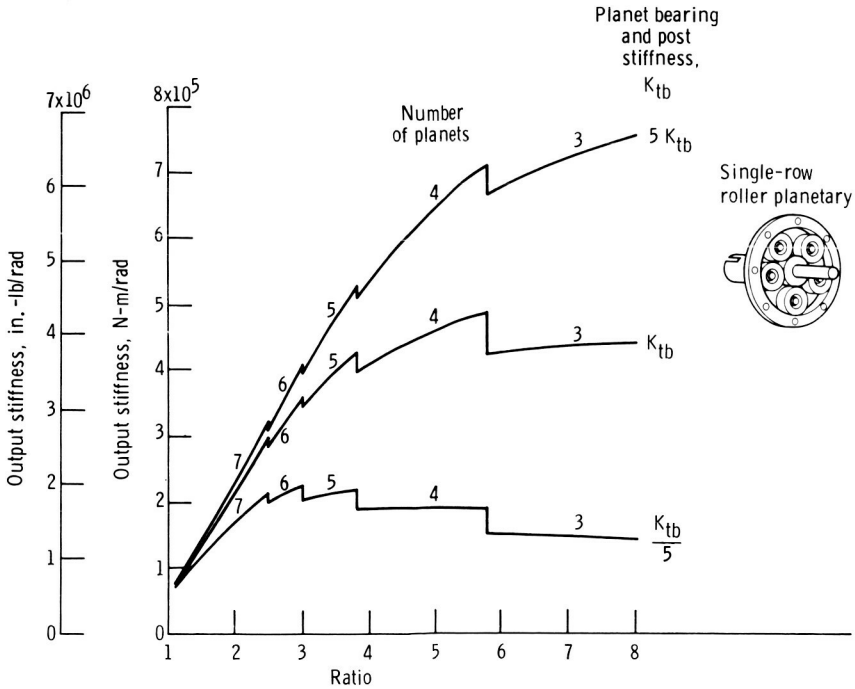


Figure 3. - Maximum torsional stiffness of single-row roller planetary as a function of ratio. Output torque, traction coefficient, contact ellipticity, ring diameter, and input and output shaft stiffnesses are constant. The number of planets is limited by planet-to-planet interference.

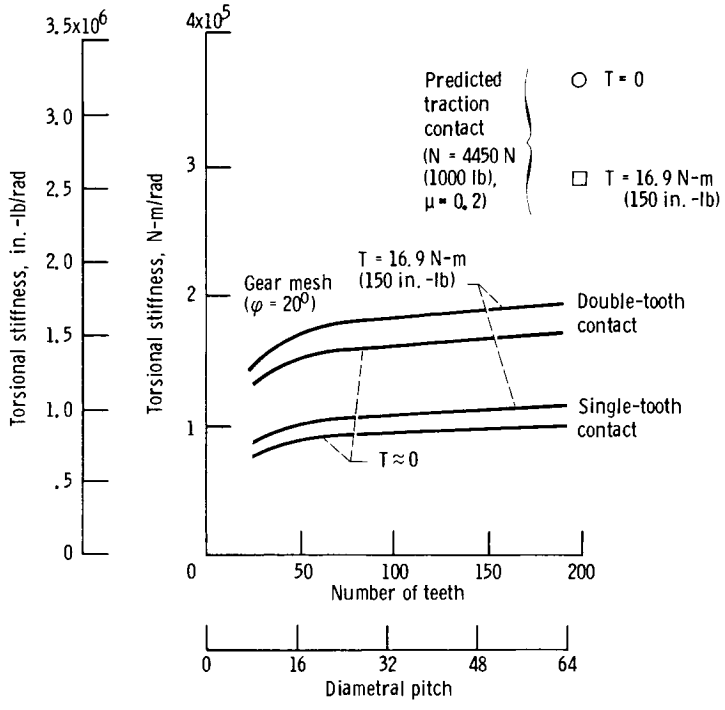


Figure 4. - Theoretical comparison of gear mesh and traction roller contact torsional stiffness at equal diameters, 76.2 mm (3.0 in.), widths, 4.57 mm (0.18 in.), and loads (ref. 13).

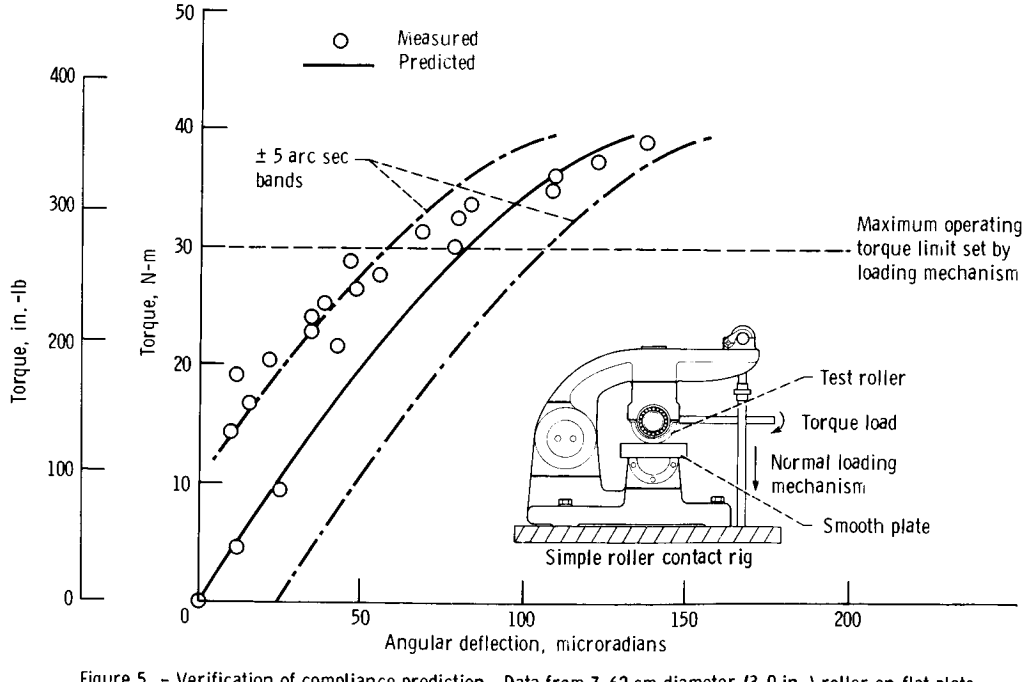


Figure 5. - Verification of compliance prediction. Data from 7.62 cm diameter (3.0 in.) roller on flat plate. Ellipticity ratio, 4.3; available traction coefficient, 0.24; normal force, 4450 N (1000 lb).

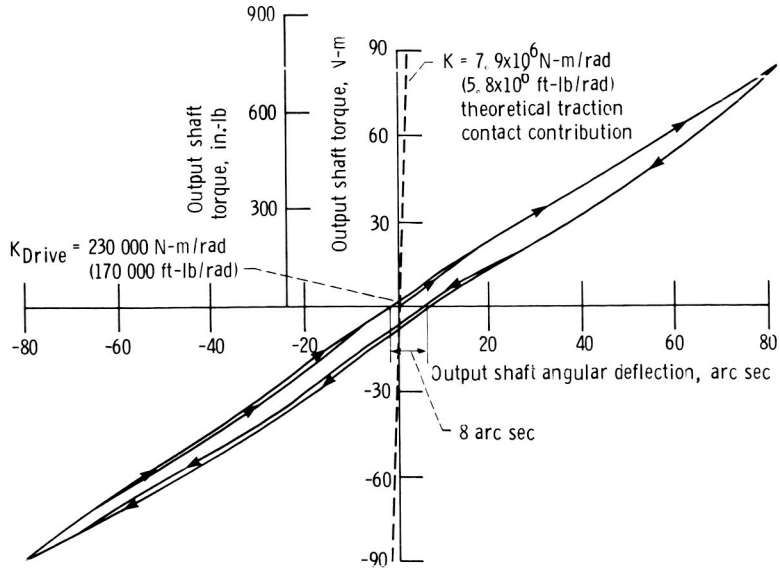


Figure 6. - Roller drive output shaft torque versus output shaft angular deflection. Sun input shaft locked; roller normal loads, 50 percent of maximum; data shown are for two full cycles of positive and negative torque.

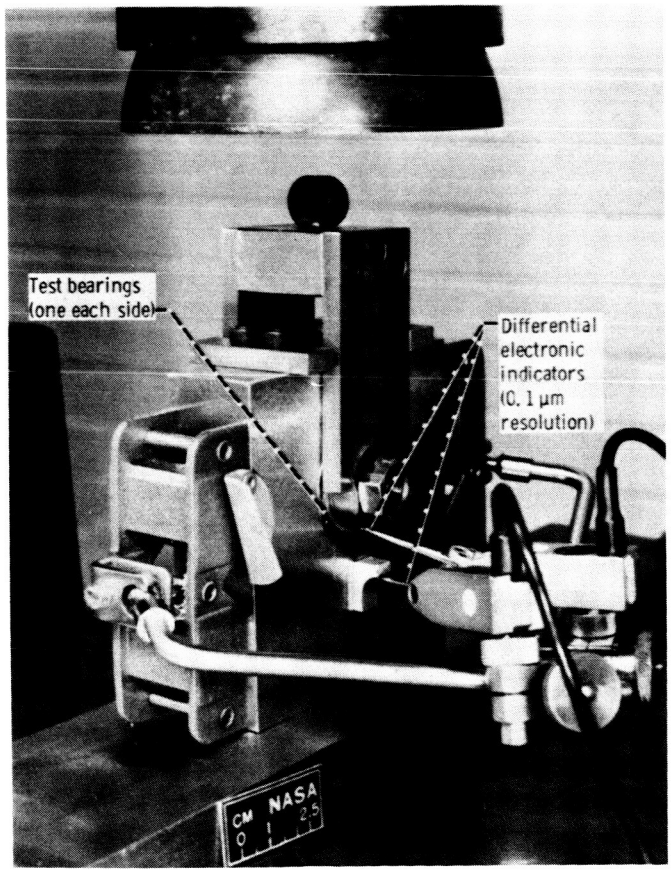


Figure 7. - Roller bearing radial stiffness test fixture.

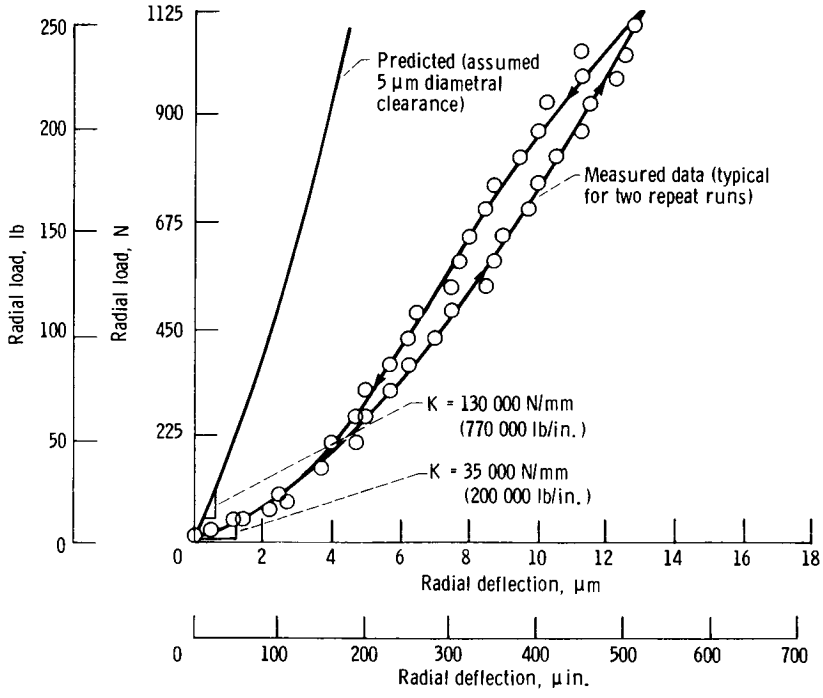


Figure 8. - Comparison of measured and predicted (using ref. 9) load-deflection characteristics for planet roller bearing. (All bearing clearance removed before taking readings.)

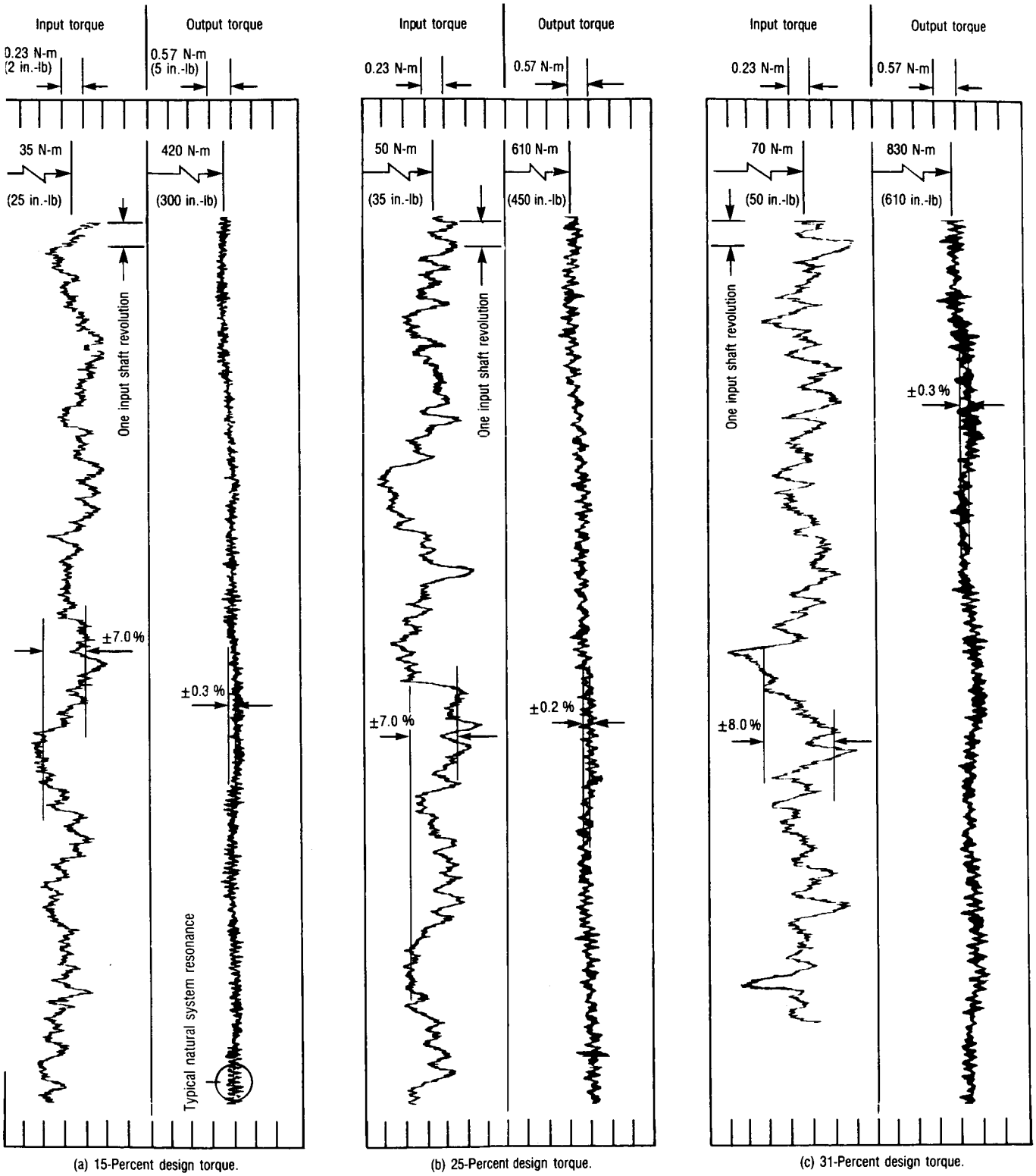


(a) 15-Percent design torque.

(b) 25-Percent design torque.

(c) 31-Percent design torque.

Figure 9. - Effect of torque on roller actuator torque signatures at input speed of 28 rpm. One full output shaft revolution shown for each torque; one input shaft revolution as indicated.

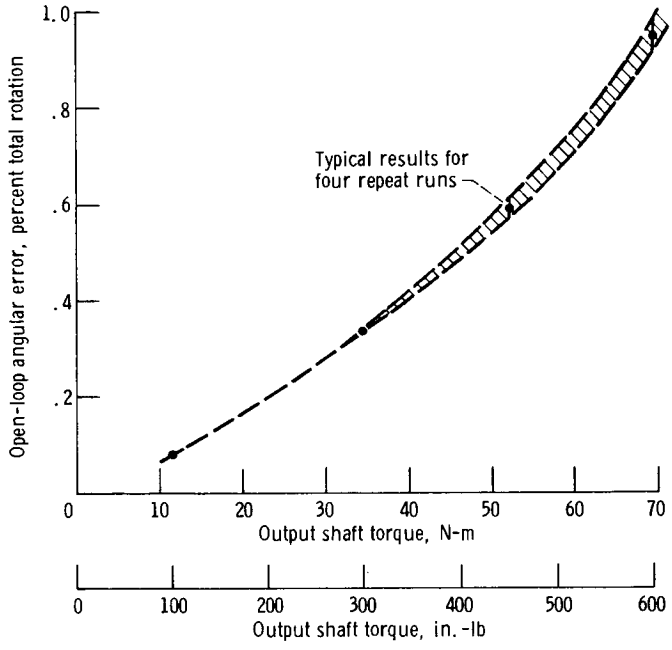


Figure 10. - Open-loop positional accuracy of roller actuator as percentage of total rotation.

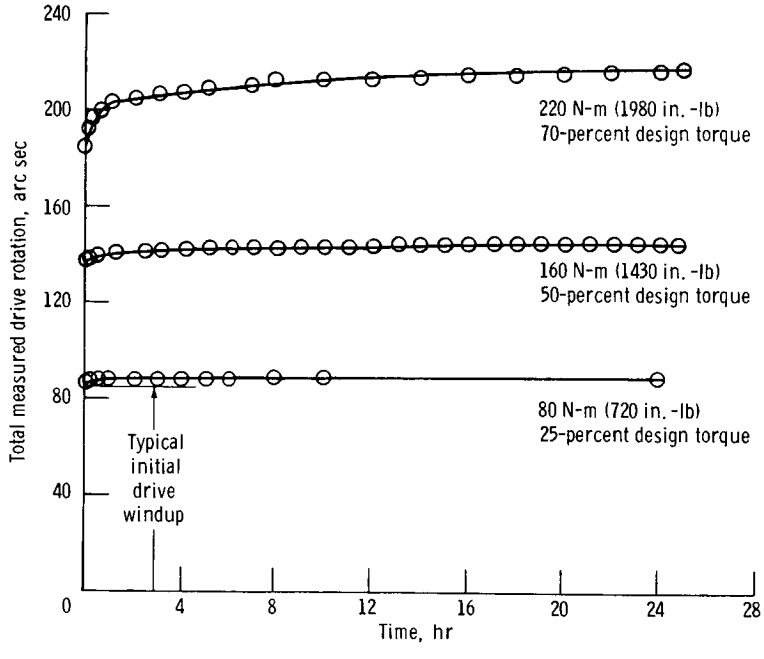


Figure 11. - Roller actuator long-term holding ability as function of percent maximum design torque. Input shaft locked; roller normal loads, 75 percent of maximum.

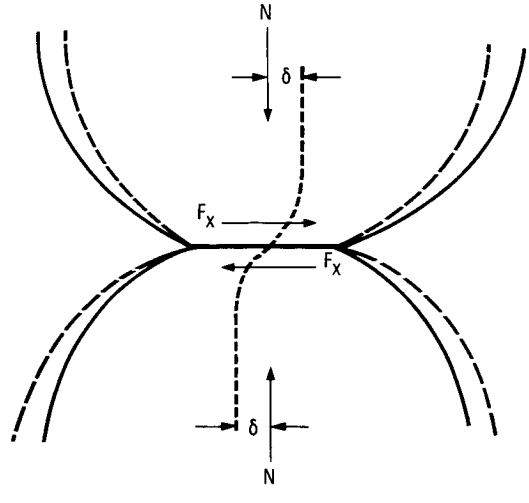


Figure 12. - Tangential deflection δ of bodies in contact under combined normal N and tangential $F_x$ loads.

# A PRECISION, THERMALLY-ACTIVATED DRIVER FOR SPACE APPLICATION

Robert C. Murray*, Robert F. Walsh*, and William H. Kinard**

This paper describes a space qualified, precision, large force, thermally-activated driver that has been developed jointly by the NASA Langley Research Center and PRC Kentron. The driver consists of a sealed hydraulic cylinder containing a metal bellows, a bellows plug, a coil spring, a spring retainer, an output shaft, a shaft guide, and a quantity of silicone oil. Temperature changes cause the silicone oil to expand or contract thus contracting or expanding the bellows/spring assembly thereby extending or retracting the output shaft.

## INTRODUCTION

The primary objective of the first reflight of NASA's Long Duration Exposure Facility, the LDEF-1B mission planned for mid-1987, will be to establish the abundance of the rare actinide group elements in cosmic rays. These abundances, which hold clues to the origin and evolution of cosmic rays, will be determined through analysis of energetic particle tracks in stacks of thin plastic sheets after the sheets have been exposed in space for 2-1/2 years on the LDEF.

When energetic particles such as the actinide cosmic rays penetrate certain plastics, the molecular bonds in the plastic at the track site are damaged, and the degree of damage is proportional to the energy that was dissipated along the track. If the plastic sheets are etched after they are penetrated by elements, conical pits will result at each track site. The damaged plastic at the track site etches much faster than the undamaged plastic, and the increase in etch rate is a precise indicator of the degree of damage to the plastic molecular structure.

With proper information and control, scientists can determine the element responsible for a given track from the observed dimensions of the etch pits. By ratioing the number of tracks in the LDEF exposed plastics which result from elements of known abundance (the platinum-lead group) to the number of tracks which result from actinides, the abundance of the actinide elements will be established.

The main problem in implementing this experiment, however, results from the fact that the temperature of the plastic stacks at the time a track is produced is a critical item of information in the analysis of etch pits. It must be known to within 1°C. The precision, Thermally-Activated Driver

*PRC Kentron, Aerospace Technologies Division; Hampton, Virginia.
**NASA Langley Research Center; Hampton, Virginia.

(TAD) which is described in this paper was developed to be the heart of the Event Thermometer (ET) system that will be used on the LDEF-1B mission.

The ET system concept is functionally illustrated in figure 1. Two plastic sheets are mounted above the detector stacks as shown. The upper sheet is movable and its position relative to the lower sheet is controlled, as a function of the temperature of the detector stacks, by the TAD. During the postflight analysis of the etched plastics, the temperature of the stack at the time a given track is produced will be determined by aligning the track etch pit in the movable sheet with the track etch pit in the fixed sheet and noting the stack temperature that was required for the driver to so position the sheets. The pits were obviously so positioned when the track was originally produced.

The specific requirements which were imposed on the TAD design to ensure that its performance will satisfy the ET requirements for the LDEF-1B cosmic ray experiment are as follows:

(1) Temperature range: -62°C(-80°F) to +49°C(+120°F)
(2) Displacement over temperature range: 5.08 cm (2.0 in.)
(3) All materials must be non-magnetic
(4) Fluids must be non-hazardous for Shuttle operations
(5) Accuracy of .046 cm per degree C(.010 in. per degree F)
(6) Adequate axial stiffness to restrain attached ET sheet during launch and landing vibration environment
(7) Minimum size and weight
(8) Maximum dimensions: 3.332 cm (1.312 in.) wide, 3.510 cm (1.382 in.) deep, and 109.38 cm (43.06 in.) long
(9) Reliability

## OPERATION

The operation of the TAD, as schematically shown in figure 2, is a result of the expansion or contraction of an incompressible fluid as the temperature of the fluid changes. A coil spring controls the position of the output shaft by applying a resisting force to the pressure force on the piston. The system will remain in equilibrium as long as the spring force balances the piston pressure force.

The operation of the TAD is dependent on the thermal expansion of the charging fluid. Referring to figure 3, potential energy is stored in the bellows and coil spring when the TAD is pressurized at room temperature. As the temperature decreases and the volume of fluid contracts, the bellows and coil spring release some of their potential energy to keep the bellows piston area in contact with the oil column. As the temperature increases, potential energy is increased in the bellows and coil spring. Since the output shaft is welded to the bellows plug, the output shaft tracks the movement of the bellows and fluid.

## HARDWARE

The sizing of the driver is dependent upon the coefficient of thermal expansion of the charging fluid; therefore, the first component of the driver selected is the fluid. Dow Corning 200, 10 centistokes silicone oil was chosen for the following reasons: (1) large rate of thermal expansion, (2) high flash point, (3) low pour point, (4) non toxic, (5) readily available, and (6) relatively inexpensive. The outside diameter of the TAD was constrained to be no greater than 3.332 cm (1.312 in.) in order to fit in the allotted experiment canister space. Seamless, 321 stainless steel tubing, 3.175 cm outside diameter x 2.565 cm inside diameter (1.25 in. x 1.01 in.) was selected for the pressure shell. A thin, flexible metal bellows was selected as a means of storing and releasing potential energy during temperature cycles while sealing around the output shaft to prevent fluid leakage. The bellows was designed to function over the operating displacement range for $>10^6$ cycles while mechanical stresses remain within the proportional limit of the bellows material. A coil spring was designed to increase the axial stiffness of the TAD and to assist the bellows by releasing potential energy at the lower temperature range where the bellows has expanded to its "as-formed" length. The bellows material is 321 stainless steel, .0152 cm (.006 in.) thick. The coil spring material is Inconel X750, .318 cm (.125 in.) diameter wire. The output shaft is made of 321 stainless steel rod, .794 cm (.3125 in.) dia. The output shaft is guided in the front support by a bushing, and supported in the oil reservoir by a cylindrical guide. Both of these parts are made of phosphor bronze, CDA 54400. The phosphor bronze provides a good sliding surface on stainless steel while closely matching the thermal growth rate of stainless steel. The coil spring is captured between the cylindrical shaft guide and a spring retainer made of 347 stainless steel. The front support and rear support are made of 347 stainless steel.

## ASSEMBLY AND PRESSURIZATION

After machined parts are completed and the bellows is formed, the bellows assembly is fabricated by loosely assembling the front support, bellows, bellows plug, and output shaft. Weld joints at three locations seal the bellows to the front support, bellows plug, and output shaft (figure 4). The bellows assembly is placed inside the pressure shell and a full penetration weld joins the front support and pressure shell. From the open end of the pressure shell the remaining internal parts are assembled in the following sequence: (1) coil spring retainer, (2) coil spring, (3) shaft guide, and (4) capture nut (figure 5). Figure 6 shows the assembly of the internal components; for clarity, the pressure shell is omitted. The capture nut is torqued in order to stretch the bellows .96 cm (.38 in.) which increases the effective length of the bellows. The rear support is positioned in the pressure shell and a full penetration weld joins the two (figure 7). Radiographic and dye penetrant inspections of each weld are performed sequentially during the assembly process to ensure the integrity of each joint. After the TAD components are assembled, a vacuum pump is

attached to the fill tube through a valving arrangement. The internal cavity of the driver is evacuated and valved off. A valve attached to the liquid sump/pump is opened, allowing the silicone oil to fill the driver. The hand pump is then operated slowly to increase internal pressure to ~1723.8kPa (~250 psig). Since manufacturing variations in the bellows and coil springs will result in slightly different spring rates for each item, shaft displacement rather than internal pressure determines when the pressurization process is completed; thus ensuring a practically equal amount of fluid is pumped into each TAD. The fill tube is flattened, pinched off (under pressure), and dipped in solder. The TAD assembly and pressurization procedure is now complete.

## TESTING

Three types of tests are conducted on the TAD: (1) pressure testing to verify structure integrity, (2) thermal testing for calibration and survivability demonstration, and (3) vibration testing to verify workmanship and structural integrity for Shuttle induced accelerations.

Pressure testing of the TAD is an integral part of the pressurization procedure. As the output shaft reaches its calculated extended position at ~1723.8kPa (~250 psig) internal pressure, it is restrained from further movement while internal pressure in increased to ~2585.6kPa (375 psig) which is approximately 1.5 times nominal pressure. The shaft restraint is necessary to prevent the bellows and coil spring from collapsing excessively, which would exceed the material yield strength of one or both.

Thermal testing of the TAD is conducted in a NASA/LaRC thermal vacuum chamber. The driver is suspended in a bath of Dow Corning 200 silicone oil and a Direct Current Displacement Transducer (DCDT) is attached to the output shaft. Thermocouples are attached to the outer surface of the pressure shell, suspended in the oil bath, and suspended in the vacuum chamber. The chamber is cooled by liquid nitrogen which becomes gaseous as it is injected into and circulated around the chamber. The chamber is warmed by resistance heaters. Since the thermal chamber can be controlled to only $\pm$2.8°C($\pm$5°F), the oil bath is used to dampen the temperature variations.

Vibration testing of the TAD to achieve desired acceleration levels is conducted on an Unholtz-Dickie shaker fixture at NASA/LaRC. The driver is mounted in a cavity of the experiment canister and accelerated to 5.0g's in the longitudinal axis, 16.5g's in the axis orthogonal to the longitudinal axis, and 10.0g's in the other orthogonal axis. These acceleration levels generate loads which are 1.4 times limit loads due to Shuttle launch or landing.

## CONCLUSIONS

The TAD is a precision, large force driver that meets the very stringent requirements of the ET system for the LDEF-1B cosmic ray experiment. Forty-five TAD's will be flown on the LDEF-1B mission, and it is expected that TAD's will also find use in a number of other space and terrestrial applications. With properly selected fluids, fluid volumes, and bellows sizes, TAD's can offer a wide choice in performance variables--namely displacements, operating temperatures, driving forces, and response times.

TAD's obviously have applications in fluid control systems where precision valve controls are needed; for example, in manufacturing processes and in safety control systems.

A single TAD may be used to drive a large bank of thermal control louvers for spacecraft or for terrestrial buildings. The fact that part of the fluid volume can be remotely located and piped to the driver allows flexibility in the thermal control designs and, in some cases, performance improvements.

TAD's may also be used to compensate for thermal expansion and distortion of spacecraft structures where extreme dimensional stability is essential.

In conclusion, the TAD features may be summarized as follows:

- Precision, thermally-activated displacement and position control
- Wide choice in performance and operating variables
- Reliablility, and
- No power required

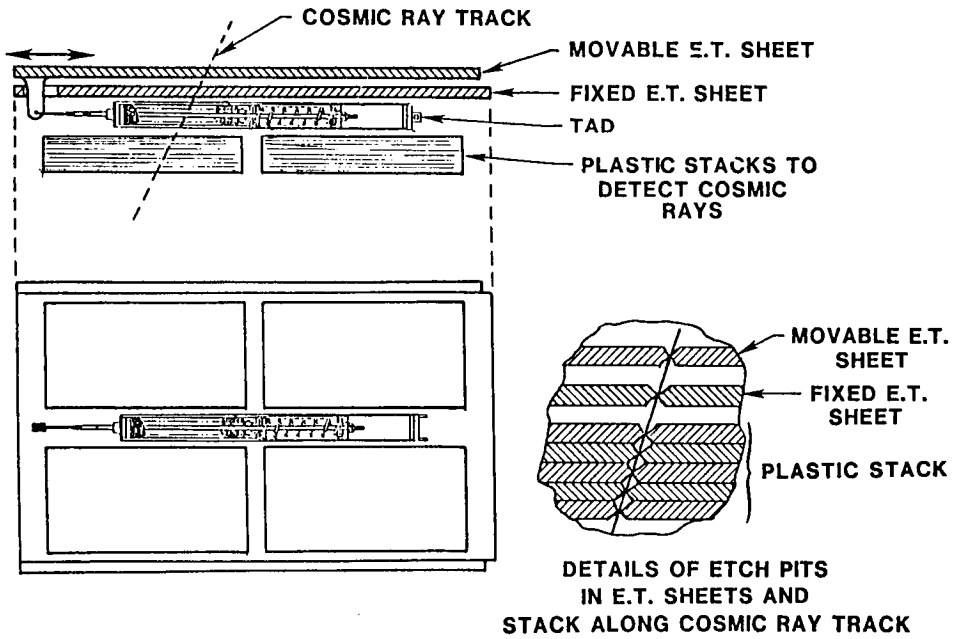


Figure 1. - Schematic of event thermometer for cosmic ray experiment to fly on LDEF 1B mission.

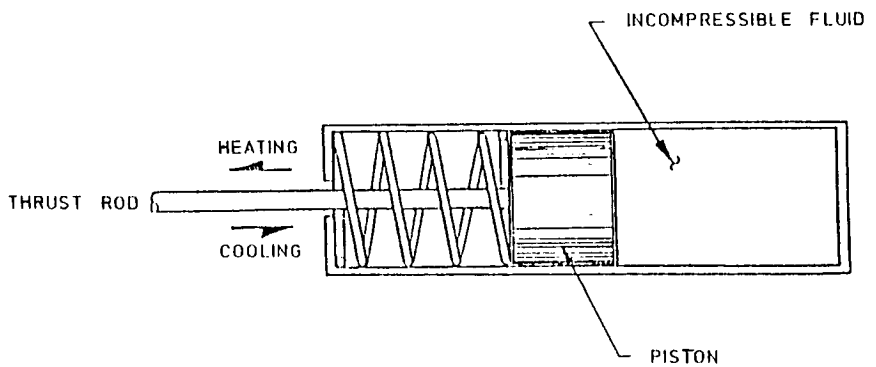


Figure 2. - Operating principle schematic.

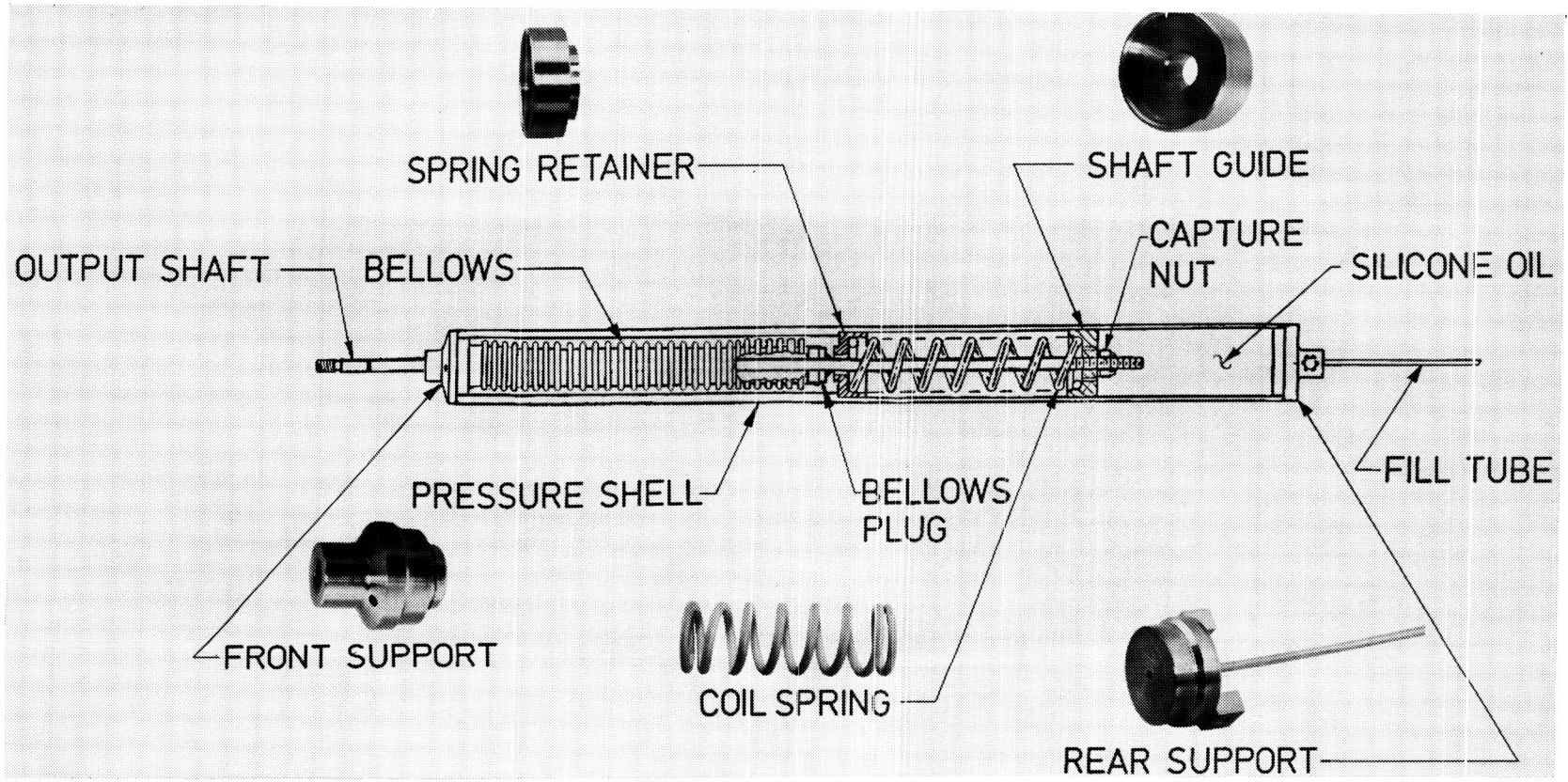


Figure 3. - Thermally-activated driver schematic.

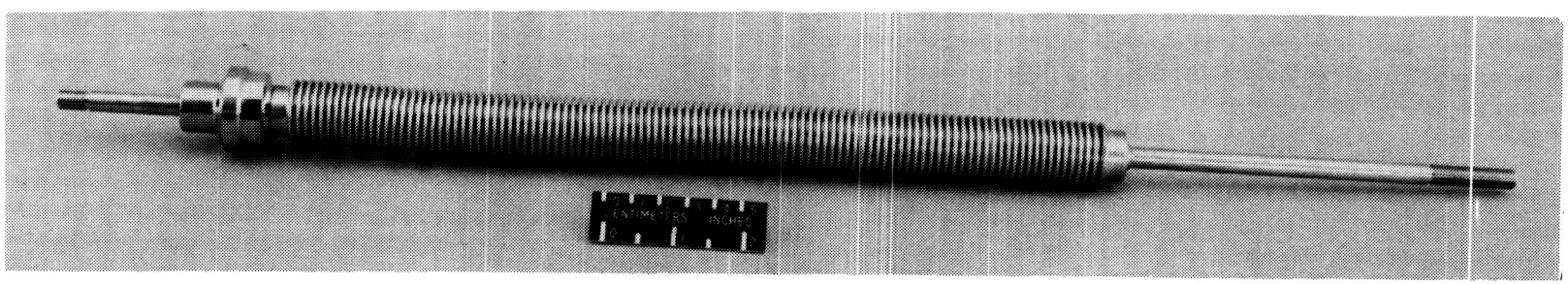

Figure 4. - Bellows assembly.

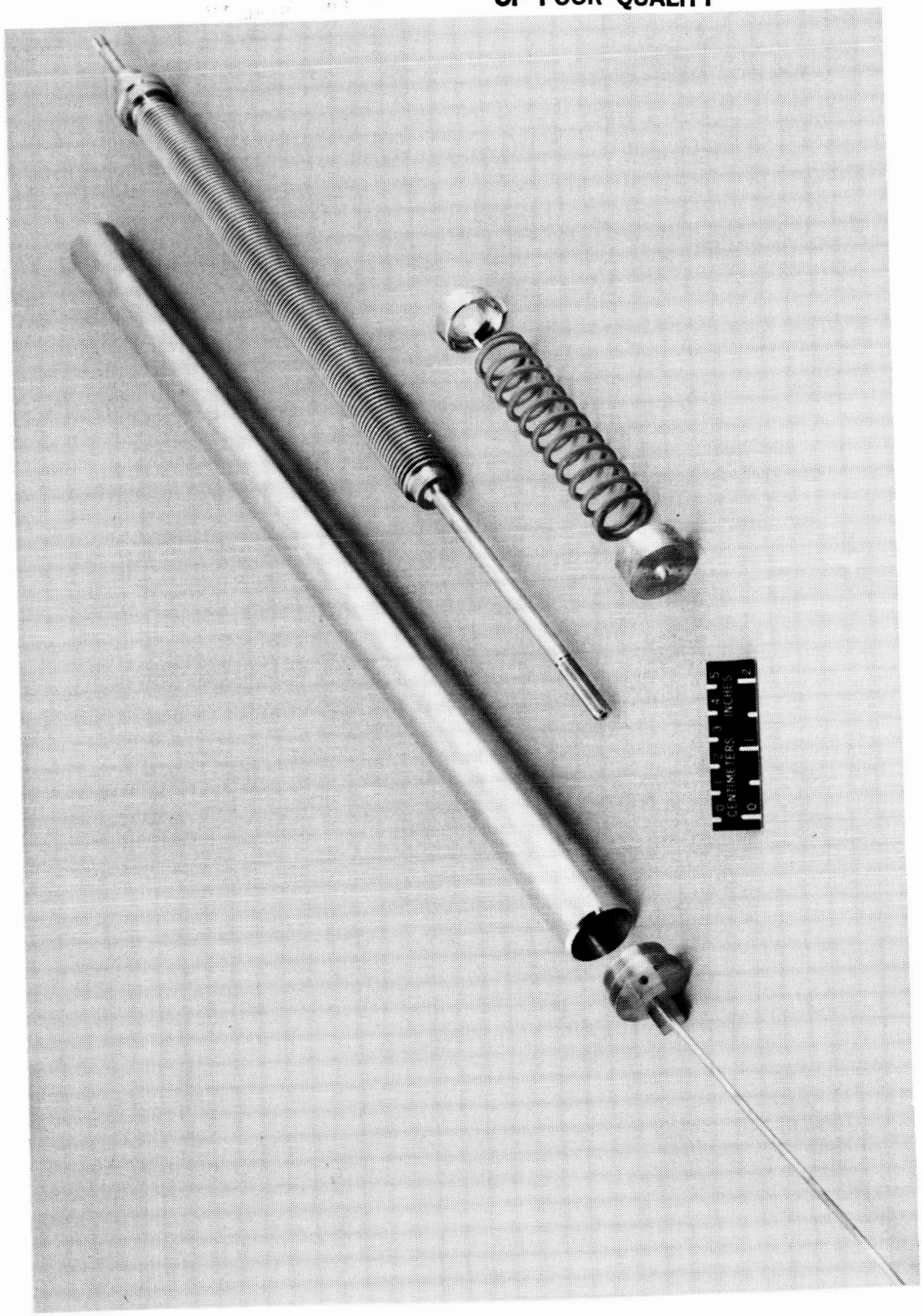

Figure 5. - Thermally-activated driver components.

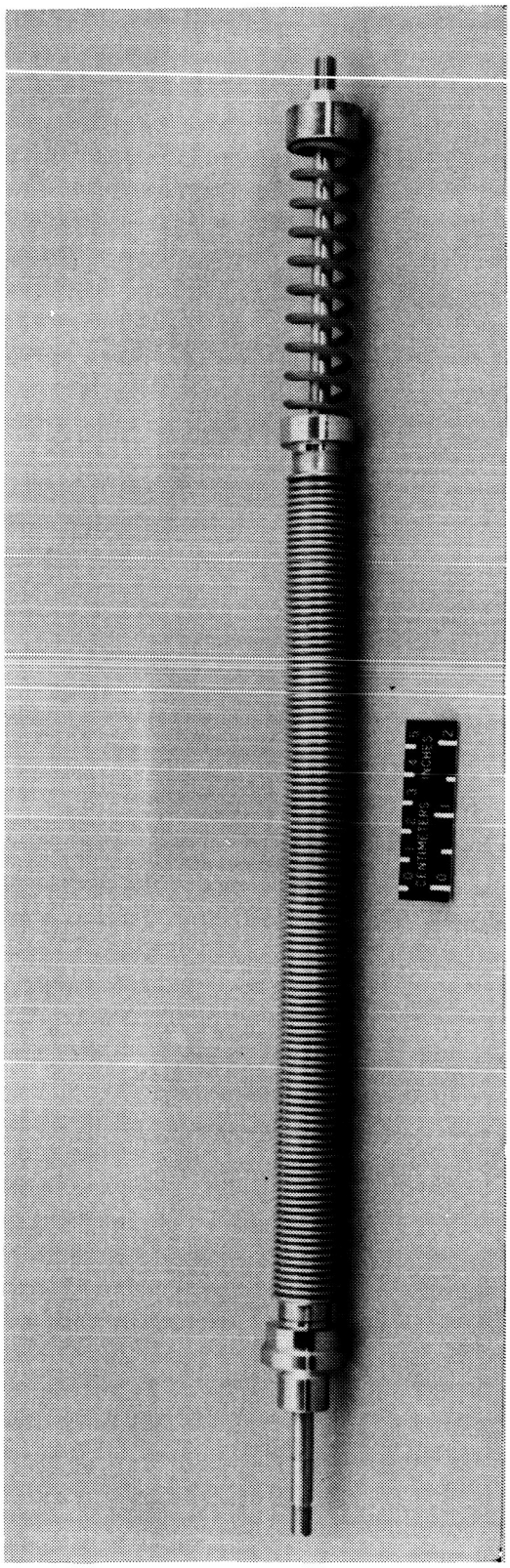

Figure 6. - Thermally-activated driver assembly without pressure shell.

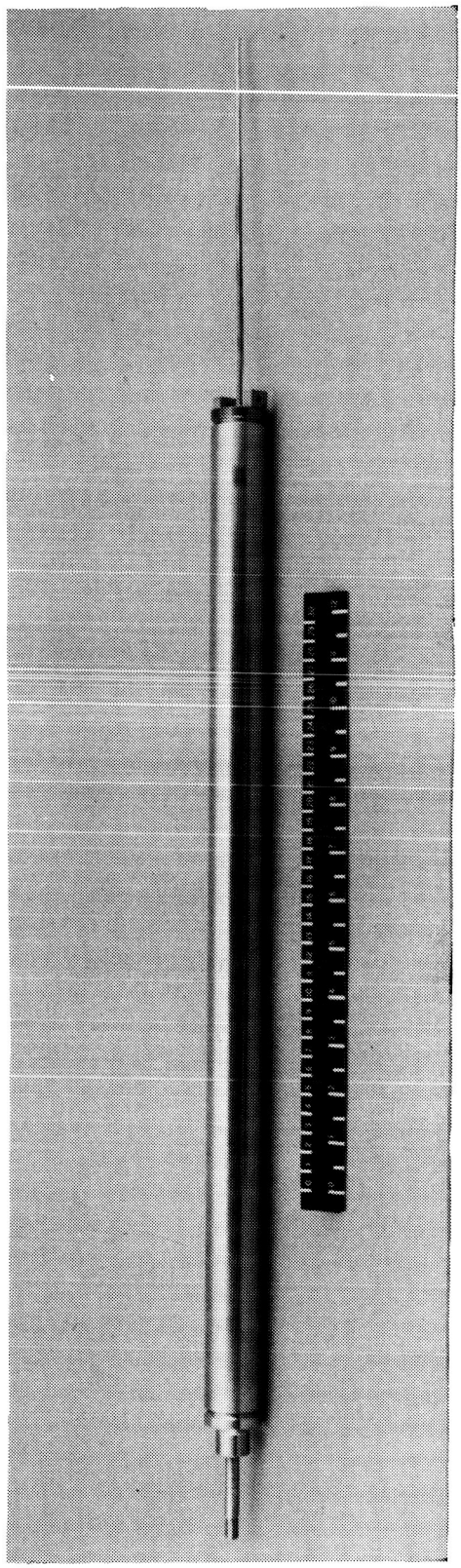

Figure 7. - Thermally-activated driver final assembly.

# SPACE STATION ROTARY JOINT MECHANISMS

Glen W. Driskill*

This paper describes the mechanism which will be used on the Space Station to position the solar arrays and radiator panels for sun pointing and sun avoidance, respectively. The unique design features will be demonstrated on advanced development models of two of the joints being fabricated under contract to NASA-MSFC.

## INTRODUCTION

The Space Station, to be placed in low Earth orbit in the early 1990s presents some new challenges for rotary joint drive mechanisms, power transfer and fluid transfer, because of the large size, long life, and EVA maintenance requirements. Other requirements include high structural stiffness to avoid low frequency structural modes and trouble-free, autonomous operation. Existing technologies have been adapted from other applications to fit these new demands. Table I lists the presently defined requirements for the Advanced Development Project units.

## ROTARY JOINT TYPES

There are three different rotary joint types on the Space Station structure (Refer to Figure 1); The solar alpha joint, which allows the boom supporting the solar collectors to track the sun at orbital rate, 2) the solar beta joint, which allows the solar collectors to be individually rotated to track orbital declination and seasonal variations, and 3) the radiator panel joint orientated in the alpha axis, but with tracking to avoid the sun. Of the three joints, the solar array alpha joint is the most challenging because of the size, the requirement to maintain the structural stiffness of the truss across the joint, and the requirement to transfer greater than 100 kW of power across the rotary interface.

The solar alpha joint requirements for the reference (IOC) configuration for the Space Station called for a size and stiffness compatible with a 2.7-m (9-ft) truss. These requirements led to an optimized design based on stiffness/weight trade-offs which utilize a 2.7-m (108-in.) wire race bearing and a shell structure from the square truss to the bearing. Power transfer in each alpha joint will be one half of the total station power and will be handled by the continuous rotation roll-ring assembly developed by Sperry. The joint will be driven by a dual-redundant drive assembly, which uses a direct-drive brushless dc motor with a pinion gear engaging a ring gear incorporated in the inner race of the wire race bearing. Figure 2 shows the alpha joint cross section.

*Sperry Corporation, Aerospace & Marine Group, Space Systems Division, Phoenix, Arizona.

Table 1. Key Requirements for Rotary Joints

| Characteristic | Requirement |
|---|---|
| Stiffness | No reduction across joint. |
| Redundancy | Fail-safe, redundancy, as required, to meet 20-year life. |
| Rate/Position | Both sides of joint; position sensor accuracy of 1 percent, rate sensor accuracy of 3 percent. |
| Output Torque | 54.2 N.m (40 ft-lb), minimum, solar alpha;<br>27.1 N.m (20 ft-lb), minimum, other joints. |
| Range | Continuous on solar alpha; 270 degrees on other joints. |
| Power Transfer | 100 kW, minimum at 120 V dc across solar alpha |
| Fluid Transfer | Ammonia; three 1.3-cm (1/2-in.) lines, three 0.65-cm (1/4-in.) lines. |
| Life/Maintenance | 20-year life; EVA replaceable. |

In the solar beta axis, the joints will interface with the deployable solar panels and will use a 91-cm (36-in.) wire race bearing. Here the power transfer requirement will be one fourth of the solar alpha joint. Since this joint only tracks the orbital inclination and seasonal variation, it does not require full rotation and, therefore, power transfer can be by roll ring or wind-up cable. Present thinking tends toward a roll-ring assembly.

The radiator panel joint can be made full rotation since it also tracks orbital rate or it can be limited rotation with rewind on the dark side of the orbit. Full rotation requires a rotary fluid coupling joint, which is more complicated than a hose wind-up used for limited rotation. The mechanical part of the joint is the same as the solar beta joint and uses the same drive assembly as all the joints. Figure 3 shows an outside view of the joint.

## DESIGN DESCRIPTIONS

### Drive/Engagement Module

The drive assembly design, which is used on all of the joints, consists of a brushless dc motor, commutation resolver, multispeed/single-speed position resolver, pinion gear and follower bearing (See Figure 4). The drive assembly is mounted on a pivoting arm into an orbital replaceable module, which also contains the mechanism to engage or disengage the drive pinion to

the ring gear on the wire race bearings. A follower bearing adjacent to the pinion gear rolls on a follower surface, machined accurately relative to the pitch diameter of the ring gear. Complete mechanical redundancy is achieved by incrementing the drive/engagement module axially so that one of the two drive assemblies per joint engages one row of teeth on the ring gear and the other engages the second row of teeth.

The drive motor is a 16-pole, permanent magnet, two-phase motor that is continuously commutated from a 16-pole resolver. Use of continuous versus discrete commutation by an optical or hall-effect switch provides a high efficiency and a lower ripple torque. The paired motor and commutation resolver are coupled through a pulse-width-modulated signal with a voltage (torque) amplitude proportional to the excitation level to the resolver.

A combination single-speed/multispeed resolver is incorporated in the drive assembly. The single-speed resolver provides position information for the joint but, because of the gear ratio, it must be processed to obtain output angle. A power-down will cause loss of absolute alpha position information, but the absolute angular position can be establised from the resolver on the outboard side of the joint. The absolute position resolver is located in the power/signal module. Rate information is derived from the multispeed resolver using a tracking converter.

The pinion bearing used in the drive assembly is a preloaded pair of thin section bearings. These bearings and the follower bearing are the only bearings that are constantly loaded when the drive assembly is being used since they must counter the engagement spring force. The engagement force must be high enough to withstand the gear separation forces which result if the output is locked and full stall torque is applied to the motor. If sufficient engagement force is not applied, the pinion gear teeth will ratchet over the ring gear teeth and possibly result in damage.

Engagement and disengagement of the drive pinion is provided by an eccentric arm driven by a gear train motor. Switches are incorporated to indicate engagement, disengagement or transition in between. The engage/disengage motor will be used only a few times in the 20-year life and does not have to be high quality.

Orbital change out of the module or manual operation of the drive motor and the engage/disengage motor can be performed EVA. Any drive/engagement module can be used in any joint without complicated change-out procedures or realignment. The drive/engagement module can be changed out by releasing three quick-release, hold-down devices and two electrical connectors.

## WIRE RACE BEARINGS

The 2.7-m (108-in.) and 91-cm (36-in.) bearings used in all the joints will be "wire race" type, which uses aluminum for the structural members and stainless-steel raceways and rollers at the wear interfaces. Thermal expansion differential effects between the steel and aluminum members are

minimized by making the raceways noncontinuous within the aluminum main structure. The use of an all-steel bearing would not avoid a thermal expansion problem since it must be mated with an aluminum or graphite epoxy transition structure. There are three vendors who supply the wire race-type bearing in addition to more conventional bearings. Current applications for bearings of this size include heavy machininery, gun turrets and other heavily loaded turntable-type applications. In the Space Station application, the design driver, at least for the 2.7-m (108-in.) bearing, will be moment stiffness. Load capacity and fatigue life will be much higher than required. Life is predicted to be 100-plus years and the probability of success for 20 years is 0.999995 due to the low operating stresses.

The ring gear and follower surface are incorporated into the design of the inner race of the bearing (see Figure 4). Specific data on long term use of a large aluminum gear in space is not available, but Sperry has run accelerated life tests in vacuum on steel gear sets which used 45.7-cm (18-in.) gear and a follower bearing to control backlash, and GSFC has run aluminum gear tests in vacuum (Reference 1). The normal use of these types of bearings with gears is in severe load situations. Life is not expected to be a problem, based on the related data available, but cannot be shown by a specific AGMA analysis.

Other types of bearings and bearing arrangements were investigated but did not meet key requirements of being weight-efficient, simple to apply, or of having ease of orbital change-out.

## INTERFACE STRUCTURE

Several key configuration types and iterations within the type categories were investigated by Rockwell International under subcontract to Sperry for the Rotary Joint Advanced Development Project. The basic requirement was to interface with the 2.7-m (9-ft) square box truss (in the IOC configuration) through the bearing without a loss in structural stiffness. Trade-offs were made for weight, stiffness, and cost to fabricate. Configurations considered included truss, box, monocoque and a ring and shell type. The truss type had the disadvantage of asymmetric load transfer to the bearing; the box type was heavy; the monocoque was a good option but is complex to build. A simple, weight-efficient, and easy-to-fabricate type is the ring and shell type (Figure 5). The interface structure will consist of two identical welded and/or riveted main elements consisting of a square bulkhead plate to interface with the box truss, a ring (or cylinder) to transfer torque, and uniform loads to the bearing and the four corner shells to distribute the corner loads uniformly to the ring. A closeout ring mates with this structure and the bearing races.

Rockwell International also investigated a range of bearing sizes to determine the optimum bearing diameter. The 2.7-m (108-in.) bearing was the best, based on direct-load path considerations, but a bearing down to 80 percent of the truss size was found to be workable. Material trade-offs were made, with the result that aluminum was determined to be cheapest to

fabricate, but graphite epoxy was the lightest. It is not within the budget of the Advanced Development Project to develop the graphite epoxy structure.

## POWER TRANSFER

Power transfer across the solar alpha joint, which is one half of the total station supply, will utilize a roll-ring transfer device (References 2 and 3). This device, when compared to rotary transformer types, is much lighter, requires no heat dissipation device, and can transmit ac or dc power. When compared to conventional slip-ring devices, it exhibits comparatively little debris generation because of rolling versus sliding contact and hence does not have a life limited by wear or debris accumulation. An eight-ring model of the roll ring has been in test at LeRC for almost a year with accelerated life tests at 100 KW of power and equivalent to several Space Station lifetimes. The roll-ring assembly, to be supplied in the Advanced Development Project solar alpha joint, will be a 12-ring model with greater than 100 kW capacity at 120 V dc. The power capacity of the roll-ring unit is a function of the voltage and, perhaps, frequency which is yet to be evaluated at LeRC. Further details of the roll-ring unit will not be described here because the data is readily available in other papers (References 2 and 3). Reference 3 contains LeRC test data up to October 1985.

A position resolver will be incorporated in the Power/Signal Module to provide absolute angular alpha-angle position of the solar arrays. The sensor used will be a single-speed resolver, accurate to 3 minutes of arc, which was developed for, and is used in, single-axis control moment gyroscopes for gimbal angle sensing. Also incorporated in the module is a signal-level roll-ring assembly with 30 signal circuits.

The Power/Signal Module is an orbital replaceable unit with quick-release fasteners for the power leads and the structural assembly. A ribbed diaphram-type structure supports the module to the stationary and rotary parts of the bearing. The coupling misalignments of the rotating part of the module are accommodated by a two-axis leaf spring type of coupling.

## FLUID TRANSFER

Transfer of fluid in the Advanced Development Project radiator joint is simplified by making it limited rotation with programmed rewind on the dark side of the orbit. There are advantages to a continuous rotation joint, but also disadvantages in mechanical complexity and reliability. LaRC is presently testing a continuous rotation joint and JSC has issued a subcontract for another development source. The limited rotation joint, which will be demonstrated on the contract, is the least mechanically complicated but, if used on the Space Station, would cause a large disturbance to the station once each orbit when the radiators are stopped, rewound, and then restarted.

The fluid line scheme chosen over several alternatives is a four-turn wrap around the radiator boom with a 38.1-cm (15-in.) pitch. To accommodate

a 270-degree total travel, a significant fluid line pitch diameter change occurs during rotation. The greater the number of turns, the lower the diameter change, but beyond four turns for this excursion angle, the trade-offs are less than optimum. No specific data exists relative to ammonia permeability through the walls of flexible hoses since most conventional ammonia applications are in rigid-pipe ground applications (ice plants). Ammonia offers the highest liquid/vapor latent heat values of available refrigerants, which is why it was chosen for Space Station application. Two types of flexible lines are being considered for the limited-angle fluid transfer: 1) Teflon®-lined, steel-braided hydraulic hose, and 2) convoluted stainless-steel tubing, which can also be supplied with a steel-braid outer wrap. Teflon-lined, braided hose has advantages in weight, coiling behavior and availability, but the hose manufacturers and Teflon manufacturer (DuPont) do not have permeability (leakage) values for Teflon. They do concur that it has the best chance, among all plastics, of doing the job. Stainless-steel or convoluted-type bellows are compatible with ammonia and would have the best chance for zero leakage, initially, but long-term fatigue effects are yet to be evaluated and the coiling behavior is yet to be addressed. Hose change out on orbit will be facilitated by a low-pressure, drop-ball cock valve on each side of the hose joints and a quick disconnect at each end. The valves will prevent any significant amount of ammonia venting during the change-out process.

## DRIVE/CONTROL ELECTRONICS

Each joint in the Space Station will operate autonomously and will have built-in health monitoring, but fault signals, which may require switch-over to redundant devices, will be processed through the main computer. Autonomous operation will be accomplished with a microprocessor-based control system that will interface with the main computer. Each joint will have a controller, which will communicate with the central computer, control the engage/disengage mechanism for the dual-redundant torquer module, and interface with the dual-redundant drive electronics. In the Advanced Development Project, a minicomputer, with a printer, display screen and an instruction keyboard, will substitute for the flight model embedded microprocessor unit. Electronic boxes (one interface and two redundant drive) with the same part number can be used on all joints, but some joints may require algorithm and compensation filter changes directed from the central computer. Figure 6 is a diagram representation of the solar alpha joint.

The drive electronics will excite the torque motor from a pulse-width-modulated bridge with the amplitude of the continuous commutation signals proportional to the excitation level of the commutation resolver. This scheme is extensively used by Sperry in CMGs and RWAs because of simplicity of design and low torque ripple considerations. A digital commutation and control approach will be considered for the flight configuration to be more compatible with microprocessor-based electronics if increased torque ripple can be tolerated.

## SPECIAL CONSIDERATIONS

There are peculiarities in the Space Station application, as in all space hardware, but the added considerations are on-orbit change-out of components for long-term use of the station, on-orbit maintenance, and the enormity of the structure.

Temperature effects on the rotary joint mechanisms appear to be a manageable problem according to predictions from the Rockwell thermal analysis. The combination of multilayer insulation, high thermal capacitance and good internal thermal paths serves to minimize temperature swings and thermal gradients. Absolute temperature changes of less than 11°C (20°F) are predicted for orbital and seasonal variations. These variations are easily accommodated in the thermal design of the drive mechanisms and the follower bearing concept for backlash control. Temperature gradients between the outer ring and inner ring of the joint bearing can cause preload changes which could result in drag torque problems or loss of stiffness in the extreme cases. With a 279.75 kg (7500-lb) preload on the alpha joint bearing, it would take an 4.4°C (8°F) differential inner/outer ring gradient to go to zero preload or double preload. The Rockwell prediction is for a 2.2°C (4°F) worst-case differential. If the predicted gradients are shown to be greater than 2.2°C (4°F) in later analyses, the preload can be increased and/or heater control can be provided to reduce the gradient.

On orbit change-out of boxes, drive/engagement modules, power/signal modules and fluid hoses is accommodated in the design. Change-out of joint bearings has been rejected in favor of total structural joint change-out due to considerations of total EVA time. Bearing health can be monitored by drag torque, temperature, and stiffness (by observing structural frequencies). Signs of deterioration would allow time to schedule transportation of a replacement joint in a future shuttle flight. Spares for the boxes and drive/engagement module could be stored on orbit because of the small size and common utilization on all twelve joints.

## ACKNOWLEDGEMENTS

The following people at Sperry have been instrumental in the design: Dave Thum, Mechanical design; Ryan Porter, Power/Signal Module design; Ernie Fisch, Electronics design and Jim Medberry, Control Systems design. NASA participants have been: Charlie Cornelius and Jim Lominick of MSFC; John Gustafson of LaRC; and Dave Renz of LeRC. Rockwell International: John Lewis, Bill Wiley, et al, under subcontract have performed the transition structure design and provided other information from their Phase B Station activities.

## REFERENCES


1. Vest, Charles E. et al, "Evaluation of Gear Materials for Space Applications," ASLE/ASME Lubrication Conference, October 1969.

2. Porter,Ryan, "Rotating Electrical Transfer Device," Nineteenth Aerospace Mechanism Conference, May 1985.

3. Jacobson, Peter, "Advanced Space Power Transfer Device," EASCON 85 Eighteenth Annual Conference, October 1985.


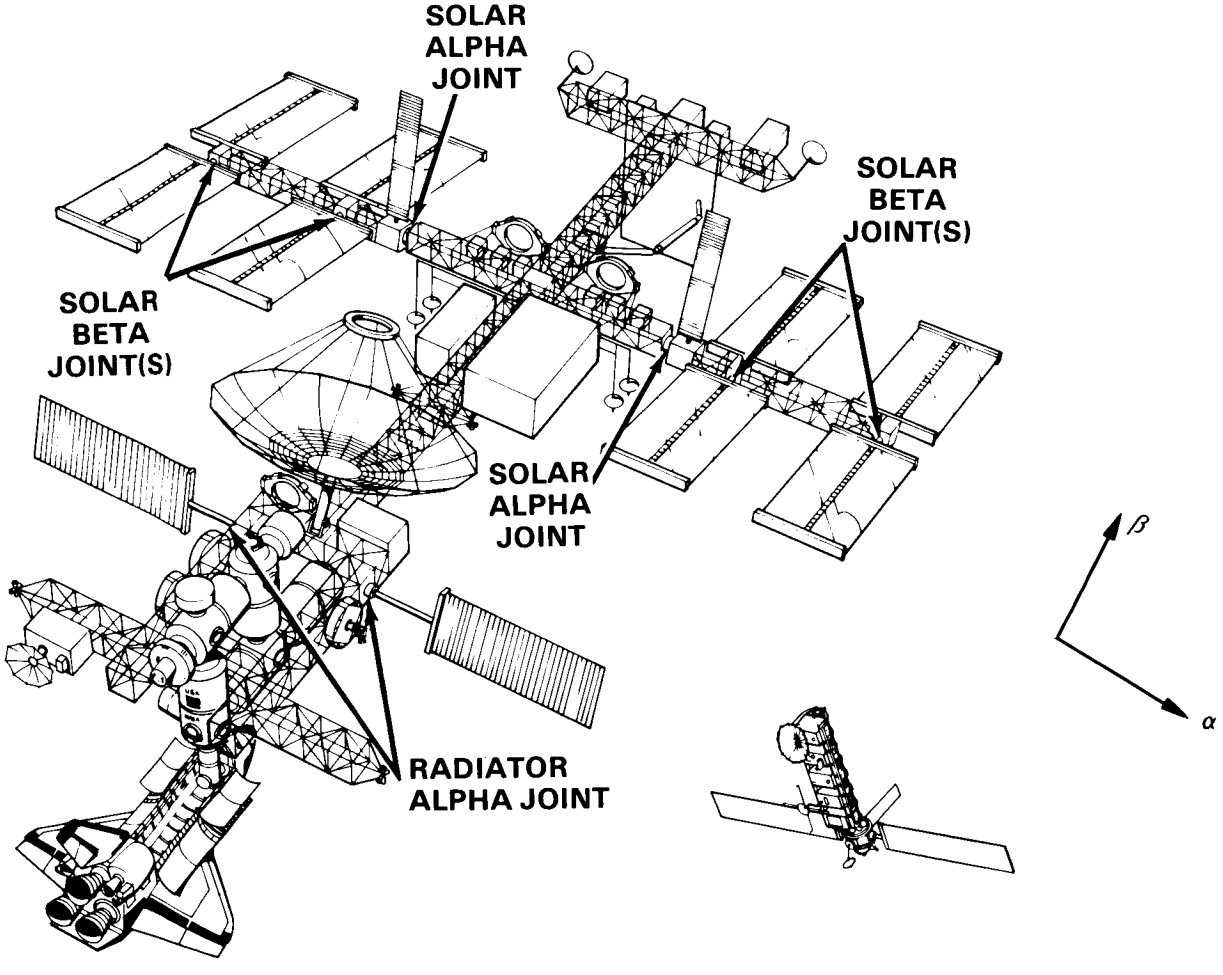


Figure 1. - Space station reference configuration.

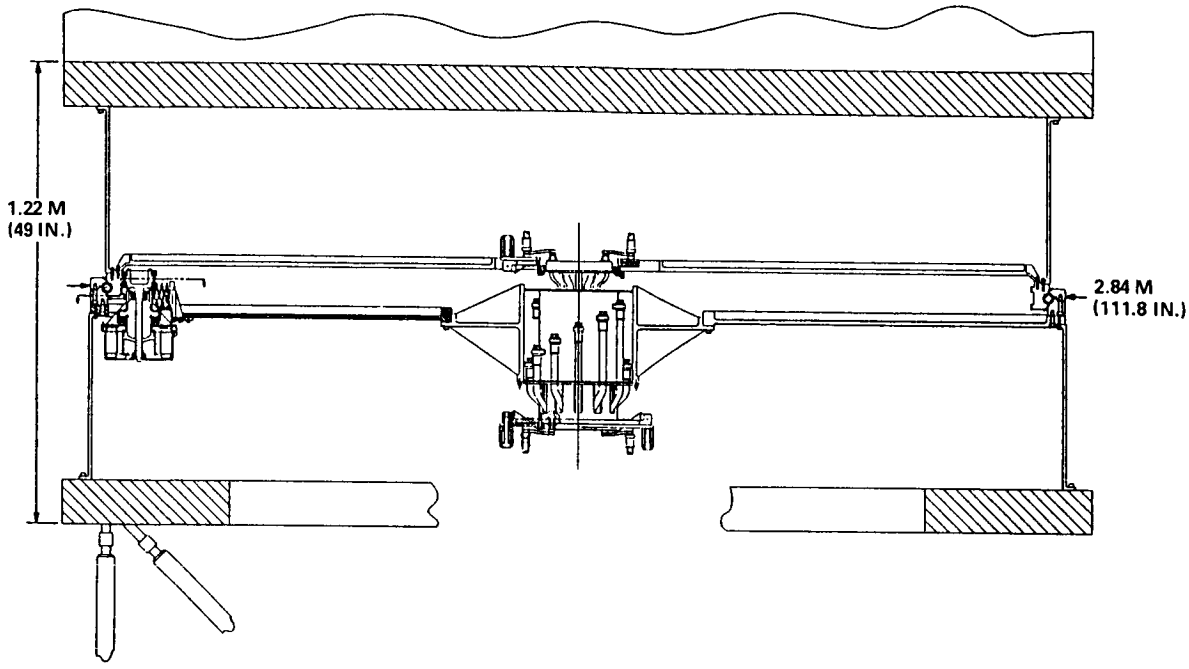


Figure 2. - Solar alpha joint.

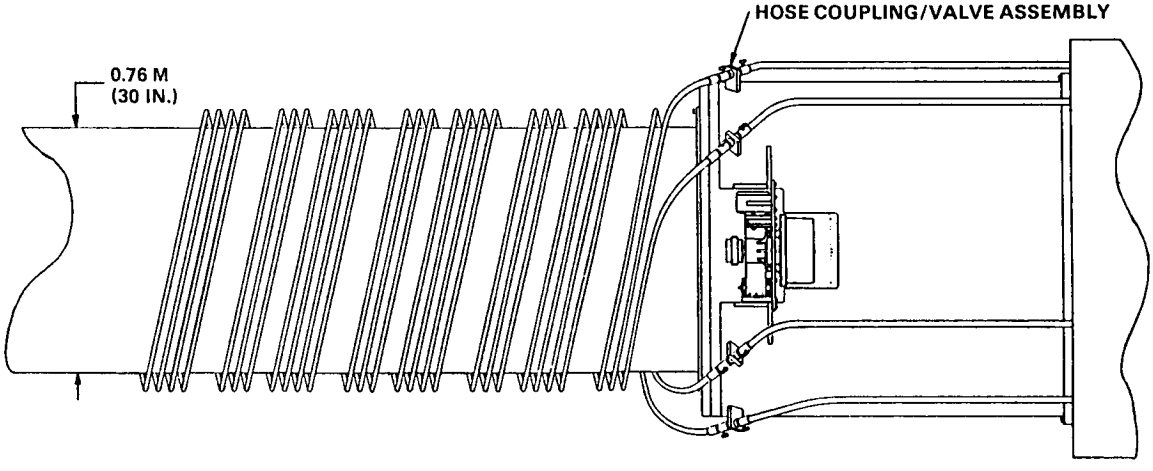


Figure 3. - Radiator alpha joint.

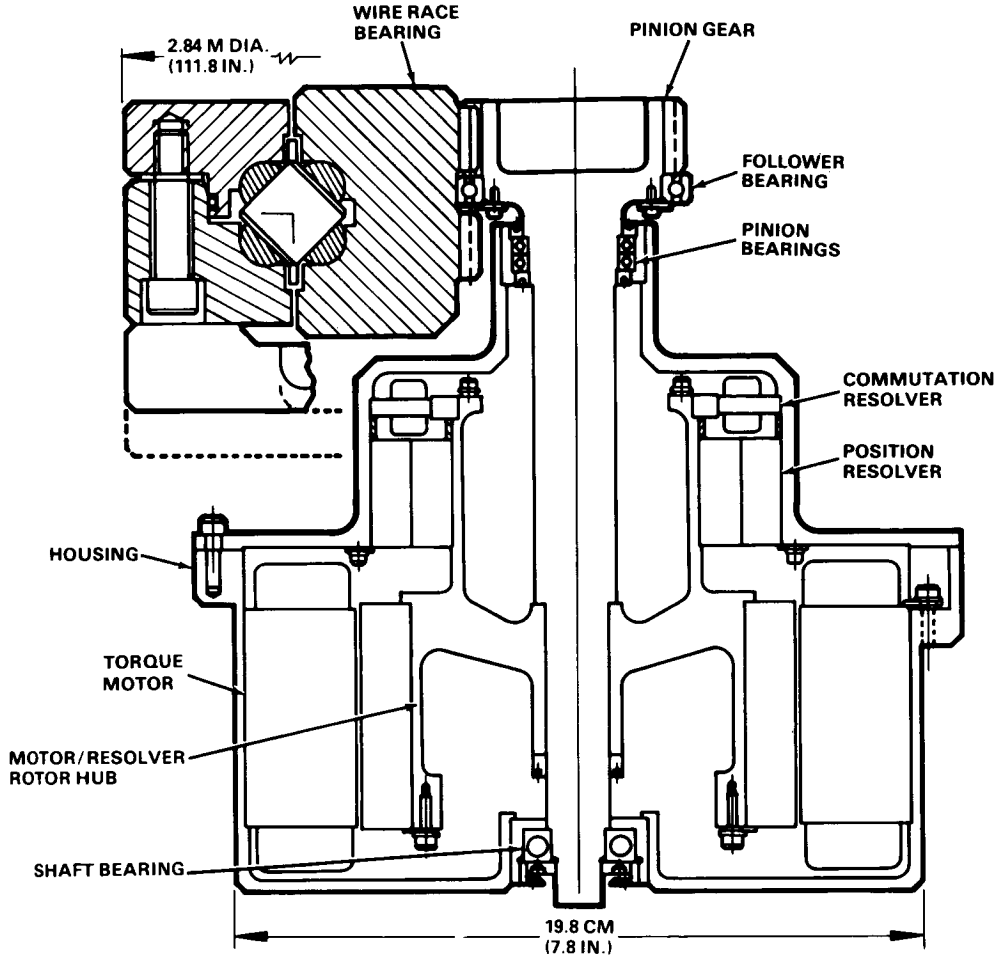


Figure 4. - Drive assembly.

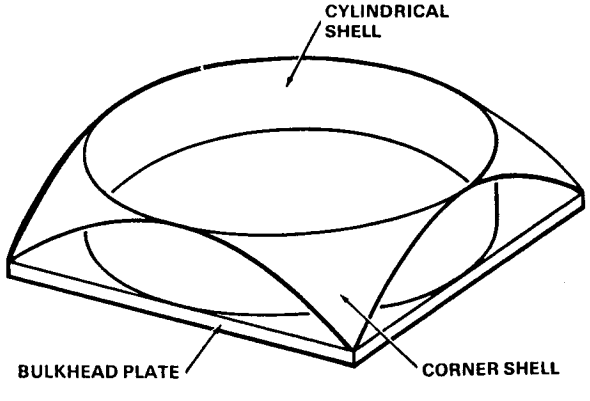


Figure 5. - Alpha joint transition structure.

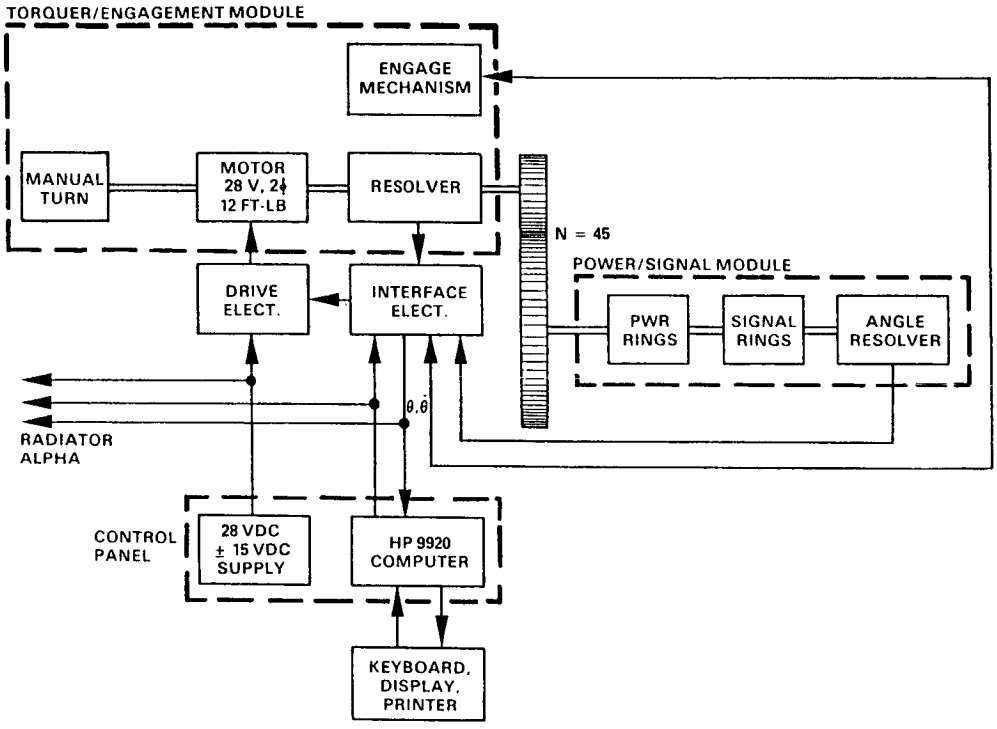


Figure 6. - Solar alpha joint.

# HYDRAULIC MECHANISM TO LIMIT TORSIONAL LOADS BETWEEN THE IUS AND SPACE TRANSPORTATION SYSTEM ORBITER

James R. Farmer*

The Inertial Upper Stage (IUS) is a two-stage booster used by NASA and The Defense Department to insert payloads into geosynchronous orbit from low-Earth orbit. The hydraulic mechanism discussed in this paper was designed to perform a specific dynamic and static interface function within the Space Transportation System's Orbiter. This paper discusses requirements, configuration, and application of the hydraulic mechanism with emphasis on performance and methods of achieving zero external hydraulic leakage. The work was performed on Air Force Contract FO4701-78-C-0040, Headquarters Space Division (AFSC).

## INTRODUCTION

The mechanisms discussed herein were designed to function in the natural environments of space and induced environments associated with orbiter boost, payload deployment, and reentry of the space shuttle Orbiter. The environments are severe and require design solutions unavailable in normal industrial applications.

The IUS interface with the Orbiter cargo bay is the IUS Airborne Support Equipment (ASE). The ASE structure consists of (1) an aft support frame that provides support for IUS X, Y, Z, Mx, and Mz loads, and (2) a forward support frame that provides support for IUS Y and Z loads during boost. A keel pin between the forward ASE frame and IUS carries the Y loads. The aft frame pivots during deployment to elevate the IUS to a position to clear the Orbiter cargo bay. The hydraulic mechanism is an integral part of the forward ASE frame. Figure 1 shows the Orbiter and its relationship to the forward and aft ASE frames.

During Orbiter boost to low-Earth orbit, the hydraulic load-leveler mechanism minimizes torsional loads applied to the IUS and absorbs part of the dynamic energy being transmitted to it. If attempts to deploy the payload are unsuccessful and an ASE Payload Retention Latch Actuator (PRLA) motor failure occurs during abort restow, the hydraulic mechanism can displace one actuator up and the opposite actuator down to restow the payload and maintain IUS to Orbiter alignment.

The major problem and drawback of using hydraulic systems for space applications is potential hydraulic oil leakage and contamination. Considerable test experience has established a design application, assembly technique, and screening test program that meet zero external leakage requirements.

*Boeing Aerospace Company, Seattle, Washington.

## DESIGN REQUIREMENTS

Natural environments and Orbiter-induced environments present design requirements for all mechanisms used in the Orbiter, such as:

a. Complete a minimum of 100 IUS shuttle flights over a period of approximately 10 years.
b. Operate in zero gravity.
c. Survive temperatures as low as -59 °C (-75 °F).
d. Have an operating temperature range of -23 to + 52 °C (-10 to +125 °F).
e. Be contained within the allowable dynamic envelope.
f. Use materials and finishes that will not outgas.

Specific hydraulic mechanism design requirements are:

a. Allow zero external leakage of hydraulic fluid.
b. Limit maximum operating pressure to 3000 $lbf/in.^2$.
c. Have an active life expectancy of 50,000 cycles without refurbishment.
d. Limit differential load due to friction to less than 450 lb.
e. Provide a damping coefficient of 225±50 $lb\text{-}sec^2/in.^2$, and limit load-leveler piston velocity to 14.0 in./sec and the maximum differential load between the two load levelers to 14,000 lb.

## HYDRAULIC LOAD-LEVELER MECHANISM

The load leveler mechanism on the forward ASE (fig. 2) is a closed loop hydraulic system that limits torsional loads applied to the IUS while providing determinant support in static and dynamic environments. The forward end of the IUS and spacecraft is supported and restrained by double-acting pistons within the two load-leveler actuators. The upper chambers of each actuator are plumbed together and the lower chambers are plumbed together. Any upward displacement of one actuator is matched by an equal but opposite deflection of the opposite actuator to maintain positive engagement of the ASE keel pin in the IUS socket. In the event the left hand and right hand PRLAs do not open simultaneous during deployment or close simultaneously during abort restow, mechanical stroke limiters on the load-leveler actuator rods limit the maximum possible height differential between the two PRLAs to approximately 1.25 in. A hydraulic accumulator, with a metal bellows type diaphragm, is connected to the upper chamber tubing to accommodate thermal expansion and contraction of the hydraulic fluid. The pressurant side of the accumulator is pressurized to 1080 $lbf/in.^2$ (nominal) with gaseous nitrogen.

The hydraulic tubing connecting the lower chambers of the load-levelers has two orifices installed to provide a controlled damping coefficient of the total system. The damping coefficient requirement of 225 $lb\text{-}sec^2/in.^2$ nominal optimizes a trade off between load-leveler system travel and dynamic loads transmitted to the spacecraft. A reduction in damping coefficient reduces transmitted loads but exceeds total load-leveler piston travel available. Increasing the damping coefficient results in higher dynamic loads being transmitted to the spacecraft.

## HYDRAULIC MECHANISM DAMPING

Adjustment of the load-leveler mechanism damping coefficient and verification that resultant maximum differential loads and piston velocities were within required limits were demonstrated by test. A summary of the results is discussed herein.

The governing equation for summation of load-leveler system forces is

$$F_D = F_F \frac{|V|}{V} + CV|V| + MA$$

where

$F_D$ differential force, lb; 14,000 lb maximum

$F_F$ static friction force, lb; 450 lb maximum (acceptance test data show nominal friction force of 300 lb)

V piston velocity, in./sec; 14.0 in./sec maximum

C damping coefficient, lb-sec$^2$/in.$^2$; 225±50 lb-sec$^2$/in.$^2$

A piston acceleration, in./sec$^2$

M effective load leveler system mass, lb mass

|| absolute value

The effective load-leveler mechanism mass was calculated by externally driving the load-leveler system at varying velocities and measuring the applied force and the acceleration of the driven piston relative to its housing. Measurements were taken at the time of maximum piston acceleration. The tests were conducted with no inline orifices to minimize damping. The results are summarized in table I. As shown, the average effective mass of the load-leveler mechanism was 10,980 lb mass; within 2% of the predicted value of 10,750 lb mass.

The load-leveler mechanism was tested with several orifices to establish the required damping coefficient. Test data for the production configuration are summarized in table II. The damping coefficient is calculated from measurements of the force applied to the driven piston and the velocity of the driven piston relative to the housing, calculated by differentiating the relative displacement curves. Again, the measurements were taken at maximum piston velocity. As shown, the average damping coefficient is 227 lb-sec$^2$/in.$^2$. The data scatter fall within the 225±50 lb-sec$^2$/in.$^2$ requirement.

The governing equation for the load leveler system forces becomes:

$$F_D = 300 \frac{|V|}{V} + 227\ V|V| + 10{,}980\ A$$

Figure 3 presents a comparison of the analytical prediction of system performance and actual test results. The analytical prediction was based on the assumption that the relative velocity between the piston and housing is sinusoidal and the maximum velocity amplitude is 5.8 in./sec (table II). As shown, predicted and test results are consistent, and maximum differential forces are approximately 10,000 lb.

Moreover, increasing the static friction force, $F_F$, and damping coefficient, C, to their maximum design values increases the maximum calculated value of $F_D$ less than 20%. The resultant maximum calculated value for the differential force satisfies the 14,000 lb maximum design requirement.

## ZERO EXTERNAL LEAKAGE

The ASE hydraulic load-leveler mechanism meets all system design requirements. The hydraulic mechanism was selected during the design phase because it provided the desired stiffness characteristics and load paths for a mechanical system, and met limited envelope requirements. In addition, flow limiter (orifices) were easily changed-out during system tests to obtain desired damping coefficients.

The major drawback of a hydraulic system for space application is external leakage. Small amounts of hydraulic oil discharged into a vacuum rapidly expand and are attracted to cold surrounding structures. A film of oil on critical hardware, such as star scanner, can potentially impact an entire mission.

The ASE hydraulic system was designed to limit the number of potential leakage paths. All tubing is welded, with seals (redundant) used only at tubing to load-leveler joints. The load leveler, shown in cross section in figure 4, includes redundant, primary and secondary, seals at all static and dynamic seal locations. In addition, storage cavities for primary seal leakage are used at all dynamic seal positions. Primary seal leakage of one drop per day at dynamic seals is allowed. Storage cavities are periodically drained through vent vent port plugs.

The O-rings used in the load leveler are fluorosilicone with a 70 to 80 durometer. Fluorosilicone was selected because of the extreme low-temperature survival requirements (-59 °C). The production configuration had nominal O-ring squeezes of 10% for dynamic seals and 15% for static seals consistent with standard O-ring design practices.

Following delivery of all production units, numerous leakage problems occurred during ground storage at ambient conditions. Intensive review by BAC* Engineering, Customer Representatives, and Parker Seal** design engineers, in addition to an extensive test program, identified five key elements of the design, which, if controlled carefully, result in zero external leakage.

*Boeing Aerospace Company.
**Parker Seal Group O-ring Division, Lexington, Kentucky.

TABLE I. - TEST DATA USED TO DETERMINE EFFECTIVE LOAD-LEVELER MECHANISM MASS

| Forcing function | Force at V = 0, kips | Relative acceleration*, g's | Effective mass, LMB x $10^3$ (M = F/A) |
|---|---|---|---|
| 2 kip at 4 Hz | 1.55 | 0.15 | 10.3 |
| 4 kip at 4 Hz | 3.63 | .39 | 9.3 |
| 6 kip at 4 Hz | 5.30 | .51 | 10.4 |
| 8 kip at 4 Hz | 6.9 | .6 | 11.5 |
| 10 kip at 4 Hz | 9.1 | .79 | 11.5 |
| 12 kip at 4 Hz | 10.25 | .90 | 11.4 |
| 14 kip at 4 Hz | 11.5 | .95 | 12.1 |
| 6 kip at 6 Hz | 5.5 | .46 | 12.0 |
| 8 kip at 6 Hz | 7.3 | .68 | 10.7 |
| 10 kip at 6 Hz | 9.0 | .83 | 10.8 |
| 4 kip at 7 Hz | 3.5 | .35 | 10.0 |
| 8 kip at 7 Hz | 7.0 | .60 | 11.7 |

*Relative acceleration of load-leveler piston to housing. Results (based on geometry and fluid mass considerations): (1) $M_{AVG}$ = 10,980 lb mass; (2) Predicted $M_{AVG}$ = 10,759 lb mass.

TABLE II. - TEST DATA USED TO DETERMINE DAMPING COEFFICIENT OF LOAD-LEVELER MECHANISM

| Forcing function | Force at maximum velocity, F, kips | $V_{MAX}$*, in./sec | Damping coefficient, lb(in./sec)$^2$ |
|---|---|---|---|
| 2 kip at 4 Hz | 1.2 | 2.0 | 225 |
| 4 kip at 4 Hz | 2.3 | 3.2 | 195 |
| 6 kip at 4 Hz | 4.5 | 4.3 | 227 |
| 8 kip at 4 Hz | 6.2 | 5.2 | 218 |
| 10 kip at 4 Hz | 8.6 | 5.8 | 247 |
| 2 kip at 1 Hz | 1.7 | 2.4 | 243 |
| 4 kip at 1 Hz | 3.7 | 3.8 | 235 |

*$V_{MAX}$ obtained by differentiating deflection data. Results: (1) $C = (F - F_F)/V^2_{MAX}F_F$ = 300 lb**; (2) $C_{AVG}$ = 227 lb-sec$^2$/in.$^2$; (3) Tolerance C = (1 + 0.20)$C_{AVG}$.

**Average of friction force measured for each ASE at ambient (launch) conditions.

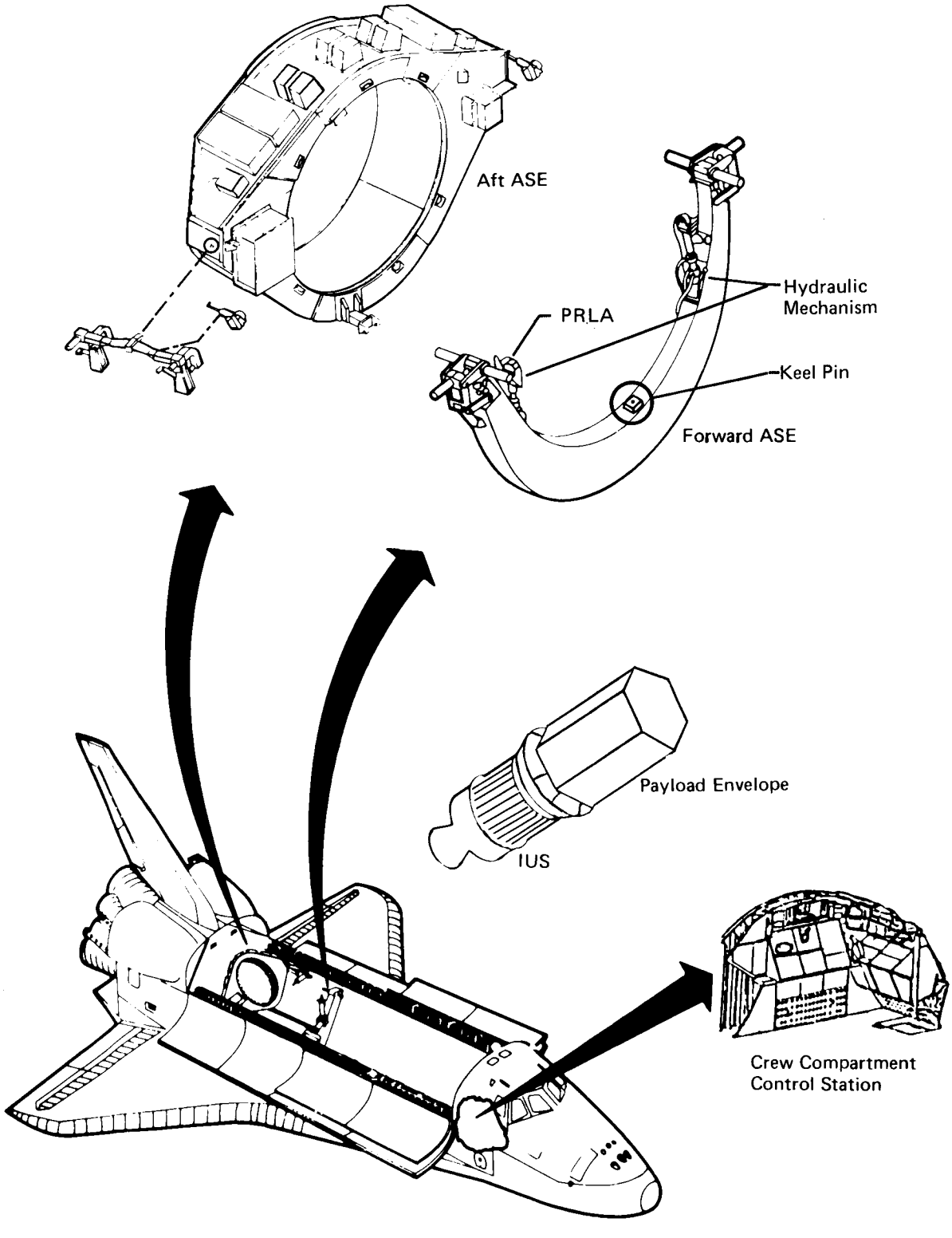


Figure 1. - IUS Airborne Support Equipment.

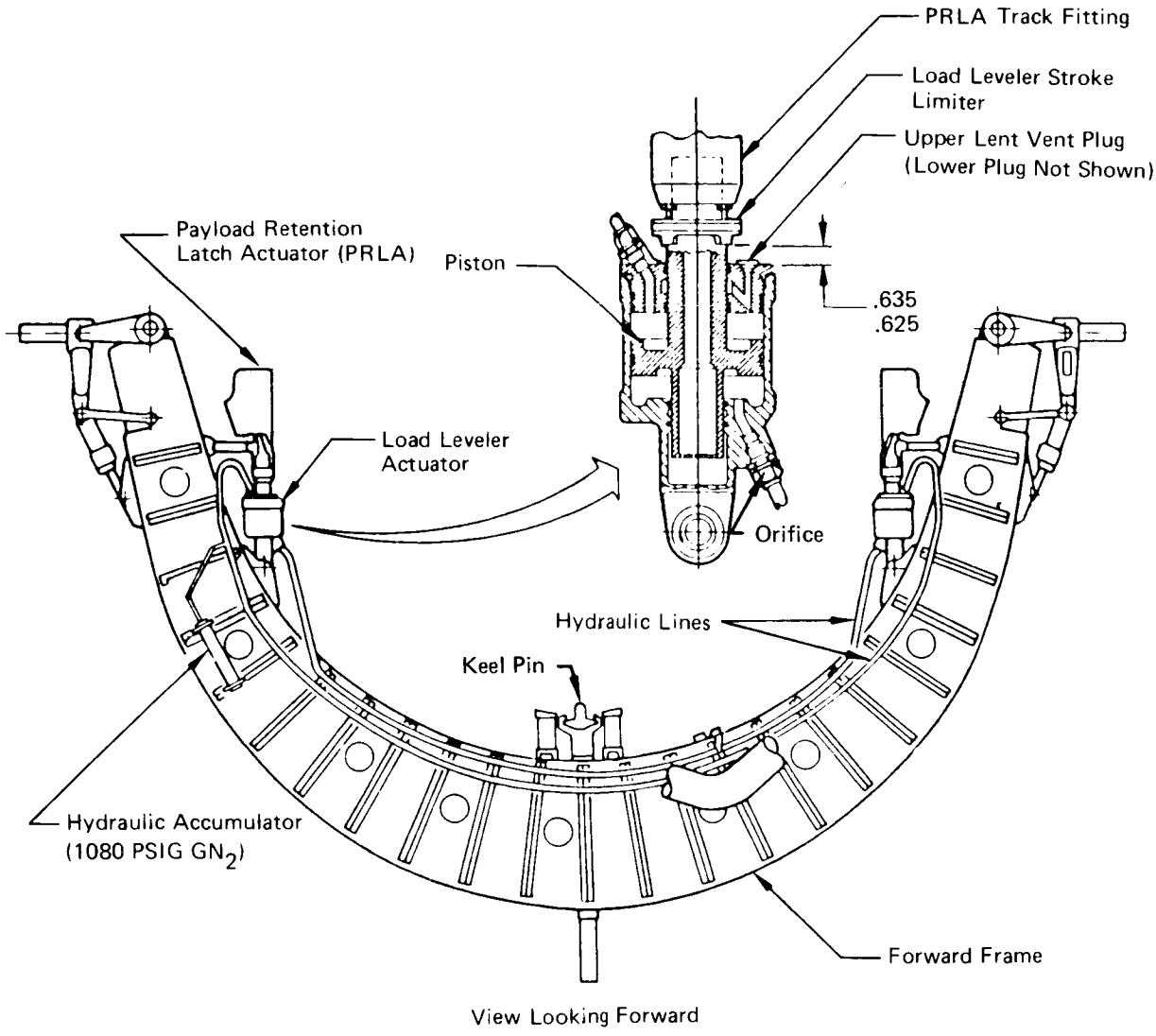


Figure 2. - Forward ASE load-leveler system.

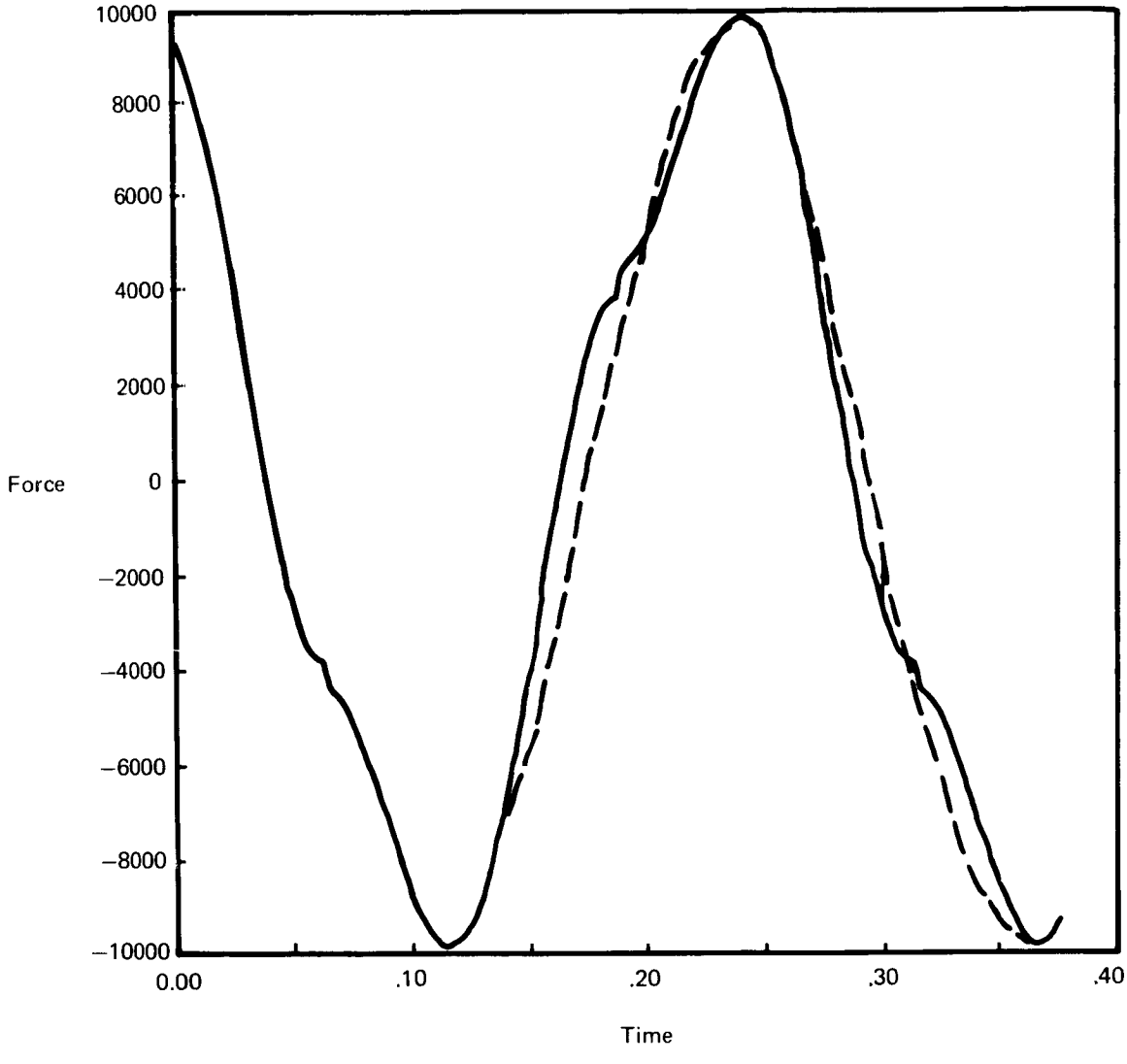


Figure 3. - Comparison of analytical and test piston loads.

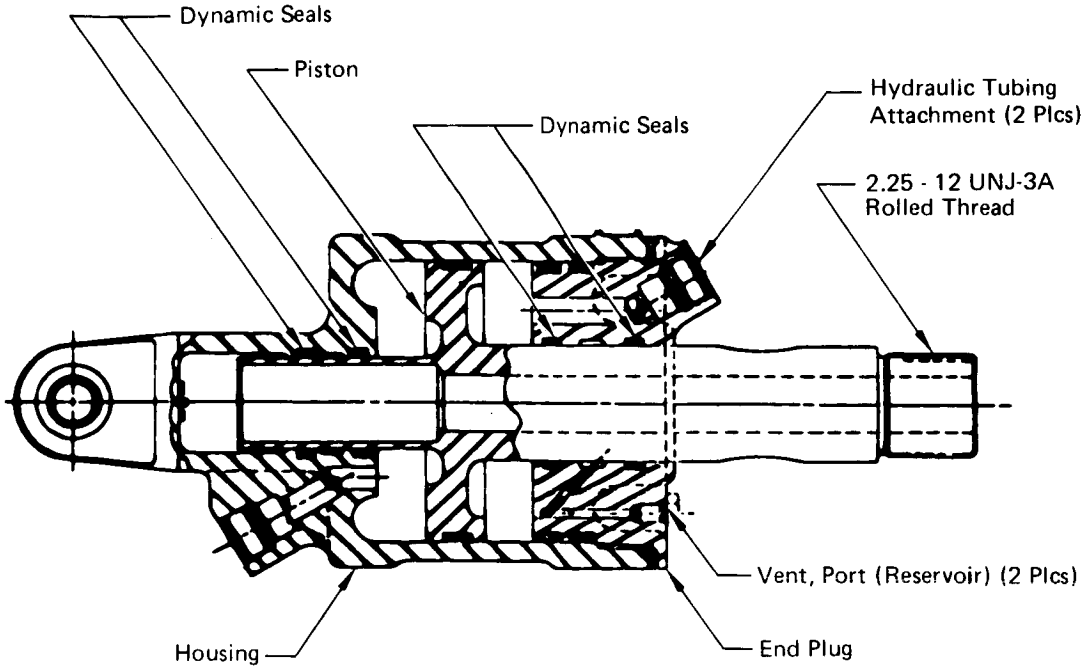


Bleed-Fill Valve 2 Places (Not Shown)
Located 90° From HYD. PORTS.

Seals Per MIL-R-25988/1 Dynamic
Seals Per MIL-R-25988/4 Static

Figure 4. - Load leveler actuator.

# DESIGN AND DEVELOPMENT† OF A LARGE DIAMETER HIGH PRESSURE FAST ACTING PROPULSION VALVE AND VALVE ACTUATOR

K.V. Srinivasan*

This paper describes the design and development of a large diameter high pressure quick acting propulsion valve and valve actuator. The valve is the heart of a major test facility dedicated to conducting full scale performance tests of aircraft landing gear systems. The valve opens in less than 300 milliseconds releasing a 46-centimeter- (18-in.-) diameter water jet and closes in 300 milliseconds. The four main components of the valve, i.e., valve body, safety shutter, high speed shutter, and pneumatic-hydraulic actuator, are discussed. This valve is unique and may have other aerospace and industrial applications.

## INTRODUCTION

The NASA Langley Research Center's (LaRC) Aircraft Landing Dynamics Facility (ALDF) in Hampton, Virginia, plays a critical role in the dynamic testing of landing gear systems for commercial aircraft, military aircraft, the space shuttle, and general aviation. Dynamic testing of these systems is performed from a 45,400-kilogram (50-ton) carriage which travels along a 1036-meter (3400-ft) track, at speeds up to 424 kmph (265 mph). The carriage is a free wheeling cart which is accelerated up to full speed in just under 122 meters (400 ft) by a propulsion system which produces over 746,000 kilowatts ($1 \times 10^6$ hp) (theoretical). The propulsion system utilizes an innovative quick acting propulsion control valve (Figs. 1(a) and (b)) that is driven by a unique actuator mechanism, both designed by the S & Q Corporation of Morgan Hill, California. The propulsion system greatly expands the testing capability of the ALDF allowing it to remain in the forefront of dynamic testing.

## SYSTEM/FACILITY DESCRIPTION

The Aircraft Landing Dynamics Facility (Fig. 2) consists of four major components: (1) An "L" vessel that is 2.44 meters (8 ft) in diameter,

---

*S & Q Corporation, Morgan Hill, California.

†The design and development work described in this paper was carried out by the S & Q Corporation, Morgan Hill, California, under a contract with the National Aeronautics and Space Administration, Langley Research Center, Virginia.

approximately 7.63 meters (25 ft) long, and 7.63 meters (25 ft) high; (2) a programmable propulsion control valve which releases a 46-centimeter- (18-in.-) diameter column of water with a thrust force of up to 374,000 kilograms (413 tons); (3) a carriage weighing 45,400 kilograms (100,000 lb) with an impulse bucket on the back end and approximately 1036 meters (3400 ft) of track; and (4) an arresting gear system that engages and stops the carriage after the test has been completed. The facility operates as follows. The "L" vessel is filled with water and pressurized with air through a 122-centimeter- (48-in.-) diameter header to a maximum pressure of 22.4 megapascals (3250 psi). The carriage, with its test payload, is placed ahead of the propulsion valve, and the valve is preprogrammed to give a desired impulse to the carriage. The system is now ready for testing. The valve opens in less than 300 milliseconds and releases a 46-centimeter- (18-in.-) diameter jet of water into the impulse bucket mounted on the rear of the carriage. The resulting impulse causes the carriage and its test payload to accelerate to 424 kmph (265 mph) within 122 meters (400 ft) of travel. The test landing gear is then lowered, impacting the runway and duplicating full-scale dynamic loading in real time. There is almost 610 meters (2000 ft) of testing runway after the carriage gets to a desired speed where landing gears can be tested for braking, skidding, hydroplaning, hitting at an angle, tire wear, etc. At the end of the test, the carriage is brought to a stop by the arresting gear. After the test is completed, water is pumped back into the "L" vessel, the carriage is pushed back to the start position, the arresting system is reset, the valve actuator is recharged, and the system is ready for the next test. This is an extremely cost effective way of accelerating such a large carriage. The energy cost per test is the electrical energy required to pump 37,900 liters (10,000 gallons) of water against a 22.4-megapascal (3250-psi) head. The energy cost is approximately $50. A very interesting comparison of the acceleration capabilities of the carriage is to compare it with the world record dragster. The present record holder is a vehicle weighing 454 kilograms (1000 lb) which accelerates to 424 kmph (265 mph) in a quarter mile, i.e., 433 meters (1420 ft). The ALDF's carriage weighs 45,400 kilograms (100,000 lb) (100 times as heavy) and is capable of reaching a speed of 424 kmph (265 mph) in less than one-third the distance.

## VALVE DESCRIPTION

The propulsion valve (Fig. 3(a)) is a double shutter spherical segment valve. The inner shutter acts as a safety gate and the other performs as a high speed shutter. The inner shutter is located in the valve body and rotates to a position above the flow nozzle when opened. The outer shutter is located on the outside of the valve body and is supported by an external yoke. The safety shutter is hydraulically actuated, and the high speed shutter is hydraulically controlled and pneumatically operated by an axisymmetrical double acting high speed accumulator-piston arrangement. The actuator along with all the supporting hydraulic and pneumatic controls is packaged as a unit and is located above the valve.

## DESIGN REQUIREMENTS

The major design considerations were as follows:

1. Valve to accommodate nozzles with exit diameters up to 50.8 centimeters (20 in.).

2. Open or close in 300 milliseconds and stay open from 0 to 3 seconds, maximum.

3. Control of both opening and closing time shall be repeatable to within 5%.

4. Instantaneously close if there is any fault, electrical failure or malfunction, i.e., "fail safe".

5. Recycle time of 15 minutes.

6. Designed in accordance with the nuclear section of the ASME Code for pressures up to 22.4 megapascals (3250 psi).

7. Valve to be microprocessor controlled and be programmable to tailor impulse for specific test conditions.

8. Minimum 25-year operation life.

9. Valve must produce a coherent jet of water.

10. Safety shutter to have zero leakage at 22.4 megapascals (3250 psi).

11. All wetted pressure boundary surfaces to be made corrosion proof.

## VALVE DESIGN

Since no existing valve could perform or meet the specified requirements and conditions, a new valve and valve actuating system were developed by the S & Q Corporation. The assemblage (Figs. 3(a) and (b)) consists of four main components: (1) valve body, (2) safety shutter (SS), (3) high speed shutter (HSS), (4) valve actuator. The valve body is a spherical section with a 10.16-centimeter- (4-in.-) thick wall. It was designed in accordance with Sect. III, Class 1 of the ASME Code for nuclear pressure vessels, and since it is the primary pressure barrier, a thorough finite element analysis was made using a Nastran program on a Cray computer. The SS is a spherical segment which is located within the valve body and seals with the valve body on a "O' ring type seal. The SS is opened by translating it backwards, off its "O" ring seat, and rotating it into a cavity above the flow nozzle. The SS is made of stainless steel (17-4 PH) and is operated, relatively slowly, by a hydraulically powered eccentric crank mechanism which is independent of the HSS.

Sealing the SS was accomplished by using a 4.8-millimeter- (3/16-in.-) diameter "O" ring viton seal between two carefully lapped spherical surfaces. The two surfaces are preloaded through the eccentric system to assure a leak proof seal at low "L" vessel water pressure. With full "L" vessel pressure of 22.4 megapascals (3250 psi), the force at the sealing surface is over 5,500 kilonewtons ($1.25 \times 10^6$ lb), and in operation, the SS has been 100% leak tight over the entire operating pressure range of the "L" vessel.

The high speed shutter is the actual control element which initiates and terminates the jet of water; therefore, it controls the impulse the carriage sees. Placing the high speed shutter outside the valve body results in a valve design which allows the shutter to be larger than the opening it covers. Therefore, the shutter can be accelerated to its maximum opening velocity prior to initiating or interrupting the jet of water. This results in a very crisp, precise jet action on the impulse bucket and makes possible the required 300-millisecond opening and closing time.

With the SS open, the force of approximately 6,200 kilonewtons ($1.4 \times 10^{-6}$ lb) causes the HSS support system to deflect, resulting in a 3.2-millimeter (0.25-in.) gap between the valve body and the HSS. To bridge this gap, the HSS is equipped with an outer sealing sleeve (Fig. 4) which is pneumatically forced backward against the valve body. The labyrinth type sealing surface on the HSS sleeve and its mating surface on the valve body are overlaid with Stellite, and the spherical surfaces are precisely lapped to minimize leakage. Prior to activation of the HSS, the pneumatic pressure forcing the sleeve against the valve body is released, the sleeve moves back approximately 3.2 millimeters (0.125 in.), allowing the HSS to be rotated upward opening the valve. During the closing cycle, the HSS is rotated to the closed position and then the HSS sleeve is forced against the valve body terminating flow. This closing sequence allows for a very rapid and precise termination of the jet with respect to the carriage, and, by controlling the closing rate of the HSS sleeve, "water hammer" is controlled. Water hammer, or overpressurization due to the rapid closing of the valve, was of concern during design and was extensively analyzed. The resulting spherical valve design allowed for a very short section of high velocity flow, approximately 1 meter (3 ft) of nozzle, with the bulk of the water in the "L" vessel moving at a relatively low velocity. This, plus the control of the final 100% shut off with the HSS sleeve, eliminated water hammer.

The valve can accommodate nozzles up to 510 millimeters (20 in.) in diameter. During operation, the jet does not touch any part of the valve body (coherent jet) resulting in a very efficient nozzle.

## VALVE ACTUATOR

Activating a valve of this size in 300 milliseconds is no simple task. In addition, reversing the motion immediately upon opening and closing the valve again in 300 milliseconds further complicates the problem.

As mentioned earlier, the actuator (Fig. 5) consists of an inner piston that is contained within an outer piston which also acts as the cylinder for the inner piston. When the actuator is charged, it has compressed nitrogen on one side of each piston balanced by hydraulic oil on the other side. All the energy necessary to open or close the valve is contained within the inner and outer piston nitrogen chamber. To open the valve, a flow control valve on the oil discharge side of the inner piston opens, and the piston is forced backwards by the nitrogen pressure. To close the valve, oil is released from the oil discharge side of the outer piston, and the outer piston moves forward and closes the valve. Control of the opening and closing times is achieved by controlling the flow control valves on the oil side of each piston. The actuator must now be recharged prior to another operation. The actuator was designed for 34.5 megapascals (5000 psi) (60,000 lb force equivalent) system operating pressure because of uncertainties as to the force necessary to interrupt the water jet. Theoretically, and as verified with a small test model, the force should be comparatively negligible. This minimal force in actuality, however, depends on the dimensional accuracies of the valve assembly, and even small misalignments can result in large forces. Actual operational experience with the valve indicates that the force necessary to interrupt the jet is in fact minimal, and actuator pressures of 13.8 megapascals (2000 psi) (24,000 lb force equivalent) are adequate for valve repeatability regardless of "L" vessel pressure.

## VALVE OPERATION

With the safety shutter closed and the HSS in the horizontal position, the safety shutter seal is translated closed. Water is then admitted from the "L" vessel to the valve cavity through a fill line. When the pressure across the SS reaches 690 kilopascals (100 psi) or less, the SS is retracted and rotated clear. The HSS seal is then translated backwards (to generate the necessary clearance between the HSS and the valve body) then the HSS is rotated open by the actuator.

The closing sequence is the reverse of the opening sequence. The actuator rotates the HSS down, and the seal is translated forward. The SS is then rotated into position and translated closed, and the HSS seal is subsequently released. As indicated, the whole procedure is microprocessor controlled and the opening and closing sequence can take as little as 250 milliseconds (1/4 sec). This short time is accomplished even though the force on the HSS is approximately 5,500 kilonewtons ($1.25 \times 10^6$ lb) just prior to opening.

## SUMMARY

The valve is the heart of the ALDF propulsion system which has greatly expanded the simulation capabilities of LaRC. Extensive finite element analyses were performed on various valve components, and rigorous quality control was exercised throughout the design, fabrication, assembly, and testing of the valve system. The valve has achieved or exceeded all

specified performance requirements. It has successfully controlled pressure surges (water hammer) and the water jet continuity is excellent. Safety shutter sealing is 100%, and the high speed shutter is drip tight exceeding the specified requirements. Repeatability of the valve opening and closing time is independent of "L" vessel pressure and is well within the 5% specified. The specified open and closing time of 300 milliseconds has been exceeded by 50 milliseconds, and the limit has not as yet been reached.

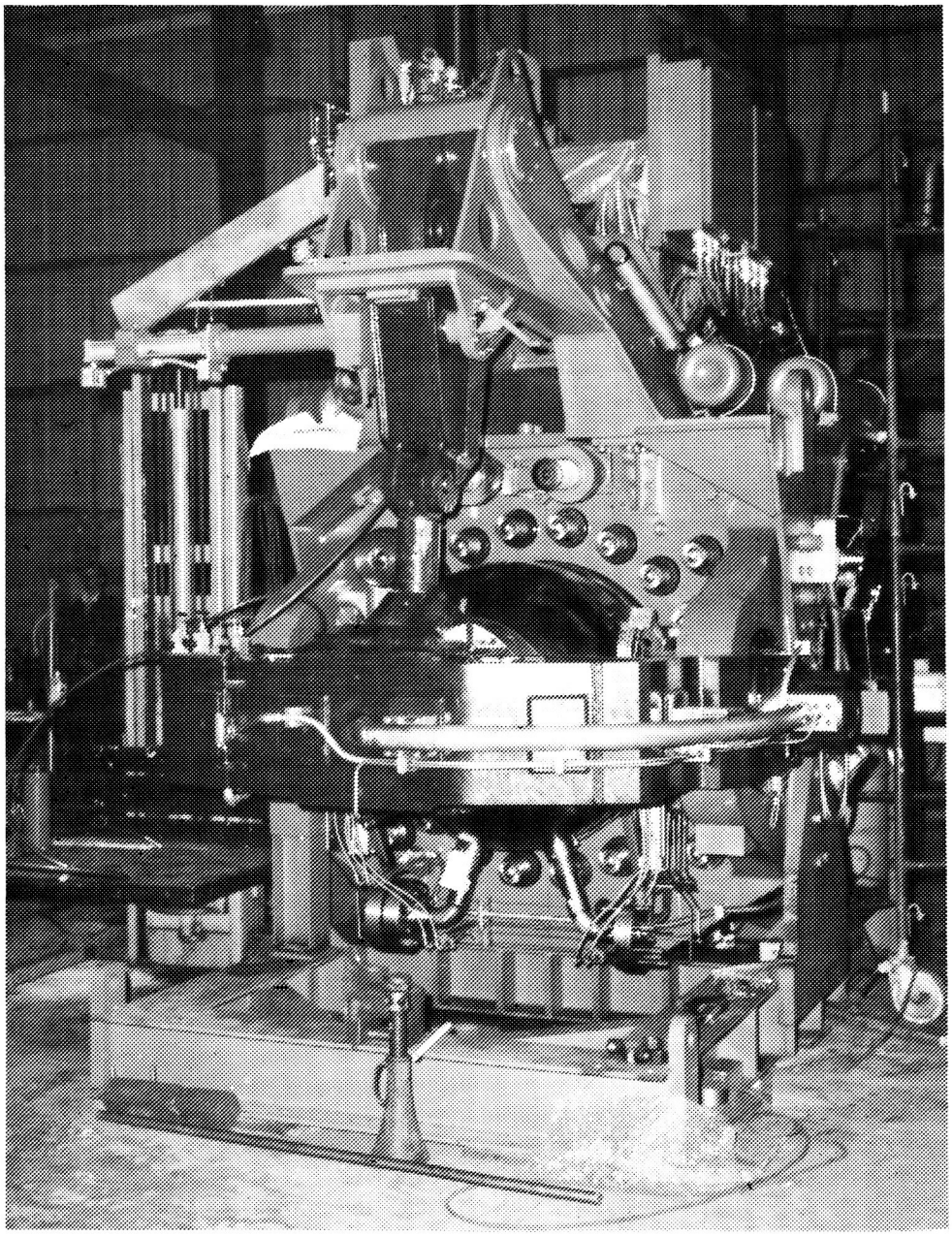

(a) Closed position.

Figure 1. - Propulsion control valve.

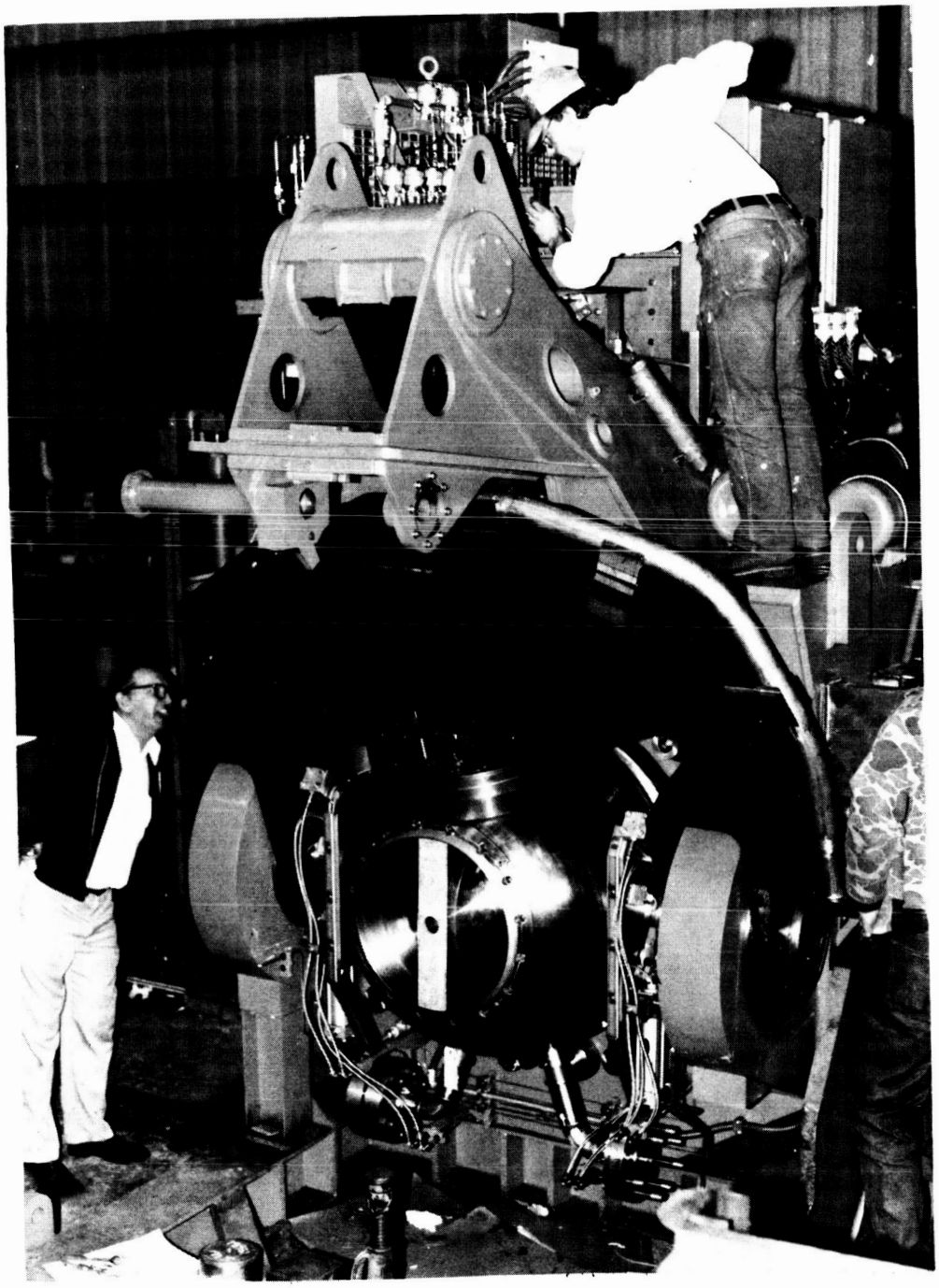

(b) Open position.

Figure 1. - Concluded.

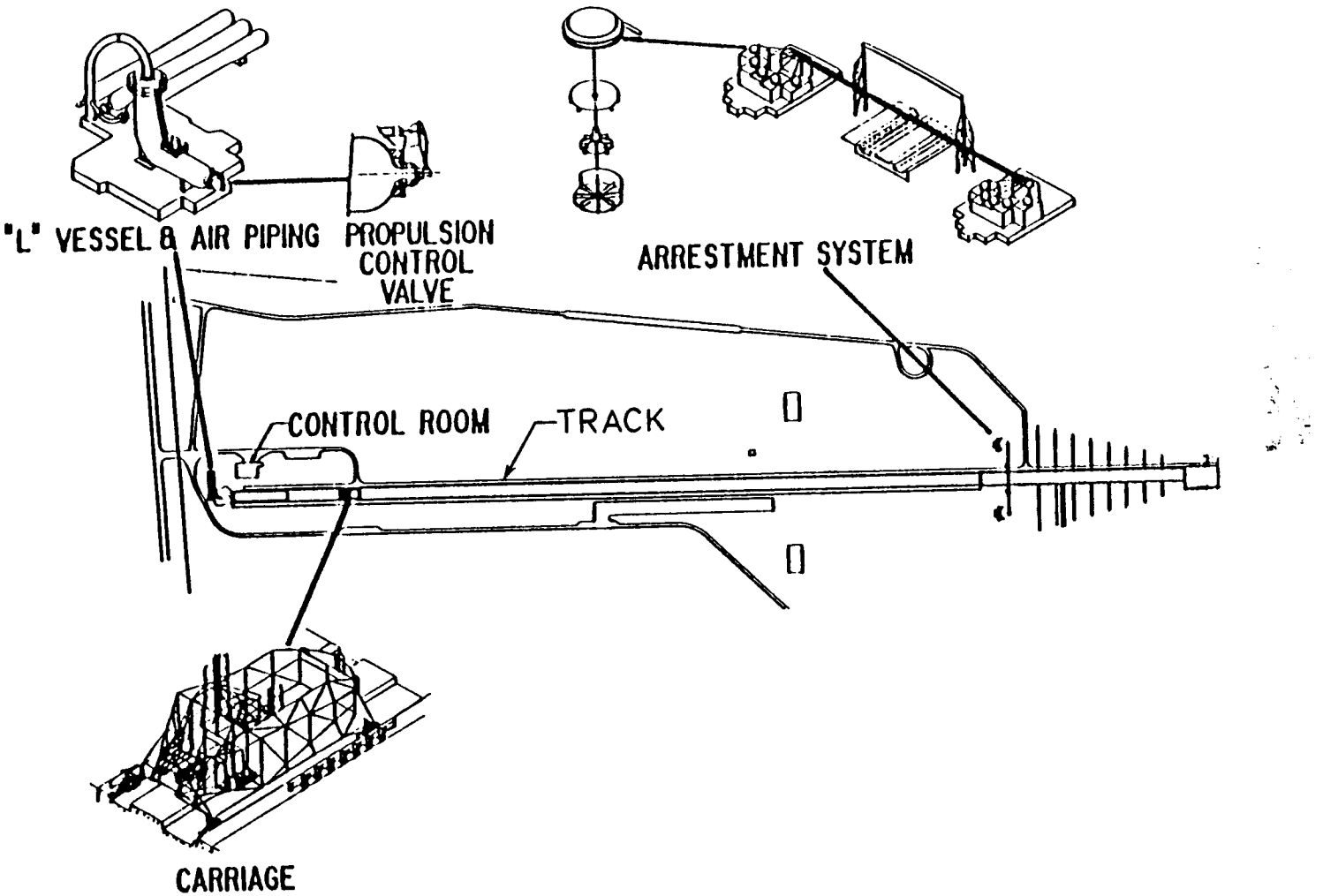


Figure 2. - Test facility general arrangement.

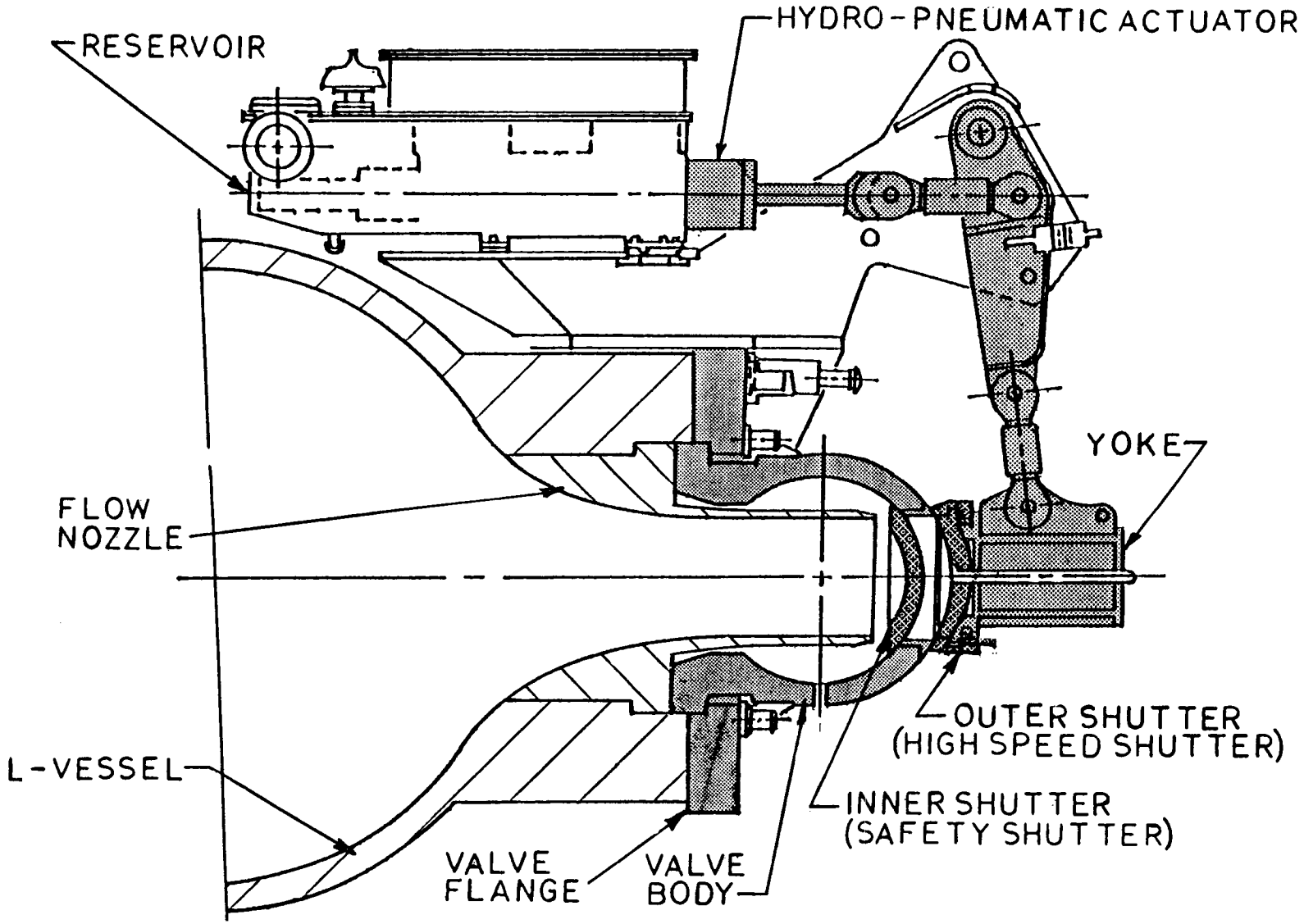


(a) Closed position.

Figure 3. - Valve cross section.

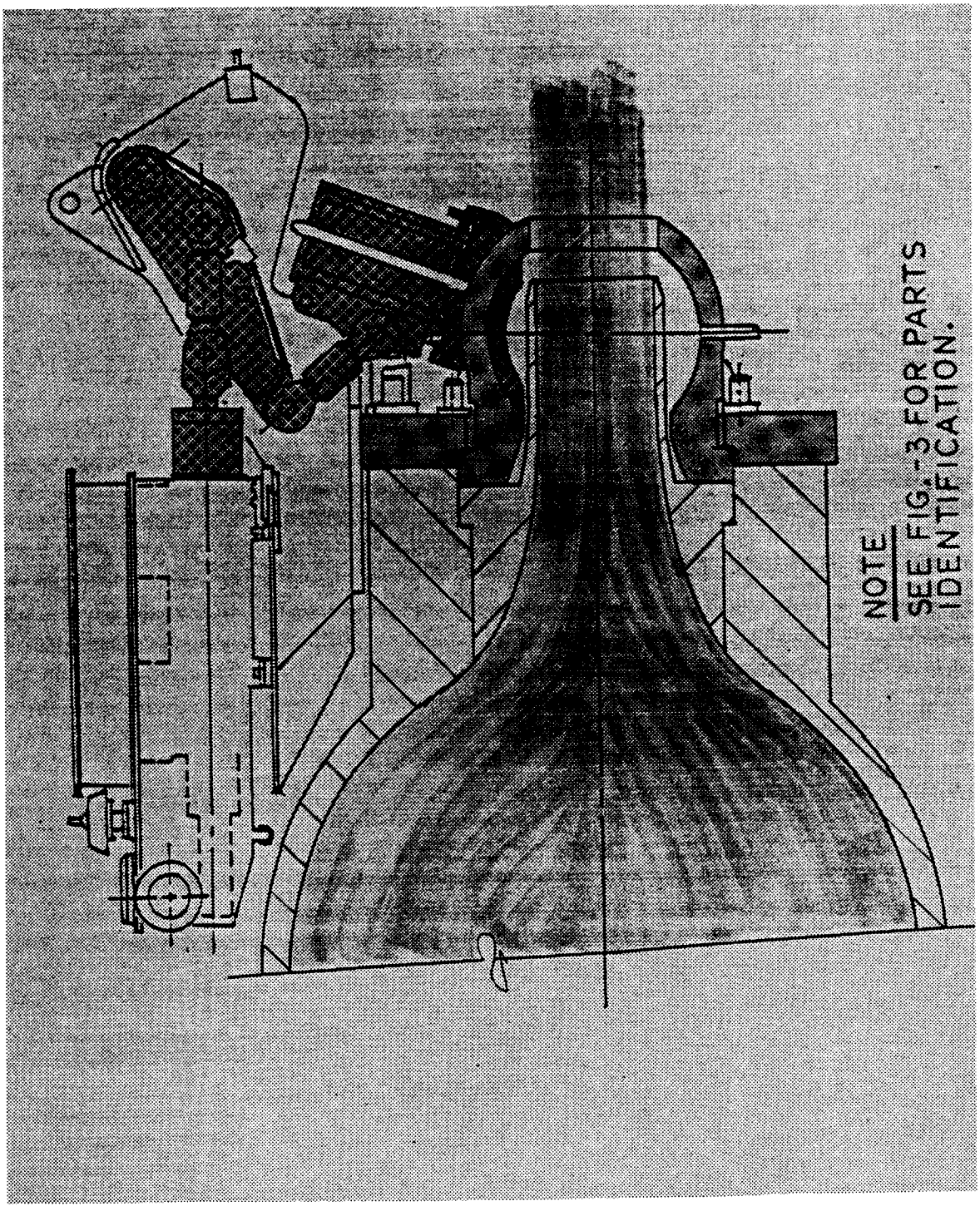


(b) Open position.

Figure 3. - Concluded.

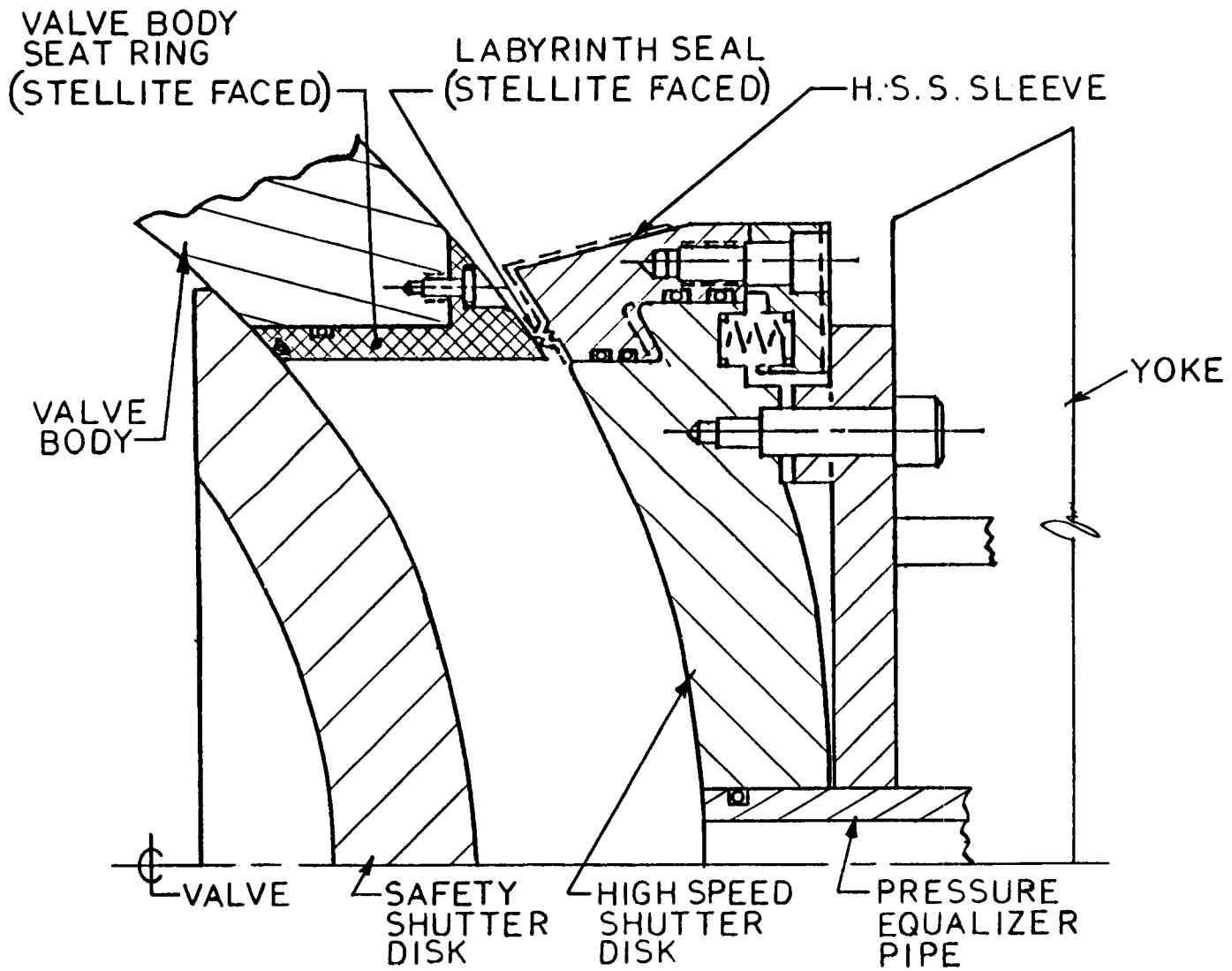


Figure 4. - High speed shutter seal cross section.

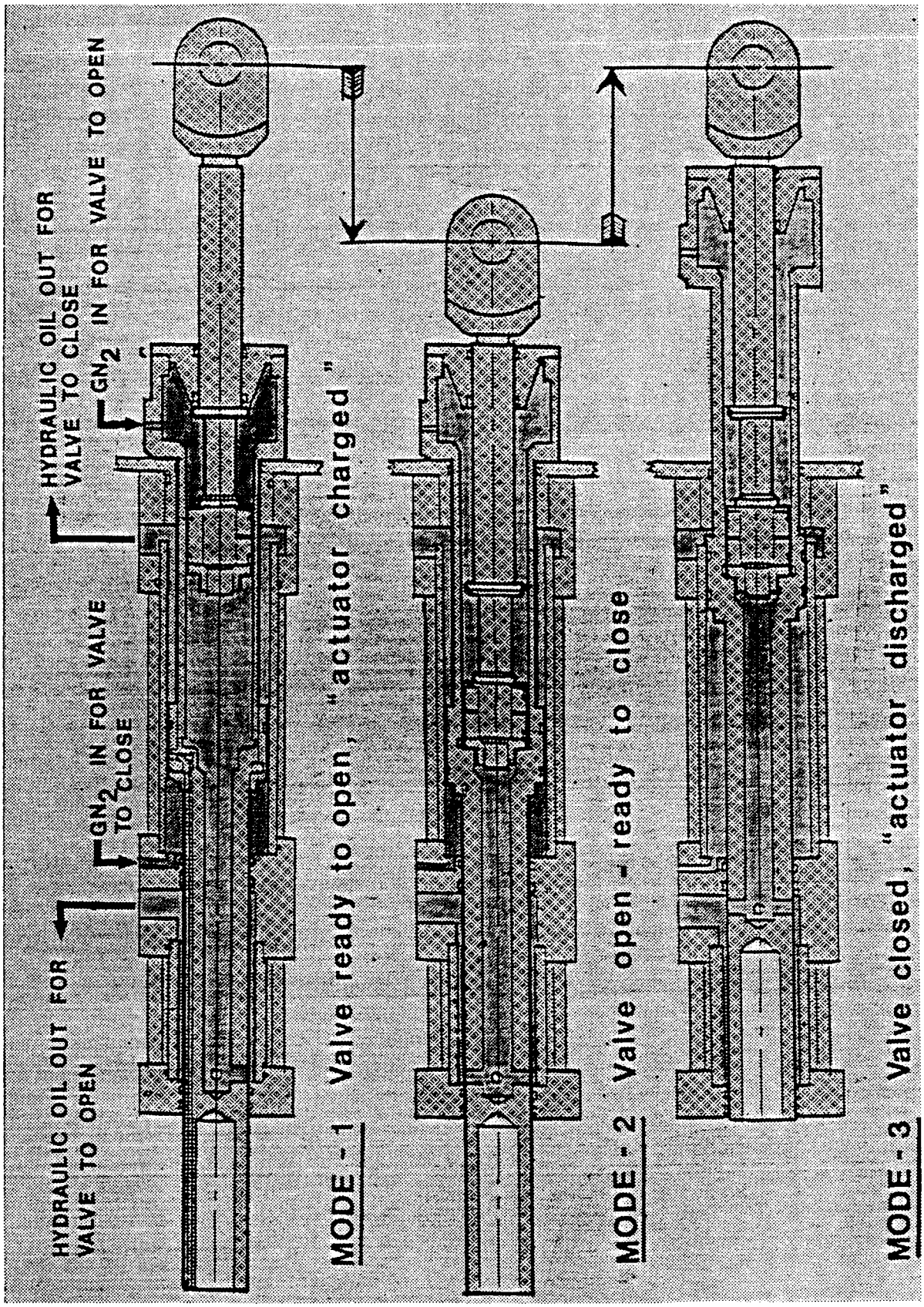


Figure 5. - Valve actuator cross section.

# DISCRETE MECHANISM DAMPING EFFECTS IN THE SOLAR ARRAY FLIGHT EXPERIMENT

E. D. Pinson*

Accelerometer data were collected during on-orbit structural dynamic testing of the Solar Array Flight Experiment aboard the Space Shuttle, and were analyzed at Lockheed Missiles and Space Co. to determine the amount of damping present in the structure. The results of this analysis indicated that the damping present in the fundamental in-plane mode of the structure substantially exceeded that of the fundamental out-of-plane mode. In an effort to determine the source of the higher in-plane damping, a test was performed involving a small device known as a constant-force spring motor or constant-torque mechanism. Results from this test indicate that this discrete device is at least partially responsible for the increased in-plane modal damping of the Solar Array Flight Experiment structure.

## INTRODUCTION

A common feature of large, lightweight, flexible structures is the dominant, and typically very low-frequency, first vibrational mode. Since most of the vibrational energy of these and other types of structures tends to be concentrated in the first mode, the amplitude of oscillations at the corresponding frequency can be relatively large. In situations where this is a problem, strategically placed damping devices and/or materials can help to reduce the magnitude of the ensuing motions.

In the design of the Solar Array Flight Experiment (SAFE), a small device known as a constant-torque mechanism (CTM) was found to be effective in damping certain motions of the structure. The devices were not installed in the experiment for this purpose, but their effect on the fundamental in-plane vibrational mode of the SAFE is evident when comparing the damping factors obtained from the analysis of accelerometer data. The damping characteristics of these mechanisms are further demonstrated by the test described in this report.

## SAFE BACKGROUND INFORMATION AND HARDWARE DESCRIPTION

The National Aeronautics and Space Administration (NASA) launched Space Shuttle mission STS-41-D on August 31, 1984. One of the goals of this mission was to deploy and perform various tests on the SAFE which would both verify and improve present methods of dynamic response prediction for

*Lockheed Missiles & Space Company, Sunnyvale, California.

large, lightweight, flexible structures. Pursuant to this goal, two finite-element (FE) models of the deployed SAFE "wing" were formulated at Lockheed Missiles and Space Co. (LMSC). One model simulates the wing at 70% extension while the other simulates full deployment of the array. Both models were constructed using the EAL/SPAR FE code and were used both before and after on-orbit testing to obtain natural frequencies and mode shapes as well as simulate transient response of the SAFE structure during several excitation scenarios.

The SAFE structure (see Figure 1) was designed and integrated at LMSC in Sunnyvale, CA under contract to Marshall Space Flight Center (MSFC) in Huntsville, AL (contract number NAS8-31352). The mast assembly, produced by Able Engineering Company, Inc. of Goleta, CA, incorporates a canister deployment mechanism which allows the entire mast length of 32 m (105 ft.) to be coiled into a cylinder 1.5 m (5 ft.) long. The triangular mast, only 36 cm (14.4 in.) in circumscribed diameter, can be deployed/retracted at a nominal rate of 4 cm/sec. (1.5 in./sec.) and has an effective EI of 43.6 kN-$m^2$ (15.2 X $10^6$ lbs-$in^2$).

The solar array blanket weighs 1.35 kN (303 lbs.) and consists of 84 rectangular panels each 4 m (13.125 ft.) by 37 cm (14.49 in.) and structurally capable of supporting solar cells. However, only one of these panels, located near the top of the blanket, was populated with active solar cells during on-orbit testing - all others were fitted with aluminum plates simulating the thickness and mass of solar cells. The panel which contained active solar cells was constructed of two 25.4 micro-meter (1.0 mil) Kapton substrates with copper circuitry sandwiched between. Five of the panels were stiffened by a graphite-epoxy framework (all others were stiffened by an aluminum framework) and joined to adjacent panels along the longest sides utilizing an s-glass rod which formed the rib of a "piano-hinge" construction. Small springs were placed at discrete points along the hinge-line to guarantee that the panels would fold in the proper directions during retraction. Although they have little effect in a 1-g environment, these springs were quite effective during the on-orbit tests.

During launch and landing, the blanket was folded into a containment box which exerted a compressive force of 13.3 kN (3000 lbs.) on the 9 cm (3.5 in.) stack of panels. The entire jettisonable structure (including the canister, mast and blanket) weighs approximately 3 kN (673 lbs.) - one-third the weight of conventional solar arrays.

The SAFE wing was designed to function at full and 70% deployment. During full deployment, approximately 23.1 N (5 lbs.) of tensile force was applied to the lower edge of the blanket through springs attached to a tension bar and then to two parallel tension wires. Additionally, a similar apparatus applied approximately 55.6 N (12.5 lbs.) to the upper 70% of the blanket. During 70% deployment, only the latter tensioning system was used. The forces transmitted through the tension bars were regulated by two separate pairs of CTMs which were designed to provide constant tension on the blanket during all structural motions. To guide and lightly hold the

position of the blanket, three stainless-steel guide-wires, placed in the middle and to either side of the centerline of the blanket, were connected to the containment box lid, laced through eyelets in the blanket, and connected to three separate CTMs in the containment box. Each of these CTMs applied approximately 8.9 N (2 lbs.) tension to the guide-wires.

## DESCRIPTION OF THE CONSTANT-TORQUE MECHANISMS

In general, CTMs consist of three component parts:

1. A take-up drum or reel,
2. One or more thin, flat spring bands, and
3. An equal number of spring storage drums.

The take-up drum is typically divided into two segments - one reserved for the tension-wire or band and the other reserved for the constant-force spring(s). Usually, this reel is placed between two or more spring storage drums, although one such drum could be used. The constant-force springs are manufactured with an inherent tendency to coil at a certain natural radius ($R_n$). This natural radius should be slightly smaller than the radius of the spring storage drum and approximately 50% smaller than the spring segment of the take-up drum, according to current design practice. In the SAFE design, at zero deployment of the tension-wire, the constant-force springs are wound almost completely around the storage drums. As the tension-wire deploys, the springs wind around the take-up drum in a direction opposite to that in which they were stored.

The amount of force applied to the tension-wire is dependent on the number of and size of the constant-force springs, and the relative diameters of the two segments of the take-up drum - the spring segment and the tension-wire segment (see Figures 2 and 3). Ideally, constant-force springs of the same cross-section, material, and natural radius should supply identical torques to the spring-segment of the take-up drum, which provides tension to the tension-wire (with the moment arm equal to the radius of the tension-wire segment). The force in the tension-wire due to one CTM is thus given by the following equation (the contributions of several CTMs may be superimposed):

$$T_T = \frac{Ebt^3}{26R_S R_T}(r + 1)^2 \qquad (1)$$

where: $T_T$ = Tension in the tension-wire,
$E$ = Modulus of elasticity of the spring material,
$b$ = Width of the spring,
$t$ = Thickness of the spring,
$R_T$ = Radius of the tension-wire segment of the take-up drum,
$R_N$ = Natural radius of curvature of the spring,
$R_S$ = Radius of the spring segment of the take-up drum, and
$r$ = $R_S/R_N$.

Figure 2 shows the locations of all but one of the CTMs used in the SAFE relative to the centerline of the containment box. (The CTM regulating tension in the center guide-wire is not shown, but is identical to the other guide-wire CTMs.) As noted in this figure and discussed above, the inner CTM regulates the tension applied to the upper 70% of the solar array blanket. Adjacent to this mechanism, is the device which supplies tension to the lower tension bar, and farthest outboard is the CTM regulating the force applied to the lid of the containment box. Although the width of the springs in the outboard CTM is considerably smaller than the other two, several qualitative observations may be made: Notice the relative number of spring storage drums for each of the three mechanisms. The inboard device, supplying the most force, has five constant-force springs acting in concert while the other two, each supplying considerably less force, have fewer springs connected to them. Note also the relative diameters of the two segments of the take-up drums (labeled on only the outboard mechanism).

## SAFE DAMPING FACTORS AND PRELIMINARY INVESTIGATIONS

As mentioned earlier, accelerometer data that was obtained during on-orbit structural dynamic testing was analyzed at LMSC to determine various characteristics of the SAFE. One of the explicit goals of this analysis was to determine the modal damping factors applicable to the structure. The on-orbit tests were divided into three categories: out-of-plane (O/P), in-plane (I/P), and multi-modal (M/M). Several tests from each of these categories were performed at 70% deployment of the SAFE, but only one O/P and one M/M test was performed at full deployment. A total of fourteen such tests were performed, some during orbital night and some during orbital daytime. Details regarding the performance of these tests and the subsequent accelerometer data analysis are contained in Reference 1 and are not included in this report. However, a summary of the average damping factors resulting from this analysis is contained in Table 1.

In this table, the reader will notice a small difference in modal damping factors between orbital night and daytime, a large difference in all modal damping factors between 70% and 100% deployment, and a large difference between the fundamental O/P and I/P modal damping factors (i. e., the first and second modes of the structure, respectively) for all test categories. Damping differences due to thermal effects (orbital night and daytime) are well known and documented for most engineering materials, therefore this difference was somewhat expected. The modal damping factor differences between 70% and 100% deployment are not fully understood as yet, but may be attributable to the larger structrual displacements (and hence more "slip" than "stick" in joint motions) at full deployment. The remaining difference, evident in Table 1, and the subject of this paper, is the difference in damping factors between I/P and O/P modes.

Upon close inspection of the table, it is seen that the ratio between the I/P and O/P modal damping factors for any given category of test (i. e., daytime, 70% deployment) is consistently greater than 1 and rarely below 2. (The obvious, and unexplained, exception to this rule is seen in the

results of the analysis of file 10.) This fact leads the analyst to conclude that a basic and relatively constant difference between I/P and O/P motions of the SAFE structure is responsible for the observed differences in modal damping factors. Intuitively, one such difference, which was later verified by transient response analyses, is the greater participation of all CTMs during I/P motions of the array. Results from these analyses show that, during I/P tests, the lower corners of the blanket oscillated along the mast axis at approximately ten times the amplitude observed during O/P tests. Since the lower edge of the blanket was attached to one of the two tension bars during all tests performed and the motions of the tension bars were regulated by one of two CTM pairs, the devices were ten times more active during I/P tests than they were during O/P tests. Other differences between I/P and O/P motions, such as twisting of the mast, do not exhibit the same dramatic participation changes and are thus assumed to have less impact on overall modal damping factors.

In order to determine whether the CTMs could indeed be responsible for the additional damping in the fundamental I/P mode, several calculations were performed. The maximum kinetic energy of the structure was over-estimated by a rigid body motion similar to the structural mode in question. In performing this calcu.. the following assumptions were made:

1. The blanket was modeled as a rigid, rectangular plate of the appropriate dimensions and mass,
2. The mast was modeled as a rigid, slender rod of the appropriate dimensions and mass, coupled to the blanket during all I/P motions - a conservative assumption,
3. The blanket-mast composite body was assumed to be hinged at the at the base, making it free to rotate in the I/P direction - a conservative assumption, and
4. The angular rate at which the composite body was assumed to rotate was calculated by multiplying the maximum I/P amplitude by the natural frequency of this mode - a conservative assumption. (This method is analogous to determining the velocity of a single degree-of-freedom oscillator.)

In actuality, the mast is not hinged at the base and motions of the mast and blanket are coupled only at the mast tip. Further, the SAFE structure is not a single degree-of-freedom system (i. e., all of the mass does not participate equally in the fundamental I/P mode). However, in spite of the overly conservative assumptions, the kinetic energy was estimated to be only 0.4 J (0.39 in-lbs).

Next, the assumption was made that the kinetic energy estimated above would be totally dissipated in one cycle of oscillation. This was further assumed to be accomplished solely by a force imbalance between the two guide-wires which were attached to opposite ends of the containment box lid and tethered to the outboard CTMs. Under these constraints, a force imbalance (i. e., the difference in force applied by the CTM during deployment and retraction) of only 3.4 N (0.8 lbs.) would be required. Since the force imbalance required was so small, a test was devised to measure the actual force hysteresis.

## CONSTANT-TORQUE MECHANISM TEST DESCRIPTION

In an effort to accurately characterize the subtle force differences that were possibly inherent in the guide-wire CTM, the test plan contained in Reference 2 was devised. The plan required that two access panels be removed prior to re-routing the guide-wire around the guide-wire pulley which is detailed in Figure 5. This was done to avoid the effects of friction between the guide-wire and the SAFE blanket grommets and containment box orifices through which the guide-wire passed during on-orbit testing. Further, this allowed the test apparatus to be placed conveniently underneath the SAFE hardware. A comparison between the operational and test configuration routes of the guide-wire is presented in Figure 6.

The end of the re-routed guide-wire, connected to the containment box lid during on-orbit testing, was attached to a load cell. The load cell was then connected to a pulley which was offset from the shaft of an electric drive motor. Photographs, taken prior to the test, of the outboard CTM mounted in the SAFE and the test configuration are presented in Figures 7 and 8, respectively.

Prior to performing the test, the load cell was calibrated to register the nominal 8.9 N (2 lbs.) to within 0.2 N (0.05 lbs.) during operation of the motor. This accuracy was also verified in increments of 0.2 N (0.05 lbs.) up to a maximum of 11.1 N (2.5 lbs.). During the test, which was performed at standard temperature and pressure in an LMSC building, the motor cycled at a nominal speed of 1 r.p.m., the pulley offset was varied from 0.64 cm (0.25 in.) to 2.54 cm (1 in.), and force hysteresis was measured at four deployment positions (zero, 35%, 70%, and 100%). Early test results indicated that the force hysteresis was relatively insensitive to variations in the pulley offset, therefore during most of the time when measurements were recorded, the pulley was offset from the motor shaft a distance of 2.54 cm (1 in.).

## CONCLUSIONS AND IMPLICATIONS

Results of the CTM damping test, presented in Table 2, show that a definite force hysteresis exists. Further, the magnitude of the variation in force supplied to the guide-wire is large enough to account for most, if not all, of the added damping found in the fundamental I/P mode of the SAFE based on the approximate calculations presented in this report. The fact that these mechanisms are able to provide such relatively large levels of damping is both surprising and encouraging: With the advent of large, lightweight space structures, and the associated structural dynamic problems, the relatively simple CTMs may find a new range of application as discrete damping devices. It is suggested that further research be done to enhance the capabilities of these devices to provide predictable levels of modal damping to other space structures, such as trusses and antennas.

## ACKNOWLEDGEMENTS

The FE element model of the SAFE, an indispensible tool during these investigations, was constructed by B. A. Simpson and modified by T. J. Venator and E. D. Pinson (all employed by LMSC, Structural Dynamics). The author wishes to thank M. D. Menning (LMSC, Solar Array Projects) for his generous contributions, both technical and organizational during the preparation of this report. Appreciation is also due to the SAFE program office at MSFC for allowing LMSC to perform this and other tests involving the SAFE hardware.

## REFERENCES

1. Damping Characteristics of the Solar Array Flight Experiment, by E. D. Pinson, paper presented at the Vibration Damping Workshop II held in Las Vegas, Nevada, March 5-7, 1986.

2. Procedure for SAFE Post Flight ...(CTM)... Test, by M. D. Menning, LMSC Doc. Number F027194, approved August 9, 1985.

Table 1: Modal Damping Values for the SAFE Structure Observed by Accelerometer Data Analysis Performed at LMSC (Abridged Listing)

| | | | Modal Damping [% of critical] | |
|---|---|---|---|---|
| File | Day/Night | Type | Mode 1 (O/P) | Mode 2 (I/P) |
| 5 | Daytime | O/P, 70% | 3.0 | N/A[1] |
| 6 | Nighttime | O/P, 70% | 6.0/9.0[2] | N/A |
| 10 | Daytime | M/M, 70% | 7.0 | 8.0 |
| 11 | Nighttime | M/M, 70% | 3.0 | 11.0 |
| 12 | Daytime | O/P, 70% | 4.5 | N/A |
| 13 | Nighttime | I/P, 70% | N/A | 11.0 |
| 14 | Daytime | M/M, 70% | 4.5 | 11.0 |
| 15 | Nighttime | M/M, 70% | 4.5 | 11.0 |
| 17 | Daytime | O/P, 100% | 2.0 | N/A |
| 20 | Daytime | M/M, 100% | 2.0 | 4.0 |
| 26 | Nighttime | M/M, 70% | 6.0 | 11.0 |
| 27 | Daytime | M/M, 70% | 3.0 | 9.0 |
| 28 | Nighttime | I/P, 70% | N/A | 15.0 |
| 29 | Daytime | I/P, 70% | N/A | 11.0 |
| Avg. | Daytime | 70% | 4.4 | 9.8 |
| Avg. | Nighttime | 70% | 5.1 | 11.8 |
| Avg. | Daytime | 100% | 2.0 | 4.0 |

NOTES:

1. N/A denotes that the test performed was not intended to measure the damping present in that mode.

2. The damping values given for file 6 represent values observed when a) zero initial conditions were assumed, and b) modal initial conditions were approximated in the transient response anlysis, respectively.

3. Files 26, 27, 28, and 29 represent tests having a longer excitation duration than the others that are listed in this table.

Table 2: CTM Force Hysteresis Test Results

| | % SAFE Deployment / Pulley Offset [in] | | | | |
|---|---|---|---|---|---|
| | 0 / 0.5 | 0 / 1.0 | 35 / 1.0 | 70 / 1.0 | 100 / 1.0 |
| Force Hysteresis[1] [pounds] | 0.62 | 0.66 | 0.62 | 0.74[2] | 0.68 |

NOTES:

1. Force hysteresis was determined by subtracting the tensile force in the guide-wire during retraction from the tension in the wire during extension.

2. The force hysteresis value presented for 70% SAFE deployment is the average of three hysteresis values obtained during separate tests at this position.

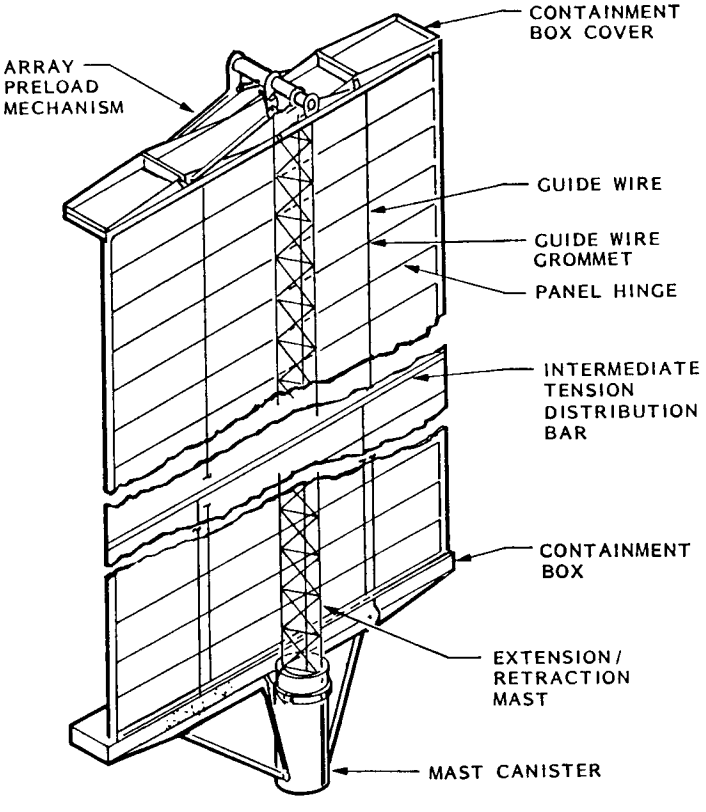


Figure 1. - SAFE hardware components.

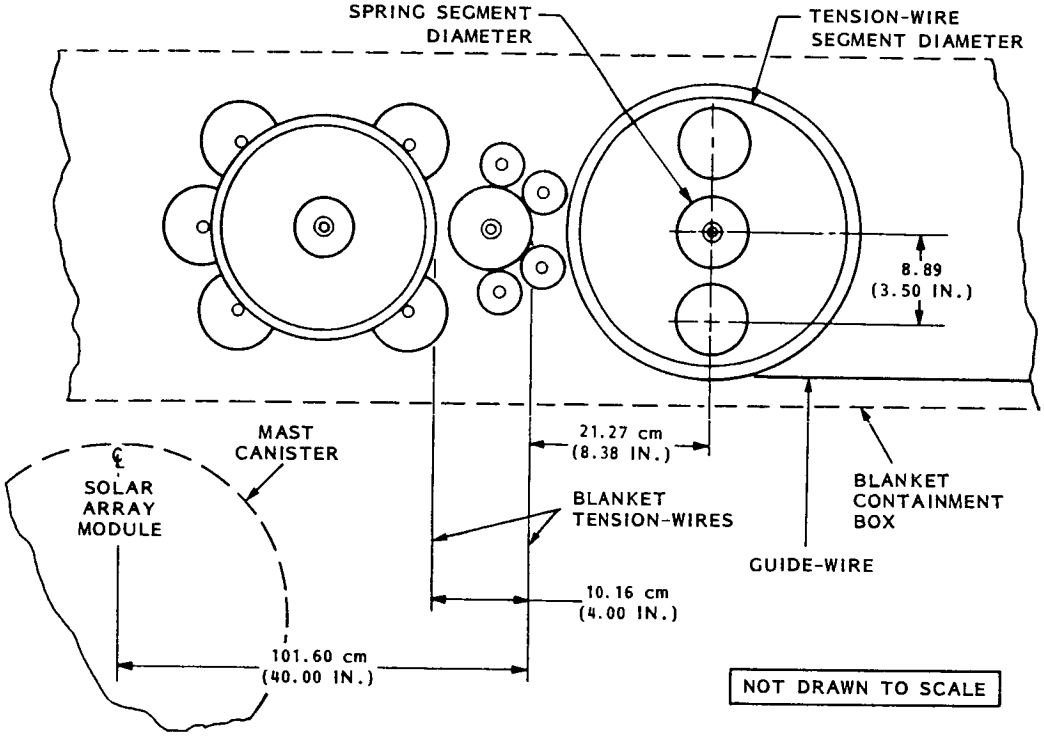


Figure 2. - Guide-wire and blanket tensioning mechanisms.

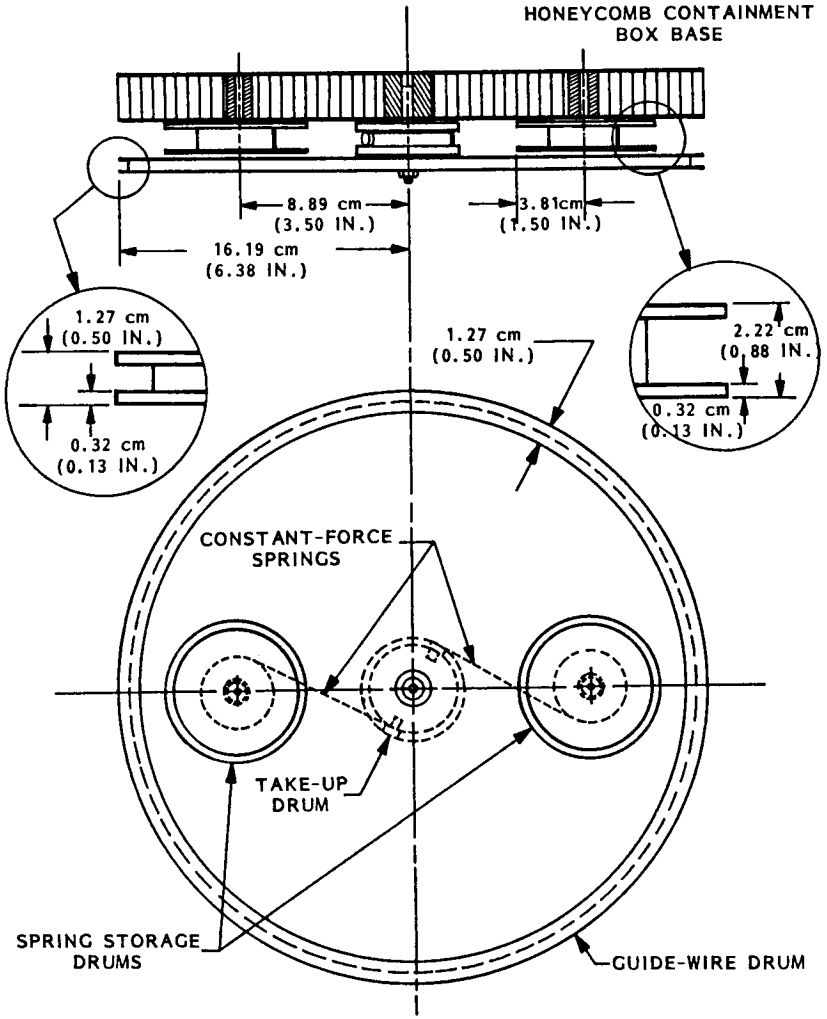


Figure 3. - Design details of guide-wire CTM.

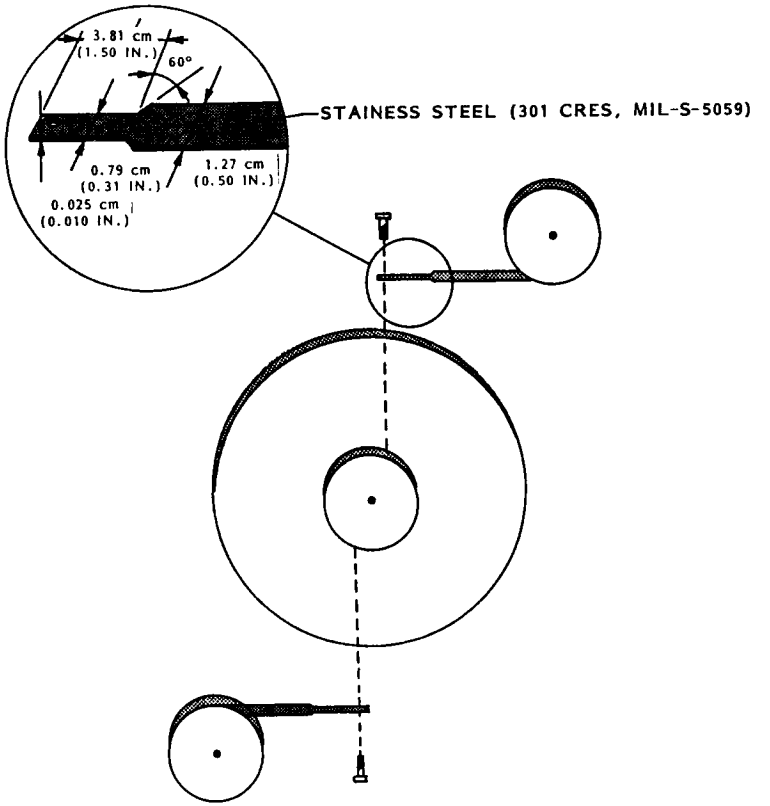


Figure 4. - Exploded view of guide-wire CTM.

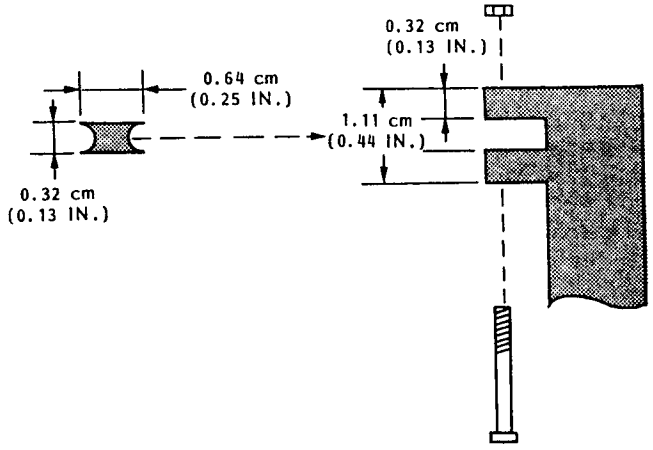


Figure 5. - Exploded view of guide-wire pulley assembly.

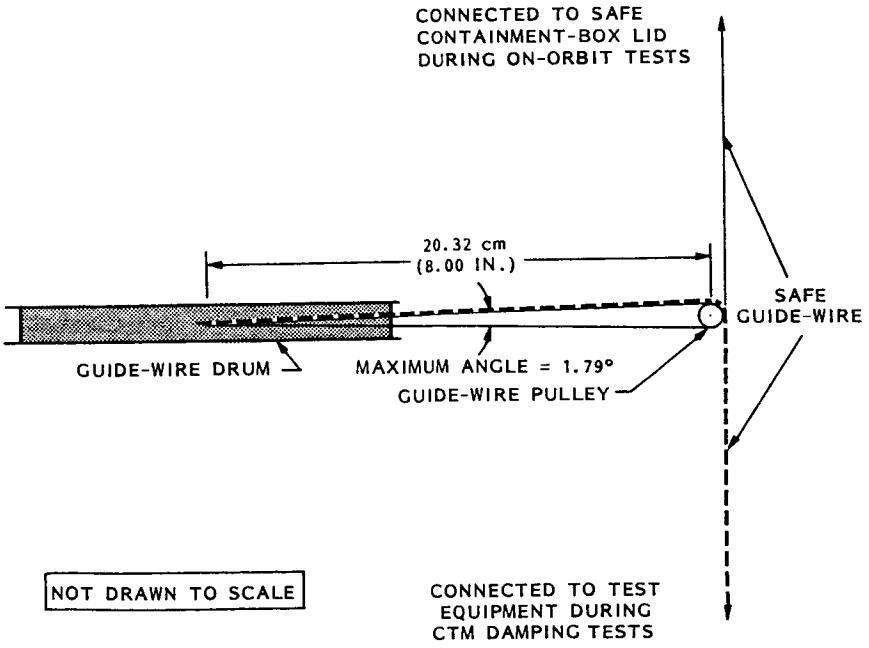


Figure 6. - Guide-wire paths during on-orbit and CTM damping tests.

Figure 7. - CTM as installed in SAFE.

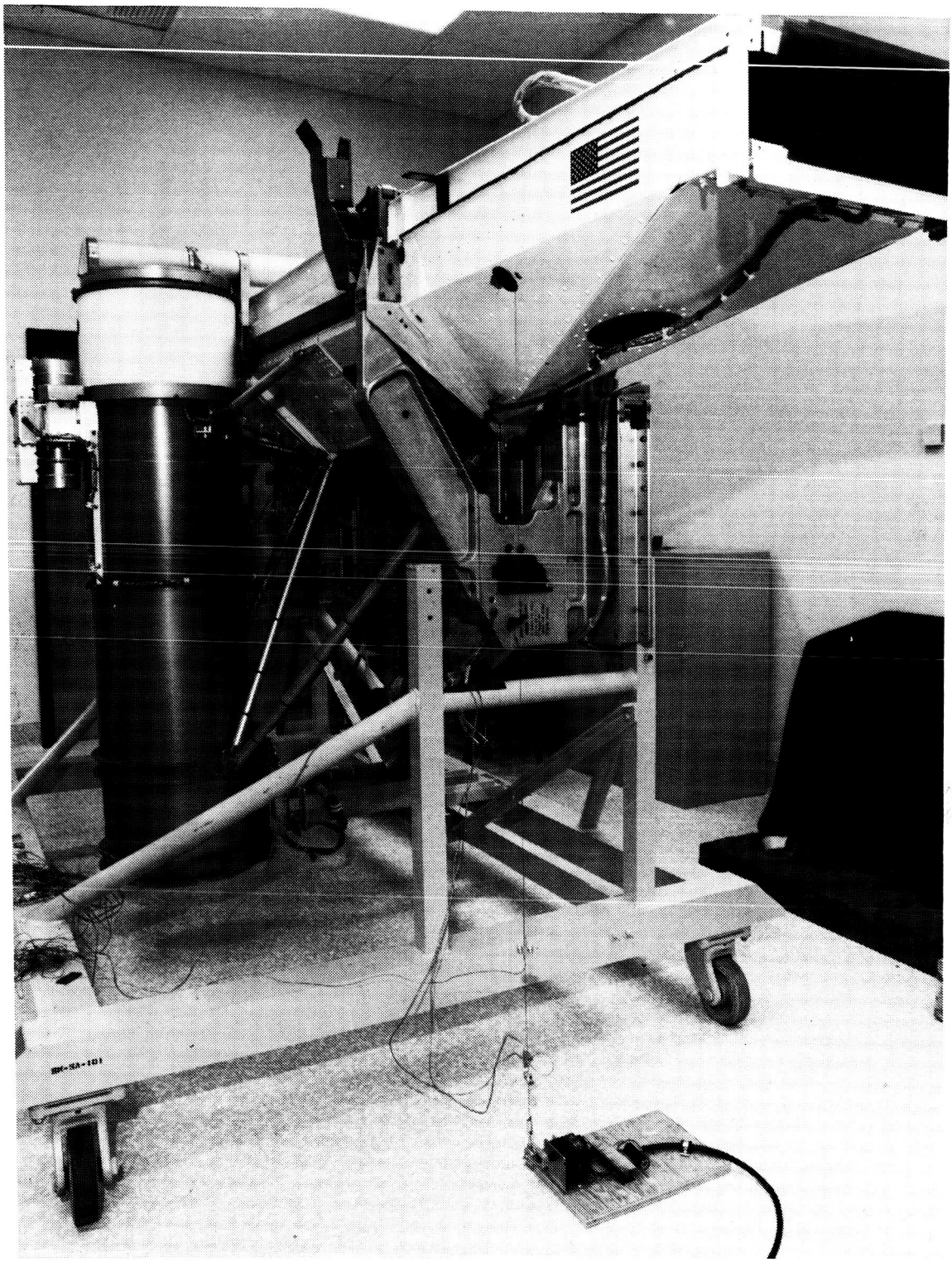

Figure 8. - CTM damping test configuration.

# A MECHANISM FOR PRECISE LINEAR AND ANGULAR ADJUSTMENT UTILIZING FLEXURES*

J. R. Ellis†

This paper describes the design and development of a mechanism for precise linear and angular adjustment. This work was in support of the development of a mechanical extensometer for biaxial strain measurement. A compact mechanism was required which would allow angular adjustments about perpendicular axes with better than $10^{-3}$ degree resolution.

The approach adopted was first to develop a means of precise linear adjustment. To this end, a mechanism based on the toggle principle was built with inexpensive and easily manufactured parts. A detailed evaluation showed that the resolution of the mechanism was better than 1 μm and that adjustments made by using the device were repeatable.

In the second stage of this work, the linear adjustment mechanisms were used in conjunction with a simple arrangement of flexural pivots and attachment blocks to provide the required angular adjustments. A series of experiments conducted with an autocollimator showed that the resolution of the mechanisms was better than $10^{-3}$ degrees. Also, the mechanism met all requirements regarding size, weight, and mechanical simplicity.

Attempts to use the mechanism in conjunction with the biaxial extensometer under development proved unsuccessful. Any form of in situ adjustment was found to cause erratic changes in instrument output. These changes were due to problems with the suspension system. However, the subject mechanism performed well in its own right and appeared to have potential for use in other applications. One important advantage of flexure-based mechanisms is that they can be designed to operate independently of screw threads. This raises the possibility that they can be used for precise linear and angular adjustment in a space environment.

## INTRODUCTION

The many difficulties associated with conducting mechanical tests under complex loading conditions have received considerable attention during the

---

*Research sponsored by the Office of Breeder Technology Projects, U.S. Department of Energy, under Contract N-7405-ENG-26 with the Union Carbide Corporation, and by NASA Lewis Research Center under Grant NAG 3-379.

†University of Akron, Akron, Ohio 44325.

past 10 years (ref. 1). As a result of this attention, test systems have been developed which allow tubular specimens to be tested under combinations of axial load, torsional load, and internal and external pressure. The mechanical design and electronic control features of such test systems have been fully developed, and they present no difficulty. However, one associated aspect of multiaxial testing, that of precise strain measurement, has received little attention.

This deficiency was recognized at the Oak Ridge National Laboratory, and an effort was directed at developing a mechanical extensometer capable of measuring axial, torsional, and diametral strains at elevated temperatures (ref. 2). The basic approach is illustrated schematically in figure 1. Two sensors incorporating ceramic probes grip the specimen by means of friction. The assumption is that, once installed, the point of contact of each probe remains fixed on the specimen. The probes, therefore, transmit specimen displacements and rotations to the body of the instrument. A further assumption is that a suspension system can be designed to constrain the sensors to planes parallel to the X-Y plane in figure 1(a). Two such planes are the DEFG and HIJK planes shown in the figure.

The method of strain measurement is now described. Under axial loading, the vertical distance between the sensors, BB in figure 1(a), changes and is used as a basis for axial strain measurement. This is achieved by positioning proximity transducers on the top sensor and a target on the bottom sensor. With regard to diametral strain measurement, changes in specimen diameter resulting from radial loadings are transmitted via the hinge to the mounting arms. Relative movement between the mounting arms, AA in figure 1(a), is used for measurement purposes by positioning the core of a linear variable differential transformer (LVDT) on one mounting arm and the coil on the other. Under torsional loading, the sensors rotate different amounts about the Z-axis within their respective reference planes. This difference in angular rotation, $\theta$ in figure 1(a), is used for torsional strain measurement. A system of levers and rotary variable differential transformers (RVDT's) is used for this purpose.

One difficulty encountered during the development of the instrument was that very precise angular alignment of the target relative to the HIJK reference plane was needed to avoid crosstalk between the axial and torsional components of straining. A mechanism was required to give angular adjustment about two perpendicular axes with a $10^{-3}$ degree resolution. Furthermore, since space was limited, the mechanism was to be compact and occupy a cube with sides no greater than 5 cm. Also, the weight of the device was to be kept to a minimum to avoid difficulties in experiments involving rapid loadings.

This paper describes the design and development of a positioning mechanism to meet these requirements. It will be shown that the toggle principle can be used to advantage in this application, with linear and angular accuracies better than 1 μm and $10^{-3}$ degrees ultimately being achieved. Finally, possible improvements to the mechanism are discussed and some alternative applications are suggested.

## MECHANICAL DETAILS

The approach adopted in resolving the alignment problem was first to develop a means of precise linear adjustment using the principle of the toggle (ref. 3). With this method, small displacements are obtained by modifying the curvature of flexural elements. This approach was preferred as it offered the advantages of mechanical simplicity and low weight.

### Linear Adjustment Mechanism

In the present design, the initial curvature of four rectangular section flexures is modified by using a tapered adjustment screw (fig. 2(a)). These curvature changes cause the button attached to the free end of the flexures to displace axially. The magnitude of these displacements is governed by the initial curvature of the flexures and by the type of thread and taper on the adjustment screw. A means of coarse linear adjustment is provided by enclosing the toggle mechanisms in an externally threaded sleeve (fig. 2(b)). The screw thread used had 40 threads per inch (TPI), which allowed the usual form of micrometer adjustment.

One difference between this and earlier applications of the toggle principle for precise linear adjustment is that the mechanism was assembled from a number of easily manufactured parts (fig. 3). The flexures consist of straight lengths of spring steel with hardened steel balls located at their midsections. The balls, which were attached by spot welding, provide point contact between the flexures and the tapered adjustment screw.

Curvature of the flexures in the assembled form was obtained by constraining the flexures to follow 10° tapers over 6-mm lengths at each end. The clamping force necessary to achieve this condition was provided by collars held in position by spot-welded straps.

Assembly of the mechanism was not straightforward and involved the use of a number of special purpose fixtures. One such fixture, shown in figure 4, ensured precise alignment of the button and the screw holder while allowing the distance between these components to be varied in a controlled manner. Adjustments of this type were necessary as the flexures were forced to assume the required curvature. In addition, less complicated fixtures were used for attaching the balls to the flexures and for supporting the mechanism during installation of the straps.

### Angular Adjustment Mechanism

The mechanism used to convert linear adjustment to the required form of angular adjustment utilizes the cylindrical type of flexural pivot (ref. 4). These pivots consist of two cylindrical elements joined by crossed flexures. This arrangement has the advantage of allowing rotation between mating parts without any associated friction or backlash.

The approach adopted in the present application is shown schematically in figure 5. Pairs of flexural pivots are gripped along two perpendicular axes in an attachment block. One pair of pivots is then attached to the target plate with two clamp blocks while the other pair is attached in a similar manner to the base plate. Inspection of figure 5 shows that this arrangement allows angular adjustment of the target plate about two perpendicular axes.

Operation of the subject mechanism is further illustrated in figures 6(a) and (b). Coarse adjustments are made by rotating the linear adjustment mechanisms relative to the base plate using the knurled drums. When the required coarse setting is achieved, the locking arrangement is used to prevent further rotation. Fine adjustments are then made by rotating the adjustment screw of the toggle mechanism. Again, knurled drums are provided to facilitate these adjustments.

## TESTING AND RESULTS

The performance of the device was evaluated in two stages in a dimensional inspection facility. The experiments were conducted under closely controlled environmental conditions on an inspection-grade granite surface table. All experiments were performed using forward rotations of the various adjustment screws, as this was the intended mode of operation during biaxial experiments.

### Evaluation of the Linear Adjustment Mechanism

The first series of experiments was conducted with the target plate removed from the assembly, which allowed the characteristics of the toggle mechanisms to be checked independently. This was accomplished by cementing small targets to the buttons of the mechanisms and using proximity transducers to measure the displacements resulting from known rotations of the adjustment screws. Since this measurement system is noncontacting, the performance of the toggle assemblies was unaffected by the measurement method. The instrumentation used for this work, the Hitec Proximic type, was calibrated so that 1 μm (39.4 μin) was equivalent to 39.4 mV. Typical results obtained for two revolutions of the adjustment screw are shown in table I and figure 7. As indicated, the experiments were conducted five times to determine the repeatability of the data.

### Evaluation of Angular Adjustment Mechanism

The approach adopted in evaluating the mechanism's capabilities for making precise angular adjustments was to mount an optically flat mirror on the target plate and to use an autocollimator to measure angular changes. The procedure followed was to cover two revolutions of screw adjustment in five division increments and to record the corresponding angular changes.

The autocollimator allowed angular measurements to be made down to 0.1 sec or $3.0 \times 10^{-4}$ degrees. The results obtained for angular rotations about the X-X axis are shown in table II and figure 8(a). Similar data obtained for rotations about the Y-Y axis are shown in figure 8(b). As in the earlier experiments, five repeat runs were made to gain some insight regarding the repeatability of the data.

A final series of experiments was conducted to determine the angular changes resulting from coarse adjustments over a 0.25-mm range in 0.05-mm steps. As the range of the autocollimator was limited, the procedure followed was to reset the instrument to zero after measuring the angular changes resulting from each 0.05-mm adjustment. Measurements of this type were made for adjustments about both the X-X and Y-Y axes.

## DISCUSSION

Consideration is given first to the performance of the linear adjustment mechanism. Table I shows that one complete revolution of the adjustment screw caused the button to displace 9.04 μm (356 μin). By way of comparison, a similar displacement would be obtained by rotating a screw with 3000 TPI through one revolution. Using the various scales provided for fine adjustment, one division of adjustment gave a displacement of 0.29 μm (11.5 μin). In light of this result, the resolution of the toggle mechanism was judged to be about two orders of magnitude better than that of micrometers utilizing 40 TPI screw threads. Another characteristic of the data shown in table I is that the displacements resulting from particular screw settings are repeatable. A detailed analysis showed that the displacements obtained in the five repeat runs fell within $\pm 1$ percent of the mean.

The relationship between button displacement and screw setting is illustrated in figure 7. This relationship is nearly linear up to settings of about 40 divisions. At higher values, the relationship becomes progressively more nonlinear. A series of curve fits shows that a second-order polynomial could be used to represent the data over the full range of interest. The rms error for the expression subsequently obtained by least squares is 0.61 (fig. 8).

The performance of the mechanism in making fine angular adjustments was similar to that just described. As indicated in table II, one revolution of the appropriate fine adjustment screw caused the target plate to rotate $21.38 \times 10^{-3}$ degrees about the X-X axis. The corresponding rotation for one division of screw adjustment is $6.9 \times 10^{-4}$ degrees. In the case of adjustments about the Y-Y axis, these values are $25.11 \times 10^{-3}$ and $8.1 \times 10^{-4}$ degrees, respectively. Again, the data were repeatable, the maximum and minimum percentage deviations falling, for the most part, within $\pm 1$ percent of the mean.

Figures 8(a) and (b) illustrate the performance of the mechanism over the full range of interest. The relationships between screw settings and angular rotation are approximately linear up to settings of 40 divisions and

nonlinear at higher values. Second-order polynomials were used to fit the data with the result shown in the figures. The rms error for the X-X adjustments was 0.29 while that for the Y-Y adjustments was 0.84. The latter, less than desirable result was caused by systematic errors occurring at particular adjustment screw settings. The source of these errors is unknown at the time of this writing.

The performance of the mechanism in making coarse angular adjustments was similar for both the X-X and the Y-Y axes, the angular change produced by two divisions of coarse setting falling in the range of $133.61 \times 10^{-3}$ to $156.28 \times 10^{-3}$ degrees. The average value for all settings was $141.91 \times 10^{-3}$ degrees, and the deviations of repeat data fell, for the most part, within $\pm 3$ percent of the mean. Thus, the fine and coarse adjustment ranges are complementary provided the target plate is roughed into position within 0.5 coarse setting divisions or $35.0 \times 10^{-3}$ degrees.

The intent of this work was to develop a compact mechanism providing angular adjustment about two axes with a $10^{-3}$ degree resolution. The results described showed that the subject mechanism met these design requirements, at least under ideal bench checkout conditions. However, attempting to use this device to minimize crosstalk in multiaxial experiments proved unsuccessful. This was because any form of in situ adjustment caused the relative position of the sensors to change in an uncontrolled manner. It was concluded, however, that the problem lay with the method of extensometer suspension rather than with the subject mechanism. Thus, this approach was discontinued in favor of one ensuring a more positive location of the target relative to the proximity transducer.

However, because the mechanism performed well in its own right, some consideration was given to design improvements and alternative applications. One obvious shortcoming of the device in the form described is that its output was nonlinear. This problem could be overcome without much difficulty by using a predetermined profile on the adjustment screw rather than a straight taper. Also, the resolution of the device could be improved by using a finer thread on the adjustment screw.

An alternative application might be to use the device in its present form for ultrafine adjustments in setting up microscopes or optical systems. An important advantage of the toggle mechanism is that in principle it can be used independent of screw threads. This situation could be achieved by using a linear actuator to drive the tapered pin against the flexures. Thus, the problems usually associated with screw threads would be eliminated, and extreme precision could be achieved. Also, elimination of screw threads might allow the device to be used to advantage for precise linear and angular adjustment in hostile environments.

## CONCLUSIONS

The following are the conclusions reached regarding the design, manufacture, and performance of the flexure-based adjustment mechanism:

1. The toggle principle was used to provide linear adjustments with better than 1-μm resolution. The advantages of the approach were viewed as being mechanical simplicity and low weight.

2. The flexure-based mechanism was fabricated successfully from inexpensive and easily manufactured parts. However, the assembly of the device was not straightforward.

3. Linear adjustment mechanisms were used in conjunction with a simple arrangement of flexural pivots to give a two-axis angular adjustment with better than a $10^{-3}$ degree resolution. The resulting mechanism was both mechanically simple and compact.

4. Attempts to use the mechanism to resolve alignment problems associated with biaxial strain measurement proved unsuccessful. However, the difficulty lay with the extensometer design rather than with the subject mechanism.

5. The toggle mechanism can be made to operate independently of screw threads. This raises the possibility that mechanisms of this type could be used to advantage for precise linear or angular adjustment in space environment.

## REFERENCES


1. Brown, M.W.: Low Cycle Fatigue Testing Under Multiaxial Stresses at Elevated Temperatures. Measurement of High Temperautre Mechanical Properties of Materials, M.S. Loveday, M.F. Day, and B.F. Dyson, eds., H.M.S.O., London, 1982, pp. 185-203.

2. Ellis, J.R.: A Multiaxial Extensometer for Measuring Axial, Torsional, and Diametral Strains at Elevated Temperatures. Oak Ridge National Laboratory Report, ORNL/TM-8760, June 1983.

3. King, H.M.; and Weir, J.B.: Adjusting Device Incorporating an Ultrafine Movement. J. Sci. Instrum., vol. 39, no. 1, Jan. 1962, p. 31.

4. Troeger, H.: Considerations in the Application of Flexural Pivots. Automatic Control, vol. 17, no. 4, Nov. 1962, pp. 41-46.

TABLE I. - EVALUATION OF LINEAR ADJUSTMENT MECHANISM

[1 revolution of the adjustment screw corresponds to a setting of 31 divisions; 1 μm = 39.4 μin, equivalent to 39.4 mV.]

| Screw setting, divisions | Button displacement | | | | | | | | | |
|---|---|---|---|---|---|---|---|---|---|---|
| | Run 1 | | Run 2 | | Run 3 | | Run 4 | | Run 5 | |
| | μm | μin | μm | μin | μm | μin | μm | μin | μm | μin |
| 0 | 0 | 0 | 0 | 0 | 0 | 0 | 0 | 0 | 0 | 0 |
| 6 | 1.80 | 71 | 1.91 | 75 | 2.21 | 87 | 2.13 | 84 | 2.16 | 85 |
| 11 | 3.28 | 129 | 3.38 | 133 | 3.63 | 143 | 3.51 | 138 | 3.51 | 138 |
| 16 | 4.72 | 186 | 4.83 | 190 | 5.11 | 201 | 5.03 | 198 | 5.05 | 199 |
| 21 | 6.12 | 241 | 6.10 | 240 | 6.30 | 248 | 6.20 | 244 | 6.25 | 246 |
| 26 | 7.44 | 293 | 7.49 | 295 | 7.57 | 298 | 7.62 | 300 | 7.65 | 301 |
| 31 | 8.94 | 352 | 9.02 | 335 | 9.09 | 358 | 9.07 | 357 | 9.07 | 357 |
| 37 | 10.77 | 424 | 10.95 | 431 | 10.87 | 428 | 10.85 | 427 | 10.80 | 425 |
| 42 | 12.14 | 478 | 12.32 | 485 | 12.27 | 483 | 12.17 | 479 | 12.09 | 476 |
| 47 | 13.31 | 524 | 13.51 | 532 | 13.46 | 530 | 13.28 | 523 | 13.26 | 522 |
| 52 | 14.43 | 568 | 14.58 | 574 | 14.45 | 569 | 14.40 | 567 | 14.30 | 563 |
| 57 | 15.47 | 609 | 15.67 | 617 | 15.49 | 610 | 15.54 | 612 | 15.37 | 605 |
| 62 | 16.76 | 660 | 16.89 | 665 | 16.69 | 657 | 16.69 | 657 | 16.61 | 654 |

TABLE II. - EVALUATION OF MECHANISM FOR FINE ADJUSTMENT ABOUT THE X-X AXIS

| Fine screw setting, divisions | Rotation about X-X axis | | | | | | | | | |
|---|---|---|---|---|---|---|---|---|---|---|
| | Run 1 | | Run 2 | | Run 3 | | Run 4 | | Run 5 | |
| | min:sec | deg | min:sec | deg | min:sec | deg | min:sec | deg | min:sec | deg |
| 0 | 0 | 0 | 0 | 0 | 0 | 0 | 0 | 0 | 0 | 0 |
| 6 | 0:15.4 | $4.28 \times 10^{-3}$ | 0:15.6 | $4.33 \times 10^{-3}$ | 0:15.6 | $4.33 \times 10^{-3}$ | 0:15.9 | $4.42 \times 10^{-3}$ | 0:15.8 | $4.39 \times 10^{-3}$ |
| 11 | 0:28.8 | 8.00 | 0:28.6 | 7.94 | 0:28.5 | 7.92 | 0:28.8 | 8.00 | 0:28.7 | 7.97 |
| 16 | 0:40.8 | 11.33 | 0:40.5 | 11.25 | 0:40.6 | 11.28 | 0:40.7 | 11.31 | 0:40.8 | 11.33 |
| 21 | 0:51.7 | 14.36 | 0:52.2 | 14.50 | 0:52.0 | 14.44 | 0:52.5 | 14.58 | 0:52.5 | 14.58 |
| 26 | 1:4.0 | 17.78 | 1:4.4 | 17.89 | 1:5.2 | 18.11 | 1:5.5 | 18.19 | 1:4.7 | 17.97 |
| 31 | 1:16.7 | 21.31 | 1:16.8 | 21.33 | 1:17.1 | 21.42 | 1:17.2 | 21.44 | 1:17.0 | 21.39 |
| 37 | 1:29.7 | 24.92 | 1:29.9 | 24.97 | 1:29.5 | 24.86 | 1:29.9 | 24.97 | 1:30.0 | 25.00 |
| 42 | 1:40.4 | 27.89 | 1:40.0 | 27.78 | 1:39.6 | 27.67 | 1:40.0 | 27.78 | 1:39.9 | 27.75 |
| 47 | 1:49.8 | 30.50 | 1:49.8 | 30.50 | 1:50.0 | 30.56 | 1:50.3 | 30.64 | 1:50.0 | 30.56 |
| 52 | 1:58.6 | 32.94 | 1:59.3 | 33.14 | 1:58.8 | 33.00 | 1:59.4 | 33.17 | 1:59.3 | 33.14 |
| 57 | 2:9.2 | 35.89 | 2:9.3 | 35.92 | 2:8.2 | 35.61 | 2:9.6 | 36.00 | 2:9.4 | 35.94 |
| 62 | 2:18.2 | 38.39 | 2:18.4 | 38.44 | 2:18.1 | 38.36 | 2:18.5 | 38.47 | 2:18.3 | 38.42 |

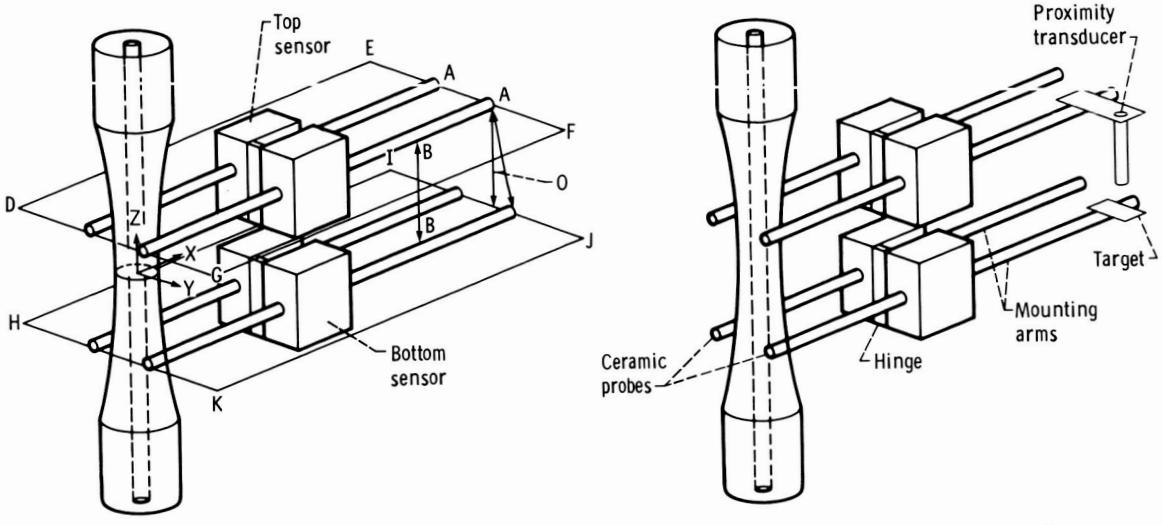


(a) Basic approach.

(b) Method of axial strain measurement.

Figure 1. - Multiaxial extensometer for measuring axial, torsional, and diametral strains at elevated temperatures.

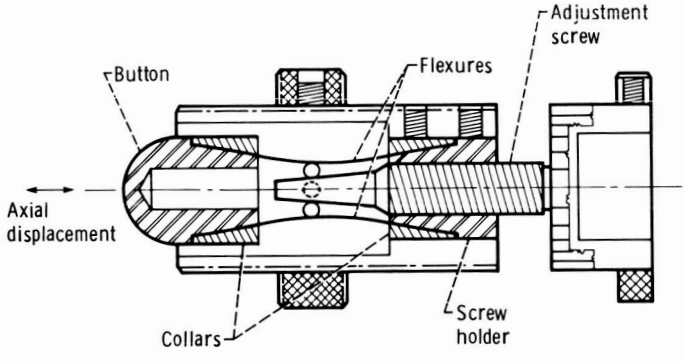


(a) Sectional view.

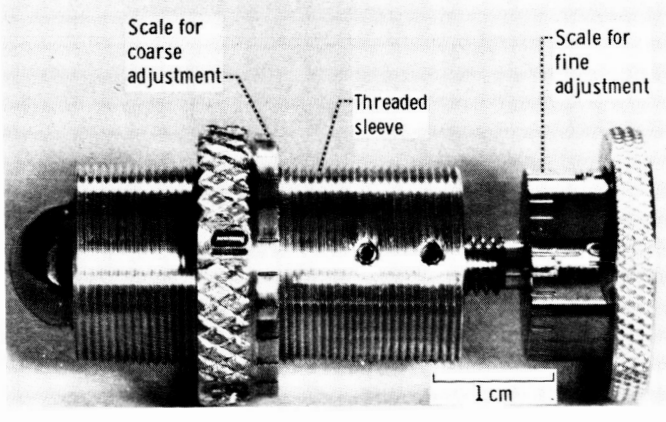


(b) Sleeve details.

Figure 2. - Linear adjustment mechanism.

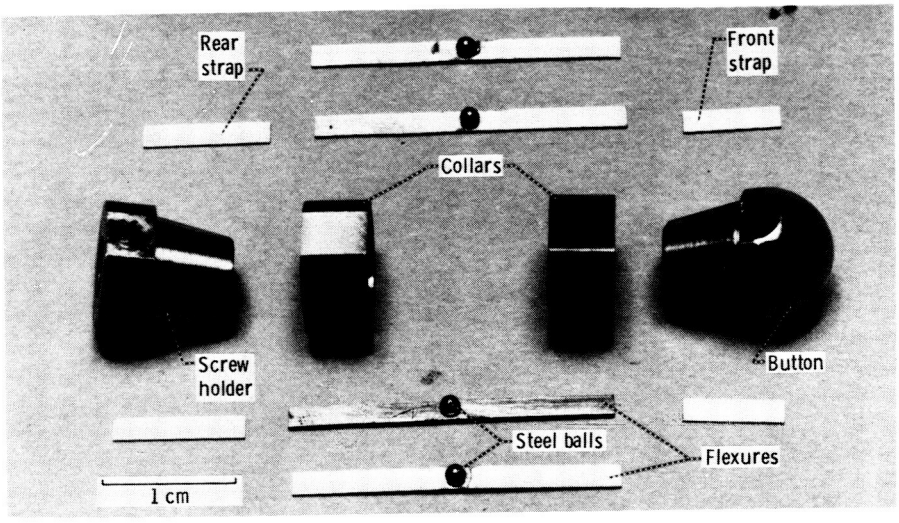


Figure 3. - Parts of toggle mechanism.

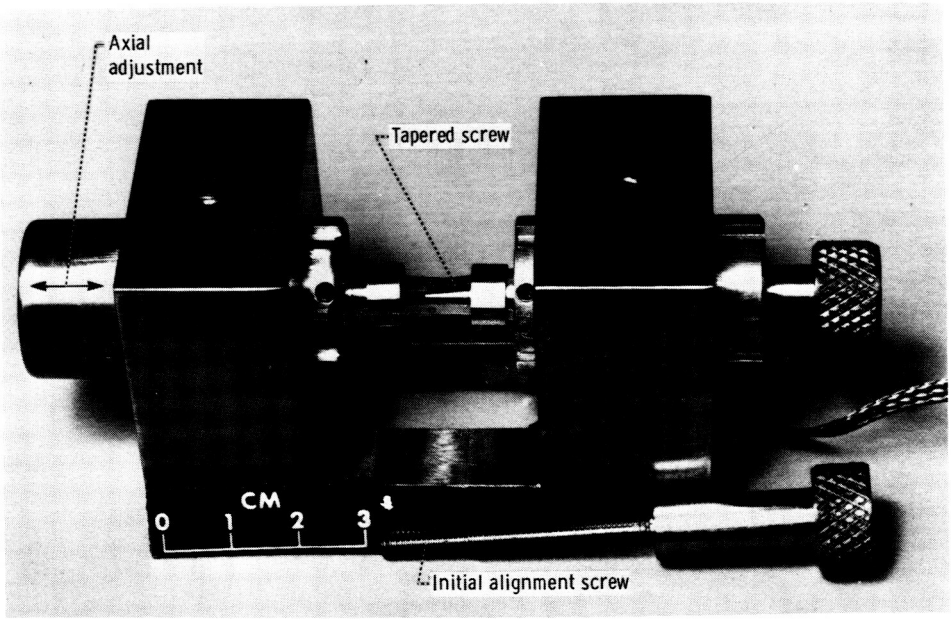


Figure 4. - Fixture used to assemble toggle mechanism.

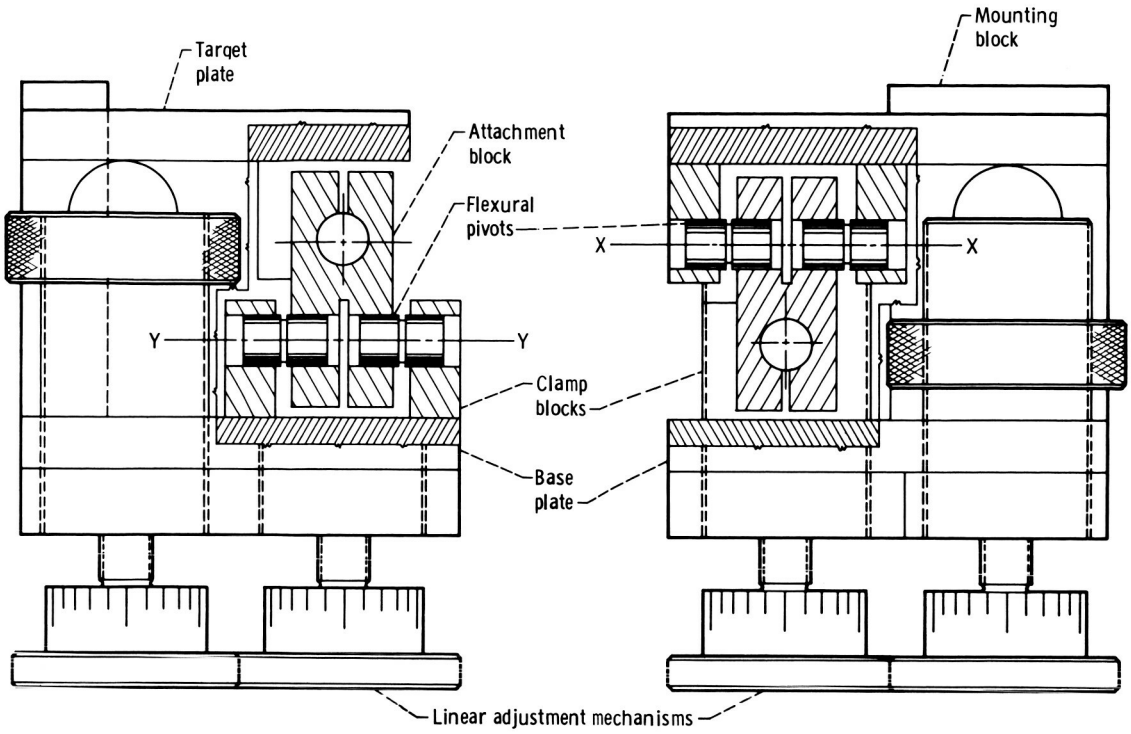


Figure 5. - Schematic of angular adjustment mechanisms.

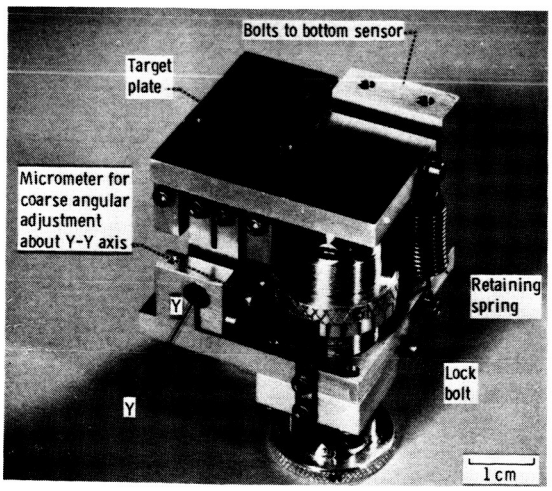


(a) Viewed from above.

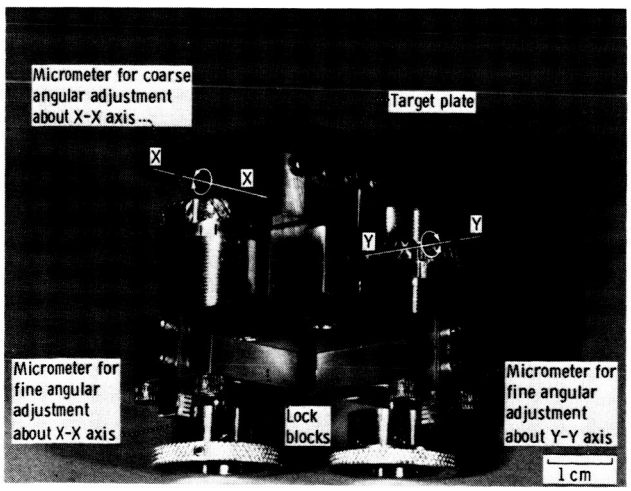


(b) Viewed from below.

Figure 6. - Angular adjustment mechanism.

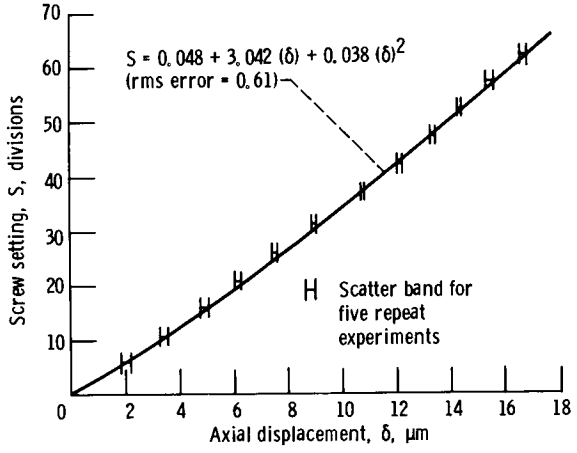


Figure 7. - Evaluation of linear adjustment mechanism.

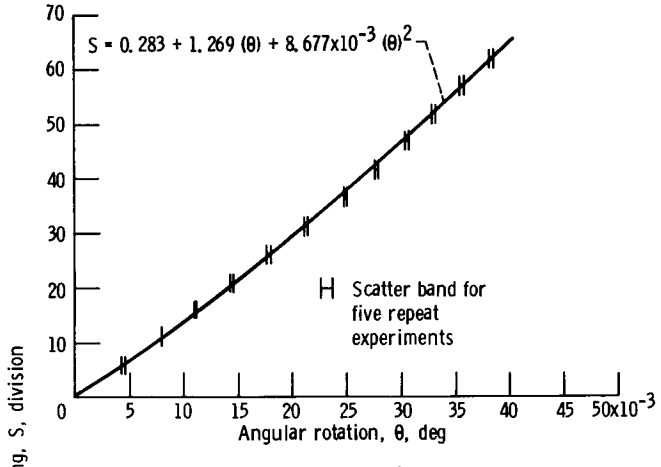


(a) About X-X axis.

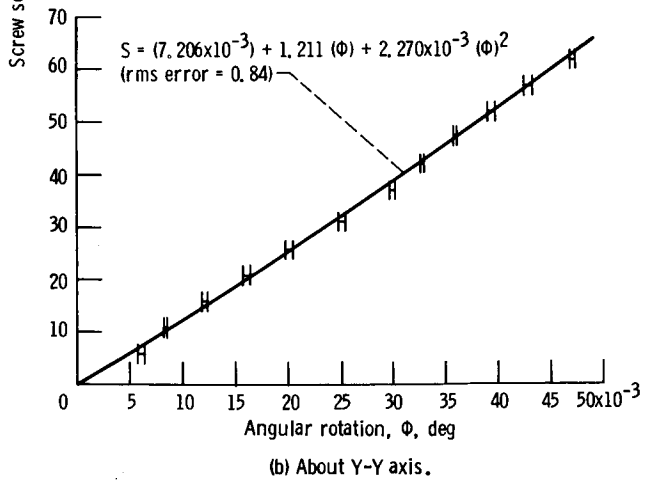


(b) About Y-Y axis.

Figure 8. - Evaluation of angular adjustment mechanism for fine adjustments.

# WEIGHT AND POWER SAVINGS SHAFT ENCODER INTERFACING TECHNIQUES FOR AEROSPACE APPLICATIONS

Donald H. Breslow*

Many aerospace applications for shaft angle digitizers such as optical shaft encoders require special features that are not usually required on commercial products. Among the most important user considerations are the lowest possible weight and power consumption. This paper will describe a variety of mechanical and electrical interface techniques that have large potential weight and power savings. The principles to be presented apply to a wide variety of encoders, ranging from 16 to 22 bit resolution and with diameters from 152 to 380 mm (6 to 15 in.).

## MECHANICAL CONSIDERATIONS

Mechanical architecture usually keynotes the basic encoder design. There are three basic architectural configurations which may be considered for integration into the user system: housed, unhoused (kit encoder), and cartridge. Schematics of the basic bearing and coupling layouts are shown in Figure 1. A section view of a typical housed or cartridge encoder is shown in Figure 2. A later section will explain the subtle differences between housed and cartridge encoders.

Encoders are characterized by an ultra stable, ultra low runout base and bearing spindle assembly which supports the rotation of the code disk past fixed reading stations. Code disks frequently have patterns of 40 line pairs per millimeter (1000 lines per inch). When photo electrically read out against the fixed slit, diffraction phenomena coupled with readout geometry produces periodic spatial high fidelity sinusoids. One readout period (360 degrees electrical) is produced by rotation through one code cycle. Since phase shifts between reading stations of one or two degrees are readily detected by commonly used processing circuitry, mechanical motions of 1/360 of a code cycle equal to 0.025/360, or about 70 micrometers (3 microinches) are readily inferred. Hence encoder mechanical design is always concerned with creating stable structures such that the observed readout is due to the rotation of the code disc about the axis it is desired to encode, and not spurious bending or deflection of the encoder structure. Given an encoder and another mechanism which must carry the same loads, the encoder structure and bearings are usually considerably oversize and stiffer with respect to their counterparts for general purpose mechanisms.

*Itek Measurement Systems, Newton, Massachusetts.

A housed encoder (Figure 1(a)) has several advantages, but also several disadvantages. The biggest advantage is that the encoder can be procured, inventoried, and installed as a free standing, self-contained item. The encoder can also be returned to the supplier for repair or modification. The advantages are primarily logistical. The biggest disadvantages are weight and volume penalities.

Inspection of Figure 1 will show that there are duplicate bearings and encoder structure, as well as a shaft coupler. Shaft couplers are required to avoid excessive misalignment loads in the encoder. Couplers capable of transmitting shaft motion to the encoder with under 1.0 second of arc transmission error are often slotted structures in the form of a 100 to 150 mm (4 to 6 in.) diameter by 100 mm long right circular cylinder (19 to 22 bit systems). The coupler can add approximately 100 mm of axial length to the system; larger diameter encoders (250 mm (10 in.) and above) are often provided in a hollow shaft configuration. In some cases part of the through hole can be used to package a coupler (Figure 3) at the expense of using some of the shaft space. Although the hollow shaft configuration may avoid the axial length penalty, it is not a minimum weight configuration. Weight can be reduced to a point by using light weight materials such as titanium and beryllium. However the basic system architecture shown in Figure 1(a) precludes very large savings because the encoder base, shaft, bearings, and shaft coupler are redundant relative to the absolute minimum unhoused configuration shown in Figure 1(b).

In order to eliminate the redundant structural members and their associated weight, some users interface with unhoused kit type encoders such as shown in Figure 1(b). Kit type encoders are characterized by a minimum number of parts. As long as the user can provide a spindle with encoder quality, low runouts over all loads and environments, bearings, encoder structure, and couplers are conserved. The weight and volume savings are an obvious advantage. There are two disadvantages to this technique. First, in some cases it may be impractical to build the user's "power spindle" to the low runout tolerances required by the encoder. Secondly, the encoder is very highly integrated into the user's bearing structure. As a result, the encoder cannot be stocked as a subassembly procured in advance, and the logistics of assembly and repair are often difficult. These encoders are typically assembled either by sending a trained assembler from the encoder supplier to the user's factory or by the user shipping an unencoded spindle to the encoder supplier, which after some time is returned in encoded form.

As an example of what can be done, the encoder shown in Figure 2 was custom designed for a classified application. Following are key parameters:

| | |
|---|---|
| Resolution | 21 bits (0.62 arc sec) |
| Overall Diameter | 381 mm (15 in.) |
| Shaft Thru Hole Diameter | 254 mm (10 in.) |
| Principal Materials | BE/TI |
| Bearing Size (DF) | 279 mm Bore X 305 mm OD (11 X 12 in.) |
| Bearing Load Capacity | Approx 115 kg radial and axial (250 lbs.) |
| Bearing Stiffness | Approx 9 X $10^4$ kg/mm (5 X $10^6$ lbs./in.) |
| Starting Torque | 0.85 N-m (7.5 in.-lbs.) |
| Weight | 11.4 kg (25 lbs.) |
| Power | 1.5 watts peak |
| | 0.2 watts avg. (200 Hz Update Rate) |

By way of comparison, a catalog housed unit of 21 bits resolution in a stainless steel housing and a 203 mm (8 in.) thru hole weighs 32 kg (70 lbs.). A stainless steel shaft coupler weighs an additional 5.5 kg (12 lbs.). In the example shown, the user took responsibility for supplying the bearings for the encoder as well as coordinating the design of a stator diaphragm coupler. The interface was very carefully designed and tolerenced so that the encoder fit the user's structure in a manner that effectively line bored the parts.

The cartridge encoder has the advantage that the encoder may be built and inventoried and shipped as a self contained end item. The user of a cartridge system may field remove the encoder and substitute a spare. In addition, many users of cartridge encoders will procure a "dummy encoder" to support one end of their shaft should encoder removal be required. Compare the logistics with a kit encoder, where the apparatus is so highly integrated that many significant repairs to the user's bearing structure require an encoder teardown/rebuild.

Clearly, the cartridge approach can offer superior minimum weight, minimum volume performance. However, it should be noted that a lot of engineering analysis and coordination are required. This is why usage tends to be restricted to space applications where the engineering costs can be justified in the context of required system performance.

## ELECTRICAL CONSIDERATIONS

Encoders are generally classified into two types, incremental and absolute. Incremental encoders are usually two track devices; the two tracks are a main counting track and a once per revolution index track. By zeroing or resetting a counter with the once per revolution index it is possible to dead reckon and derive a multiple bit position word. Absolute encoders on the other hand have many tracks, all of which must be read out and processed.

Incremental encoders have what is termed a volatile output. That is to say if power is ever lost or interrupted, the encoder does not establish a correct position count until the once per revolution index is detected. Absolute encoders on the other hand have data storage in the form of the multiple track code patterns. These encoders are capable of providing a correct readout within a very short time after power is turned on since there is no need to rotate by the once per revolution index.

Some systems, such as high speed scanners, run by the index as often as every few milliseconds; other systems move at Earth's rate. Most systems operate somewhere between these extremes. In many high speed applications an incrementral encoder is satisfactory, while for Earth's rate applications, an absolute encoder is usually required.

Conventional wisdom has been that since the incremental encoder only has two tracks compared with upwards of 15 to 20 in a high resolution absolute encoder, that all things being equal, it would have a much lower power consumption, and if data acquisition times to acquire a current index position were acceptable, it would be the preferred encoder. This is no longer true. It is a fact that most absolute encoders used in space-craft have very low output word data update rates, usually from 20 per second up to about 1000 per second. By using a data acquisition multiplexing and storage system it is possible to design absolute encoders where the encoder is kept mostly unpowered except for a 100 to 150 microsecond interval, when it is desired to update data.

As an example, Figure 5 shows the power consumption profile of a typical 19 bit incremental encoder. Since the encoder depends on pulse counting to maintain the position data current, operation must be continuous. On the other hand, the absolute encoder in Figure 6 can be operated in an Interrogate or sampled data update acquisition mode. A low power "receiver" circuit is kept energized to detect receipt of the user's Interrogate, or Update request pulse. When it is received, a power switch circuit in the electronics unit turns on encoder power, acquires the current shaft position, stores it in memory, and transmits the updated position to the user. When the transmission is completed, the encoder circuits, except for the receiver, are returned to the unpowered state. The cycle is repeated as often as desired.

This pulsed data acquisition has two operating characteristics not common to continuous reading systems. First there is a delay to the user in reading the data. 100 to 150 microseconds is typical. This is not usually serious. The growing use of microprocessors and other computer devices make it possible to easily correct for delay time. Since shaft speed can be reconstructed from the past position data, correcting position to the start of Update is not difficult.

Also, with 100 Hz sampling rates (10,000 μsec period), the acquisition delay is a small percentage of the total updata period. Usually real time servo control is the most demanding application and the effect of 100 to 150 μsec acquisition delay on servo stability is small compared with most servo bandwidths.

A second feature of the Update mode of operation is the power profile, as shown in Figure 6. The power profile is characterized by a low, steady base load (receiver) and an additional pulsed load for data acquisition and transmission. The average power is low, and its function of readout rate is shown in Figure 7. For the example in Figure 6, the average power up to 5000 updates/sec. is lower than the incremental example in Figure 5. If the pulsed currents with a high form factor (ratio of peak to average) are a problem, a filter circuit/energy storage device can be used to smooth out the power profile seen by the user's power supply.

## SUMMARY

Basic architectural principles of mechanical and electrical interfacing of encoders have been presented. By understanding the basic principles, users are in a position to interface encoders, selecting those logistic, weight, or power saving techniques that will optimize the encoder for their particular application. Users wishing to study mechanical or electrical interfacing techniques in more detail are referred to two earlier papers by the author.

## REFERENCES

1) Installation and Maintenance of High Resolution Optical Shaft Encoders, SPIE Conference Proceedings, Volume 134, Photo and Electro-Optics in Range Instrumentation, March 1978

2) High-Performance Optical Encoders Can Have Small Size, Weight, and Cost, Electro-Optical Systems Design, Cahners Publishing Company, Sept. 1981

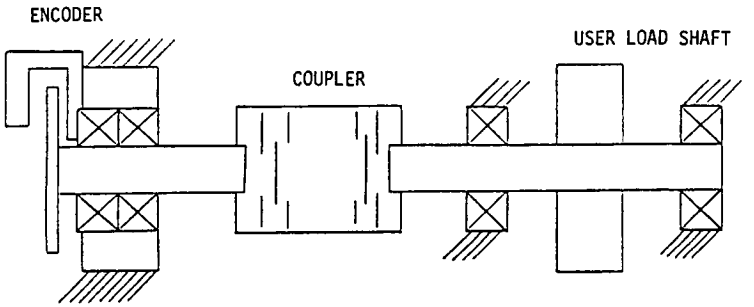


(a) Housed encoder.

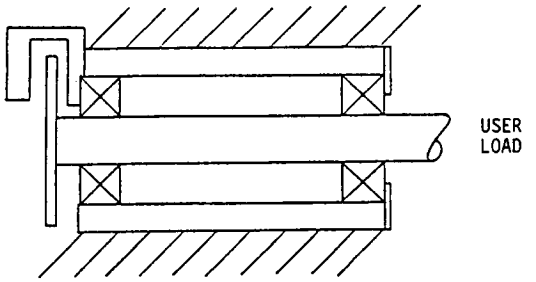


(b) Unhoused kit.

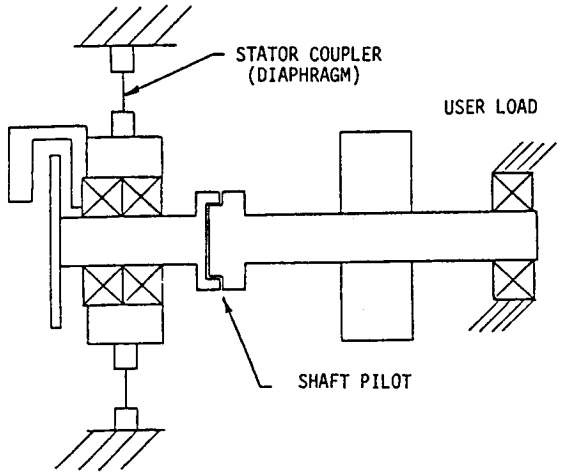


(c) Cartridge.

Figure 1. - Encoder mechanical interface architecture.

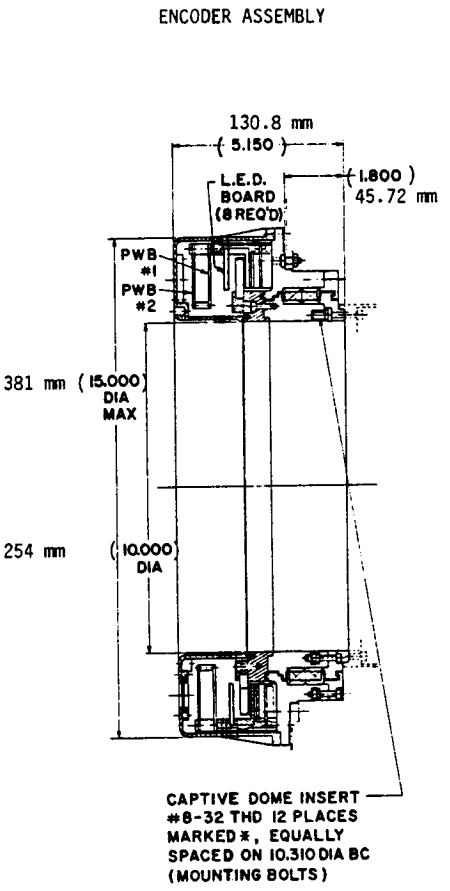


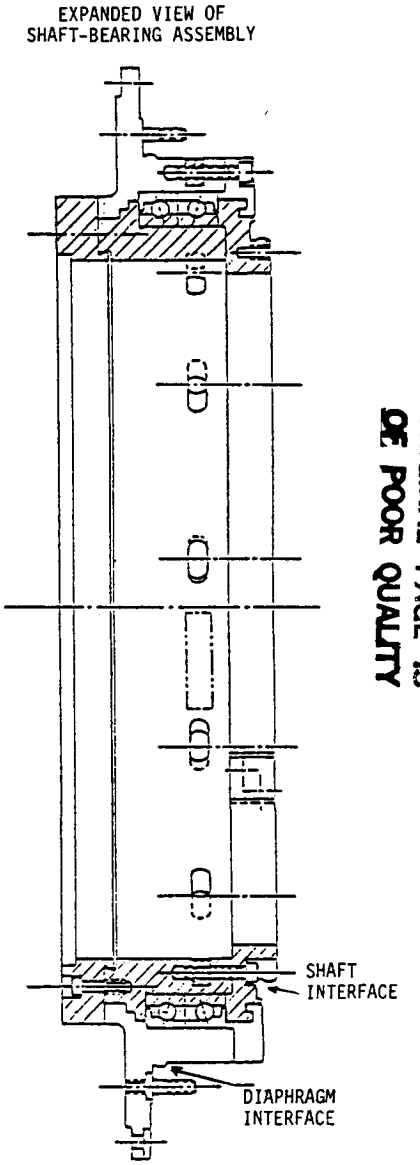




Figure 2. - Section views of a 21-bit cartridge encoder.

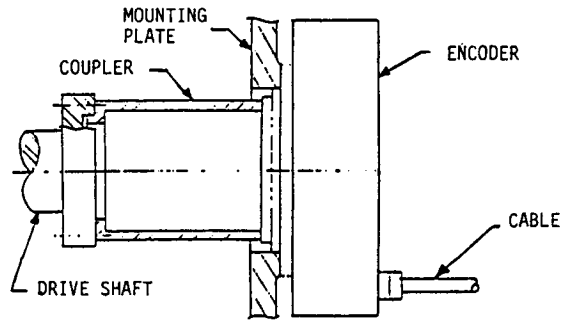


(a) External installation outside encoder.

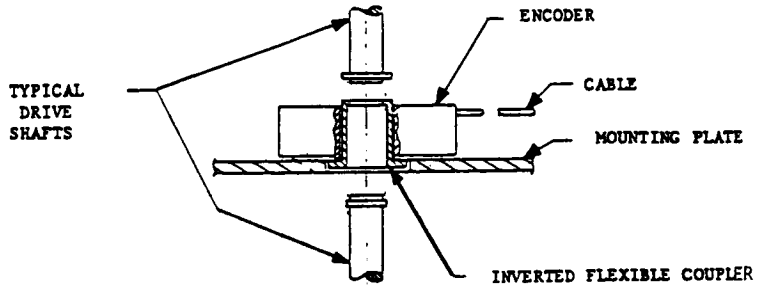


(b) Internal installation inside shaft through hole.

Figure 3. - Shaft coupler installation.

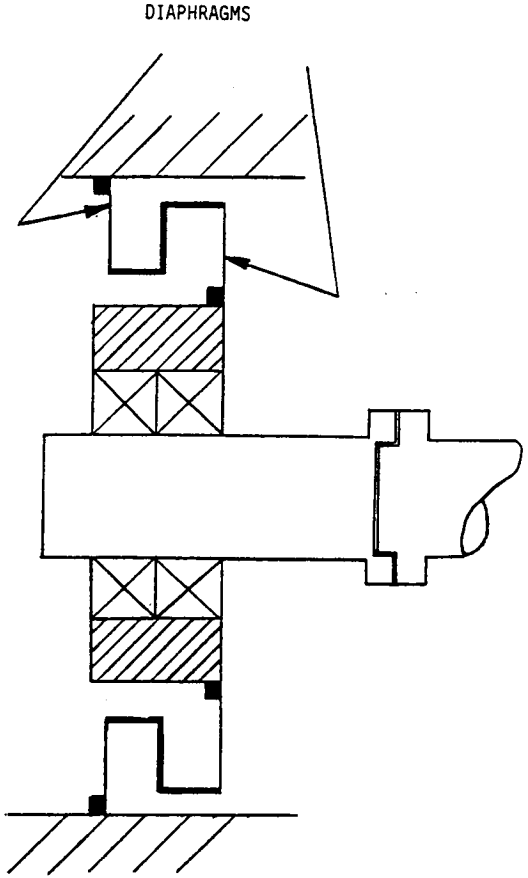


Figure 4. - Stator (body) coupler.

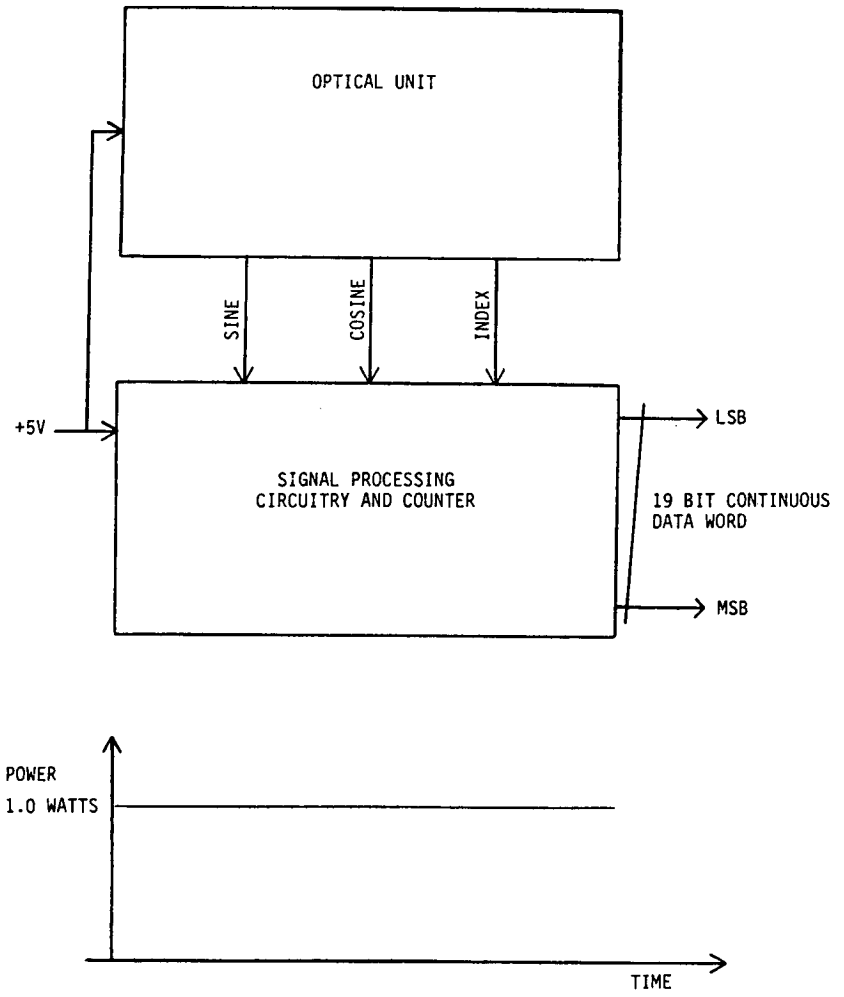


Figure 5. - Block diagram and power profile of 19-bit incremental encoder.

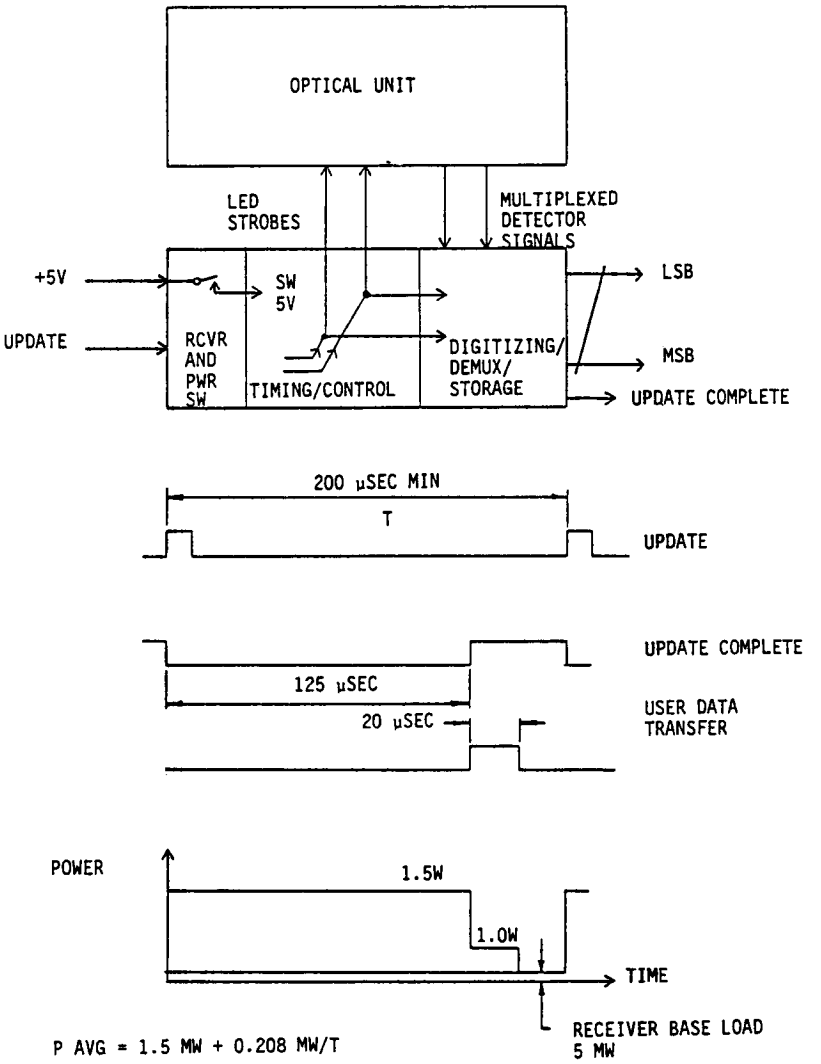


Figure 6. - Absolute, multiplexed encoder simplified block diagram and power profile.

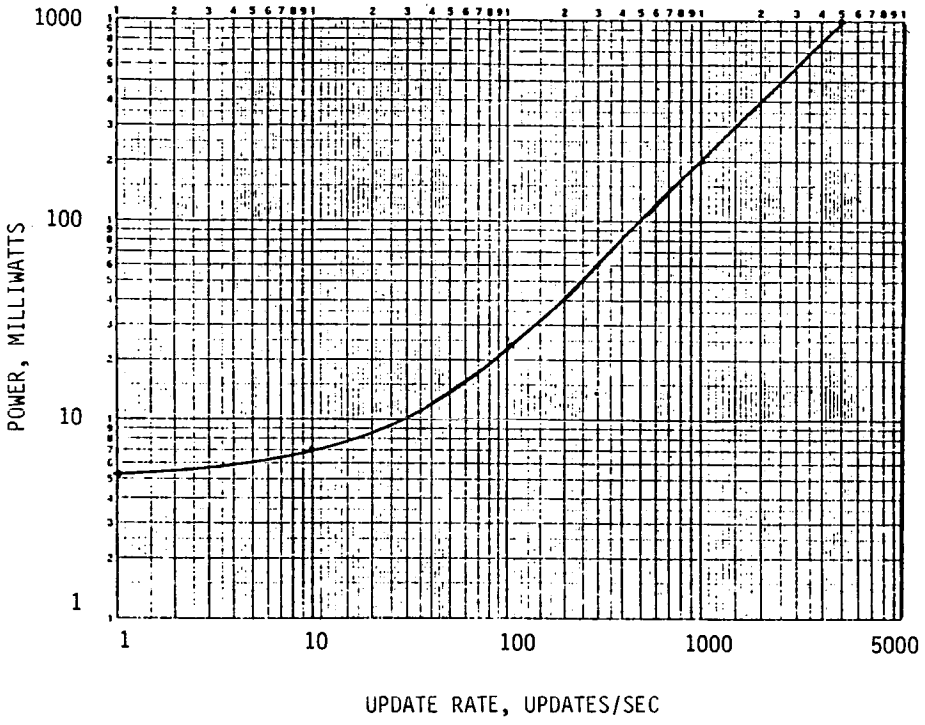


Figure 7. – Average power consumption as function of update rate of encoder shown in Figure 6.

| 1. Report No. | 2. Government Accession No. | 3. Recipient's Catalog No. |
|---|---|---|
| NASA CP-2423 (Revised) | | |

| 4. Title and Subtitle | 5. Report Date |
|---|---|
| 20th Aerospace Mechanisms Symposium | May 1986 |
| | 6. Performing Organization Code |
| 7. Author(s) | 8. Performing Organization Report No. E-2904 |
| | 10. Work Unit No. |
| 9. Performing Organization Name and Address<br>NASA Lewis Research Center<br>Cleveland, Ohio 44135 | 11. Contract or Grant No. |
| | 13. Type of Report and Period Covered<br>Conference Publication |
| 12. Sponsoring Agency Name and Address<br>National Aeronautics and Space Administration, Washington, D.C. 20546; California Institute of Technology, Pasadena, CA 91109; and Lockheed Missiles & Space Company, Inc., Sunnyvale, CA 94088 | 14. Sponsoring Agency Code |

15. Supplementary Notes

Minor revisions have been made to the proceedings distributed at the conference.

16. Abstract

The proceedings of the 20th Aerospace Mechanisms Symposium, hosted by the NASA Lewis Research Center, Cleveland, Ohio, on May 7-9, 1986, is documented herein. During the 3 days, 23 technical papers were presented by experts from the United States and Western Europe. A panel discussion by an international group of experts on future directions in mechanisms was also presented; this discussion, however, is not documented herein. The technical topics addressed included deployable structures, electromagnetic devices, tribology, thermal/mechanical/hydraulic actuators, latching devices, positioning mechanisms, robotic manipulators, and computerized mechanisms synthesis.

| 17. Key Words (Suggested by Author(s)) | 18. Distribution Statement |
|---|---|
| Actuators; Space lubricants; Rolling-element bearings; Mechanisms; Robotic manipulators; Thermal actuators; Traction drives; Positioning mechanisms; Tribology; Deployable structure; Electromagnetic devices; Electric motors; Hydraulic actuators; Sliprings; Latching devices | Unclassified - unlimited<br>STAR Category 39 |

| 19. Security Classif. (of this report) | 20. Security Classif. (of this page) | 21. No. of pages | 22. Price* |
|---|---|---|---|
| Unclassified | Unclassified | 329 | A15 |

*For sale by the National Technical Information Service, Springfield, Virginia 22161

NASA-Langley, 1986